TOWARDS SIMULTANEOUS ELECTROENCEPHALOGRAPHY AND FUNCTIONAL NEAR-INFRARED SPECTROSCOPY FOR IMPROVING DIAGNOSTIC ACCURACY IN PROLONGED DISORDERS OF CONSCIOUSNESS: A HEALTHY COHORT STUDY

by

MOHAMMED JUJAR RUPAWALA

A thesis submitted to the University of Birmingham for the degree of

DOCTOR OF PHILOSOPHY

School of Chemistry
College of Engineering and Physical Sciences
University of Birmingham
July 2020

Abstract

Qualitative clinical assessments of the recovery of awareness after severe brain injury require an assessor to differentiate purposeful behaviour from spontaneous behaviour. As many such behaviours are minimal and inconsistent, behavioural assessments are susceptible to diagnostic errors. Advanced neuroimaging tools such as functional magnetic resonance imaging and electroencephalography (EEG) can bypass behavioural responsiveness and reveal evidence of covert awareness and cognition within the brains of some patients, thus providing a means for more accurate diagnoses, more accurate prognoses, and, in some instances, facilitated communication. As each individual neuroimaging method has its own advantages and disadvantages (e.g., signal resolution, accessibility, etc.), this thesis studies on healthy individuals a burgeoning technique of non-invasive electrical and optical neuroimaging—simultaneous EEG and functional near-infrared spectroscopy (fNIRS)—that can be applied at the bedside. Measuring reliable covert behaviours is correlated with participant engagement, instrumental sensitivity and the accurate localisation of responses, aspects which are further addressed over three studies. Experiment 1 quantifies the typical EEG changes in response to covert commands in the absence and presence of an object. This is investigated to determine whether a goal-directed task can yield greater EEG control accuracy over simple monotonous imagined single-joint actions. Experiment 2 characterises frequency domain NIRS changes in response to overt and covert hand movements. A method for reconstructing haemodynamics using the less frequently investigated phase parameter is outlined and the impact of noise contaminated NIRS measurements are discussed. Furthermore, classification performances between frequency-domain and continuous-wave-like signals are compared. Experiment 3 lastly applies these techniques to determine the potential of simultaneous EEG-fNIRS classification. Here a sparse channel montage that would ultimately favour clinical utility is used to demonstrate whether such a hybrid method containing rich spatial and temporal information can improve the classification of covert responses in comparison to unimodal classification of signals. The findings and discussions presented within this thesis identify a direction for future research in order to more accurately translate the brain state of patients with a prolonged disorder of consciousness.

بسم الله الرحمن الرحيم

TO MY PARENTS AND WIFE

THANK YOU

Acknowledgements

I gratefully acknowledge funding from EPSRC through a studentship from the Sci-Phy-4-Health Centre for Doctoral Training (EP/L016346/1)

I gratefully acknowledge collaborations with the Cruse Lab, Medical Imaging and Image Interpretation Group and Sci-Phy-4-Health CTD at the University of Birmingham.

I gratefully acknowledge my supervisors Damian Cruse, Hamid Dehghani, Sam Lucas and Peter Tino for their mentorship and in my development as a scientific researcher. I specifically thank my principal investigator Damian Cruse for driving me to constantly develop my skills as a computer scientist and guiding me in my career within academia.

I gratefully acknowledge Matthaios Doulgerakis-Kontoudis for joint collaboration in setting up the functional near-infrared spectroscopy imaging system and in the development of analysis tools.

Table of Contents

List of publications

An edited version of this publication has been used throughout this thesis.

Rupawala, M., Dehghani, H., Lucas, S, J, E., Tino, P., and Cruse, D. (2018) Shining a Light on Awareness: A Review of Functional Near-Infrared Spectroscopy for Prolonged Disorders of Consciousness. *Front. Neurol*. 9, 350. doi: 10.3389/fneur.2018.00350.

List of figures

List of tables

List of abbreviations

AUC	Area under the curve
BCI	Brain computer interface
BOLD	Blood oxygenation level dependent
cm	Centimetres
CMW	Complex Morlet wavelet
CRS-R	JFK Coma Recovery Scale-revised
CSD	Current source density
CSP	Common spatial pattern
CWL	Continuous-wave-like
EEG	Electroencephalography
EMCS	Emergence from a Minimally Conscious State
EMG	Electromyography
ERD	Event-related desynchronisation
ERP	Event-related potential
ERS	Event-related synchronisation
FD	Frequency-domain
FIR	Finite impulse response
fNIRS	Functional near-infrared spectroscopy

fMRI	Functional magnetic resonance imaging
HbO	Oxygenated haemoglobin
HbR	Deoxygenated haemoglobin
HbT	Total haemoglobin
Hz	Hertz
I_{AC}	Amplitude-modulated intensity
IIR	Infinite impulse response
LDA	Linear discriminant analysis
LiS	Locked-in syndrome
MCS	Minimally Conscious State
mm	Millimetres
MRI	Magnetic resonance imaging
ms	Milliseconds
NIRS	Near-infrared spectroscopy
PDOC	Prolonged Disorders of Consciousness
PMA	Premotor area
ROC	Receiver operating curve
ROI	Region of interest
s	Seconds

SMA	Supplementary motor area
SNR	Signal-to-noise ratio
STFT	Short-time Fourier transform
SVM	Support vector machine
UWS	Unresponsive Wakefulness Syndrome
VS	Vegetative State
WHIM	Wessex Head Injury Matrix
Θ	Phase
$\Delta[\cdots]$	Change in concentration

Chapter 1

Literature review and aims

1.1. Introduction

In the UK, every three minutes an individual is hospitalised due to a traumatic (e.g. fall, assault, motor vehicle accident) or non-traumatic (e.g. stroke, brain haemorrhage, anoxia) brain injury, equating to approximately 300,000 admissions per year (Headway, 2017). Many of these patients will experience little or no long-term effects and will rapidly transit through the following states of Prolonged Disorder Of Consciousness (PDOC) during recovery: Coma, Vegetative State (VS) (which is also frequently referred to as Unresponsive Wakefulness Syndrome (UWS) in the literature (Laureys et al., 2010)), Minimally Conscious State (MCS) and emergence from MCS (EMCS) (figure F1.1) (Gosseries et al., 2011). This recovery path is consistent with the two aspects of consciousness; in the first instance an individual's level of consciousness is recovered, i.e. wakefulness, followed by the re-building of its contents, i.e. awareness (Bayne et al., 2016; Zeman, 2001). Patients in a VS/UWS are clinically awake, with eyes open and preserved reflexes, yet appear to be unaware of their surroundings or of themselves (for a detailed review of the PDOC states please refer to (Laureys et al., 2004)). Patients in a VS/UWS can be categorised into three groups, specifically: 1) transitory, where a patient very briefly displays signs of a VS however rapidly progresses towards independence; 2) continuing, which is defined as a sustained VS present one month after acute traumatic or non-traumatic brain damage, and 3) permanent, when it is still present six months after non-traumatic brain damage, or twelve months after traumatic injury (Laureys et al., 2004; Royal College of Physicians, 2020; The Multi-Society Task Force on PVS, 1994). Patients in a minimally conscious state exhibit inconsistent but purposeful evidence of awareness, such as visual pursuit and following verbal commands (Giacino et al., 2002). The classification of PDOC is not to be confused with the branch of Locked in Syndrome (LiS), which is a condition due to a specific brain stem injury in which patients are aware but have limited or no means

to move or communicate (Bauer et al., 1979; Laureys et al., 2005). As a result, LiS patients share similar challenges as those diagnosed with PDOC (i.e. patients in an early minimally conscious state are clinically aware but can lack the mobility to respond to commands).

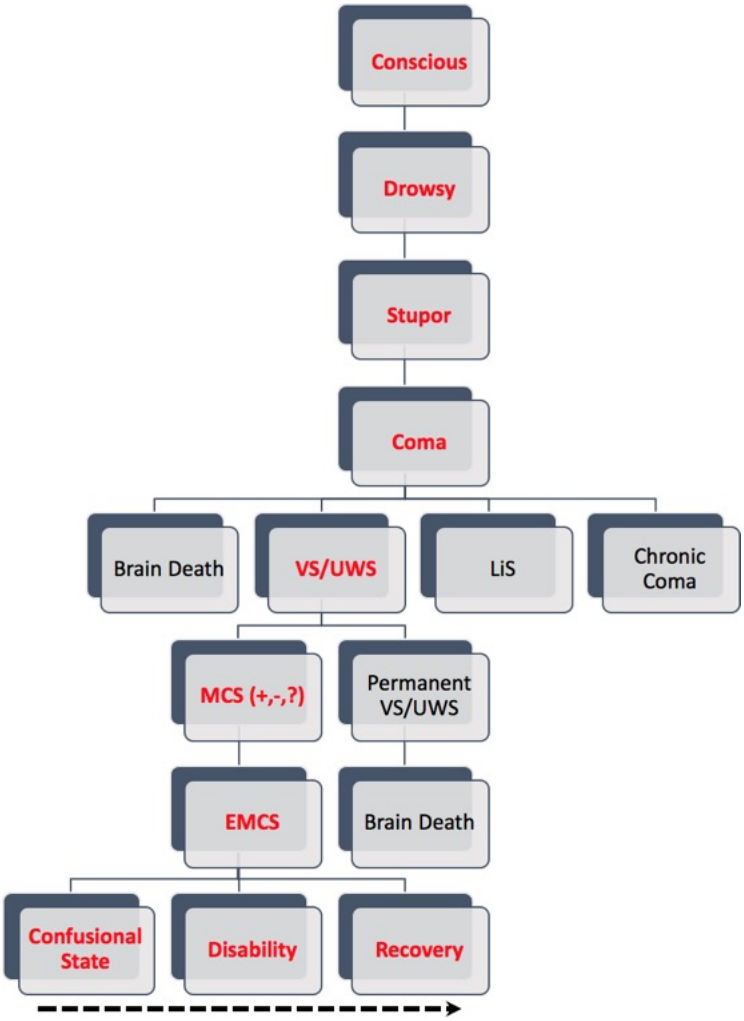

Figure F1.1: A potential route towards recovery following severe traumatic brain injury. LiS, locked-in syndrome; VS, vegetative state; UWS, unresponsive wakefulness syndrome; MCS, minimally conscious state; MCS^{+}, minimally conscious state plus; MCS^{-}, minimally conscious state minus; $MCS^{?}$, vegetative state with covert awareness; EMCS, emergence from a minimally conscious state. Figure adapted from (Laureys et al., 2004). No permissions were required.

The progression between each of the states of PDOC is generally smooth (Gosseries et al., 2011) and therefore the difficulty lies in accurately determining and diagnosing a patient in a single

state using qualitative clinical assessment methods. The need to accurately detect awareness remains a thorough subject of research as misdiagnoses can lead to inappropriate healthcare decisions, such as instances of pain perception (Demertzi et al., 2009) or end-of-life decisions (Demertzi et al., 2013). Standardised behavioural assessments such as the JFK Coma Recovery Scale-Revised (CRS-R) and Wessex Head Injury Matrix (WHIM) are the current "gold standard" for detecting signs of awareness (Giacino et al., 2004; Morrissey et al., 2018; Shiel et al., 2000). Various other methods, including skin conductance response, diameter of the pupils, breathing control and mini movement micro-switch have also been proposed to advance the diagnosis and assessment of PDOC (Charland-Verville et al., 2014; Lancioni et al., 2012; Scott et al., 2011; Stoll et al., 2013). However, as clinicians must rely on observable behaviours to determine a patient's level of awareness, it is possible that a significant proportion of patients can be misdiagnosed (approximately 40% (Schnakers et al., 2009)) if they are unable to produce purposeful behaviours due to a motor impairment. Indeed it has been estimated that 15% of patients (Kondziella et al., 2016) who meet the behavioural gold-standard for vegetative state have a cognitive-motor dissociation (Schiff, 2015) or covert awareness (Fernández-Espejo et al., 2015) that can only be detected with brain imaging. This therefore stresses the need for objective multimodal assessments that can cover all aspects of brain functioning including:

- Positron Emission Tomography (Laureys et al., 1999; Schiff et al., 2002) to assess metabolism,
- Magnetic Resonance Imaging (MRI) (Fernández-Espejo et al., 2010a) to capture structural images,
- Functional MRI (fMRI) (Owen et al., 2006), functional Near-Infrared Spectroscopy (fNIRS) (Kempny et al., 2016) and functional Transcranial Doppler (Naro et al., 2018) to record haemodynamic responses,
- Diffusion Tensor Imaging (Cavaliere et al., 2015; Fernández-Espejo et al., 2010b, 2011) to obtain structural changes in the white matter,
- Electroencephalography (EEG) (Cruse et al., 2011) and Magnetoencephalography (Schiff et al., 2002) to map dynamics of cortical activations.

In the first demonstration of covert command-following, Owen and colleagues asked a patient who fulfilled all clinical criteria for a diagnosis of vegetative state to undertake two motor imagery tasks in an MRI scanner (i.e. applied an fMRI methodology); the first involved playing a game of tennis and the second, a spatial navigation task, involved imagining visiting the rooms of their house (Owen et al., 2006). As is seen in healthy individuals when completing the same tasks, significant activity was observed in the patient's supplementary motor area (SMA) whilst imagining playing tennis, and in the parahippocampal gyrus, the posterior parietal cortex, and the lateral premotor cortex (PMC) when imagining moving around their house. This brain-imaging evidence of the patient following the commands indicated that the patient was aware, despite the fact that they were unable to demonstrate it with their behaviour. Subsequently, by assigning each imagery task to a 'yes' or 'no' communication output, several patients have been able to answer a series of questions about themselves and their lives (Bardin et al., 2011; Fernández-Espejo and Owen, 2013; Monti et al., 2010; Naci and Owen, 2013), hinting at the potential for brain-computer interfaces (BCIs) and assistive devices for this patient group. Here a BCI is defined using the definition proposed by Wolpaw and colleagues: a device that "provides the brain with a new, non-muscular communication and control channel" ((Wolpaw et al., 2002), page 768). In this context a BCI serves to directly measure neural activity associated with the users' intent and translate the recorded signals into corresponding control signals for BCI applications.

Following this work, Vogel and colleagues were able to predict recovery in patients diagnosed as vegetative or minimally conscious using the same paradigm of tennis playing and room navigation. In contrast to the study by Owen and colleagues whereby fMRI activation profiles of the two tasks were compared to rest (Owen et al., 2006), Vogel and colleagues contrasted the two profiles to each other thereby reducing the false positives rate (Vogel et al., 2013). By examining the neural regions of interest (ROIs) that are expected to show significantly increased activations for each contrast they were able to identify 100% of patients (5 out of 5) in a VS that progressed into an MCS state and 67% of patients (6 out of 9) in an MCS state that transitioned into an EMCS state. Furthermore, none of the patients in a vegetative or minimally conscious state that presented no activations in the ROIs progressed towards recovery.

Despite the success of fMRI in the field of PDOC, the technology is limited because many patients' reduced mobility requires them to be transported to advanced facilities that feature such equipment. However, recently Fernández-Espejo and colleagues demonstrated that single subject activations of ROIs during mental imagery tasks could be achieved in approximately 80% of cases using both 3T and hospital grade 1.5T MRI scanners lending the technique to widespread clinical use (Fernández-Espejo et al., 2014). Nevertheless, the need to bring patients to a scanner makes repeated assessments difficult, and can overlook evidence of awareness in patients whose arousal levels fluctuate throughout the day (Bardin et al., 2011). Furthermore, the fMRI approach is unsuitable for those with metallic implants, is highly sensitive to motion artefacts, and requires patients to lay supine. A portable, inexpensive, and non-magnetic method for measuring the same haemodynamic response as measured by fMRI could be used to translate the successes of fMRI to the bedside.

Following in the footsteps of fMRI research in PDOC, the overarching goal of this thesis is to improve the accuracy of detecting covert command-following at the bedside. The limitations of fMRI together with the need for continuous bedside neuroimaging methods suggest further exploration of portable EEG and NIRS technology in their capabilities to accurately and sensitively measure cortical activity from the scalp. In order to achieve this overarching goal, the aim of the presented research is to specifically investigate the utility of fNIRS and simultaneous EEG-fNIRS for detecting covert command-following using motor imagery. The research within this thesis, whilst concentrated on healthy individual data collection and analysis, incorporates select challenges faced in patient assessments and therefore acts as the fundamental building blocks for extending the proposed simultaneous EEG-fNIRS technology and methodology into the clinic. With further development of this research it is possible that we may be able to achieve continuous bedside monitoring that ultimately improves diagnostic accuracy of a patient's level of awareness and communication between clinicians and patients in a PDOC.

The remainder of this chapter provides an overview of both EEG and fNIRS technology, and the literature surrounding its use for covert command-following using motor imagery. Furthermore, this chapter explores research that has been performed using simultaneous EEG-fNIRS, discusses limitations of the hybrid technology and methodology in its current form, and provides notable

examples of where the technology has been piloted for use in patients with PDOC or LiS for either awareness detection or communication. This chapter concludes by summarising key discussion points and detailing the hypotheses and rationale for each of the three experimental chapters within this thesis. The three experimental chapters work towards developing a simultaneous EEG-fNIRS imaging methodology for covert command-following detection. The outputs of these chapters are then discussed together in a final conclusions chapter with respect to the method's clinical potential for awareness detection in patients with PDOC.

1.2. Electroencephalography

Electroencephalography is a portable, non-invasive, inexpensive tool for recording neural activity and is widely growing popular within the field of PDOC as an alternative method to fMRI and behavioural assessments to determine the level of awareness in patients. EEG activity primarily arises from the temporal synchronised activity of populations of cortical pyramidal neurons as revealed by the summation of postsynaptic potentials at their apical dendrites (Pfurtscheller and Lopes da Silva, 1999). The ability to directly measure these electrical fields enables EEG to benefit from high temporal resolution (millisecond time-frame). The creation of an extracellular voltage that is more negative at these dendrites than elsewhere along the neuron results in randomly oriented groups of neurons of like charges repelling one another and an impeded "wave" of charge traveling through the extracellular space. This process of volume conduction is responsible for the propagation of the EEG signal within the brain and is aided by cerebrospinal fluid and various ion-filled substances in the brain that are very good conductors of this electrical charge (figure F1.2). Once the volume conducted signal reaches the end of its volume such as the dura layers, skull, scalp and electrode, capacitive conductance is responsible for propagating the signal between these layers (figure F1.2). The size of the inner charged pool of ions, and the distance between the pool of charged ions and the insulating layer will determine the extent of capacitive conduction. Each layer will have its own volume conduction effect that propagates in multiple directions. As such, a negative by-product of this at the scalp electrodes is a spatially smeared signal. At the scalp insulating layer, the conducted neural signals propagate through

the electrode gel and can be amplified at active electrodes (Mathewson et al., 2017) before reaching the acquisition computer. Both the electrode gel and amplifier aim to increase the signal-to-noise ratio (SNR), however in different ways. Prior to application of the electrode gel the skin is extensively prepared (skin aberration), thereby minimising the resistance of the electrode-scalp connection. At the electrode, amplification of the signal is dependent on the impedance of the electrode which drops the voltage to an extent that significantly reduces electrical noises that may enter the system as the signal propagates along the wires to the computer (Jackson and Bolger, 2014).

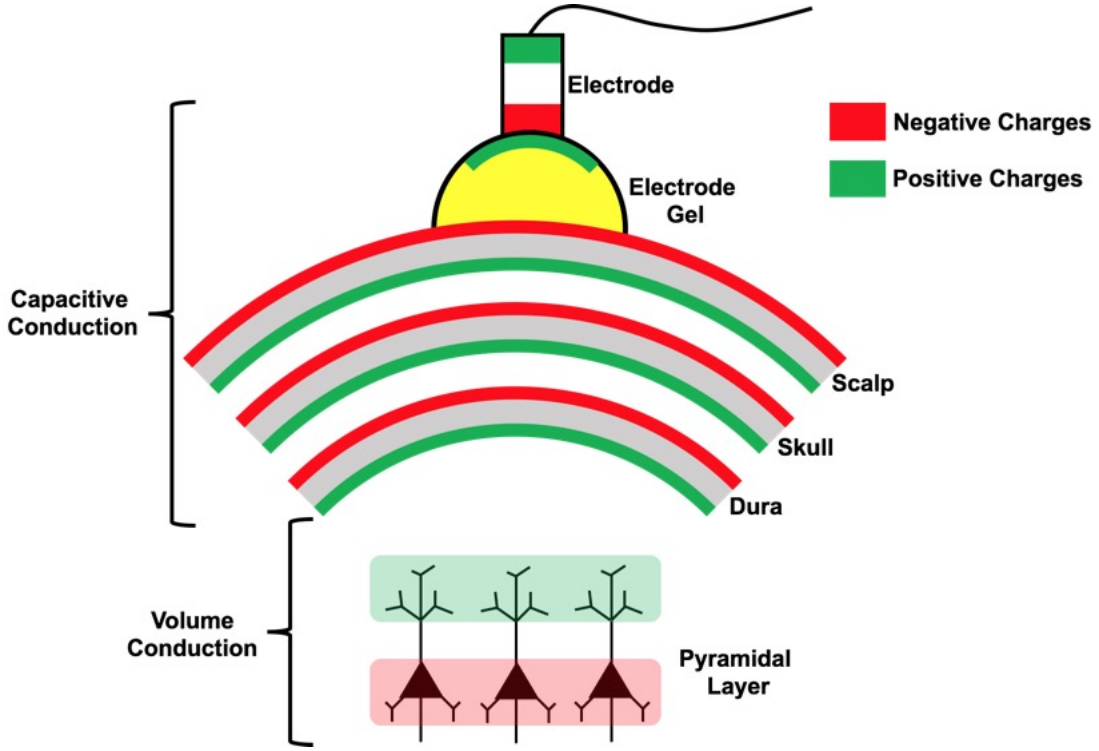

Figure F1.2: An example of an electrical signal propagation pathway through the brain. A difference in charge between the soma and apical dendrites of several radial dipoles results in a net positivity in the immediate vicinity. Through the process of volume conduction (repulsion of like charges in all directions in a homogeneous medium) this positive charge propagates across the brain till it reaches a capacitive layer. The electrical signal propagates across several capacitive layers, including the layers of brain, dura, skull, scalp and electrode gel through the repulsion of like charges at the boundary surfaces (the size of this repulsion depends on the thickness of the boundary). The gel is a conductor and hence less attenuation allows more of the signal to reach the electrode. Figure adapted from (Jackson and Bolger, 2014). No permissions were required.

The output of an EEG signal is a waveform encompassing multiple frequencies. The frequency characteristics of the signal are predominantly categorised into five groups that reflect different aspects of brain activity, including delta (<4 Hz), theta (4-8 Hz), alpha (8-13 Hz), beta (13-30 Hz) and gamma (>30 Hz). An individual at rest with their eyes closed generates the posteriorly dominant alpha rhythm. Both alpha frequency and amplitude are generally symmetrical over the two hemispheres of the head and any deviation from this (i.e. slower oscillations) may suggest abnormal cerebral functioning. Unilateral or bilateral alpha band activity over the sensorimotor cortices are termed mu (Kuhlman, 1978). Rolandic mu rhythms are unrelated to eye opening and are sensitive to movement, somatosensory stimuli and thoughts of movement. Such cortical alpha rhythms are correlated with conscious awareness and are abnormal in patients in a VS due to their lack of awareness (Hughes, 1978). Unlike alpha, beta frequencies are lower in amplitude and are sensitive to the functions of the sensorimotor cortex, whilst also being enhanced by drowsiness (Britton et al., 2016; Kumar and Bhuvaneswari, 2012). As such, both mu and beta rhythms are most commonly explored in the context of motor function and mental imagery in the field of PDOC. The amplitude of the raw EEG is relatively small and as such subtle functional changes induced by sensory, motor or cognitive activities cannot be observed unless the data are averaged. Averaging increases the SNR therefore revealing activity that is time-locked to the stimulus, so called Event Related Potentials (ERPs) (Lehembre et al., 2012). Each ERP may represent frequency specific changes that can be identified by either decreases (event-related desynchronisation or ERD) or increases (event-related synchronisation or ERS) of the power in given frequency bands. Such fluctuations are associated with increases or decreases in synchrony of the underlying neural populations (Pfurtscheller and Lopes da Silva, 1999).

An EEG in a patient in a VS will show a marked general slowing of their electrical brain activity (Schiff et al., 2014). EEG power spectra for patients in a VS are concentrated at very low frequencies (<1 Hz) whereas those of patients in an MCS show prominent peaks within the theta (3-7 Hz) and beta (15-30 Hz) frequency bands (Schiff et al., 2014). It has additionally been shown that patients in a continuing VS with some level of consciousness and patients in an MCS can have low alpha rhythm activity (8-13 Hz) across parietal and occipital brain regions (Babiloni et al., 2009). As such, if a patient were misdiagnosed then their ability to follow commands and display signs of awareness would be

reflected in heightened brain activity in the regions corresponding to the task, provided that they were structurally present. In the first study of its kind, Cruse and colleagues demonstrated the utility of EEG to detect command following, and as such awareness, in three out of sixteen patients who met the CRS-R definition of VS using motor imagery of the right-hand and toes (Cruse et al., 2011). Here, motor imagery is defined as imagined movement of the body while keeping the muscles still. Motor imagery tasks can be divided into visual and kinaesthetic tasks. In the former, the participant visualises the movement whilst in the latter the participant imagines the feelings and sensations produced by the movement. Kinaesthetic motor imagery is more often used as it has been shown to recruit more of the cortical motor system (Guillot et al., 2009). Motor imagery tasks can provide proxies of command-following for those patients who may be aware but unable to produce purposeful overt behaviours. However, motor imagery blood-oxygen-level-dependent (BOLD) activation is not always detectable in all participants; indeed, Fernández-Espejo and colleagues found no appropriate activation in 20% of healthy participants in one study (Fernández-Espejo et al., 2014). Nevertheless, the patients in the study by Cruse and colleagues took part in four to eight blocks (median 114 trials) of right-hand and toes imagery (Cruse et al., 2011). Having derived a single feature vector for each trial containing band-power activity from the alpha and beta frequency ranges at each timepoint within the action period, the team were able to classify trials of the two types of motor imagery using a support vector machine (SVM) classifier with an average accuracy of 70% for the three patients. This study highlighted that potentially misdiagnosed patients capable of following commands were able to modulate the appropriate frequency bands of the EEG signal that are associated with motor imagery, over the same regions of the head where this activity is known to occur in healthy individuals. A follow up study by Cruse and colleagues used only four electrodes for analysis (in comparison to the previous 25) on a single patient diagnosed in the VS for 12 years (Cruse et al., 2012). The patient was asked to perform left- and right-hand movements, and following single trial classification, significantly above chance accuracies at a maximum of 67% were found between left-hand and rest. Overall, Cruse and colleagues were able to identify that it was possible to detect ‘attempts’ to follow commands by patients in the VS even in the absence of any overt motor output.

Feature classification, as used to differentiate EEG responses to the two different commands in the above studies, is a pattern recognition technique used to categorise data into different classes. The feature vector is a collection of defining or characteristic observations from the pooled data (thus forming points in a feature space) that have similar values for one class and different values for another class. A combination of these features from a subset of trials with known class labels can then be used as a training set to train a classifier (supervised learning). During this period, points within the feature space are transformed in a manner that allows their effective separation into two or more well separated class spaces (i.e. a pattern is derived). Trials of a test data set are then applied to this learned-classifier in order to separate brain-signal patterns into different classes to a degree of accuracy (Bishop, 2006; Jain et al., 2000; Lotte et al., 2018; Naseer and Hong, 2015). For a two-class problem (i.e. left- and right-hand imagery) support vector machine (SVM) classifiers are greatly favoured, as they attempt to maximise the distance between the separating hyperplane and the nearest training points – or so-called support vectors thereby increasing generalization capabilities (Lotte et al., 2007, 2018; Naseer and Hong, 2015). Other classifiers include linear discriminant analysis (LDA, another linear classifier similar to SVM), multi-layer perceptron (a type of neural network classifier), hidden Markov models (a type of Bayesian classifier) and k-nearest neighbour (a type of nearest neighbour classifier) (Lotte et al., 2018; Naseer and Hong, 2015). The choice of classifier depends on several factors including how noisy the data is and thus the number of outlier features, the stationarity of signals, dimensionality and complexity (i.e. are the classes linearly or non-linearly separable) of the feature space, the number of training sets, and the required classification speed (Lotte et al., 2007). The classified signals are then sent to an external device to generate the desired response. Based on the typical BCI definition, such desired responses are translated outputs from neuronal electrophysiological user inputs that can be used to control electrical devices. However, in the context of motor imagery research for awareness detection, the desired response is a display of the accuracy of the users' intent, based on their brain activity allowing self-regulation of brain functions.

Alongside motor imagery, several other imagery strategies have also been explored including auditory imagery, face imagery, mental rotation, mental singing, mental subtraction, spatial navigation, word generation (Banville et al., 2017; Curran et al., 2004; Friedrich et al., 2012), and emotion-induced

imagery (Bigirimana et al., 2020; Iacoviello et al., 2015; Sitaram et al., 2011). Curran and colleagues reported higher EEG classification accuracies across a group of 10 healthy participants for navigation and auditory imagery tasks over classical left-/right-hand motor imagery movement tasks (Curran et al., 2004). In contrast, Bigirimana and colleagues showed comparable (Bigirimana et al., 2017) or greater (Bigirimana et al., 2020) EEG single-trial classification accuracies for simple motor imagery tasks verses emotion-induced imagery. In their most recent publication (Bigirimana et al., 2020), using a computer game to better engage the participants attention with the task, participants were instructed to imagine moving their left-/right-hand when directed to the left-/right-side cue respectively during the motor imagery run. For the emotion-induced imagery task participants were instructed to recall a sad/happy event for the left-/right-side cue respectively. Across a group of 12 healthy participants, 10 had higher average single-trial classification scores for motor imagery over emotion-induced imagery tasks. Furthermore, of these 10 participants, 7 had average scores above 70%. Reasons for the greater effectiveness of motor imagery over emotion-induced imagery include the consistency of the imagined action (unspecified emotional imageries can be highly varied across participants), spatial patterns consistently highlighting activation of the sensorimotor cortex (Pfurtscheller and Neuper, 1997) (depending on the vividness of the imagery, an emotional-induced task may activate several areas of the brain (Addis et al., 2007)), and long duration frequency activation in alpha and beta bands (for emotional-induced imagery, frequencies activated in these bands are short lived) (Bigirimana et al., 2020). Nevertheless, alterative imageries can be beneficial for those who cannot control a motor imagery BCI.

Beyond simple motor imagery commands, progress in the field has involved assessing the scope of more complex mental imagery tasks. Gibson and colleagues measured EEG accuracies of healthy participants performing a range of simple (right-hand, left-hand and both hands) and complex (juggling with two hands, playing a guitar, clapping) mental imagery tasks with the aim of detecting increased brain activity during complex motor imagery and obtaining higher classification accuracies than when imagining relatively simpler actions (Gibson et al., 2014a). Further to this, pianists were recruited to perform imagery of simple piano playing followed by imagery of a complex piece to determine whether prior motor familiarity of a task could boost classification accuracies for a complex

yet familiar task. The authors presented that when single trial classifying against rest, complex imagery marginally out-performed simple imagery (average classification scores for simple and complex imageries were 61% and 63% respectively). This was likewise true for skilled participants such as the pianists, which achieved scores of 66% and 70% during simple and complex piano imagery respectively. Their results highlighted the potential for customised complex imageries to be used for detecting covert command-following in, and even communicate with, behaviourally non-responsive patients and stressed to confer with care-givers to identify actions with which the patient had experience and that would activate multiple sensory brain regions. Following this, Goldfine and colleagues demonstrated a patient in the MCS and one in a LiS to perform swimming and room navigation imageries using power spectral analysis at multiple frequencies (Goldfine et al., 2011). Horki and colleagues extended this to detect mental imagery of playing a sport of one's choice and navigating around a room and attempted movements of feet dorsiflexion using classification in six patients in a MCS (Horki et al., 2014). Using the data from 32 EEG electrodes, band power features were calculated for multiple frequency bands and classified using an LDA classifier. The authors showed that classification accuracies above chance were reached in all three tasks, with motor tasks yielding significant results more often than navigation. Furthermore, the two motor tasks (sport imagery and attempted feet movements) accounted for 62% of sessions yielding significant accuracies in line with previous studies (Friedrich et al., 2012).

Due to the heterogeneity of aetiology and pathology in patients with a PDOC, multiple imaging techniques and functional tasks can additionally improve the accuracy in identifying a patient's covert ability to follow commands. Gibson and colleagues in a later publication demonstrated the effectiveness of multimodal imaging (EEG and fMRI) in comparison to behavioural assessments as measures of awareness (through covert command-following) in patients in VS and MCS states (Gibson et al., 2014b). fMRI motor (tennis) and spatial (navigation) imagery commands were identical to those previously used (Fernández-Espejo et al., 2014; Owen et al., 2006; Vogel et al., 2013), whereas with EEG imagery commands were in the form of squeezing the right-hand (Cruse et al., 2011) and dialling a phone number. Interestingly, by studying the fMRI ROIs for tennis and navigation imagery (see section 1.1) and power spectral estimates of the two electrode channels, Gibson and colleagues were

able to identify that of three patients that were unable to follow commands, one patient in the VS produced evidence of covert command-following in both the fMRI and EEG tasks and two patients (one in the VS and one in the MCS^-) exhibited evidence of command following in the spatial navigation fMRI task only (Gibson et al., 2014b).

Having seen that patients with signs of awareness can discriminate motor imageries of multiple tasks using EEG, it is possible to extend this classification into a communication tool as previously demonstrated with fMRI (Bardin et al., 2011; Fernández-Espejo and Owen, 2013; Monti et al., 2010; Naci and Owen, 2013). Guger and colleagues compared the efficacy of motor imagery in comparison to vibro-tactile stimulation as a communications means for patients in a LiS (Guger et al., 2017). Patients were given vibro-tactile stimulation on the left- and right-wrists and a stronger distractor stimulation on the back or shoulder. Patients were then asked to count stimuli to a target hand (left or right) resulting in the generation of a P300 event related potential. When extending towards communication, patients were asked questions and a reply of 'yes' or 'no' was determined by the patient counting stimuli on either the left- or right-hand respectively. In comparison, during motor imagery patients answered 'yes' or 'no' by imagining hand movements of the left- or right-hand accordingly. Nine patients took part in the vibro-tactile communication task resulting on average in 80% classification accuracy (8 of 10 questions answered correctly), whereas for the three patients that took part in the motor imagery-based communication task, the classification accuracy achieved was 94%. The different patient group sizes taking part in motor imagery based and vibro-tactile stimulation based communication make it difficult for direct comparisons to be made, however previous research has found P300-based systems to typically need less training time and to achieve higher accuracies than motor imagery-based BCI systems (Acqualagna et al., 2016; Guger et al., 2003). A follow-up study using the P300 vibro-tactile stimulation as a communication means in patients with UWS resulted in more than 60% of the questions being answered correctly (Guger et al., 2018).

Dayan and colleagues on the other hand used a sensorimotor rhythm-based BCI protocol to assess awareness in patients with PDOC whilst additionally testing a communication paradigm using closed questions with known answers (Dayan et al., 2019). Sensorimotor rhythms are defined as the oscillatory changes in mu and beta frequency bands during sensorimotor processing (Coyle et al.,

2005a; Pfurtscheller et al., 1998; Pfurtscheller and Lopes da Silva, 1999). In the first EEG study, three patients diagnosed with UWS and two patients diagnosed with MCS performed hand/feet imagery whilst receiving stereo-auditory feedback given as broadband noise or music samples (Coyle et al., 2015). These patients were able to modulate their brain activity in the initial motor imagery assessment (average classification accuracy of 67%), which further improved in the presence of feedback (average classification accuracy of 77%). Having identified patients with UWS as reporting significant above chance accuracies conflicted with their diagnosis of lacking awareness. Furthermore, the authors noted that average classification accuracies across multiple assessment/feedback sessions for both patients with UWS and MCS were insignificantly strongly positively correlated to the CRS-R and WHIM behavioural scores. These findings demonstrate that such EEG-based sensorimotor rhythm BCIs may provide supplementary diagnostic information not detected by standard behavioural tests designed for assessing patients with UWS. In the second EEG study, two patients (one of the three patients with UWS and one of the two patients with MCS) and two healthy individuals performed hand or feet motor imagery as 'yes' or 'no' responses to 48 questions that were semantically similar e.g., "You are 33 years old" verses "You are 47 years old". The authors reported above chance classification accuracies of 69% (UWS) and 73% (MCS) respectively for the patients that were lower than the scores obtained by the two healthy individuals (77 and 81%). Despite having kept the patients engaged with the task through question being delivered by family members, the authors highlighted an important future need for a third task as a response to "I don't know" to prevent patients from performing a complex dual response or an entirely different response when the answer to a question was unclear.

Mangia and colleagues demonstrated EEG-based communication imagery in five patients with a PDOC (predominantly in a MCS) by measuring modulations in sensorimotor rhythms following extraction of power values from frequency band analysis (Mangia et al., 2014). They initially performed imagery investigations of the right-hand and right-foot to determine whether the patients' level of cognitive activity was sufficient to allow attempts to communicate through the tasks. This yielded mean classification scores of approximately 85%. Assigning an affirmative answer to the imagery of the right-hand and a negative answer to the imagery of the right-foot to personalised questions yielded communication imagery scores of 92%, which was measured for correctness from the patients' relatives

after the study. Interestingly, the authors statistically tested for the best electrodes post classical imagery and identified a subset of eight electrodes that would enhance communication imagery classification. One of these was C3 corresponding to the right-hand area of the human homunculus whereas the others were more right of C4 and occipitally located. This is interesting as foot activation is thought to be more mid-central (Pfurtscheller et al., 2006b, 2008), shedding light on the wider or altered neural activation patterns in patients with PDOC following traumatic brain injury, in comparison to that generated by the norm.

The studies presented in this section highlight brain electrical responses to motor imagery being well correlated with those generated by the physical performance of the action due to a relatively consistent activation of the sensorimotor cortex. In this regard, EEG is a powerful tool as it directly samples this activity (i.e. task-related electrical potentials) at the scalp level. The consistent encoding of adult motor task signatures within narrow frequency bands (i.e. alpha and beta frequency bands) thereby enables activity in recovering patients to be compared with spatial patterns from healthy individuals. The challenges of EEG motor imagery research are however related to the type of task, i.e. simple verses complex/goal-directed motor imageries. Whilst the latter, for example imagining playing tennis or a piano, can better stimulate the participants engagement with the task, they in-turn can also activate a wider brain response beyond the sensorimotor cortex due to the required trajectory planning and the synergy of multiple joints (Zhang et al., 2017b). Nevertheless, signal classification of complex motor imagery responses have shown to yield greater accuracies than those following signal classification of simple motor imagery responses. Cross study classification comparisons are generally difficult due to the range of participants, number of trials, number of testing sessions, and pre-processing and classification tools used. However, from these studies it is clear that provided a participant/patient has received some training and is fully engaged/motivated with the task, clinical standard classification accuracies can be achieved. From studies that have extended EEG motor imagery classification into a BCI communication tool in patients, it is also evident that there is a need for unique tasks for each possible response to a question/statement as using a resting brain activity response to convey “no” or “I don’t know” can increase the false positive rate.

Whilst motor imagery can therefore be considered to be a promising medium by which individuals can present their brain state or communicate when unable to perform the corresponding overt action, there is an important need to localise sources from scalp recorded signals in order to confirm the physiological plausibility of the response. Although EEG is greatly beneficial for its temporal resolution, it is strongly limited by the lack of spatial localisation present; a resolution of 50-90 mm can be achieved using high-density electrode montages which decreases (i.e. >100 mm) with lower density setups (Burle et al., 2015; Ferree et al., 2001). This is because randomly distributed and oriented dipoles acting in all directions propagate the electrical field through volume conduction to scalp electrodes resulting in a strongly measured signal far from the original source. Source localisation methods are one way of achieving spatial information from EEG data, however at best these are estimates making use of several assumptions in order to model the propagation of the EEG electric field from a source (Kim et al., 2018; Michel and He, 2019). Other ways of achieving good spatial information involve the simultaneous use of EEG alongside spatial resolution rich imaging devices such as positron emission tomography (Chennu et al., 2017) and fMRI (Edlow et al., 2017; Gibson et al., 2014b). However, as previously discussed, the lack of portability of these instruments and individual contraindications limit the scope of their use for patients with PDOC. As an alternative, next discussed is the optical imaging method of functional near infrared spectroscopy and its potential use for simultaneous imaging alongside EEG.

1.3. Functional near-infrared spectroscopy

Functional near-infrared spectroscopy (fNIRS) is an alternative method to fMRI that similarly measures blood-oxygenation-level-dependent (BOLD)-like haemodynamic responses (Huppert et al., 2006; Villringer and Chance, 1997) (for an in-depth review please refer to (Ferrari and Quaresima, 2012)). The haemodynamic response is a collective term for the set of physiological responses that take place during the onset of neuronal activations. These include changes in cerebral blood flow, cerebral metabolic rate of oxygen and cerebral blood volume (Buxton et al., 2004). The BOLD signal detected in fMRI systems are indirectly sensitive to increases in these elements (i.e. metabolic demands) during

neural activation. The increasing oxygen demands of active neurons causes the expansion of blood vessels which in turn changes the ratio of oxygenated haemoglobin (diamagnetic as no unpaired electrons) to deoxygenated haemoglobin (paramagnetic as four unpaired electrons) in the blood. This shift in neuronal vascular magnetic properties results in local gradients in the magnetic resonance field whose strength, and thus recovered signal, depends on the degree of deoxygenation (Glover, 2011). fNIRS is a portable, inexpensive, fast, non-invasive method that has limited contraindications in comparison to fMRI (Gratton et al., 1995a; Strangman et al., 2002; Villringer and Chance, 1997). Nevertheless, without sophisticated hardware and signal processing techniques, the technology offers significantly reduced spatial resolution, due to the diffuse nature of light propagation in tissue. The typical fMRI voxel size for clinically available systems is between 3-4 mm^3 (Glover, 2011), however a spatial resolution of 500 microns or less can be achieved using higher field magnets (7 Tesla) (Shmuel et al., 2007). Unlike fMRI, the NIRS image resolution is between 10-20 mm (Cui et al., 2011) and can increase to <10 mm using high-density diffuse optical tomography (Eggebrecht et al., 2014; White and Culver, 2010). This lower resolution in comparison to fMRI is predominantly due to the strong scattering and attenuation of near infrared photons and the ill-conditioned inverse problem of reconstructing three-dimensional brain activity maps (see later discussions for further details) (Cui et al., 2011). fNIRS is an optical neuroimaging method that records counts (intensity), phase shifts and the time-of-flight of scattered and reflected source photons (near-infrared light) at detector fibres which in turn can be used to derive (by modelling light propagation in tissue) changes in the concentrations of oxygenated (Δ[HbO]) and deoxygenated (Δ[HbR]) haemoglobin molecules in the blood depending on the degree of near infrared light attenuation (Rupawala et al., 2018). Therefore, like fMRI, fNIRS is also an 'indirect' neuroimaging tool in the sense that it monitors haemodynamic responses to neural activations on the basis that neural activations are tightly coupled to vascular processes; a process known as neurovascular coupling. Several models have been derived in order to explain the coupling between these two processes, and simply, it is understood that postsynaptic activation at the apical dendrites drive dynamic molecular changes in the terminus resulting in an amplitude-coupled increase in the local cerebral blood flow, later followed by a transient increase in local oxygenation tension (Buxton et al., 2004; Buxton and Frank, 1997; Lourenço et al., 2014). Based on these properties, fNIRS

has been shown to have a broad spectrum of uses including studies of vision (Gratton et al., 1995a), hearing (Zaramella et al., 2001), speech (Cannestra et al., 2003), learning (Leon-Carrion et al., 2010), emotion (Leon-Carrion et al., 2006) and pain (Yucel et al., 2015), and as such, recently has also begun demonstrating its use within the field of PDOC (Kempny et al., 2016; Molteni et al., 2013; Zhang et al., 2018b). Furthermore, as a component of neurovascular coupling relies on end-to-end asynchronous electrical signalling to drive neural activations, there is growing interest in simultaneous electroencephalography (EEG)-fNIRS - both of which share similar advantageous properties (e.g. portability, inexpensive and non-invasive) (Kempny et al., 2016).

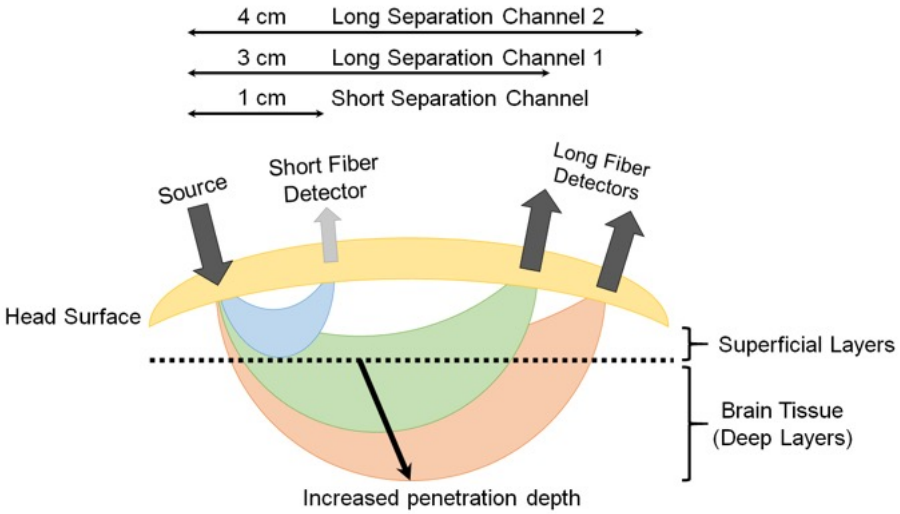

Figure F1.3: Sensitivity maps of the sampled fNIRS signal at multiple source detector distances. A single source and detector constitute the simplest NIRS channel. Depending on the source-detector separation distance, and the subjects' skull and scalp thicknesses, the light may or may not sufficiently penetrate the superficial layers to sample the deeper layers. A separation of 3 cm is commonly used however increasing this to 4 cm can increase the penetration depth of the light sampled tissues. Short separation channels are located within 1 cm of the source and can provide physiological (noise) data within the superficial layers. This activity can then be regressed from the long separation channel, resulting in a signal corresponding to activity solely within deep brain tissues. Figure adapted from (Davies et al., 2015). No permissions were required.

Spectroscopy is based on the study of interactions between matter and electromagnetic radiation. In the near-infrared (NIR) range of light, with wavelengths between ~600-900 nm, biological

tissues are effectively transparent. The low molar absorptivity of lipids and water in this region enables light to effectively penetrate and be maximally absorbed by oxygenated (HbO) and deoxygenated (HbR) haemoglobin (Ferrari et al., 1985; Jobsis, 1977). These primary light-absorbing compounds in tissue in the NIR range are called chromophores (Jobsis, 1977). Optical neuroimaging using fNIRS typically requires the use of a set of light-emitting diodes (light sources) on the scalp, and an equal or larger set of detectors, depending on the number of source-detector channels required. NIR light of wavelengths specific to each biological chromophore will be absorbed primarily by that chromophore (HbO, HbR and cytochrome c-oxidase). Scattered light then follows a trajectory back towards the surface of the scalp, in a characteristic 'banana'-shaped photon path, where it is captured and recorded by, for example, photodetectors (figure F1.3) (Gratton et al., 1994). This banana-shaped trajectory is referred to as the "spatial sensitivity profile" of a source-detector pair (Strangman et al., 2013).

Absorption and scattering are the two main attenuating interactions that take place between light and tissue (figure F1.4). As light from a source penetrates through the layers of the head, specific wavelengths will be absorbed by the absorbing (chromophore) components within the different media. The photons that reach the detector on the scalp are primarily those that have scattered within the medium, and therefore have travelled a greater distance than the geometrical (straight-line) distance between the light source and detector. The measured intensity at multiple wavelengths is then used to separate the absorption due to different chromophores. Due to the scattering properties of light on route to the detector, the fNIRS signal has limited spatial resolution (8-20 mm (Cui et al., 2011)) of the underlying chromophore concentrations with respect to its location in the head but contains rich contrast (i.e. a small change in attenuation change will result in a large measured intensity change).

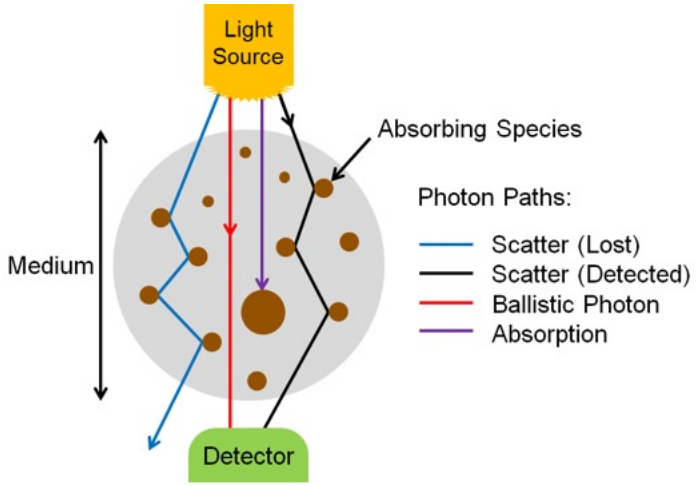

Figure F1.4: Light propagation paths through a medium. Depending on the wavelength of the emitted light, photons may either be absorbed by the medium, scatter to the extent that they are no longer detectable, scatter and yet be detected, or travel through the scattering medium in a straight line (ballistic photon). For fNIRS devices, ballistic photon paths are highly unlikely to occur due to source and detectors being positioned on the surface of the head, and the light propagating directly into the brain. Figure adapted from (León-Carrión and León-Domínguez, 2012). No permissions were required.

The depth within the skull that can be studied using fNIRS is largely dependent on the inter-optode distance, or source-detector separation distance as it is also referred. As a general approximation, the penetration depth achievable is approximately a third-to-half the source-detector separation distance (Cui et al., 1991; Strangman et al., 2002), up to a maximum of ~25 mm beyond which the resolution of the final image is severally compromised due to greater light attenuation (Doulgerakis et al., 2019a; Gunadi et al., 2014). At greater source-detector separation distances, deeper penetration of light is achieved at the cost of poorly resolved signals due to less light being captured by the detector (figure F1.3). Diffuse optical tomography can improve this resolution by employing a large number of overlapping measurements, each generating their own sensitivity map. Combining these signals allows a deeper three-dimensional reconstruction of the haemodynamic signals from the brain (Gervain et al., 2011).

Haemodynamic signal integrity can be readily compromised by the effect of superficial layers on the detected signal. These layers of tissue are assumed to have a constant attenuation effect on the

light signal; however there is a slight effect due to extracerebral signal components (Kohl-Bareis et al., 2002). The attenuating layers in the head include the skin, scalp, skull, cerebrospinal fluid, grey matter and white matter, in addition to the chromophores within the blood. Of these however, the scalp and skull have been shown to be most significant (Strangman et al., 2014). Traditionally, it was assumed that haemodynamic changes in the overlying tissues layers were uncorrelated with the changes in brain function. However, research has shown that the systemic physiological signals from superficial layers can exponentially decay the light from the emitter (Boas et al., 2004); that is to say that NIRS measurements are inherently most sensitive (i.e. have largest magnitude) to tissue nearest the source and detector (Boas et al., 2004). Major contributors of physiological interference include heartbeat (1~1.5 Hz) (Gratton and Corballis, 1995), respiration (0.2~0.5 Hz) (Franceschini et al., 2002), low-frequency oscillations including Mayer waves (~0.1 Hz) (Obrig et al., 2000), and task-related changes in systemic physiology (Kirilina et al., 2012).

The mean scalp plus skull thickness in an adult human is typically 10-18 mm (average modelled values of ~7 mm for scalp and ~6 mm for skull as reported by (Strangman et al., 2014)). Okada and Delpy showed that increasing the skull thickness from 4-10 mm would result in an 80% loss in NIR signal intensity (Okada and Delpy, 2003). In contrast, Strangman and colleagues argued that the scalp consistently had a greater influence on NIRS brain sensitivity than skull (Strangman et al., 2014). In addition, they looked at how source-detector separations could overcome this and found that as separations increased above 20 mm (mean sensitivity of 0.06), the effect of the superficial layers became less influential, with near-maximal sensitivity to brain tissue being achieved at or above 45 mm (mean sensitivity of 0.19) (Strangman et al., 2014). Other methods of effectively detecting absorption changes from deep brain tissues whilst keeping a normal source-detector separation distance (e.g. 45 mm) include the use of independent component analysis (Katura et al., 2008), principal component analysis (Virtanen et al., 2009), and model-based analysis such as the general linear model (Plichta et al., 2007).

With multiple-distance optodes (i.e. a short separation channel and long separation channels), some groups have shown this method to advance a general linear model approach in eliminating superficial effects (Gagnon et al., 2011, 2012; Yücel et al., 2015). In this approach, short separation

detectors that are located in the activation area but have shorter source-detector separation distances (<10 mm) are more sensitive to activity in the superficial layers, whereas the signal received at the long separation detectors are sensitive to both the brain and superficial layers (figure F1.3). Regressing out the short separation signal from the long separation signal effectively filters out the superficial component (see (Kirilina et al., 2012) for more information about how the data from the short separation channel is regressed from that of the long separation channel). Other approaches to improve deep tissue spatial resolution with multiple-distance probes include the use of multi-distance probes along with independent component analysis (Funane et al., 2014), and diffuse optical tomography (Dehghani et al., 2009). Alternatively, low processing options to eliminate physiological signals include low pass filtering (only to eliminate cardiac oscillations) (Franceschini et al., 2003) and wavelet filtering (Lina et al., 2008). Recently, using an advanced frequency domain (FD) NIRS imaging system (see discussions below) it has also been shown that the additional phase information is inherently less-sensitive to superficial activity (Doulgerakis et al., 2019a).

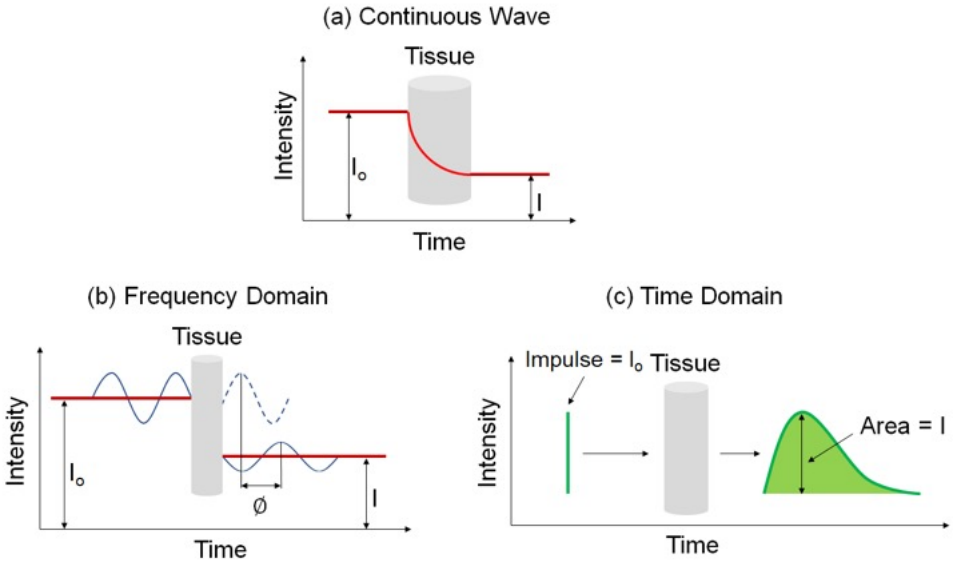

Figure F1.5: Illustration of three different fNIRS techniques. The simplest and most commonly used method is continuous-wave near-infrared imaging (top), which measures changes in light intensity having passed through the tissue. Two other methods – FD (bottom left) and time-domain (bottom right) – are variations of this and provide increased information content (see text for further details). I_0: incident light signal, I: detected light signal and Φ: phase shift. Figure adapted from (Scholkmann et al., 2014). No permissions were required.

The three types of systems that are primarily used for near-infrared imaging are continuous-wave (figure F1.5a), frequency-domain (figure F1.5b) and time-domain/resolved (figure F1.5c). Of these, continuous-wave devices are the most common instruments for measuring the fNIRS signal. These devices emit light at a constant intensity and measure changes in the intensity of the re-emerging (i.e. diffusely reflected) light, having passed through the tissues. To quantify chromophore concentrations from the recorded light intensities requires modelling of the medium through which the light has propagated. The earliest model is the Beer-Lambert law, proposed in 1729 by the French mathematician Bouguer (Bouguer, 1729). This type of spectroscopy represents a linear relationship between absorbance and concentration of an absorbing species, and as such has been widely used in colorimetric analysis, with similar principles applied to biological tissue. Biological tissue, such as the brain, is a highly scattering environment. To account for such scattering of light, Delpy and colleagues developed the modified Beer-Lambert law (Delpy et al., 1988; Patterson et al., 1989). This has been used widely in continuous-wave devices as a means to derive concentration changes of each chromophore (Δ[HbO], Δ[HbR] and total haemoglobin, Δ[HbT]).

In addition to continuous-wave measurements, two other diffuse optical measurements that have been developed include FD and time-domain fNIRS. In the former, light sources emit light continuously, like continuous-wave-fNIRS, however the amplitude is modulated at frequencies in the MHz range. The absorption and scattering properties of tissues are then obtained by recording the amplitude decay and phase shift (delay) of the detected signal with respect to the incident beam (Obrig et al., 2000). In time-resolved fNIRS, short (picosecond) incident light pulses are introduced into tissues and as they penetrate through the various layers (i.e. skin, skull, cerebrospinal fluid and brain) the signal is broadened and attenuated. As the photons leave the tissue, the recorded temporal distribution by the time-domain system, and the shape of this distribution, provides information about tissue absorption and scattering. Advantages and disadvantages of these three systems are summarised in table T1.1. Table T1.1 indicates that whilst continuous-wave fNIRS devices offer a cheap and portable method of rapidly capturing brain haemodynamic activity, their simplicity limits the spatial resolution and the penetration depth that can be achieved in comparison with frequency- and time- domain fNIRS systems.

Table T1.1: Advantages and disadvantages of the three commonly used fNIRS techniques. Table adapted from (Strangman et al., 2002).

Measurement type	Advantages	Disadvantages	References
Continuous-wave	▪ High sampling rate – up to 100 Hz ▪ Can be miniaturised – ease in portability ▪ Simple to use ▪ Low cost	▪ Low penetration depth – increased sensitivity to superficial layers ▪ Difficult to separate absorption and scattering	(Blankertz et al., 2008; Fazli et al., 2012)
Frequency-domain	▪ High sampling rate – up to 50 Hz ▪ Relatively accurate separation of absorption and scattering ▪ Phase measurements are less sensitive to activity in the superficial layers	▪ Moderate penetration depth ▪ Intensity measurements are increasingly sensitive to activity in the superficial layers ▪ Phase measurements can be more susceptible to noise	(Doulgerakis et al., 2019a; Graimann et al., 2010; Koo et al., 2015)
Time-domain	▪ High spatial resolution ▪ High penetration depth – mean time-of-flight and variance values can separate brain tissue from superficial layers ▪ Most accurate separation of absorption and scattering	▪ Low sampling rate – greater loss of photons ▪ Instrument size/weight is larger ▪ Stabilisation/cooling required ▪ Costlier system as most advanced ▪ Can be more susceptible to noise – can impact the usefulness of studying variance values	(Holper and Wolf, 2011; Zich et al., 2016)

A variety of motor imagery paradigms have been examined for use with fNIRS, the majority of which require activation of the hand and foot areas of the cortical homunculus (Abdalmalak et al., 2016; Hsu et al., 2017; Wriessnegger et al., 2008). Coyle and colleagues used a continuous-wave-fNIRS system to demonstrate that when three healthy participants imagined squeezing a ball, their Δ[HbO] increased reliably above that from rest in the C3 and C4 regions of the motor cortex (based on the EEG international 10-20 system), regions predominantly associated with hand movements (Coyle et al., 2007). Interestingly, after averaging each participants' data over 20 trials, haemodynamics following motor imagery activation could be prominently distinguished by eye from that of baseline prior to signal processing. Although this may indicate that such experimental paradigms can generate profound neuroactivational changes, it is important to note that their findings were based off a small cohort of

three participants. Nevertheless, the authors were further able to show that, by solely studying Δ[HbO], motor imagery could be used to correctly classify a user's intent ~80% of the time. Other types of motor imagery paradigms that have established significant haemodynamic signal changes with fNIRS include tennis arm-swinging motion (Abdalmalak et al., 2016) and a finger tapping sequence (Iso et al., 2015).

Aside from these, of popular interest with fNIRS is the ability to differentiate activations from left- and right-hand movements, whether that be tapping, gripping or flexing of the wrist. Sitaram and colleagues reported that fNIRS recordings of motor imagery for left- and right-hand tapping were similar to motor execution recordings, but smaller in magnitude (Sitaram et al., 2007). Nevertheless, from the data it was clear that the haemodynamic responses for left-hand and right-hand motor imagery had distinct patterns that could be used by a classifier to discriminate between the two classes. As such, the researchers of this study were able to achieve approximately 89% accuracy using their classifier, with similar results being achieved by others (87% accuracy achieved when distinguishing between imagined right-wrist and left-wrist flexion) (Naseer and Hong, 2013; Sitaram et al., 2007).

To add to the hand tapping motor imagery paradigm, recently there has been significant interest in separating left- and right-foot tapping's using fNIRS. When using a four-class motor imagery paradigm (left/right foot/hand) in a BCI setting, Batula and colleagues achieved an average classification accuracy of approximately 46% over three participants (chance = 25%; two participants had a classification accuracy over 50%) (Batula et al., 2014). Nevertheless, the authors suggested that improved performance could be achieved by utilizing more informative features or classifiers through a more detailed inspection of the activation patterns, or a better selection of motor tasks. However, from their confusion matrix, it can be seen that right-foot was most frequently misclassified. This is not surprising as distinguishing between left- and right-foot using fNIRS is challenging as the foot motor areas are near or within the longitudinal fissure between brain hemispheres (Cheyne et al., 1991). Nevertheless, improvements to classification accuracies could be achieved by using a single "feet" or leg motor imagery task (Hsu et al., 2017), or by providing feedback training to strengthen the participants motor imagery abilities (Miller et al., 2010).

Many of the NIRS systems currently employed in motor imagery research are continuous-wave, and so require extensive montage (source and detector layout) development and data processing.

However, time-domain-NIRS devices have the potential to enhance depth sensitivity as they record the arrival times of individual photons to build a distribution of times of flight (Diop and Lawrence, 2012; Diop and St. Lawrence, 2013). Early work by Abdalmalak and colleagues assessed the feasibility of time-domain-fNIRS to detect brain activity during motor imagery (Abdalmalak et al., 2016). Seven participants performed tennis-playing imagery of which four showed prominent activity in either the PMC alone or PMC and SMA, as detected by fMRI. During the task, increases in blood flow and volume in the PMC and/or SMA led to an increase in light absorption, and thus a decrease in the number of photons, N, reaching the detector and their mean time-of-flight, $\langle t \rangle$. These changes in N and $\langle t \rangle$ precisely occurred during the onset of motor imagery and not during rest for the four participants that likewise showed BOLD signal change as measured by fMRI. On a small scale, this study demonstrated good agreement between both imaging modalities, strengthening the argument for the use of fNIRS in motor imagery. However, in three of the seven healthy participants, who were demonstrably aware, no activity was detected by either imaging modality. While no method will be perfectly sensitive (see (Fernández-Espejo et al., 2014)), it is clear that considerably greater levels of sensitivity are required before this method may be used clinically. Therefore, the same authors tested 15 healthy participants with the same tennis-playing imagery task and instead evaluated the mean and variance, which have greater depth sensitivity, and report sensitivity values between 86 and 93% in the SMA and PMC, respectively, the highest being for <t> as the data are less influenced by noise (Abdalmalak et al., 2017a). Furthermore, of the 15 participants that took part in the study, 93% generated responses that were detectable by fMRI and 87% by fNIRS, a considerable improvement over their earlier work (Abdalmalak et al., 2016) and a clear demonstration of the power of advances in physical and computational methods to improve detection of clinically-meaningful information from fNIRS signals. These promising results also confirm that time-domain-fNIRS is an alternative means of reducing scalp contamination and for enhancing the sensitivity to brain activity, and thus may be a well-suited tool for use on patients with PDOC. At this time, time-domain-fNIRS data have not yet been reported in patients with PDOC but the technology has been applied for stroke and traumatic brain injury assessments (Lange and Tachtsidis, 2019).

Research in patients with PDOC has, however, been accomplished using other fNIRS devices. Molteni and colleagues detected residual functional activity in two minimally conscious state patients using a commercially available NIRS device (although undefined in the manuscript) and a protocol that involved somatosensory, passive movement, and active movement stimulations (Molteni et al., 2013). Whilst somatosensory stimulation (using a vibrating pillow) elicited a weak response over the somatosensory cortex, passive movement stimulation (hand movement with the assistance of the experimenter) generated clearer haemodynamic responses (increase in Δ[HbO], decrease in Δ[HbR]). Active movement tasks (self-performed hand opening and closing) generated the weakest haemodynamic response in the hand region of M1 in both patients, however this was expected as the patients were unable to move their hands autonomously and showed no signs of engagement with the task. Furthermore, their T1-weighted MRI brain scans indicated the presence of severe atrophy that could have allowed for fluid accumulation. An excess of cerebrospinal fluid would have increased attenuation of the NIRS signal (see earlier discussions) thereby reducing the chance of a measurable response to the task. Overall, as a primary study, the authors were able to show that residual brain activity can be detected in patients with PDOC using fNIRS, and favours the use of motor imagery with fNIRS as a means of overcoming the need for patients to execute movements, which may not always be possible.

In a study by Kempny and colleagues, 16 patients (11 in a MCS and 5 in a VS) performed a kinaesthetic motor imagery task of squeezing a ball with their right-hand whilst being evaluated with continuous-wave-fNIRS (Kempny et al., 2016). In addition, healthy participants were asked to physically perform and kinaesthetically imagine the same task in order to obtain patterns that could be used to validate responses in patients with PDOC. A typical fNIRS response to movement and motor imagery is an increase in the Δ[HbO] accompanied by a less pronounced decrease in the Δ[HbR] (Leff et al., 2011; Sato et al., 2007). However, the groups in this study exhibited two types of responses during motor imagery; the typical responses and an inverted response (decrease in Δ[HbO] and an increase in Δ[HbR]). Furthermore, patients in a MCS, in comparison to those in a VS, more often exhibited a haemodynamic response that was similar to that of healthy participants. Fluctuations in haemodynamic patterns have been shown to depend on the location of the probe and the difficulty of the task (Mihara

et al., 2012), highlighting the importance of normative data from healthy individuals against which to compare a given patient's response. Kempny and colleagues further identified that the greatest reduction in Δ[HbO] was found on the right hemisphere of the head across all three groups during motor imagery (Kempny et al., 2016). Regions of haemodynamic activation were in line with previous studies (Leff et al., 2011; Wilson et al., 2014), with greater activation observed on the ipsilateral side (see (Batula et al., 2017) for similar results). Whilst this may seem unusual as one would expect primarily activation of the contralateral areas during hand motor imagery, Batula and colleagues demonstrated that this is not always the case, in particular when the left-hand is involved, which generated a more bilateral activational pattern during motor imagery (Batula et al., 2017); a pattern confirmed by fMRI (Cramer et al., 1999; Verstynen et al., 2005).

The above studies demonstrate the feasibility of fNIRS in the field of PDOC. However, there is much to do to ensure that the signals measured are sufficiently reliable and interpretable for use in clinical contexts. Next discussed is one potential means of achieving that goal.

1.4. Simultaneous EEG and fNIRS

The neurovascular coupling model (as previously discussed in section 1.3) fundamentally connects regional increases in cerebral blood flow (and thus an increase in oxygen influx) to synchronised bursts in electrical activity by populations of neurons. As outlined above, both these components can be independently sampled using inexpensive portable devices such as EEG and fNIRS. Nevertheless, both of these technologies are in some form limited with respect to their image resolution capacity: EEG can sample electrical neural activity at a millisecond time frame however offers poor spatial resolution (50-90 mm) due to volume conduction effects (Burle et al., 2015), whereas NIRS indirectly measures the slow haemodynamic changes in the brain (similar to fMRIs BOLD response where the peak signal occurs approximately 5–6 s after the onset of a brief neural stimulus (Glover, 2011)) to a relatively good spatial resolution only (8-20 mm) (Cui et al., 2011). Therefore, simultaneously recording both haemodynamic and electrical signals by positioning both EEG and NIRS

sampling systems on the scalp offers an improved means of rapidly measuring and better localizing changes in brain function and health in response to tasks.

The majority of EEG-fNIRS studies to date have been within the field of BCIs. BCIs are used for several applications including spelling devices, environmental control, navigation in virtual reality, simple computer games, cursor control applications and control of prostheses and robotic arms (Blankertz et al., 2007; Millan et al., 2004; Sellers and Donchin, 2006; Velliste et al., 2008). The most commonly studied signals in BCI are those of EEG, with features derived from either the ERP or frequency band analysed ERD or ERS windows (Guger et al., 2017; Han et al., 2019). There have been several applications of EEG-based BCI in the field of PDOC, rehabilitation, and for other conditions resulting from a traumatic brain injury or motor impairing disease (for a detailed list of references please refer to (Mikołajewska and Mikołajewski, 2014), and discussions within section 1.2).

In fNIRS-BCI, features for classification are mostly extracted from haemodynamic signals (Δ[HbO], Δ[HbR] and Δ[HbT]), such as peak amplitude, mean value, variance, slope, skewness, kurtosis and coefficients of a wavelet transform (Naseer and Hong, 2015). fNIRS is a relatively novel technique in the field of motor imagery-based BCIs, with EEG still viewed by many as the gold standard. As such, several research groups have opted for a hybrid BCI approach whereby NIRS features are used to support and complement EEG-based BCIs. Koo and colleagues demonstrated the reliability of a hybrid (fNIRS and EEG) self-paced motor imagery based BCI using a FD NIRS system (Koo et al., 2015). Here self-paced motor imagery is where the onset of motor imagery is not known, and neither are the brain signals corresponding to the detected motor imagery (in cue-based motor imagery, the start or cue of the motor imagery is known, hence a BCI system can recognise the motor imagery from the participants brain signals). Whilst a FD system was used for the study, which aided in the hybrid BCI achieving true positive rates of 88% (i.e. the BCI well recognised the intentions of the participants), it was clear that no phase data was extracted and analysed, and thus the instrument was analysed as if it were a continuous-wave system. The majority of work using FD systems beyond continuous wave-like systems has been limited to motor execution studies (i.e. tapping tasks), with those using the device having either evaluated both FD signals (intensity and phase) (Gratton et al.,

1995b), or fast optical signals (Morren et al., 2004; Wolf et al., 2002) (see (Gratton and Fabiani, 2009, 2010) for more information regarding fast optical signals and event related optical signals).

Fazli and colleagues conducted a motor execution and EEG-based, visual feedback controlled motor imagery study on 14 healthy right-handed volunteers required to perform left- and right-hand gripping (Fazli et al., 2012). Twenty-four fNIRS channels (8 sources and 16 detectors) and 37 EEG electrodes were used for data acquisition. The NIRS data were low pass filtered (0.2 Hz) and baseline corrected before using the modified Beer-Lambert law to calculate concentration changes of haemoglobin. Using a sliding window approach, time–averaged concentration changes (Δ[HbO] and Δ[HbR]) were used as features for LDA classification. EEG bandpass filtered coefficients in the alpha and beta bands were spatially filtered using a method known as Common Spatial Patterns (Blankertz et al., 2008) before the LDA classifier was computed. The LDA results from EEG, Δ[HbO], Δ[HbR], and combinations of all three were fed into a meta-classifier before testing. For motor imagery, combining EEG with either Δ[HbO], Δ[HbR], or both, resulted in classification accuracy scores of ~83%, ~81% and ~83% respectively, that were statistically different from the accuracies of the individual methods (EEG: ~ 78%, Δ[HbO]: ~72%, Δ[HbR]: 65%). However, it has recently been shown that both age and feedback can affect motor imagery patterns during simultaneous EEG-fNIRS data acquisition (Zich et al., 2016).

In studies by Fazli and colleagues (Fazli et al., 2012), Blokland and colleagues (Blokland et al., 2014), and Buccino and colleagues (Buccino et al., 2016), different EEG windows were used to simultaneously extract EEG features with fNIRS. The drawback with this is that false EEG signal detections may be introduced into the hybrid classifier yielding lower classification accuracies. As such, Khan and colleagues proposed the use of a novel classifier using a modified vector phase diagram and the power of the EEG signal for early prediction of hemodynamic responses without knowing the start time of a brain task (Khan et al., 2018). In this method a circle based on the magnitude of Δ[HbO] and Δ[HbR] during the baseline period is placed in a four-quadrant vector diagram. A second smaller circle is placed in the vector diagram using the magnitudes of Δ[HbO] and Δ[HbR] corresponding to the window in which EEG is activated. Using a FD fNIRS system comprising of twelve sources and three detectors, and six EEG channels surrounding the C3 region, thumb taps from the right-hand were

measured from three healthy participants. Activity was detected if the phase trajectory of Δ[HbO] and Δ[HbR] in a moving 1 s EEG time window crossed the outer and inner circles in the fourth quadrant (where Δ[HbO] is positive and Δ[HbR] has a negative value). Comparing the results from this method (which resulted in a mean accuracy of 86%) to that of traditional classification (where using LDA resulted in a mean accuracy 64%) yielded accuracies that were 22% higher.

With the improved knowledge of brain activation sources and scalp topographies in relation to motor-related tasks (Van Oostende et al., 1997), there is a growing interest into the use of a reduced subset of EEG electrodes and fNIRS channels for EEG-fNIRS BCI development as demonstrated by Khan and colleagues (Khan et al., 2018) and others (Ge et al., 2017; Li et al., 2017). There are several benefits to focusing on a small area of the scalp such as the reduced dimensionality of the data (Bellman, 1957) and the associated reduced computational costs during classification. Furthermore, from a clinical standpoint, low-density systems increase portability, reduce preparation time and improve patient comfort in comparison to that of whole head systems. However, a drawback of channel limited systems is that it is difficult to confirm the physiological plausibility of the spatial pattern maps associated with each task in the absence of real time or well documented fMRI data. Nevertheless, a top-down approach to achieving a few-channel dataset was recently demonstrated by Ge and colleagues (Ge et al., 2017). The authors demonstrated the accuracy of a few-channel BCI using EEG-fNIRS on participants conducting a left- and right-hand gripping motor imagery task (Ge et al., 2017). To validate which few-channels to use for the BCI (i.e. feature extraction and classification steps), the initial paradigm was performed simultaneously using a 64-channel EEG electrode set and 52-channel fNIRS set. Of these 52-channels however, 31 (11 detectors and 11 sources) were placed over the sensorimotor cortices (C3-Cz-C4 in 10-20 nomenclature). From the 64 EEG and 31 fNIRS channels, electrodes at positions C3, Cz and C4 and 14 fNIRS channels (6 sources and 6 detectors) centred around C3 and C4, were used for the few-channel EEG-fNIRS BCI, as these showed distinct neural activity during both left and right motor imagery tasks (see Figure 3 in (Ge et al., 2017) for further information on the montage layout). Following feature extraction, fusion of both EEG and fNIRS datasets, and classification using SVM, the researchers were able to demonstrate that few-channel EEG-fNIRS had a significantly higher

classification accuracy for 11 out of 12 participants than either of the individual modalities (average classification accuracies: EEG – 75%, fNIRS – 57%, EEG-fNIRS – 81%).

In the validation step, source analysis for both the 64 EEG and 31 fNIRS channels was performed to localise the neural signals during the motor imagery task (Ge et al., 2017). Source analysis effectively attempts to solve the question of what brain tissues/areas are being probed by a given measurement. In EEG, source analysis involves estimating solutions to the ill-posed inverse problem, which arises because of the infinite number of source configurations (i.e. radial and tangential) that generate a particular pattern of voltage at the scalp (Jackson and Bolger, 2014). Source analysis thus requires estimating the final surface voltage pattern and then working backwards to determine which neural sources generated that voltage pattern. As a result of this, the inverse problem can be seen as a NP-hard (non-deterministic polynomial-time hard) problem, where no absolute answer is available. Nevertheless, several methods are available, based on certain assumptions, to obtain approximate solutions (Grech et al., 2008; Hallez et al., 2007). In fNIRS, the question for source analysis becomes more specific as we aim to understand the depth penetration of the instrument. Light propagation through scattering media, such as the head (heterogeneous structure) is inherently complex and as such mathematical models of this process (radiative transport equation and its diffusion equation) are difficult to solve analytically (Pogue and Patterson, 1994). Estimations can however be made by solving the diffusion equation for optically homogeneous tissues with infinite, semi-infinite or slab boundary conditions (Arridge et al., 1992; Schweiger et al., 1993). Two types of numerical approaches can also be used to gain information about sensitivity and penetration depth in complex tissue: 1) approaches based on finite element and finite difference analysis, or 2) Monte Carlo simulations of photon propagation through the tissue. The latter was used by Strangman and colleagues to highlight that an increase in source-detector separation increased sensitives of higher level grey matter samples, however at the cost of exponentially decaying sensitivity in depth penetration (Strangman et al., 2013). Returning to the study of Ge et al., standardised low-resolution electrical tomographic analysis (Grech et al., 2008) was used to compute an inverse solution for the EEG motor imagery data, whereas digitised points and topographical maps of Δ[HbO], superimposed onto the surface of a standard three-dimensional head model, were used for the fNIRS data (Ge et al., 2017).

These methodological advances have ultimately aided efforts to improve BCI communication in patients with LiS at the bedside. Gallegos-Ayala and colleagues demonstrated that a single patient with LiS could be trained (using feedback) to directly communicate through their haemodynamic signatures 'yes' and 'no' answers to a number of individually tailored personal sentences (Gallegos-Ayala et al., 2014). The patient was specifically asked to think (not imagine) 'yes' or 'no' when answering the auditorily presented statements and questions. A number of sentences with known ("You were born in 1975.") and unknown ("Are you in pain?") answers were presented. Findings demonstrated that for both known (also termed closed) and unknown (also termed open) sentences there were significantly different deoxygenation levels between the thought yes and no answers. As such, SVM classification of extracted features resulted in overall performances of 76%, with a few known and unknown sentence communication sessions yielding 100% correct classification. Accuracy of the open sentence responses were based on the haemodynamic profile similarity of yes and no responses to closed sentences. The fact that these known sentence responses were inconsistent and recording sessions with known and unknown sentences were performed on different days (spread also across several days) limits the confidence in the accuracy of any single classification result. Nevertheless, this study marks a huge leap in the capabilities of fNIRS BCI, especially when compared to the study a decade ago by Naito and colleagues (Naito et al., 2007). Nevertheless, caution should be taken since these results were based on a single patient only. Additionally, the underlying neurocognitive mechanism is unclear, as responses were not detected via a proxy mental action (i.e. in motor imagery) but by apparent processing of the 'correctness' of the statements – i.e. that they were indeed in pain, rather than that they were performing a cognitive behaviour to signal that they were experiencing pain. The lack of a clear neurocognitive model may impede its utility in a wider patient group.

Furthermore, this school of thought is opposed to the more widely-used method of using proxy behaviours for communication – e.g. imagining playing tennis to answer 'yes'. This approach importantly does not rely on unclear models of neurocognitive processing but makes use of a clear signal of volitional command-following. However, command-following places higher cognitive demands on the communicator as they must map the appropriate response onto an arbitrary behaviour and produce that behaviour. Conversely, the approach of Gallegos-Ayala and colleagues (Gallegos-

Ayala et al., 2014) assumes that the communicator's passive experience of the correctness of the statement is sufficient to provide the communicative output, and is therefore a potentially more functional method for patients with limited cognitive resources as a result of brain injury.

More recently, Abdalmalak and colleagues presented a patient case report whereby a traditional proxy behaviour was used as means of communication (Abdalmalak et al., 2017b). The authors tested their previously designed four-channel time-resolved fNIRS system (Abdalmalak et al., 2016, 2017a), which enhances depth sensitivity by discriminating between early and late arriving photons (see previous discussions between continuous-wave and time-domain systems). With this technique, they detected motor imagery (imagining playing tennis) from a patient who was diagnosed with an acute form of LiS. Furthermore, by assigning this imagined action as a 'yes', the researchers could detect yes/no responses to a series of questions addressed to the same patient. The accuracy of the answers was confirmed by the patient's residual eye-movement communication channel. While this method has the potential to be translated to patients with PDOC, post-injury functional reorganisation of the brain may affect the choice of probe placement, and ischaemia or haematoma can impede scattering and absorption of light. As such, structural imaging data would contribute significantly to increasing the accuracy of fNIRS BCI methods. Furthermore, it is necessary to take into account any medications or sedatives used by the patient, as some are known to cause haemodynamic fluctuations that could be misinterpreted as being task-related (Yeom et al., 2017).

1.5. Summary and experimental hypotheses

The literature examined in this chapter highlights the significant contribution of researchers in their efforts to progress both EEG and fNIRS technology and associated experimental analysis methods in order to more accurately and sensitively examine cortical activity at the scalp level following motor imagery assessment. The portability, inexpensiveness and non-invasiveness of both devices highlights their significant potential for bedside detection of awareness, however it is also clear that much work needs to be performed in order for the technology to meet clinical standards for use on patients with PDOC. Such challenges include a manageable sparse cap montage that can be easily repositioned at the

scalp level above lesion-free brain regions, a selection of paradigms that can maintain the patients engagement and can be reliably used to validate command following, a highly discriminable classification model that can reach clinical standard accuracies from as few trials as possible (thereby allowing for a less exhaustive paradigm), and confirmation of a physiological meaningful response in the measured signals with respect to the task (i.e. noise free data).

The majority of fNIRS research has focused on detecting covert command-following via sensorimotor activity during imagined actions. However, due to the relative infancy of fNIRS, there remains significant work to do in terms of hardware, signal processing, and analyses; especially because the vast majority of fNIRS work in motor imagery has mostly been conducted with less sensitive but simpler continuous-wave devices. Motor imagery is a promising command following alterative to performing a physical action that aligns with many of the neurobehavioural functions evaluated using CRS-R and WHIM qualitative assessments. However, little evidence exists in comparing the performance differences between simple and complex (known to enhance participant engagement) motor imageries whereby two imagery types of each class (simple and complex) are classified between each other rather than to baseline (resting) activity. Nevertheless, EEG-based motor imagery in its current form has progressed well in the field of PDOC as a method that is widely explored for aiding in clinical assessments in the repeated diagnoses of an individual patients' state, having recently also shown its use as a communications tool for this patient class. However, the lack of structural and spatial information offered by EEG indicates that a simultaneous assessment approach with fNIRS can deliver the physiological meaningful results required to confirm a true response to a command. Simultaneous EEG-fNIRS BCIs have shown to be successful in preliminary clinical studies highlighting a promising pathway for reaching the standards required for clinical applicability in PDOC.

Recent investments into a FD fNIRS system by the University of Birmingham provides an opportunity to explore and assess brain behaviour at greater depths during imagined actions. Simultaneously combining the millisecond resolution of EEG with the heightened sensitivity and improved spatial resolution of FD fNIRS has the potential to improve classification of multiple contrasting behaviours, thereby significantly aiding BCI development for awareness detection and

communication in PDOC patients. With the aims of this thesis in mind, the three key hypotheses for each experimental chapter are as follows:

- EEG-sampled object-oriented motor imagery responses can yield better classification results than simple limb motor imagery actions. This hypothesis stems from minimally explored fMRI and EEG research that has identified the addition of an object or goal to enhance an individual's motor imagery ability (Li et al., 2015; Mizuguchi et al., 2013).
- The additional phase shift component of the FD fNIRS system will more sensitively sample the underlying brain tissue during motor imagery responses, thereby enhancing the classification of multiple motor imagery actions in comparison to intensity measurements alone (which are the only measure of continuous-wave devices).
- The simultaneous recording of EEG and FD fNIRS can improve the classification of imagined actions beyond that achieved by a FD fNIRS system alone.

Chapter 2

Object-oriented motor imagery detection using EEG

2.1. Introduction

Motor imagery describes the mental simulation of voluntary movements without its actual execution (Jeannerod, 1995). The persistent mental rehearsal of specific movements can drive brain plasticity activating the same cortical areas stimulated by the overt performance (Jeannerod, 1994; Lotze et al., 1999). It is a task that has been used to drive skill acquisition and motor learning in fields such as sport and motor rehabilitation (Jackson et al., 2001; Murphy, 1994; Sharma et al., 2009). Furthermore, in patients diagnosed with a Prolonged Disorder of Conscious (PDOC) or Locked-in Syndrome (LiS), such covert training has: (i) identified potential cases of misdiagnoses through the detection of neural activity in response to commands; (ii) induced brain changes (plasticity) associated with the control and rehabilitation of key motor skills, and (iii) provided a means of clinician-patient communication through extensive research and development of brain computer interfaces (BCIs) (Cruse et al., 2011; Guger et al., 2017; Horki et al., 2014; Lee et al., 2011; Owen et al., 2006; Silvoni et al., 2011).

There are two different approaches of motor imagery investigated in the literature - simple paradigms involving finger (flexion-extension or opposition), hand (grasping), arm (elbow extension-flexion), tongue, toe and foot movements (Batula et al., 2017; Ehrsson et al., 2003; Erbil and Ungan, 2007; Gerardin et al., 2000; Morash et al., 2008; Porro et al., 1996; Solodkin et al., 2004; Tavakolan et al., 2016), and the more complex paradigms based on performing sports, navigating through a room or utilising tools (Abdalmalak et al., 2017a; Owen et al., 2006; Szameitat et al., 2007; Wriessnegger et al., 2014, 2018; Zhang et al., 2017b). Most often, fMRI imaging has identified both these approaches to map onto the same homuncular organisation in the sensorimotor network (Ehrsson et al., 2003; Stippich et al., 2002; Szameitat et al., 2007), despite contradictory reports during movement imagery of stance,

walking, and running (Jahn et al., 2004), and the misperception that complex paradigms recruit large parts of the motor system with significant overlap (Schieber and Hibbard, 1993). However, unlike simple covert tasks, complex imagery movements have been shown to elicit stronger activations (Boly et al., 2007; Kuhtz-Buschbeck et al., 2003), yet are prone to achieving high false-negative rates for the bedside examination of some patients (i.e., patient and healthy participants who have shown behavioural evidence of command following do not demonstrate the expected activations during imagery) (Gibson et al., 2014b; Monti et al., 2010).

Recent efforts have focussed on translating such fMRI research to EEG through the investigation of frequency band-specific oscillatory changes over the motor regions. Wriessnegger and colleagues outlined spectral distribution patterns following two complex motor imagery paradigms (tennis and ball squeezing) (Wriessnegger et al., 2018). The authors noted that for both tasks, in the alpha frequency band (8-13 Hz), an event-related desynchronisation (ERD) over primary motor areas was accompanied by an event-related synchronisation (ERS) pattern over sensorimotor regions. Furthermore, following motor imagery training of the two tasks, a stronger (weaker) ERD was present over the contralateral primary motor area for the right-hand tennis (ball squeezing) imagery condition. The observations for the tennis imagery condition were in agreement with the results of a previous fMRI study (Wriessnegger et al., 2014). Such research has been widely extended to develop EEG-based BCI systems using a variety of pattern recognition algorithms (Padfield et al., 2019). Zhang and colleagues highlighted that simple single joint motor imagery tasks (e.g. elbow extension and flexion) can be used to successfully derive training models on which multiple goal-oriented tasks (e.g. closing a draw or lifting weights) can be classified with high accuracy, thus reducing the need for repetitive data acquisitions and model trainings (Zhang et al., 2017b).

Fundamentally, the performance of motor imagery by participants highly depends on two key components: (i) their ability to form a mental representation of an action, and (ii) their ability to stay attentive to the mental imagery for the duration of the task. The former can be achieved using complex/goal-oriented imagined movements as these have shown greater EEG-control accuracy than simple/non-goal oriented methods (Gibson et al., 2014a; Wriessnegger et al., 2018; Yong and Menon, 2015), whereas the latter can be achieved through extensive prior mental rehearsal (Li et al., 2015)

which is also known to guide motor learning in a manner that aids actual execution (Allami et al., 2008). The presence of an object has previously been shown to strengthen the ERD response to leg flexion-extension motor imagery (Li et al., 2015). Li and colleagues demonstrated that participants shown a video of a leg kicking a ball generated a contralateral suppression in the mu and beta rhythms during motor imagery (Li et al., 2015). In contrast, the same participants when shown a video of a leg in the absence of a ball only generated a contralateral ERD in the mu rhythm. Similar increased brain activation profiles have been demonstrated using fMRI involving an imagined hand squeezing task in the presence of a ball (Mizuguchi et al., 2013).

These studies highlight that complex/goal-oriented tasks have the potential to aid motor imagery performance through increasingly modulating frequency band power in sensorimotor brain regions. Furthermore, the vividness of these tasks and familiarity with individuals to their daily lives drives comparable cortical networks to those of simple mundane imagery paradigms. It is also evident that such complex tasks enable better participant engagement which in turn can induce plastic changes within the brain following repetitive mental practice. The majority of EEG motor imagery studies to date have limited comparisons of frequency band spatial profiles between either physical movement and simple imagery tasks, or simple and complex imagery paradigms. This is likewise the case for EEG BCI studies which have reported classification accuracies between tasks for these two groups with a range of participants numbers and a varying number of trials and sessions, preventing direct comparisons from being made. In the absence of this research, fundamental questions remain with respect to the physiological similarity of the spatial patterns derived from complex and simple motor imagery tasks to that generated by a closely matched physical response, and the effective classification performances by each of these three groups.

To address this gap in the literature, this EEG study aims to explore frequency-band functional responses of an object-oriented motor imagery paradigm in comparison to the responses obtained by simple mental imagery and physical execution. As prior knowledge of the task is known to influence motor imagery performance (Wriessnegger et al., 2018), the objects used for the object-oriented imagery task included a cup and a comb, and healthy individuals were expected to kinaesthetically imagine drinking from the cup and combing using the comb. The majority of prior research has

presented pictures of the object (Li et al., 2015; Wriessnegger et al., 2018; Zhang et al., 2017b) whereas here the object itself was directly positioned in front of the participant to aid in constructing a three dimensional mental picture that could be used to potentially enhance the imagined response. An initial hypothesis for this study was therefore that spatial patterns following object-oriented motor imagery would demonstrate stronger event desynchronisations across the contralateral primary motor cortex in comparison to simple hand imagery. Furthermore, these profiles should align with the responses to physical movement of the hand. Due to the limited application of an object-oriented motor imagery study in the field of BCIs, this study additionally aims to demonstrate accuracy scores for the three paradigms across a group of twelve participants who contributed clean data for classification. A second hypothesis for this study was therefore that the complex motor imagery task would yield better classification accuracies over the simple imagery paradigm, with the former yielding comparable scores to those obtained following physical movement signal classification. With respect to the overarching goal of this thesis, the EEG focussed research within this chapter will identify fundamental data analysis parameters and classification tools that will ultimately aid simultaneous EEG-fNIRS motor imagery research. Whilst exemplifying how increasingly complex motor imageries compare to actual execution in healthy individuals, this study shall provide a framework from which both the motor imagery paradigm and methodologies can be developed in order to be beneficial for clinical application.

This chapter begins with a brief review of EEG signal processing methods in order to highlight the range of data analysis and classification tools available to researches and as explored in this and subsequent chapters. Primarily the methods discussed include: 1) enabling spatial localisation of brain responses, 2) extracting frequency band encoded neural signatures and 3) transforming multidimensional signals into a lower dimensional space that can be used for data classification. Following this we present the methods and results of this study before discussing them with respect to the findings of previous literature.

2.1.1. EEG analysis methods

Raw EEG scalp potentials are known to have a poor spatial resolution. This is a combination of a volume–conduction-induced mixture (i.e. a weighted sum) of the underlying brain sources (Jung et al., 1998; Nunez et al., 1994) and the necessary use of a reference electrode to measure differences in potentials (Burle et al., 2015). Several time domain methods have been proposed to address the volume conduction problem including global average referencing (referencing the EEG data from every electrode to the average EEG over all electrodes), bipolar referencing (see chapter 4), Laplacian filter estimates and common spatial pattern (CSP) filters (primarily used for EEG-based BCIs) (Blankertz et al., 2008; Brunner et al., 2016; Lei and Liao, 2017).

Simple Laplacian spatial filters (also referred to as current source and current scalp density estimates, CSD) estimate the spherical spline surface Laplacian of recorded scalp potentials thereby providing a means of reducing correlations among scalp-recorded channels (Jackson and Bolger, 2014; Kayser and Tenke, 2015; Rathee et al., 2017; Schomer and Silva, 2012) without the need of computationally expensive inverse imaging estimates (Baillet et al., 2001). The surface Laplacian is a two-dimensional reference free spatial high-pass filter that filters out spatially broad features of the data (low-spatial-frequency activity present at most electrodes) that are likely to reflect volume-conducted potentials in the absence of head tissue conductivities and brain source locations (Carvalhaes and de Barros, 2015; Cohen, 2014b; Kayser and Tenke, 2015). As a result of this transformation there is an overall enhancement in the spatial resolution of the EEG signal amongst other benefits (Kayser and Tenke, 2015). Nevertheless, whilst known to have several shortcomings (e.g. insensitivity to deep generator sources) (Biggins et al., 1991; Kayser and Tenke, 2015; Nunez et al., 1994), this tool has been widely applied to motor imagery research (Rathee et al., 2017; Wang et al., 2004). For example, Rathee and colleagues analysed multiple referencing and Laplacian filtering methods in terms of their pairwise binary classification performance of four motor imagery tasks (left-hand, right-hand, feet, and tongue) (Rathee et al., 2017). Two key findings noted by the authors were that, firstly, in comparison to a monopolar referencing scheme (i.e. left-mastoid referencing), current source density estimates better reflected contralateral effects in the alpha and beta frequency bands for the left- and right-hand imagery

conditions. Secondly, current source density filtered data generated mean classification accuracy scores above 80% in five out of the six pairwise binary classifications and 77% for the feet versus tongue condition, which were all greater than the classification results of both monopolar and global average referencing methods.

Having more accurately localised brain activity by reducing the negative impact of volume conduction, oscillatory changes in the alpha/mu and beta frequency bands can be better observed. Event-related EEG oscillations are typically studied by decomposing EEG signals into magnitude and phase information for each frequency present in the EEG (Roach and Mathalon, 2008). Changes in these frequency characteristics over time with respect to task events give this approach the term "time-frequency analysis" (Roach and Mathalon, 2008). EEG rhythms are the product of synchronously activated neurons therefore time-frequency analysis can assess spatially localised changes in power and synchronisation across trials through event-related desynchronisations (decreases in rhythmic activity power within a particular frequency band) and synchronisations (increases in rhythmic activity power within a particular frequency band) (Pfurtscheller and Aranibar, 1977; Roach and Mathalon, 2008). Such energy changes are typically non-phased locked to an event unlike event-related potentials which are phase-locked and explained as positive and negative voltage deflections present after averaging several EEG epochs time-locked to a stimulus (Pfurtscheller, 2001). The benefit of time-frequency analysis research over event-related potentials is that the former explains the parallel information processing of the brain with frequency specific or frequency banded oscillations reflecting multiple neural processes co-occurring and interacting (Lisman and Buzsáki, 2008).

The EEG signal is a composite of multiple sine waves varying in amplitude and frequency across time. As such several time-frequency decomposition methods exist in the literature (Allen and MacKinnon, 2010; Jerbic et al., 2015; Wang et al., 2018) that estimate a complex number for each time point in the time domain signal yielding both time and frequency domain information. Most commonly used decomposition methods include continuous complex Morlet wavelet (CMW) (Ferrante et al., 2015) and filter-Hilbert transformations (Rathee et al., 2017). Complex Morlet wavelets are by definition complex-valued sine waves windowed by a real-valued Gaussian that enable temporal localisation of frequency information from a non-stationary signal (Cohen, 2019). Convolution of the

time series signal with the CMW yields a complex-valued signal from which instantaneous power can be extracted at each time point. The width of the Gaussian taper has significant importance for controlling the trade-off between temporal and frequency precision - i.e. a narrow (wider) Gaussian leads to an increased temporal (spectral) precision at the cost of decreased spectral (temporal) precision (see appendix figure AF2.1). Unlike wavelet convolution, the Hilbert transform allows extraction of a complex signal from the entire real-valued time series (Papoulis, 1977). Application of this transformation requires prior filtering of the data into specific frequency bands such that the resulting analytical signal is a reflection of the pass-band of interest. Two branches of filters commonly exist: finite impulse response (FIR - e.g. windowed linear phase) and infinite impulse response (IIR – e.g. Butterworth, Chebyshev and Elliptic). Whereas the former is considered more stable and less likely to introduce nonlinear phase distortions, the latter is known to improve the frequency specificity of the signal by plateauing maximally in the desired pass-band (see appendix figure AF2.2) (Cohen, 2014a).

Prior work by Allen and MacKinnon used multiple time frequency analysis tools to assess ERD/ERS responses over the C3 region during a finger tapping task (Allen and MacKinnon, 2010). The authors noted that whilst a 64-sample short time Fourier transform and epileptic filter separated ERD/ERS activity in the time axis, a Butterworth filter, 128-sample short time Fourier transform, and continuous wavelet transform were better at discriminating between alpha and beta activity. Interestingly, a report by Bruns which reviews wavelet, short-time Fourier and Hibert spectro-temporal analysis methods demonstrates that the derived parameters (i.e. amplitude and phase) from each of the transforms are mathematically equivalent and thus results can be effectively matched provided that analysis parameters are similar (Bruns, 2004).

Classification of multi-channel EEG potentials have been known to occur on both spectral (Pfurtscheller et al., 1998) and frequency band filtered (Wang et al., 2005) data. For the latter, the CSP algorithm is a widely accepted pre-processing tool in motor imagery-BCI research as it aims to construct optimal spatial filters that discriminate two classes of EEG measurements. The CSP algorithm was introduced in the field of EEG analysis by Koles and colleagues (Koles et al., 1990) and is based on principal component analysis decomposition (Wold et al., 1987) and can be regarded as a supervised blind source separation technique (Parra and Sajda, 2003) (similar to independent component analysis

(Comon, 1994)) whereby high-dimensional spatio-temporal raw EEG signals are projected onto a few spatial filters that are designed such that signal variances between two classes are maximised (i.e. the resulting signals carry only the most discriminative information) (Müller-Gerking et al., 1999). The spatial patterns derived from the CSP filter reflect EEG source distribution vectors and the most weighted channels within each of these patterns are likely the channels most correlated with the task specific sources.

For effective use of the CSP algorithm, several parameters need to be specified, including the EEG time interval relative to the stimulus, frequency limits for band-pass filtering, the band-pass filtering method and the subset of CSP filters (i.e. number of components) (Blankertz et al., 2008). For CSP band-pass filtering methods, both FIR (Ramoser et al., 2000) and Butterworth (Zhang et al., 2018a) filters have equally been reported in the motor imagery literature. The optimal number of filters for classification however depends on the number of channels used for recording. Limiting the classifier to only the first and last filters may limit the model's ability to fully capture discriminating features between the two classes, whereas the use of a larger number of inward filters may result in overfitting. It has therefore been suggested to use a total of between two to six CSP filters (Blankertz et al., 2008). Since the publication of the first CSP algorithm by Koles and colleagues, there have risen a range of variants to this classical approach (Koles et al., 1990). These include the class of regularised CSP methods that improve the algorithms robustness against noise and outliers and prevent overfitting (Lotte and Guan, 2011; Yong et al., 2008), and CSP methods that tackle the issues of manually setting a broad frequency range or subject-specific optimal frequency ranges prior to spatial filtering (such as common spatio-spectral pattern (Lemm et al., 2005), common sparse spectral spatial pattern (Dornhege et al., 2006), sub-band CSP (Novi et al., 2007) and filter-bank CSP (Ang et al., 2008)).

This overview highlights that a single pipeline cannot be applied to all EEG studies, and the final choice of methods is driven by the research question, the type of paradigm explored, the density of the electrode cap and its spatial coverage on the scalp, and the quality of the measured data. Whilst many EEG processes are standardised (Delorme and Makeig, 2004; Oostenveld et al., 2011), there remain several fine-tuning parameters that require identifying in order to reliably and accurately demonstrate brain responses to a cue. As such, in line with the aims of this study, results in this chapter

are presented for different analysis methods in order to develop a framework that be extended and applied to simultaneous EEG-fNIRS data analysis.

2.2. Methods

2.2.1. Experimental setup and paradigm

Twenty healthy participants (7 male, 12 female, 1 undisclosed, aged 18-33 years) that had provided written and informed consent took part in the study which had ethical permission obtained from the University of Birmingham STEM ethics board. A 64-channel, Biosemi Active Two system (Biosemi Inc., Amsterdam, Netherlands) was used to acquire the EEG data. Participants wore a headcap with 64 pre-positioned electrode holders based on the 10-20 International system of electrode placement. The holders were filled with saline gel prior to inserting the Ag-AgCl electrodes. In addition to the 64 active electrodes, two offline reference electrodes were placed on the left- and right-mastoids. Participants were then transferred to a sound-attenuating room where they sat comfortably in front of an adjustable screen.

The experimental paradigm (figure F2.1) designed in Matlab (R2016b, MathWorks, MA, USA) using the Psychophysics Toolbox extensions (Psychtoolbox-3) (Brainard, 1997; Pelli, 1997) involved the completion of three tasks as follows:

i. *Object-oriented motor imagery*: A cup and comb were positioned next to each other at an arm's distance from the participant without obscuring the screen. Participants were instructed to look at the object (i.e. cup or comb) during the preparation phase and then either kinaesthetically perform motor imagery of “drinking out of a cup” or “combing” with their right-hand during the action phase respectively.
ii. *Classical motor imagery*: Participants were presented with and would look at the words “Hand” or “Toes” on the screen during the preparation phase, following which they were required to imagine repeatedly gripping and releasing their right-hand or wiggling their toes during the action period.

iii. *Physical movement*: Participants were presented with and would look at the words "Hand" or "Toes" on the screen during the preparation phase, following which they were required to physically and repeatedly grip and release their right-hand or wiggle their toes during the action period.

Participants completed the three independent tasks in one sitting in the order of 1) object-oriented motor imagery, 2) classical motor imagery and 3) physical movement. Each task was divided into four blocks of twenty-four trials (twelve of each trial type, for example twelve trials of right-hand movements and twelve trials of wiggling of toes for the physical movement task). Between blocks and tasks participants were given a sufficient rest period and prior to the start of each block/task electrodes were ensured to be fastened correctly, impedances were corrected, and participants were instructed to remain as still as possible to minimise any movement artifacts. The trials within each task were randomised such that no more than two of the same kind were presented in a row. Each trial included a baseline period, a preparation phase and an action period. The purpose of the additional preparation phase of the study was to avoid confounds of eye movements across conditions. Having participants shift their gaze to either the screen or object during this time limited possible eye movement artifacts during the execution period of the study.

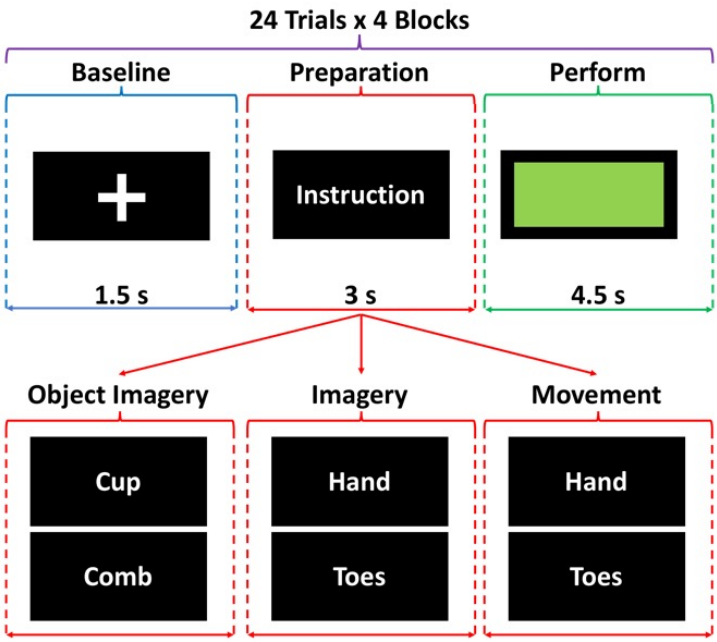

Figure F2.1: Overview of the study paradigm. Participants completed three independent tasks in one sitting (see the main text for further details on each task). A total of 96 trials were performed per task (four blocks of twenty-four trials). Each trial lasted 9 s and included a 1500 ms baseline recording, 3000 ms preparation phase and 4500 ms action period. During the baseline recording a white fixation cross was presented on the screen and participants were asked to relax and refrain from thinking about the task. During the preparation phase, the instruction for the forthcoming action was presented on the screen. Depending on the task being undertaken, the participant was instructed to either continue watching the screen or observe the object on the table. Finally, during the action period, a green square was displayed on the screen signalling to participants to perform the action corresponding to the instruction given in the preparation phase.

2.2.2. Data pre-processing

Pre-processing and analysis of the EEG data sampled at 256 Hz was performed in Matlab with the aid of functions from the EEGLAB (version 14.1.1b, Swartz Center for Computational Neuroscience, UC San Diego) toolbox (Delorme and Makeig, 2004). Of the twenty participants that took part in the study, eight were excluded from the analysis either due to instrumental errors or the failure to complete all three components of the experiment.

Initial pre-processing included referencing the 64 electrodes to the linked left- and right-mastoids, high- and low-pass filtering between 0.5 and 40 Hz to attenuate low frequency drifts and electrical noise respectively, and the rejection of high amplitude artifact contaminated trials/channels. Marked epochs/channels were identified as those with a *z*-score greater than three standard deviations from the mean trial/channel voltage. Using this method between 0 and 4 trials were removed per task per participant leaving an average number of 47 trials for each action cue within a particular task to be further analysed. Further pre-processing of the data included independent component analysis, channel interpolation, spatial filtering, and lastly the baseline correction of each epoch to enhance the effects of the preparation and execution phases of the study.

The non-directional method of independent component analysis which identifies independence between sources of the data was performed to eliminate spontaneous eye movement and blink artifacts (Hoffmann and Falkenstein, 2008). Using EEGLAB's '*pop_runica*' function, independent component analysis computation generated scalp components from which topographies representing ocular artifacts were manually identified and removed. Between 1 to 2 independent components were removed per participant that topographically predominantly represented blinks and/or horizontal eye movement activity along frontopolar electrodes. The resulting data were then back-projected and previously eliminated channels were interpolated (using EEGLAB's '*pop_interp*' function) to reinstate a complete dataset.

Following this, the signals were spatially filtered using the surface Laplacian (section 2.1.1). This was performed using the CSD toolbox (version 1.1) (Kayser, 2009; Kayser and Tenke, 2006) with a spline flexibility value of 4 (resulting in a rigid spline interpolation) and a regularization (smoothing) parameter of $1x10^{-5}$. The effects of this technique on individual and group scalp topographies in the current study are shown in figure F2.2. A single participant performing physical and repeated grips of their right-hand (figure F2.2a left) generated an alpha-band filtered topographic profile with a prominent desynchronisation over the C3 region 500s onwards post spatial band-pass filtering. Similarly, elimination of the broad spatial component to wiggling of the toes condition (figure F2.2a right) highlighted a modest desynchronisation over Cz and CPz. Interestingly, group averaging of surface Laplacian maps brought to light the hemispheric cross-talk present during repeated grips of the

right-hand (figure F2.2b right). Between 500-2000 ms a strong contralateral (C3 and CP3 scalp locations) response is present as similarly found in the single subject case, however, with an additional growing negative energy ipsilateral response around C4. Interestingly, for the condition of wiggling of the toes (figure F2.2b left), across the group the response at Cz is lost and instead a strong desynchronisation is identified around CP1-P1-Pz-CPz. This is either a sole response to the presentation of a bright green screen marking the onset of the action period of the task, and thus a lack of a detectable response of moving the toes by individual participants given its nestled location within M1 (Ehrsson et al., 2003), or a combination of the two.

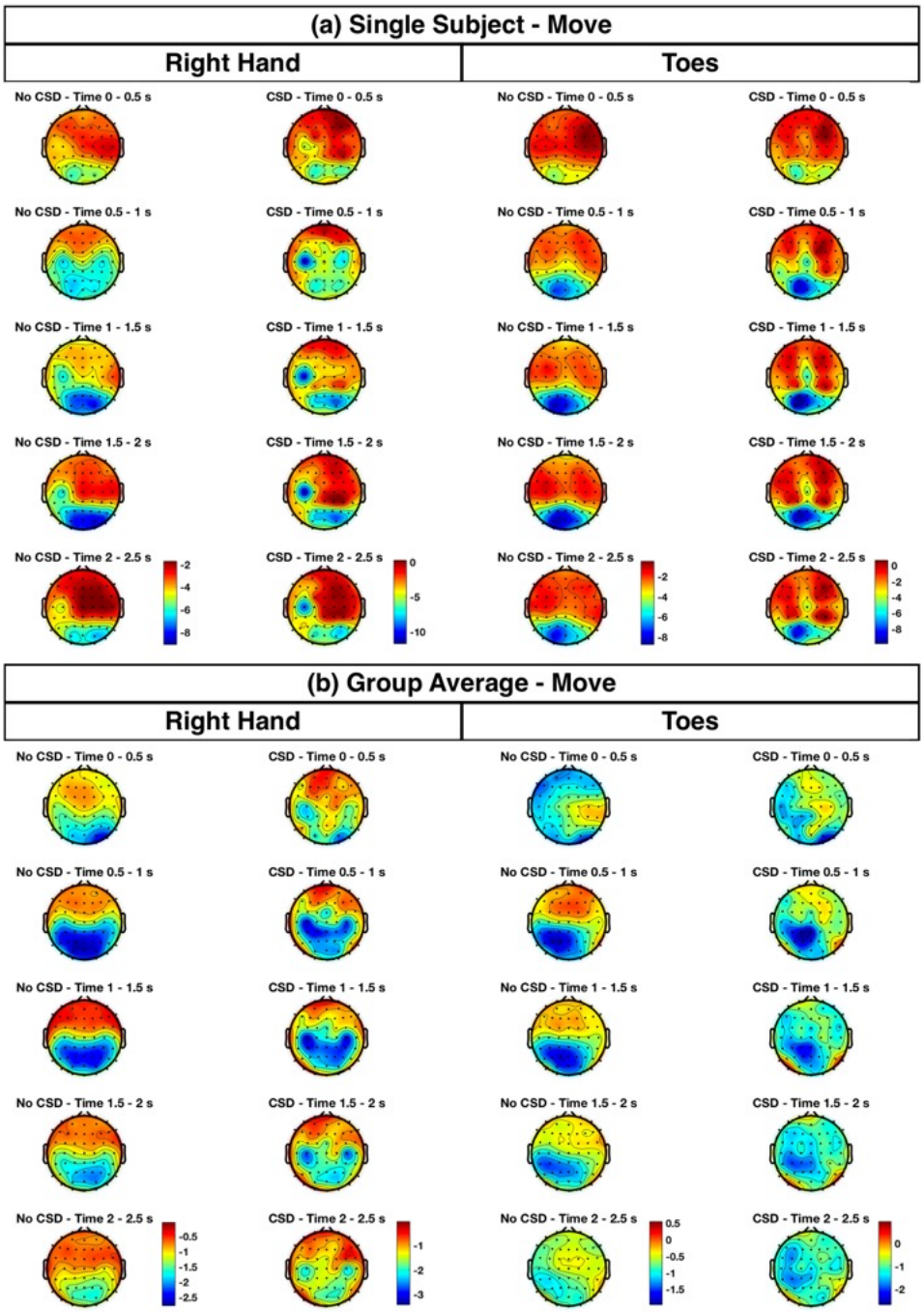

Figure F2.2: Spatial filtering effects of the surface Laplacian. These data demonstrate the alpha frequency band, physical movement topographic maps, following no CSD (left) and CSD (right) spatial filtering within the data pre-processing stage. The pre-processed data were time-frequency decomposed using a fifth-order Butterworth filter Hilbert transformation to generate the above plots. For both the single subject (a) and group average (b) topographies, the CSD spatial filter appears to eliminate a broad component spanning the central (motor) scalp electrodes thereby emphasising effects pertaining to both right-hand gripping (contralateral activation at C3 or a bilateral activation at both C3 and C4) and the wiggling of toes (activation at Cz-CPz).

After separating the pre-processed epochs into their respective conditions, the frequency band-specific power (amplitude squared) of the recorded potentials were subsequently examined. Specifically, the frequency bands of interest were that of alpha/mu (~8-13 Hz) and beta (~13-30 Hz). Three approaches of time-frequency decomposition were investigated including CMW, FIR-filter Hilbert transforms and IIR-filter Hilbert transforms (section 2.1.1). For the CMW analysis, ten-cycle wavelets, nine seconds in length were created for each frequency within the studied alpha and beta bands. These were in turn convolved with the data to yield the desired power spectral densities. For the filter Hilbert analysis, FIR filtering was performed using a thirty second-order windowed linear phase filter kernel (Matlab function '*fir1.m*') whereas IIR filtering was performed using a fifth-order Butterworth filter kernel (Matlab function '*butter.m*'). For the latter the fifth-order filter provided a good trade-off between frequency precision and the introduction of breaks and ripples within the desired pass-band (see appendix figure AF2.3). These filters were in turn applied to the time series signal using the function '*filtfilt.m*'. The resulting real-valued filtered data containing band specific frequencies specified by the frequency response of the filter kernel was Hibert transformed (using the function '*hilbert.m*') to yield the desired power spectral densities. Time-frequency analysed signals were then averaged across trials and decibel baseline normalised to allow effective comparisons.

2.2.3. Classification

Single trial and single subject classification of the two conditions within each of the three tasks was achieved through a multistep process including CSP pre-processing, feature selection and classifier training and testing. The CSP algorithm designs a spatial filter by means of spatial covariance and signal whitening. A linear transformation then projects the multi-channel EEG data into a low-dimensional spatial subspace in which only a subset of components (containing weights for channels) explain the majority of differences between classes (by way of maximising their variances) (Ramoser et al., 2000; Wang et al., 2005). Details of the algorithm published by Ramoser and colleagues (Ramoser et al., 2000) and as used in this study are presented through equations 2.1-2.8.

The CSP algorithm was applied on short centred and scaled overlapping data segments that were previously filtered into alpha and beta frequency bands using a fifth-order Butterworth filter. Specifically, the 4500 ms action period of the task was divided into 1000 ms sliding windows with a 75% overlap. The option to classify overlapping data segments was based on previous research by Asensio-Cubero and colleagues, which identified that using overlapping windows (1000 ms segments with an 80% overlap) performed better than using entire epochs and uniform segments without any overlap when attempting to classify multiple limb imagery tasks (right-hand, left-hand, feet and tongue) (Asensio-Cubero et al., 2011).

In the first step of the algorithm, the normalised spatial covariance of two different tasks were calculated as follows:

$$\boldsymbol{R}_H = \frac{\boldsymbol{X}_H \boldsymbol{X}_H{}'}{trace(\boldsymbol{X}_H \boldsymbol{X}_H{}')} \qquad \boldsymbol{R}_F = \frac{\boldsymbol{X}_F \boldsymbol{X}_F{}'}{trace(\boldsymbol{X}_F \boldsymbol{X}_F{}')} \qquad \textbf{[eq. 2.1]}$$

Here, $\boldsymbol{X}_H$ and $\boldsymbol{X}_F$ for example represent a single right-hand trial and toe trial within the physical movement task. These matrices have dimensions $N \times T$, where N is the number of channels and T is the number of sampled data points. $\boldsymbol{X}'$ is the transpose of $\boldsymbol{X}$ and *trace(**Y**)* computes the sum of the diagonal elements of $\boldsymbol{Y}$. Averaging $\boldsymbol{R}_H$ and $\boldsymbol{R}_F$ over all the trials in each group gives the averaged normalised spatial covariance matrices $\overline{\boldsymbol{R}_H}$ and $\overline{\boldsymbol{R}_F}$. Summating these values gives the composite covariance matrix, $\boldsymbol{R}_C$, which can be factored into the product of three matrices as follows:

$$\boldsymbol{R}_c = \boldsymbol{U}_c \boldsymbol{\lambda}_c \boldsymbol{U}_c{}' \qquad \textbf{[eq. 2.2]}$$

where $\boldsymbol{U}_C$ is the matrix of eigenvectors and $\boldsymbol{\lambda}_c$ is the diagonal matrix of eigenvalues. The whitening transformation matrix, $\boldsymbol{P}$, is then formed as follows:

$$\boldsymbol{P} = \sqrt{\boldsymbol{\lambda}_c^{-1}}\boldsymbol{U}_c{}' \qquad \textbf{[eq. 2.3]}$$

which then transforms the average normalised covariance matrix as follows:

$$\boldsymbol{S}_H = \boldsymbol{P}\overline{\boldsymbol{R}_H}\boldsymbol{P}' \qquad \boldsymbol{S}_F = \boldsymbol{P}\overline{\boldsymbol{R}_F}\boldsymbol{P}' \qquad \textbf{[eq. 2.4]}$$

Applying a whitening transformation matrix to the data ensures that the resulting matrices, $\boldsymbol{S}_H$ and $\boldsymbol{S}_F$, are uncorrelated. These matrices share common eigenvectors and their corresponding eigenvalues sum to one. Factorisation of $\boldsymbol{S}_H$ and $\boldsymbol{S}_F$ as:

$$\boldsymbol{S}_H = \boldsymbol{U}\boldsymbol{\lambda}_H\boldsymbol{U}' \qquad \boldsymbol{S}_F = \boldsymbol{U}\boldsymbol{\lambda}_F\boldsymbol{U}' \qquad \textbf{[eq. 2.5]}$$

yields

$$\boldsymbol{\lambda}_H + \boldsymbol{\lambda}_F = \boldsymbol{I} \qquad \textbf{[eq. 2.6]}$$

where $\boldsymbol{I}$ is the identity matrix. Thus, in the whitened measurement space spanned by $\boldsymbol{U}$, the variance accounted for by the first m eigenvectors (those corresponding to the m largest eigenvalues in $\boldsymbol{\lambda}_H$) will be maximal for $\boldsymbol{X_H}$. Furthermore, because of the sum constraint on $\boldsymbol{\lambda}_F$, the variance accounted for by these eigenvectors must then be minimal for $\boldsymbol{X}_F$. The reverse will be true for the last m eigenvectors for which the eigenvalues in $\boldsymbol{\lambda}_F$ are maximal. The whitening matrix and common eigenvectors can then be used to compute a projection matrix, $\boldsymbol{W}$,

$$\boldsymbol{W} = \boldsymbol{U}'\boldsymbol{P} \qquad \textbf{[eq. 2.7]}$$

that transforms the original time series, $\boldsymbol{X}$, into uncorrelated components, $\boldsymbol{Z}$, (i.e. the strong correlation between the two conditions are removed and both distributions are simultaneously de-correlated) using the following equation:

$$\boldsymbol{Z} = \boldsymbol{W}\boldsymbol{X} \qquad \textbf{[eq. 2.8]}$$

Each column vector of $\boldsymbol{W}$ is a spatial filter and each column of $\boldsymbol{A}$, where $\boldsymbol{A} = (\boldsymbol{W}^{-1})'$, is a spatial pattern that illustrates how the sources project to the scalp.

The first and last columns of $\boldsymbol{W}$ and $\boldsymbol{A}$ are the most important spatial filters and patterns respectively as these explain the greatest variance for the two conditions. The first column explains the greatest variance for the positive condition and least variance for the negative condition, and vice versa. As it has previously been suggested to use between one to three eigenvectors from each end of the projection matrix (resulting in a total of two to six components) (Blankertz et al., 2008), classification performances were obtained for a four-component matrix extracted from a 64-electrode dataset and subsequently a two-component matrix extracted from a reduced (35-channel) dataset as performed by Wang and colleagues (Wang et al., 2004). The latter reduced dataset focussed on fronto-central, central and fronto-parietal scalp electrodes (F1, F3, F5, FC5, FC3, FC1, C1, C3, C5, CP5, CP3, CP1, P1, P3, P5, Pz, CPz, Fz, F2, F4, F6, FC6, FC4, FC2, FCz, Cz, C2, C4, C6, CP6, CP4, CP2, P2, P4 and P6) spanning brain regions known to be active during both physical and imagined activations of the hands and toes.

After extracting a set number of eigenvectors from the projection matrix, an *m*-dimensional feature vector was then constructed from the variance of the columns of $\boldsymbol{Z}$ as follows:

$$f_q = \log\left(\frac{var(z_q)}{\sum_{i=1}^{2m} var(z_i)}\right) \qquad \textbf{[eq. 2.9]}$$

where m corresponds to the number of columns from each end of $\boldsymbol{W}$, z_q is the q-th column vector of $\boldsymbol{Z}$, and *var(z)* denotes variance as estimated from elements of z, which are viewed as realisations of a random variable (Ramoser et al., 2000).

Following feature extraction and selection, single trials were classified using a support vector machine (SVM). For a two-class problem (i.e. hand and foot movements) an SVM classifier is greatly favoured as it attempts to maximise the distance between the separating hyperplane and the nearest training points or so-called support vectors. Furthermore, SVM is known to have good generalisation properties, scales well to high-dimensionality data, can explicitly control errors, is insensitive to overtraining (in the linear SVM case) and is suitable for small training sets (Cortes and Vapnik, 1995; Jain et al., 2000). The trials from each task were equally divided into six folds and a six-fold cross-validation procedure was implemented whereby a single consecutive fold of trials was used for testing the classifier and the remaining five folds for training. Classification scores were estimated with an empirical receiver-operating curve (ROC) analysis applied on trials' predicted probabilities (King et al., 2013). The results of the ROC analysis were summarised by the area under the curve (AUC) with an AUC of 50% implying that true positive predictions and false positive predictions are, on average, equally probable, whereas an AUC of 100% indicating a perfect positive prediction with no false positives. The advantage of studying this classification result as opposed to the mean accuracy is that as a non-parametric analysis method no assumptions are implied about the distribution of the underlying data.

2.2.4. Statistical analysis

Statistical analysis was performed on the time-frequency analysed data and the AUC results following classification. Single subject and group level significance testing was determined between opposing conditions within each of the three tasks. A cluster-based permutation test was conducted using the method described by Maris and Oostenveld (Maris and Oostenveld, 2007). An example workflow corresponding to the group statistical analysis of the physical movement time-frequency decomposed data is described as follows:

1. Time point wise t-tests were performed (using the Matlab function '*ttest.m*') between the trial averages of the right-hand condition and that of the toes condition across all twelve participants. The test statistics (*t*-values) for all time points within significant clusters were summated and stored.
2. The data from the two experimental conditions were re-collected and the condition label of each participant was randomly shuffled (using the Matlab function '*randi.m*') such that the number of participants in each condition remained the same.
3. A t-test was once again performed on these randomly partitioned contrasts and the *t*-values for all time points within the largest significant cluster were summated and stored.
4. Steps 2 and 3 were repeated 1000 times to draw a histogram of permutation *t*-values. These 1000 *t*-values corresponded to the summed *t*-values (step 3) computed from each randomisation (step 2).
5. This distribution was used to test each significant cluster's summed *t*-value obtained in step 1. If the p-value of a significant cluster was smaller than the critical alpha-level (typically, $p<0.05$), then it was concluded that, within that particular time range, the data in the two experimental conditions were significantly different.

Statistical testing of temporal clusters alone does not account for the spatial connectivity recorded by each scalp electrode. Functions from the FieldTrip toolbox (version 20171231, Radboud University, Netherlands), such as "*ft_prepare_neighbours*" with a neighbourhood radius parameter of 40 mm, were therefore used to perform the spatiotemporal statistical testing on the power spectral density data (Oostenveld et al., 2011). Two-tailed t-tests were only conducted for the action period of task as this study predominantly intended to investigate significant differences between conditions of different motor responses. To account for the number of tails within the statistical test, a Bonferroni correction was further applied reducing the critical value to $p<0.025$.

In comparison to the power spectral density data, cluster-based permutation testing was applied to both the single subject and group AUC results following classification. In the single subject case individual trial labels were randomly shuffled across the two conditions during the randomisation step. Unlike the t-test based permutation statistics previously performed, to account for the non-parametric

nature of the AUC result, a one-tailed Wilcoxon-Mann-Whitney (or rank sum) test was performed with an alpha value of 0.05, and a distribution of temporally significant clusters in the action period of the task, based on the values of the *U*-test statistic, was devised. For both time-frequency and classification statistical analyses, a total of 1000 randomised permutation runs were performed at the group-level whereas 200 were performed at the subject-level due to extensive computation demands.

2.3. Results

2.3.1. Time-frequency analysis

Group averaged spectral topographies for three frequency decomposition methods are depicted in figure F2.3. For the alpha envelope during right-hand physical movement, the Morlet wavelet (figure F2.3a) highlights a strong event related desynchronisation over C3 with an equally strong ipsilateral response between 500-1500 ms. After this time the response over C4 appears to diminish whereas the contralateral response persists for a further 500 ms. In contrast, the beta response to right-hand movement has a strong contralateral desynchronisation that is present in the first 500 ms following presentation of the action command. The response over C3 remains prominent until 2500 ms after the action instruction whereas the ipsilateral response dissolves in the first 1500 ms. Interestingly, a third strong desynchronisation is present over Cz which persists across all 500 ms time windows except between 1500-2000 ms where the response is solely over C3. The alpha response to toe physical movements begins after the first 500 ms following task onset and primarily spans the region enclosing CP3-CP1-P1-Pz-CPz. The strong desynchronisation within this window continues for 1000 ms following which the parietal responses dissipate. In contrast to this profile, the beta envelope delivers a topographic picture that includes strong desynchronisations over both Cz-CPz regions and fronto-central contralateral hand regions. The Cz-CPz electrodes which were positioned directly above the midline and were hypothesised to be most responsive to toe activations had an increasing negative energy (prominent event related desynchronisation (ERD)) that was separated from the hand response between 1000-2000 ms.

In similar agreement with these responses were the profiles obtained following filter-Hilbert transformation. Unlike the alpha band profiles of right-hand movement for Morlet wavelet convolution and Butterworth filter-Hilbert transformation (figure F2.3c), FIR filtering (figure F2.3b) identified a negative (albeit weak) desynchronisation at the occipital electrodes, a response possibly in result to presentation of the green screen which marked execution of the command. Extraction of this occipital activity by FIR filtering was additionally present in the alpha band activity of toe movements. FIR filtered beta responses to right-hand and toe movements were similar to those generated by Morlet wavelet and IIR filtering. Butterworth filtered Hilbert transformations yielded right-hand and toe movement topographic maps closely matched to those generated by Morlet wavelet convolution. Strikingly, the largest difference between these two time-frequency analysis methods is seen in the beta response between 1500-2000 ms. Whereas an exclusive strong desynchronisation was present over the C3 region during this time window for Morlet wavelet convolution, filter-Hilbert transformations additionally sampled responses over the Cz-CPz region. Nevertheless, unlike Morlet wavelet and FIR filtering analyses, the power responses to Butterworth filter Hilbert transformation are of much greater strength in the negative direction thus enabling better separation of strongly and weakly activated brain regions in response to the task.

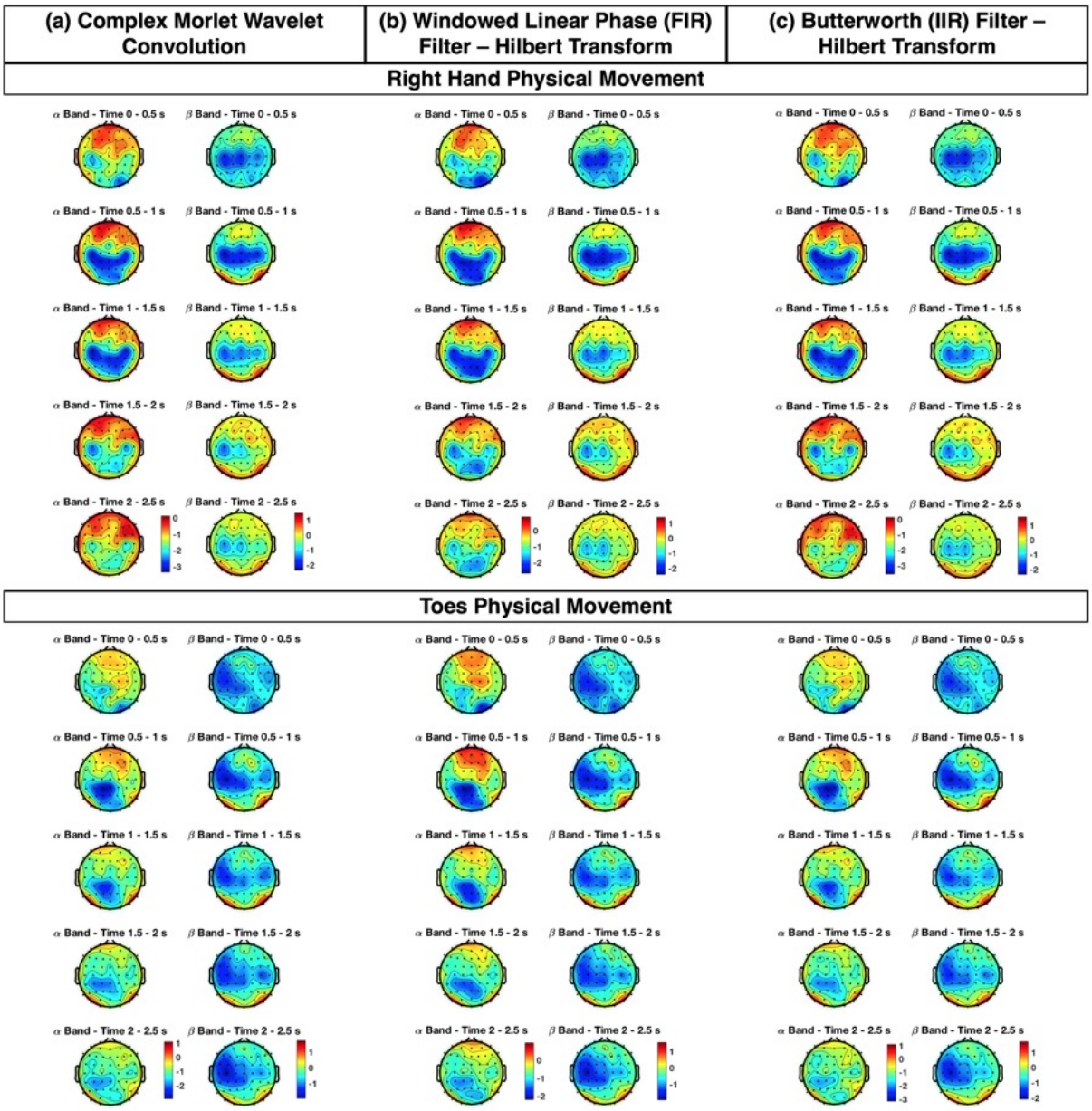

Figure F2.3: Group averaged power spectral density maps for three different time-frequency analysis methods. Alpha (left) and beta (right) frequency band results for the physical movement task are shown in the above figure. For complex Morlet wavelet convolution (a) twenty-three ten-cycle wavelets were created (each considering a single frequency between 8-30 Hz) and convolved with the data and the results averaged in the two frequency bands of interest. Prior to the Hilbert transformation, two different filtering options were also explored including the FIR windowed linear phase (b) and IIR Butterworth (c) filters. For the former, a 32-cycle filter order was applied to improve the frequency precision of the filter kernel to the slowest frequencies of interest (in this case the 8 Hz signal of the alpha window), whereas for the latter, a fifth-order filter was applied to attenuate fewer frequencies in the passband and prevent any rippling effects within the stop band. The topographic plots showcase highly similar outputs for the CMW and Butterworth filter Hilbert transform methods.

Subsequently demonstrated are group averaged, Butterworth-filtered and Hilbert transformed spectral topographies for the classical (figure F2.4b) and object-oriented imagery (figure F2.4c) tasks. Like the physical responses (figure F2.4a), the neural responses to imagery commands predominantly reflect a decrease in energy however these are of approximately half the power. In the alpha window, a strong contralateral response to right-hand imagery is present over the C3-C1-CP3-CP1 region between 500-1500 ms followed by a weaker response between 1500-2000 ms. Interestingly, whilst some desynchronisation is present over FCz and Cz, regions corresponding to foot movements, there is no ipsilateral response as noted during physical right-hand movement. In contrast, in the beta band, whilst there was a lacking ipsilateral response to right-hand physical movement after 1000 ms, this is not the case for imagery where an observable response over FC2-FC4-C2-C4 is present. Nevertheless, like the beta response to physical right-hand movement, it appears right-hand imagery likewise samples both the contralateral and midline regions, albeit more widespread across the duration 0-2500 ms. Toe imagery in the alpha and beta windows present topographic profiles similar to those of physical toe movements. The alpha window displays a weakening desynchronisation over CPz-C1-P3 from 500 ms onwards, whereas the beta window whilst portraying activation over C3 and Cz-CPz regions has an equally strong ipsilateral response following the onset of the action period of the task.

It was aimed that the alpha and beta profiles to object-oriented imagery (figure F2.4c) would share similarities to right-hand imagery responses due to the nature of the imagery task involving the activation of the hand/arm to “drink” or “comb”. In both alpha and beta analyses a lower contralateral response is present over CP3-CP1 with additional occasional recruitment of central and frontal regions in the beta window. Interestingly, the scalp response to cortical activation is rapid and is present within the first 500 ms of task onset. Unlike cup motor imagery, comb imagery in the alpha window has prominent contralateral (C3) and ipsilateral (C4) event related synchronisations (ERS) and a strong desynchronisation over the occipital region 500 ms after participants are asked to perform the task. Beta analysis however refrains from sampling the lower occipital activation and instead highlights a desynchronisation over the contralateral-central regions of the scalp. This varied response of comb motor imagery may possibly be a result of the vagueness of the command. Simply asking the participant

to comb in the absence of any direction may have resulted in a multitude of unfocused responses across the group generating such topographic maps.

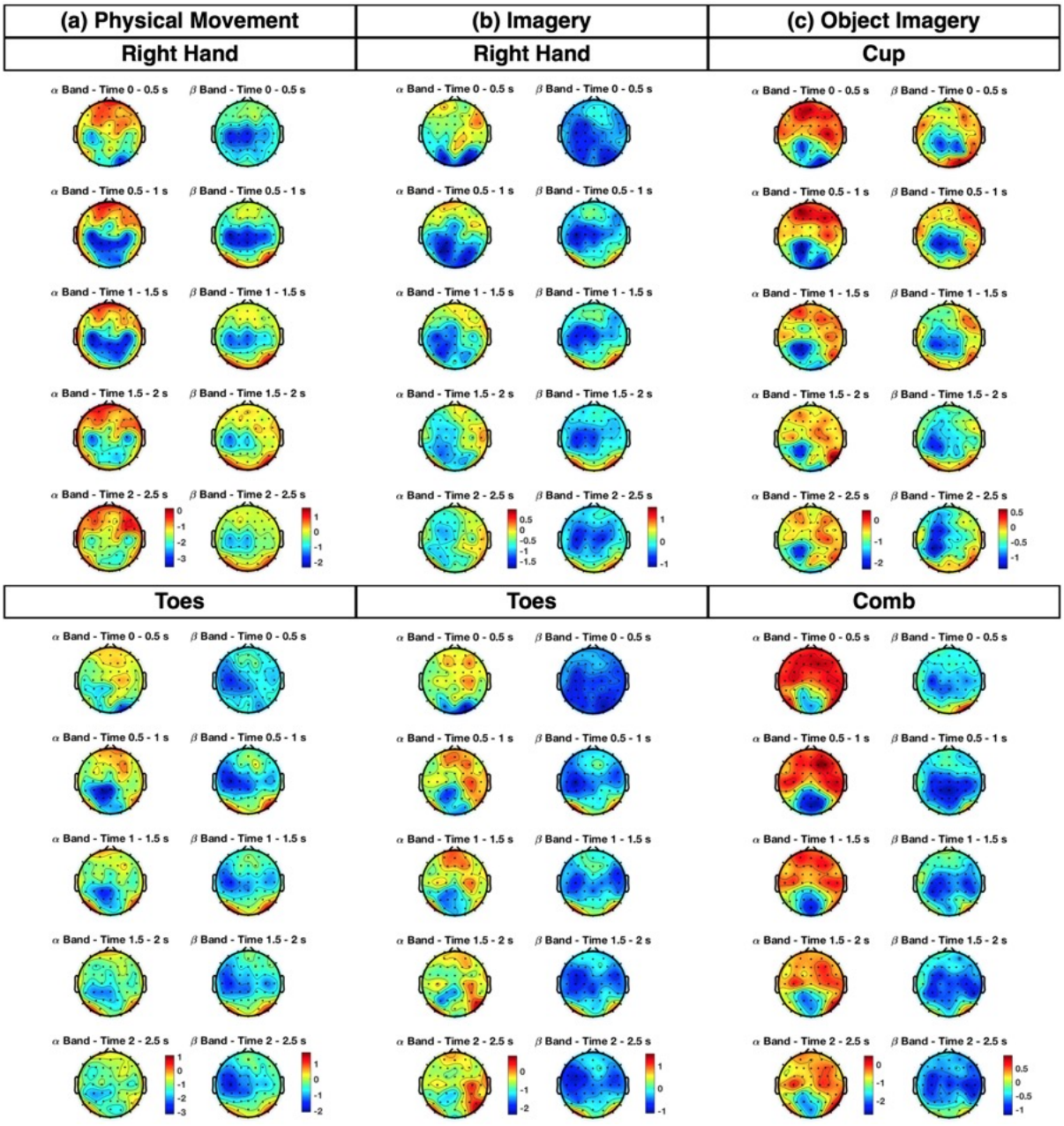

Figure F2.4: Group averaged power spectral density maps for physical movement (a), classical motor imagery (b) and object-oriented imagery tasks. The topographic images for the alpha (left) and beta (right) frequency bands were generated using a fifth-order Butterworth filter Hilbert transform. Plots were decibel baseline normalised.

Group level spatio-temporal cluster statistics yielded the results depicted in figures F2.5 and F2.6. Physical movement in the alpha window (figure F2.5, left) highlighted significantly different electrical activity ($p<0.025$, between right-hand and toe movements) spanning the parietal, and centro-parietal brain regions across the right hemisphere. The significant extent was largest over the right hemisphere whilst that across the left parietal region lasted approximately 120 ms. In the right hemisphere the significant difference was greatest over the CP4 electrode, which began 930 ms after participants were asked to perform the action and lasted approximately 800 ms. The differences in topographic plots highlight the precise time point at which significance was maximum. At 1238 ms the right-hand movement topography represents a strong desynchronisation that spans from the C3 to C4 region via the parietal lobe. In contrast, toe movements presented a map with weaker desynchronisations over Cz and lower parietal regions that spanned primarily over the left hemisphere. As such, the difference of the two topographies, whilst highlighting overall desynchronisations over C3 and CP4, found significance primarily over the latter due to neighbouring electrodes additionally portraying large differences between the two conditions.

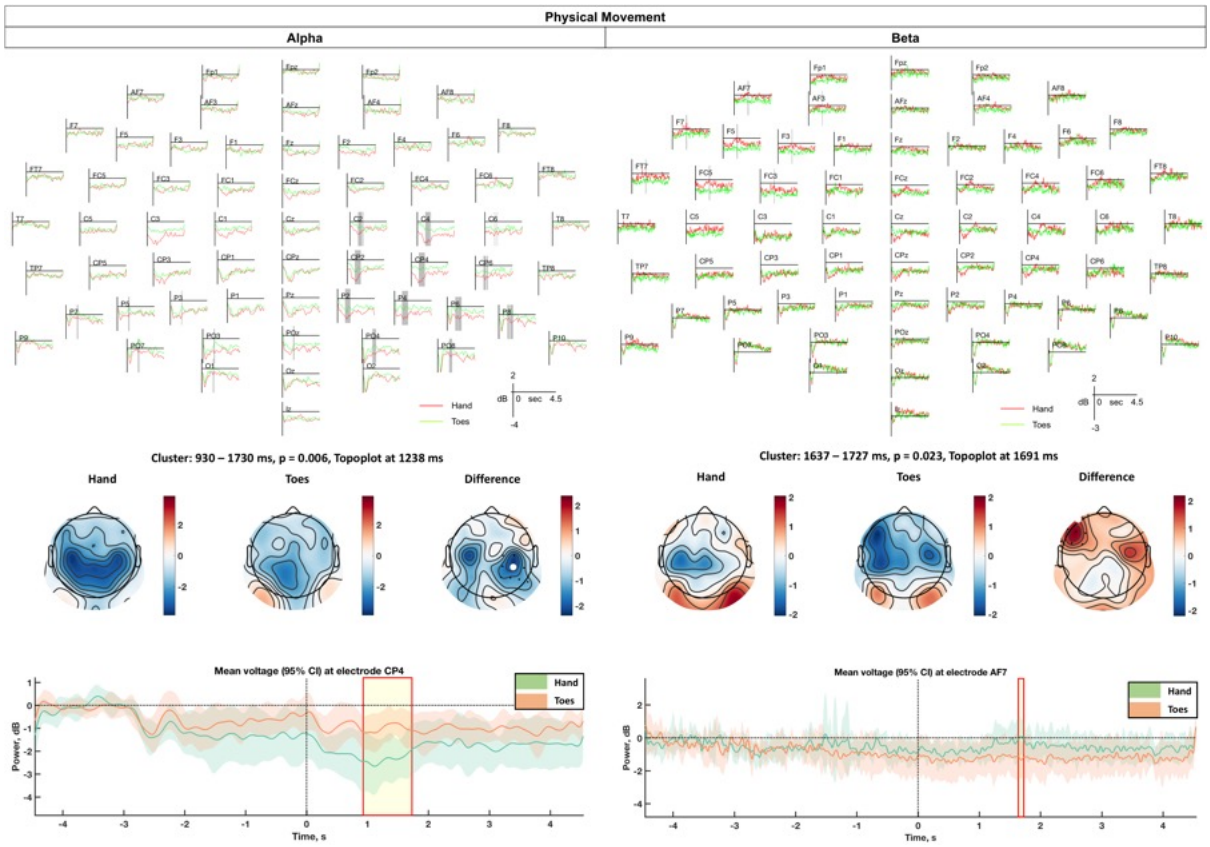

Figure F2.5: Spatio-temporal statistical analysis results for the physical movement task. The data from the alpha (left) and beta (right) frequency bands were independently analysed. The top images represent the time courses for each cue at each electrode. Statistically significant time points ($p<0.025$) are highlighted by the grey shaded regions. The middle images present the topographic distributions of each cue and the difference (third topographic plot). The electrode with the peak statistic is highlighted by a white circle in the third topographic plot. The bottom images present the average time course of all electrodes within the significant spatial cluster and overlaid (yellow shaded region) is the window of significance for the electrode that yielded the peak statistic.

Unlike the alpha window, physical movement in the beta band (figure F2.5, right) highlighted significantly different power profiles across the left fronto-central region. Peak statistical significance was observed over AFz and spanned 100 ms, ~1600 ms after task performance began. This significance region is driven by the topographic profile developed following toe movements across the group. Strong desynchronisations are present over the left M1 and span forwards into the left dorsolateral prefrontal cortex. In contrast, right-hand movements generate a map that is greatly negative over C3-Cz. Recruitment of the frontal cortex in the beta window is possible due to the spatial variability of toe

actions. Activations of this region have previously been observed for physical hand deflections and toe imagery movements using fMRI (Ehrsson et al., 2003; Hanakawa et al., 2003; Nakata et al., 2019). On the other hand, during the imagery task (figure F2.6), statistical significance in the beta band was identified across the right centro-parietal and temporal regions with greatest significance achieved at the CP4 electrode. Interestingly, the significant contrast which lasted 63 ms began more than 3000 ms after imagery onset and is primarily due to a return to baseline of right-hand elicited electrical responses.

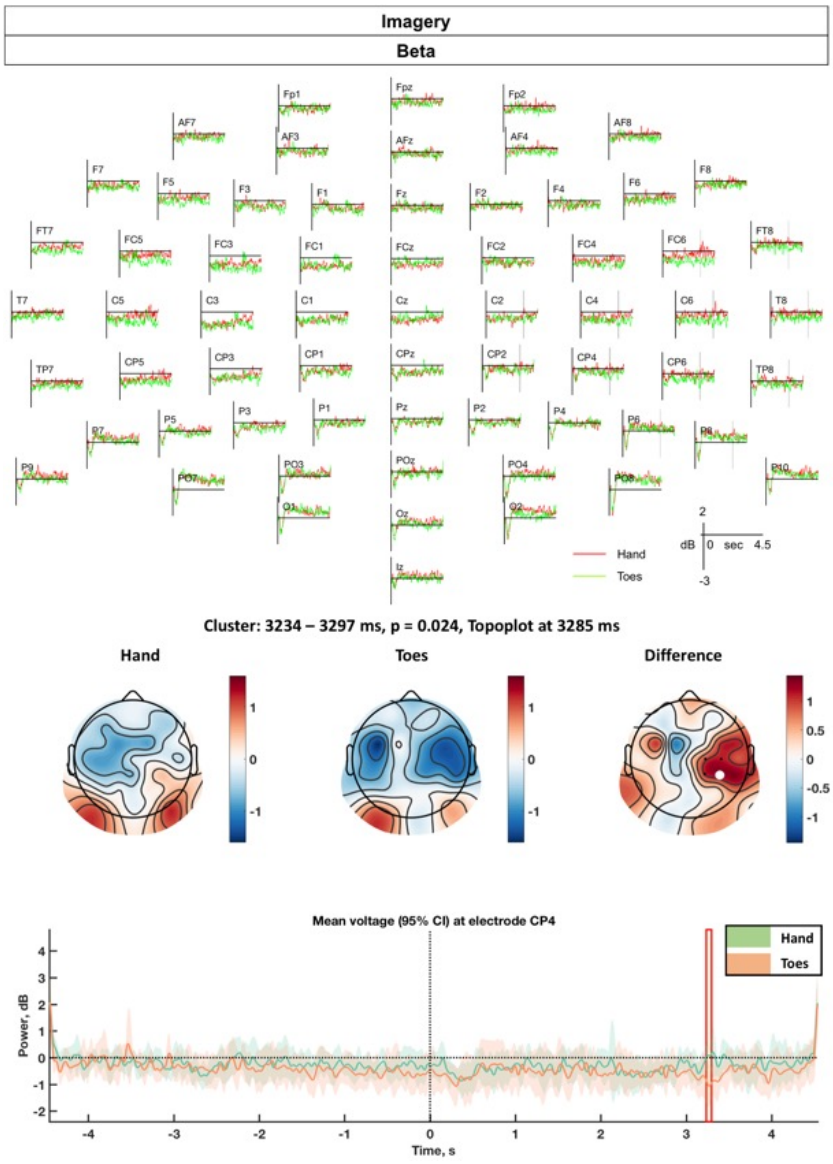

Figure F2.6: Spatio-temporal statistical analysis results for the classical imagery task. Although the data from both the alpha and beta frequency bands were analysed independently, significant clusters were only found for the latter. Refer to figure F2.5 for details on each of the plots displayed.

Unlike the group-level statistics, at the subject-level spatio-temporal regions of significant activation were additionally observed for both the classical imagery task in the alpha window and the object-based imagery paradigm (table T2.1). For the latter, peak significant clusters were identified in two participants in the alpha window spanning the occipital cortex. In contrast, filtering in the beta frequency band yielded two alternate participants with significant clusters over C3 and AFz. Given that object-oriented tasks were hypothesised to involve the recruitment of M1, significant activation at C3 highlights the greater desynchronisation of cup imagery (data not shown) which involved a directed drinking action in comparison to that of comb imagery. Physical movement and simple imagery tasks predominantly yielded peak statistically significant clusters across the right hemisphere (FC4, FC3, C4, CP2, CP4, PO8) over time windows that varied across the duration of the action period. In the alpha window however, participants 1 (movement), 2 and 3 (imagery) displayed peak channels at or immediately around the C3 electrode. This represents that in comparison to toe actions, the neural response to right-hand physical or imagined tasks was much greater for these participants.

Due to the temporal resolution of EEG being within the millisecond range it is unlikely that right-hand and toe responses for both physical movement and simple imagery tasks would be time varying such that significant differences (in the statistical sense) could be obtained at both the C3 and Cz regions. With this in mind and taking into consideration the spatial connectivity accounted for by the statistical method, a significance score in the right hemisphere and in the lower parietal regions depicts either stronger activations over both C3 and Cz regions during hand and toes cues or a lack of any response in these two regions from baseline. However, with respect to the latter theory, responses between baseline and action periods were in fact found to be significantly different ($p<0.025$) at these two electrodes (C3 and Cz) for both right-hand and toes cues when accounting for their spatial connectedness. These statistical differences were obtained by comparing the average baseline response with the average responses from 500 ms sliding windows in the action period for the group. For the physical movement task, both alpha and beta frequency band responses between baseline and all 500 ms time windows in the action period were significantly different ($p<0.025$). This was similarly the case for simple right-hand (significant differences observed between 500-3500 ms for alpha band activity and 0-4500 ms for beta band activity) and toes imagery cues (significant differences observed

between 500-4000 ms for alpha band activity). However, for beta frequency band responses from toes imagery trials the significant period was limited to 0-1000 ms which is in line with the beta rebound (beta ERS) displayed in figure F2.6 at the Cz electrode after this brief period.

Table T2.1: Participants displaying statistically significant ($p<0.025$) spatio-temporal clusters for each of the three tasks and each of the two frequency bands. Individual trial responses for each participant were randomised and the average response tested for regions of significance between the two action cues within each task to form a distribution. This distribution was used to determine overall regions of significance between the true average response for the two action cues for each participant. In addition to the participant number, also present are the electrodes and time points corresponding to the peak statistics.

Participants with a significant cluster				
Task	**Frequency bands**	**Participants**	**Peak channels**	**Peak windows (ms)**
Move	Alpha	1	FC4 C3 FC3	617 - 1176 1379 - 1621 3301 - 3633 3910 - 4180
		5	C4	430 - 895
		9	PO3	1473 - 1734
	Beta	1	FC4	2039 - 2102
		5	PO8 CP2 CP4	504 - 598 605 - 652 695 - 781
Imagery	Alpha	2	CP3	551-1016
		3	CP5	2125 - 2543
	Beta	12	PO8	3445 - 3492
Object-Imagery	Alpha	3	PO7	0 - 617 3781 - 3973
		5	Oz	3270 - 4191
	Beta	1	C3	2965 - 3016
		10	AFz	1461-1531

2.3.2. Classification

Feature extraction and selection utilised the CSP algorithm to decompose the channel data into a subset of components that maximised the variance between the two task conditions. Using a 4-

component matrix, spatial patterns (inverse of the spatial filters) for a 64- and 35-electrode set are portrayed in figure F2.7. For the 64-channel decomposition, the single subject case (figure F2.7a) prominently highlights that the spatial pattern of one task (i.e. right-hand) presents the ERD distribution of the second task (i.e. toes). From the alpha envelope for this participant (figure F2.2), the desynchronisation over C3 is dominant between 1500 and 2000 ms for right-hand movement, and as such, in component space (SP=1 in figure F2.7a) this action has an increased EEG variance over the toe area (Cz). In contrast, the weaker response to toe flexion results in close to zero EEG variance in the hand region (SP=3 in figure F2.7a). Across the group (figure F2.7c) a similar profile is seen with increased EEG variance over CPz for right-hand movement (SP=1) and a close to zero EEG power over C3-CP5 for toe movements (SP=3). In comparison to the 64-channel spatial patterns, the 35-channel maps for this participant (figure F2.7b) identifies strong EEG variances at both C3 and Cz electrodes for toe and hand movements respectively in the first-most important components (SP=1 and SP=4). This increased EEG power at C3 for hand movements is likewise noticeable at the group level (SP=4 in figure F2.7d), yet the response at Cz (SP=1 in figure F2.7d) remains extremely weak in line with the mild toe response generated by the group in figure F2.4a between 1500-2000 ms.

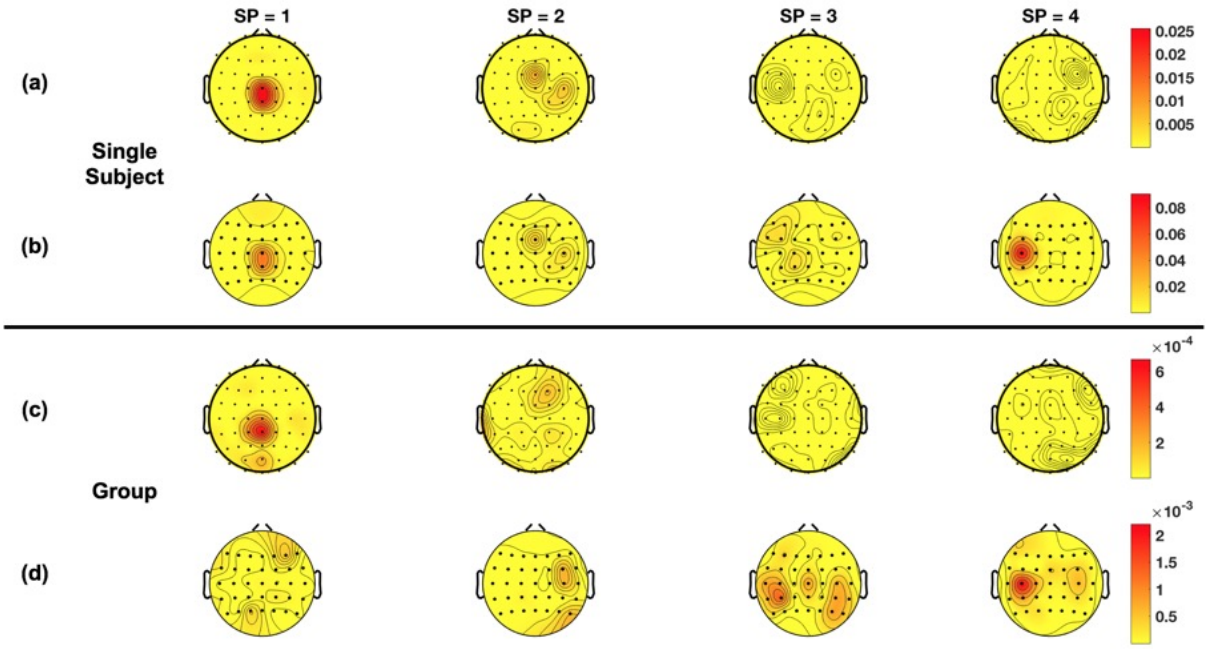

Figure F2.7: First two-most important spatial patterns determined by the CSP algorithm for the physical movement task. (a, b) Illustrative source projections on the scalp for a single participant and (b, d) average source projections across the group for both the (a, c) 64-channel and (b, d) 35-channel montages. The sliding time window used to develop these topographic maps was between 1250-2250 ms. The first-most important components (SP=1 and SP=4) explain the greatest variance between the two classes whereas inward components (SP=2 and SP=3) account for additional variances. Spatial patterns 1 and 2 predominantly correspond to hand movements whereas components 3 and 4 correspond to toe flexions.

Group classification scores for the 64 and 35 channel montages (decomposed to four and two spatial components respectively) are shown in figure F2.8. For the higher channel montage (figure F2.8a) statistically significant AUC scores ($p<0.05$) above chance (where chance was an AUC of 0.5) were observed for physical movement (beta frequency band only) and object imagery (both alpha and beta frequency bands) tasks only. In contrast, for the reduced channel classification (figure F2.8b), significant clusters were obtained in all three tasks and for both frequency bands. Whilst the group averaged AUC scores for the 64-channel layout remained below 0.60, those in the alpha band for the 35-electrode montage (figure F2.8b) peaked at approximately 0.65 and 0.61 for physical movement and imagery tasks respectively. Furthermore, group peak AUC scores for each task, frequency band and channel montage in the action period were greater than the peak AUC scores obtained following

classification of baseline responses (peak AUC scores for 64- and 35-channel montages were 0.51 and 0.53 respectively). The improved classification results found using a subset of the 64 recording electrodes represents improved spatial filtering of the two conditions within each task by the CSP algorithm.

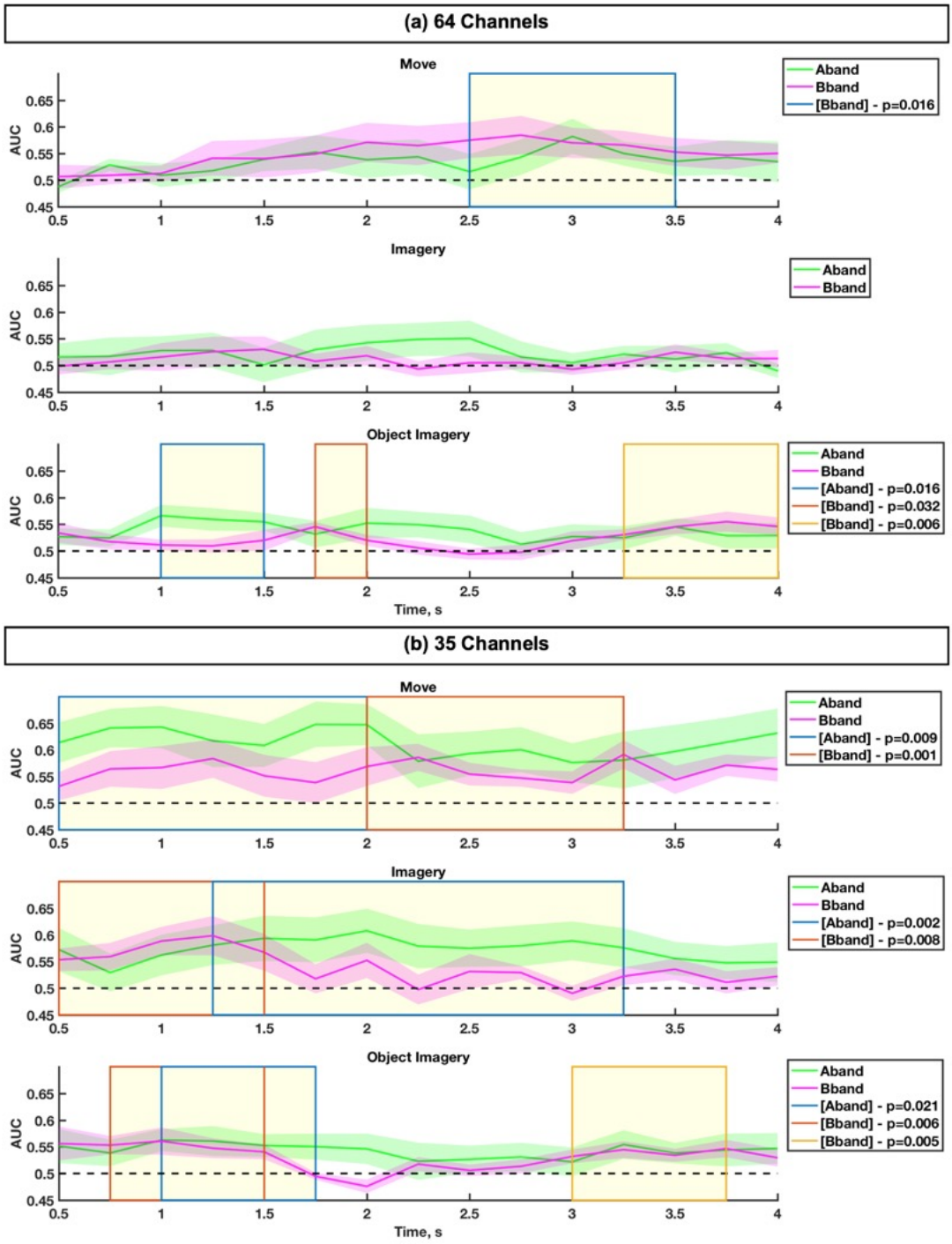

Figure F2.8: Group average classification scores for each sliding time window. SVM classification was performed between cues within each of the three tasks using a four-component feature vector derived from the 64-channel montage (a) and a two-component feature vector derived from the 35-channel montage (b). Here the first score at time 0.5 s represents the average of a time window spanning 0-1000 ms. The light shaded time course represents the standard error in the AUC scores. Clusters of statistically significant time (window) points ($p<0.05$) are highlighted as blocked yellow regions. AUC scores in the action period of the task were only compared to those of chance (an AUC score of 0.5) in the statistical test.

Having additionally classified individual trials at the subject-level, a summary of the percentage of individuals displaying at least one statistically significant cluster for each of the channel montages is displayed in table T2.2. Generally, at least one additional participant was found to display a significant cluster when classifying the 35-channel dataset. The greatest increase in participant number however was for the simple imagery task where only one participant displayed a significant AUC score when classifying the 64-channel data, which increased to five (beta) and six (alpha) participants displaying a significant cluster when classifying the 35-electrode data.

Table T2.2: Percentage of participants displaying at least one statistically significant ($p<0.05$) AUC score (or a cluster of scores at multiple time points) for each task, channel montage and frequency band. Unlike the group analysis in figure F2.8, statistical analysis was performed using the subject-level approach described in section 2.2.4.

Percentage of participants with a significant AUC score				
Task	**64 Channels**		**35 Channels**	
	Alpha (%)	**Beta (%)**	**Alpha (%)**	**Beta (%)**
Move	16.67	25.00	33.33	50.00
Imagery	8.33	8.33	50.00	41.67
Object Imagery	25.00	0.00	33.33	8.33

Peak AUC scores for all participants and both channel montages are displayed in table T2.3. Using two CSP features for classification (as derived from the 35-channel montage) yielded group average peak AUC scores that surpassed the 70% threshold for physical movement and imagery tasks in the alpha frequency band. Furthermore, except for the object imagery task in the beta frequency band, all other average peak scores for this reduced setup were greater than the highest average peak score obtained with the 64-channel montage (0.65 during physical movement). The 50% of participants that yielded at least one significant AUC time point (or cluster) for the simple imagery task (table T2.2 - 35 channels, alpha frequency band) had peak discrimination success rates of at least 70% (table T2.3), with one participant even obtaining an AUC score of 95%. This is an interesting finding given the increasing complexity of a motor imagery task and the absence of any prior training or feedback. Although no direct comparison can be made between the object and classical imagery classification results due to

the different limb areas activated within the brain, average peak scores for the former task were lower than those of the latter task (when comparing alike frequency bands for the 35-channel montage) and may likely be due to the lack of specificity provided in the instruction for comb imagery. Nevertheless, whether the addition of an object enhances an individual's motor imagery performance is unclear from this current study and as such needs to be further explored.

Table T2.3: Peak classification AUC scores for each participant. Results are presented for each channel montage, task and frequency band. The p-values on the bottom row of the table represent the results of a one-tailed Student's t-test ($p<0.05$) between the peak scores of the two channel montages. Overall classification of the two-component feature vector (as derived from the 35-channel montage) yielded higher average peak AUC scores that were significantly different from those obtained from high-density channel classification.

Peak AUC scores						
64 Channels						
Participant	**Move**		**Imagery**		**Object Imagery**	
	Alpha	**Beta**	**Alpha**	**Beta**	**Alpha**	**Beta**
1	0.82*	0.92*	0.65	0.56	0.59	0.55
2	0.64	0.60	0.61	0.60	0.67	0.69
3	0.56	0.55	0.60	0.56	0.62	0.56
4	0.59	0.49	0.59	0.56	0.62	0.59
5	0.80*	0.64	0.87*	0.78*	0.76*	0.68
6	0.57	0.62	0.64	0.63	0.68*	0.57
7	0.57	0.71	0.55	0.58	0.59	0.56
8	0.58	0.57	0.58	0.56	0.67	0.67
9	0.58	0.77*	0.56	0.59	0.59	0.55
10	0.60	0.60	0.58	0.58	0.61	0.55
11	0.64	0.58	0.57	0.53	0.56	0.57
12	0.80	0.72*	0.60	0.60	0.69*	0.68
Average	**0.65**	**0.65**	**0.62**	**0.59**	**0.64**	**0.60**
35 Channels						
Participant	**Move**		**Imagery**		**Object Imagery**	
	Alpha	**Beta**	**Alpha**	**Beta**	**Alpha**	**Beta**
1	1.00*	0.93*	0.78*	0.67*	0.63	0.69*
2	0.68	0.66	0.73	0.64*	0.68*	0.73
3	0.67	0.56	0.70*	0.59	0.73*	0.62
4	0.71	0.68	0.69*	0.57	0.71	0.60
5	0.86*	0.82*	0.95*	0.83*	0.80*	0.68
6	0.90*	0.64*	0.82*	0.64	0.75*	0.62
7	0.63	0.71	0.65	0.62	0.56	0.60
8	0.60	0.57	0.70	0.64	0.69	0.56
9	0.61	0.69*	0.72*	0.80*	0.68	0.67
10	0.64	0.64	0.65	0.62*	0.56	0.63
11	0.71	0.61*	0.54	0.62	0.66	0.52
12	0.81*	0.67*	0.62	0.65	0.66	0.77
Average	**0.73**	**0.68**	**0.71**	**0.66**	**0.68**	**0.64**
p	**0.003**	**>0.05**	**<0.001**	**0.001**	**0.021**	**0.044**

* indicates a significant AUC score ($p<0.05$) established from an empirical null distribution of classification accuracies (AUC scores) derived from random observations (i.e. shuffled class labels).

Statistical analysis of peak AUC scores between the two channel montages (table T2.3) highlighted significant differences ($p<0.05$) for all tasks and frequency bands except for the physical movement scores in the beta frequency band. To conclusively demonstrate that the two-component matrix of the 35-channel montage yielded better classification results than the four-component matrix of the 64-electrode set, table T2.4 was drawn to highlight average peak AUC scores and significance values between two- and four-component matrices derived from the reduced electrode montage. The average peak classification scores for the two-component matrix were either equal to (physical movement, alpha frequency band) or greater than those of the four-component matrix. Furthermore, the peak results of the physical movement (beta frequency band) and simple imagery (alpha frequency band) tasks were found to be significantly different ($p<0.05$) between the two component matrices.

Table T2.4: Group average peak AUC scores for classification performed using a different number of CSP components. Results are presented for the 35-channel montage, each of the three tasks and each of the two frequency bands. As shown in figure F2.7, represented here are the average peak classification results following a decomposition of the 35-channel matrix into the first-most important components (first and last spatial filters) and the first two-most important components. These correspondingly form two- and four-component feature vectors for classification. Once again, the p-values on the bottom row of the table represent the results of a one-tailed Student's t-test ($p<0.05$) between the peak scores (across the group) of the two CSP-classification methods.

Group average peak AUC scores (35 Channels)						
CSP Components	**Move**		**Imagery**		**Object Imagery**	
	Alpha	**Beta**	**Alpha**	**Beta**	**Alpha**	**Beta**
2	0.73	0.68	0.71	0.66	0.68	0.64
4	0.73	0.66	0.68	0.64	0.67	0.63
p	**>0.05**	**0.046**	**0.031**	**>0.05**	**>0.05**	**>0.05**

Overall, these classification results highlight that application of the CSP spatial filtering algorithm on a reduced number of frequency-band filtered channel potentials that are focussed around regions activated during motor imagery (based on previous fMRI research) can better extract features discriminable by a classifier. Furthermore, where a reduced montage is used, the first and last spatial patterns are sufficient for classification as these account for the greatest variability across the two

classes. The discriminable quality of these patterns correlates with the differences in spectral maps of the two classes (such as those in figures F2.5 and F2.6). For example, physical movement and simple imagery tasks that activated regions predominantly over the contralateral hand (C3) and toe (Cz-CPz) brain regions (see figure F2.2 - single subject case) yielded the greatest peak classification scores for these participants.

2.4. Discussion

2.4.1. Time-frequency analysis

This study used EEG to demonstrate frequency band spatial patterns of physical movement and increasing complex motor imagery paradigms including that of simple limb and object-oriented everyday movements. Despite the small differences between the three time-frequency analysis methods explored, alpha and beta frequency rhythms for hand and foot cues were to some extent in line with previous fMRI and EEG research (Ehrsson et al., 2003; Hanakawa et al., 2003; Lee et al., 2019b; Mizuguchi et al., 2013; Nakata et al., 2019; Wriessnegger et al., 2018). Furthermore, spatial maps derived from cup/comb motor imagery suggest an active recruitment of the hand region in the beta frequency band (Zhang et al., 2017b), and an active recruitment of the occipital/parietal brain areas in the alpha frequency band. This latter trend likely reflects a state of cortical activation in which the occipital areas process, feature extract and prepare for an imagined movement in response to the visual presentation of familiar objects (resulting in a desynchronisation of alpha band activity in the occipital areas), subsequently followed by parietal areas activating cognitive processes and mechanisms of attention (resulting in a subsequent synchronisation and desynchronisation of alpha band activity in the occipital and parietal areas respectively) (Perry et al., 2011; Pfurtscheller et al., 1994; Vanni et al., 1997).

The mathematical equivalence of CMW and FIR/IIR-Hilbert transformations (Bruns, 2004) was successfully shown in the similar topographic maps generated in figure F2.3, and is consistent with the literature. Wang and colleagues examined left- and right-hand motor imagery spectral patterns using

a Butterworth-filter Hilbert transform. The authors observed that in seven out of nine participants, peaks in the mu band were present following the stimulus, whereas in only two of those seven were additional beta peaks identified at the termination of imagination (Wang et al., 2004). Such a profile was also observed in a later publication by the same group when using complex Morlet wavelet convolution instead to study ERD/ERS patterns at electrodes C3 and C4 (Qin and He, 2005).

The Butterworth-filtered, Hilbert transformed spatial patterns in the current study portrayed a bilateral activation profile for right-hand gripping that diminished in ERD energy over time in both alpha and beta frequency bands. This is in agreement with the group average diminishing bilateral topography for both left- and right-hand finger movements displayed by Bai and colleagues (Bai et al., 2005). In contrast, simple right-hand imagery spatial patterns were more spatially lateralised with a predominant ERD response around the C3 electrode. Yi and colleagues previously demonstrated EEG scalp topographies of right-hand and foot motor imagery from a single right-handed participant that was given prior imagery training (Yi et al., 2013). The authors depicted a strong contralateral (C3) activation in the alpha frequency band following right-hand imagery, which to some extent is in agreement with the group average topographies presented in the current study. The ERD feature for foot motor imagery presented by Yi and colleagues consisted of a strong desynchronisation that began on the left hemisphere around C3 and continued through the mid-central region to the right hemisphere where it terminated around C4. This somewhat reflects the fMRI profile generated following toe imagery, which highlights significant activation profiles in the mid-central region around Cz (which is the scalp electrode directly above the foot region in the Homuncular organisation (Akselrod et al., 2017)) with localised and less intense activation patterns around C3 and C4 (Ehrsson et al., 2003). The current study's group average spatial patterns for toe imagery were also consistent with the EEG findings of Yi and colleagues, whereby some central activation in the alpha band was observed, but a more prominent C3 to Cz ERD profile was present for the beta envelope.

The choice of a large filter kernel for both alpha and beta frequency bands examined may have limited the potential to localise activity to specific brain regions and thus separate contralateral/ipsilateral/central activity across the two cues within each task. Wang and He previously highlighted that 10 and 11 Hz Butterworth filtered signals yielded Hilbert transform group average

spectral maps with strong contralateral ERDs for right- and left-hand motor imagery respectively (Wang and He, 2004). These optimal single frequencies were isolated by dividing the frequency range of 5-25 Hz into 20 overlapping bins of approximately 2 Hz bandwidth.

In a follow-up study of the same imagery paradigm, whilst examining slightly larger frequency bins (the frequency range of 6-30 Hz was divided into 13 bins where the ratio of the centre frequency over the bandwidth remained the same), the authors presented contralateral sensorimotor attribution of imagined hand movements in their differential-mode patterns (Wang et al., 2004). Here the differential-mode patterns are the difference topographic distributions of two cues. The current study's statistical results, which are akin to these differential-mode patterns, mostly reflected significant differences between hand and toe movements on the ipsilateral hemisphere. Nevertheless, from the difference topographic map for the physical movement task (figure F2.5 - alpha frequency band), weak negative and positive energy differences were observed between the regions spanning the C3 (right-hand) and Cz (toes) electrodes respectively. For the imagery task however (figure F2.6), an inverse difference pattern was observed that was consistent with the difference image found by Wang and colleagues for one out of the nine participants that took part in their research (Wang et al., 2004). Yi and colleagues on the other hand highlighted significant differences at C3 (between right-hand and combined right-hand plus left-foot imagery), and Cz (between feet and combined right-hand plus left-foot imagery) electrodes between different hand and foot imagery conditions (Yi et al., 2013). Whilst the current study likewise observed significant activity in the FC3-C3-CP3-CP5 region for some participants, this difference in results is likely to be based on the way the spectral data were statistically analysed. Unlike the methodology used in the current study, the authors performed temporal statistical tests between specific single channels only and therefore did not spatially account for the activity at connected neighbouring electrodes.

For the complex object-based imagery task, no statistical spatiotemporal differences were observed in the power responses between the two cues. Nevertheless, topographic maps for each response in the beta frequency band generally portrayed ERD patterns aligned over the contralateral hand region, corresponding to the brain region intended to be activated by such commands. This finding is in agreement with the results portrayed by Zhang and colleagues, which investigated topographic and

classification outcomes of complex elbow-centered motor imagery tasks (Zhang et al., 2017b). Across a group of 12 participant the authors depicted that imagery of "drinking a spoonful of soup" and "combing hair" generated strong activations within the 12-26 Hz frequency window at electrodes C3, C4, P3 and P4 (peak activity for these motor imagery tasks were found at C3 and P3 centred around 18 Hz). Furthermore, additional weak activity was observed between 6-14 Hz at electrodes F7 and F8, likely relating to motor planning (Hanakawa et al., 2008). In the current study however, no such ipsilateral activity was observed for the cup-related imagery cue, yet a large ERS pattern was identified over the frontal regions for both object imagery conditions.

In summary, the spectral patterns of simple imagined commands were to some extent in line with the maps of the physical movement task and those of published results. Despite all signals being spatially filtered using the surface Laplacian, simple hand gripping motor imagery had a contralaterally smeared spectral topographic pattern on average across the group. In comparison, the cup-based motor imagery maps were localised in the lower parietal cortex, indicating a greater focussing of the neural activity when performing such a hand-oriented motor imagery task in the presence of an object. Nevertheless, this conclusion does not hold for the comb-based imagery task, which in the beta frequency band had a centrally smeared response across both hemispheres. The difference in the group alpha and beta frequency band responses for the comb imagery cue is either physiological, with the frequency response to this command being highly embedded in the beta envelope and that of the visual cue being embedded within the alpha envelope, or is due to the lack of specificity provided within the instructions for this cue resulting a varied response.

2.4.2. Classification

A second element of this research investigated group and individual classification performances for all three paradigms. A sub-band CSP architecture was used to spatially filter the multi-channel data into a lower dimensional space that maximised class variances. As a result, the findings in figure F2.8 and table T2.3 showed that, CSP pre-processing and classification of data from a subset of electrodes centred around the primary motor cortex, posterior parietal cortex, premotor cortex and supplementary

motor areas yielded group- and subject-level classification accuracies for all three tasks (physical movement, simple imagery and objected-oriented imagery) that were better than the accuracies obtained following CSP pre-processing and classification of data from all 64 recording electrodes (whole head coverage). From table T2.3, improvements in the average peak classification accuracies for the 35 channel over the 64 channel analysis ranged between 3-9% across the three tasks.

Classification of the 64-channel dataset was performed on a reduced four-component feature space resembling the first two-most important CSP filters. In contrast, classification of the centrally focussed subset of electrodes was performed on a two-component feature space derived from only the first-most important CSP filters. Computing the CSP filters on a limited number of scalp electrodes is known to enhance the sensitivity of the covariance matrix estimation to channels preliminary involved with the task. Wang and colleagues demonstrated CSP spatial patterns from two different channel montages in their left- and right-hand motor imagery classification study (Wang et al., 2004). Across a 20-channel montage, the authors highlighted discriminative spatial patterns over sensorimotor areas directly above the C3 and C4 electrodes in the first-most important components. Across a 28-channel montage however, these discriminative patterns strode across the first and second most important components. Their latter results were likewise evident in the current study where foot- and hand-related spatial patterns were located in the first (SP = 1) and second (SP = 3) most important components, respectively, in the single subject case (figure F2.7a).

The findings of the group classification time courses highlighted the two-component feature vector (as derived from the centrally focussed 35 electrodes) to yield greater AUC scores for all three tasks in comparison to any four-component feature vector. This correlated with the better separated spatial pattern maps for the two classes as shown for example in figure F2.7d. Interestingly, when studying the individual peak classification scores for both physical movement and imagery paradigms in the alpha frequency band, 92% of participants had an improvement in their classification score when classifying features derived from the smaller channel set. Prior literature has observed a mean peak accuracy of 70% across 10 participants in the classification of seven motor imagery classes (rest, left-hand, right-hand, feet, both hands, left-hand plus right foot, and right-hand plus left-foot) using a 64-channel montage (Yi et al., 2013). This is much greater than the mean peak accuracy of 60.5% (average

of the mean alpha and beta band results) obtained in the current study for the same montage. Several participants obtained low classification scores (i.e. below 60% for the 64-electrode analysis and below 70% for the 35-channel analysis) for both physical movement and imagery paradigms in table T2.3. This is either due to: (i) a weak neural activation profile in response to the command; (ii) a bilateral activation profile across the central hemisphere, thereby limiting the ability for a classifier to discriminate the two cues; (iii) fatigue; or (iv) an incorrect understanding of the task instructions. Prior work by Qin and He highlighted that a few participants performing a right- and left-hand motor imagery task displayed a strong ERD in the preparation phase that continued through to the execution phase of the study, whereas a single participant exhibited two individual ERDs at the preparation and execution phases of the study (Qin and He, 2005). Although the preparation phase of the current study was not explicitly analysed, it is possible that some participants may have begun executing or imagining the given command in this period or immediately prior to the action period thereby limiting the ability of the designed analysis pipeline to identify unique channel responses to each cue.

With respect to the object-oriented imagery paradigm, the significant cluster of time points near the ends of the group AUC time courses for both channel montages are likely a result of a possible rebound in activity (ERS) after imagination, as previously detected by Qin and He (Qin and He, 2005). The post-imagery beta rebound has also been extensively studied by Pfurtscheller and colleagues who have identified terminations of motor commands to be reflected by a somatotopically specific, short lived brain state associated with the simultaneous inhibition and "resetting" of motor cortex networks (Müller-Putz et al., 2010; Neuper and Pfurtscheller, 2001; Pfurtscheller et al., 2005; Pfurtscheller and Solis-Escalante, 2009; Solis-Escalante et al., 2012). Interestingly, group average peak accuracy results for the object-oriented imagery task were above 60%, and thus higher than the maximum accuracy of 54% achieved by a previous study exploring a similar "drink" and "comb" imagery paradigm (Zhang et al., 2017b). Zhang and colleagues argued that such low inter-task accuracy scores for this and similar elbow-centred complex motor imagery tasks were likely due to a similarity in their topographic distributions, which was centred primarily over the C3 region. Likewise, results from the current study showed strong beta ERDs centred over the C3 region for both 'cup' and 'comb' cues (figure F2.4). Nevertheless, the smeared distribution across both hemispheres for 'comb' imagery is likely to have

aided improvements in classification performance. Furthermore, for alpha frequency band signals, the higher peak accuracy scores achieved at the subject-level, and early statistically significant cluster of time points observed at the group-level, are likely due to the vast differences in power values obtained between 'cup' and 'comb' responses in the sensorimotor region (whereas 'cup'-based imagery had a prominent ERD over the C3 region, 'comb'-based imagery had a strong ERS component).

Group-level AUC scores presented in this study were statistically tested for significance against a chance accuracy of 50% (AUC score of 0.5). Whilst such a threshold is frequently used in the literature for two-class paradigms to indicate total random classification (Cruse et al., 2011, 2012), it is an assumption that is strictly speaking only valid for infinite sample sizes. The chance level for a two-class classification problem is in fact 50% with confidence bounds that are dependent on the statistical alpha value and number of trials used within a study (Combrisson and Jerbi, 2015; Müller-Putz et al., 2008). These confidence intervals can be derived from the binomial cumulative distribution (Matlab function '*binoinv.m'*) (Combrisson and Jerbi, 2015; Müller-Putz et al., 2008). For an alpha significance value of 0.05, the theoretical chance level for each task in the current study (which included a total of 96 trials across two classes) was 58.3%. At this threshold it would appear that the group-level scores would no longer be significantly different from chance (i.e. the classifier does not significantly differ from a random one). The general low classification performance of the group (i.e. several participants had peak scores less than 70%) highlights limitations of a single session of motor imagery in the absence of any feedback. Whilst a single session of motor imagery does promote motor learning (Nicholson et al., 2018), the first session effectively provides participants with a familiarity of the task resulting in varied responses across the group. This session is therefore predominantly used to train a classifier (using cross-validation) to obtain subject-specific weights that can be subsequently applied to the classifier following additional motor imagery sessions providing a true indication of motor imagery classification performance (Guger et al., 2003).

In summary, the CSP filter is an efficient tool for maximising class differences for classification whilst also reducing the dimensionality of multi-channel data in feature space. However, this is most effective when performed on a small number of scalp electrodes centered more closely above brain regions directly involved with the task. This either requires the use of literature to guide which

electrodes to select for CSP processing, or the simultaneous use of instruments with good spatial information such as fMRI or fNIRS. The classification results presented in this study overall highlighted accuracies in the presence of an object being lower than the scores achieved using a classical imagery paradigm. Nevertheless, based on the above discussions, it can be hypothesised that further research using objects that activate different limb regions across the motor and sensorimotor areas (such as the foot and hand by 'kicking a ball in the presence of a ball' and 'drinking soup in the presence of a cup', respectively) will conclusively demonstrate whether the addition of these objects truly benefit motor imagery performance in individuals with no prior training or feedback.

2.4.3. Summary

The results presented in this chapter highlight that object-oriented motor imagery predominantly generated beta frequency band responses to some degree localised contralaterally around the hand region of the motor cortex. Whilst in line with the beta band responses of simple imagery and physical movement of the right-hand, the alpha band responses of the object-oriented imagery task highly varied from alpha band activities generated by other hand-oriented tasks. Furthermore, the lack of significant differences between cup- and comb-generated topographical profiles in the beta frequency band resulted in low classification performances at the group and subject levels. Nevertheless, where cues were spatially separated, such as the right hand and toes cues explored in the physical movement and simple imagery tasks, classification performances improved when a subset of centrally focussed electrodes were spatially filtered using CSP and classified. Although this study could not conclude imagery tasks in the presence of an object to yield better classification results than simple limb motor imagery actions, it is clear that the classification performances of individuals is directly related to the spatial and temporal localisation of responses as observed through spatial patterns. Such localised responses are frequency band specific and harnessing individual optimal frequency windows (within broad alpha and beta frequency bands) is likely to enhance classification performance. This coupled with multiple recording sessions is likely to generate the accuracy scores required to conclude the effectiveness of object imagery tasks and their potential future applicability in the clinic.

Chapter 3

Motor imagery detection using frequency-domain functional near-infrared spectroscopy

3.1. Introduction

Functional near-infrared spectroscopy (fNIRS) provides insights into brain activity through measuring changes in the haemodynamic response. The haemodynamic response is a homeostatic process that replenishes nutrients used by biological tissues by adjusting blood flow to areas of activity. During periods of increased activity, the rate of oxygenated haemoglobin delivery at the neuronal tissues typically exceeds the rate of oxygen utilisation, resulting in a temporary increase in the concentration of oxygenated haemoglobin and a decrease in the concentration of deoxygenated haemoglobin. When NIR light is radiated into the head from the surface of the scalp two main physical phenomena affect the photon trajectory in tissues: scattering and absorption (Jacques and Pogue, 2008). Scattering (as represented by the reduced scattering coefficient) is the dominant effect caused by microscopic refractive index changes inside the tissue resulting in the diffuse nature of light propagation through the media. Absorption (as represented by the absorption coefficient) on the other hand results from a loss of photons due to the presence of particular chromophores inside the tissue. These chromophores absorb photons in order to release, for example, radiative (i.e., fluorescence) or nonradiative (i.e., vibrational) energies. With a multiwavelength NIR light source, the contribution of each chromophore can be separated enabling the quantification of changes in or absolute levels of concentration (Lange and Tachtsidis, 2019).

Absorption and scattering contribute non-linearly to the global attenuation of light by tissues and therefore one must solve an inverse problem in order to determine changes in these parameters independently (Arridge and Schotland, 2009). Light propagation in tissue (commonly known as the

forward model) can be approximately modelled by the diffusion equation derived from the radiative transport equation given certain assumptions (Dehghani et al., 2008; Durduran et al., 2010). Whilst Monte Carlo simulations can be used to solve the radiative transport equation (Boas et al., 2002; Hiraoka et al., 1993), the diffusion equation can be solved analytically (Jacques and Pogue, 2008), by employing the finite element method through software platforms such as NIRFAST (Dehghani et al., 2008) and TOAST++ (Schweiger and Arridge, 2014).

The unique feature of frequency-domain (FD) NIRS systems is that they radiate light modulated at frequencies in the megahertz range (see background information in Chapter 1). As this light propagates deep into brain tissue it is constantly attenuated and scattered resulting in shifts in the phase of the signal. This phase parameter enables one to determine the total depth penetrated by the light (Fantini and Sassaroli, 2020). Measuring both the intensity change and phase shift at two or more source-detector distances enables the diffusion equation to be solved and absorption and scattering coefficients to be computed that relate the recorded data to changes in chromophore concentrations (Fantini, 1995).

Initial research using FD-NIRS for motor activity detection primarily focused on recording fast optical signals time-locked to the stimulus in order to gather event-related brain activity (Gratton and Fabiani, 2009). Unlike the slow haemodynamic response which corresponds to the blood oxygenation level dependent signal of fMRI, fast optical signals represent the rapid (millisecond) changes in tissue optical properties following a cue. In a hand/finger-to-thumb tapping paradigm, Wolf and colleagues recorded intensity and phase amplitudes approximately 1.5-times greater than those at rest for fibres positioned over the motor cortex (C3 region) (Wolf et al., 2002). Subsequently, Morren and colleagues highlighted using a similar paradigm and scalp-fibre montage that advanced signal processing techniques could separate fast signal components from both intensity and phase measurements where the power during the action period of the task was significantly larger than during rest (Morren et al., 2004).

More recent FD-NIRS research has extended the systems' sensitivity and improved signal processing methods in order to better capture brain responses to motor imagery commands and develop fNIRS-related brain computer interfaces (BCIs) (Chiarelli et al., 2018; Khan et al., 2017, 2018; Koo et

al., 2015). When compared to the large number of publications using continuous wave NIRS systems for data collection, the utility of advanced technologies such as FD-NIRS is much more limited and is likely due to their increased costs, albeit significantly lower than fMRI. Furthermore, several research groups that have access to an FD-NIRS system tend to be limited to examining haemodynamic concentration changes derived using only the intensity parameter along with the modified Beer–Lambert law equation (Chiarelli et al., 2018; Khan et al., 2018). This however is likely due to a limited understanding of the additional output parameters by the system and a lack of standardised operational and processing methods available to researchers within the NIRS community.

The previous EEG study within this thesis identified that the presence of an object did not yield improvements in two-class object-oriented motor imagery classification when compared to the results of simple hand/toe motor imagery movements. Recently, Batula and colleagues exhibited fNIRS generated haemodynamic profiles following right-/left- hand and foot motor imagery responses (Batula et al., 2017). The authors highlighted upper limb tasks to generate some bilateral activity, however the spatiotemporal patterns were separated enough in order to distinguish left- from right-hand responses. In contrast, spatial maps for the foot imagery task highlighted strong ipsilateral activity and generally proved difficult to distinguish between the left and right cues. In light of the previous EEG findings presented in chapter 2 and taking into consideration the results presented by Batula and colleagues (Batula et al., 2017), the objective of this study was to better characterise right- and left-hand motor imagery responses by utilising both (amplitude-modulated intensity and phase) outputs of an FD-NIRS imaging system.

Such a paradigm is well established and frequently investigated in the fNIRS-BCI community (Koo et al., 2015; Sitaram et al., 2007; Zhang et al., 2017a). Classification of NIRS measurements has been previously performed directly on pre-processed light intensities (Luu and Chau, 2009; Naito et al., 2007) and on signals corresponding to the concentration changes in oxy- (Δ[HbO]) and deoxy- (Δ[HbR]) haemoglobin (Coyle et al., 2007; Sitaram et al., 2007). While some researchers have argued against classification of the latter signals due to high computational costs (Power et al., 2010), here the aim was to demonstrate accuracy scores from both signals by using analytical methods for converting

pre-processed measurements into chromophore concentration changes that are less computationally expensive.

Through the analysis of FD measured signals (amplitude modulated intensity and phase), and haemodynamic parameters derived from these two components (Δ[HbO] and Δ[HbR]), the aim of this study was to address three key hypotheses:

1. The additional phase shift component, which is less sensitive to signal contamination from the superficial tissues (Doulgerakis et al., 2019b, 2019a), would improve contrast between the two classes of motor imagery when comparing brain haemodynamic changes.
2. Classification of measured FD signals and haemodynamic parameters (derived using both log-intensity and phase-shift components) would deliver higher accuracy scores than when classifying data in the absence of any phase information.
3. Classification of derived haemodynamic parameters would yield greater accuracy scores in comparison to the direct classification of multi-channel FD measurements.

3.2. Methods

3.2.1. Experimental setup and paradigm

An FD-NIRS device (IMAGENT^{TM}, ISS Inc., Illinois) was used to obtain NIRS-based data from 28 healthy adult volunteers (8 males, 19 females and 1 undisclosed, aged between 18-30 years with 25 right-handed and 3 left-handed) of the University of Birmingham community from which written and informed consent was obtained. This FD-NIRS study had ethical permission obtained from the University of Birmingham STEM ethics board. The FD-NIRS system consists of 32 sources, modulated at approximately 140 MHz, and 30 detector fibres. Each source is coupled to laser diodes emitting at 690 nm and 830 nm and each detector is a photomultiplier tube sampling data at 39.74 Hz. The output of such a FD system are complex numbers that can be decomposed into two parts: amplitude-modulated intensity (I_{AC}) and phase (Θ).

Two novel imaging pads were designed consisting each of one source pair bundle and four individual detector fibres (at distances of 15, 25, 35 and 45 mm away from the source). These were positioned on the participants head over the left- and right-motor cortices (left C3 region, right C4 region) (figure F3.1a). The primary function of the 15 mm detector on either hemisphere was to sample physiological activity from the superficial layers of the head, whereas the more distant detectors predominantly sampled brain tissue up to a maximum depth of ~20 mm (Cui et al., 1991; Strangman et al., 2002). Unlike previous research with continuous wave systems where increased light sampling by distant photodetectors has been achieved using a greater source to detector ratio (Strangman et al., 2013), in the current setting each individual detector was set at a different voltage bias in order to increase signal gain.

Participants were comfortably seated facing an adjustable screen while imaging pads were fastened onto their head using loop strapping. Once secure, the study involving left and right physical and imagined hand grip movements (figure F3.1b) was performed in a darkened room in order to maximise photodetector sensitivity to arriving photons that have penetrated the head. The experimental paradigm was designed in Matlab (R2016b, MathWorks, MA, USA) using the Psychophysics Toolbox extensions (Psychtoolbox-3) (Brainard, 1997). During motor execution participants were instructed to repeatedly grip and un-grip their left- or right-hand at a steady pace, whereas during motor imagery, participants were instructed to imagine the feelings of their actions (i.e. muscle contractions and relaxations) that drove the gripping and un-gripping of the corresponding hand. The study was divided into three ~30-minute blocks following which participants were allowed to rest in a re-lit room. Prior to the start of each block the voltage bias of each detector was optimised. Across the three blocks a total of 72 trials were conducted (18 of each of the four different action commands – right-hand gripping, left-hand gripping, right-hand imagined gripping and left-hand imagined gripping). The action tasks were randomised to ensure that no more than two of the same kind were presented in a row.

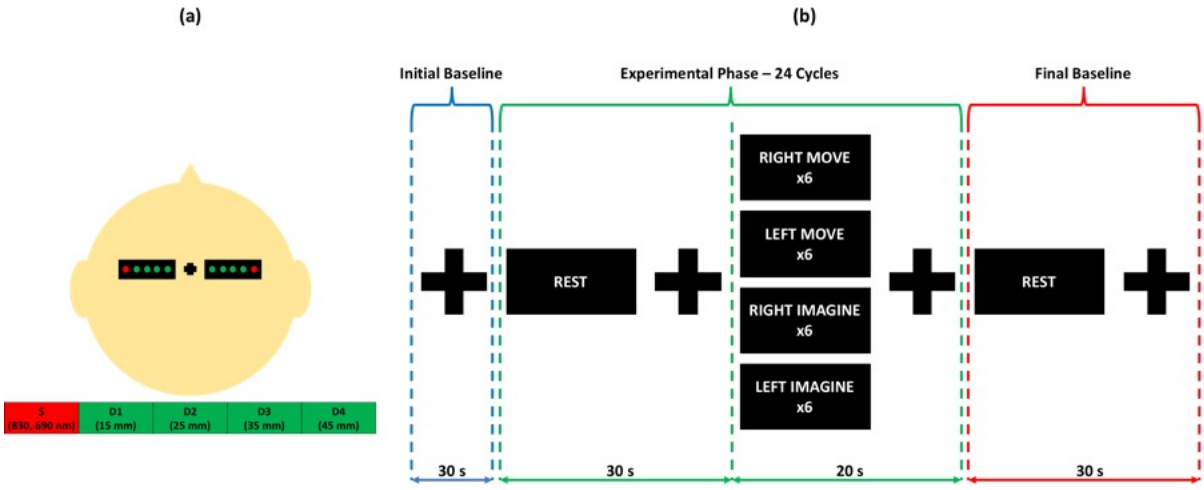

Figure F3.1: (a) Source-detector montage and scalp positioning. For each participant, the intersection between the nasion-inion and left-right preauricular points were marked to reference the Cz location. The 25 mm detector position on each pad was subsequently placed 20% of the distance from Cz to the left- and right-preauricular points, thus at locations C3 and C4 in the International 10-20 system which describes the locations of scalp electrodes (Klem et al., 1999). (b) Experimental paradigm. The study involved a computer presentation of an instruction and fixation cross on a black background. Participants were to continually perform the given instruction while the fixation cross appeared and until the next instruction was presented. (1) An initial fixation cross of ~30 s was presented at the start of the experiment to record baseline activity. (2) Twenty-four cycles of paired rest (~30 s) and action (~20 s) commands followed. The four action instructions corresponded to right-hand gripping ("Right Move"), left hand gripping ("Left Move"), right hand imagined gripping ("Right Imagine") and left hand imagined gripping ("Left Imagine"). (3) A final rest command and fixation cross of ~30 s was presented to once again record baseline activity.

3.2.2. Data pre-processing

Pre-processing of the raw amplitude-modulated intensity and phase data was performed using the software package NeuroDOT (Eggebrecht, 2017) and Matlab. For both the initial and final baseline measurements, the first-most 20 seconds and last-most 20 seconds were respectively averaged and used to form the "true" baseline for each experimental block for each participant. With this baseline (y_0), Rytov's approximation (Kak et al., 2002) was used to compute difference measurements, described as a logarithmic ratio for intensity ($y_{I_{AC}}$) and a difference in phase (y_θ), for the entire time series y

(equation 3.1). In this equation ln represents the natural logarithm, e the exponential, i the imaginary component of the signal and $y_{I0_{AC}}$ and $y_{\theta 0}$ the baseline intensity and phase measurements respectively. This approximation extends the delta optical density parameter defined in continuous wave systems (Huppert et al., 2009) to allow for changes to be measured in phase with respect to a baseline.

$$ln\left(\frac{y}{y_0}\right) = ln\left(\frac{y_{I_{AC}}e^{iy_\Theta}}{y_{I0_{AC}}e^{iy_{\Theta 0}}}\right) = ln\left(\frac{y_I}{y_{I0}}\right) + i(y_\Theta - y_{\Theta 0}) \quad \textbf{[eq. 3.1]}$$

Using this normalised dataset, the fast Fourier transform was computed to detect the presence or absence of physiological peaks (e.g. heart rate, respiration) (Doulgerakis et al., 2019b), both as a data quality measure and to identify filtering cut-off frequencies. Another measure of signal quality was to display the detector fall-off each time the imaging pads were repositioned, or the detector biases adjusted. As the detector distance increases from the source, light levels should fall off in a log-linear fashion, characteristic of photon diffusion through biological tissue. Placing a threshold of ≤7.5% temporal standard deviation for each mean normalised channel (Eggebrecht et al., 2014) identified channels for rejection. This was performed using the function '*FindGoodMeas.m*' within NeuroDOT for each block and participant. This analysis was limited to amplitude-modulated intensity data provided by the 830 nm source due to greater attenuation of the 690 nm signal (i.e. reduced signal-to-noise ratio (SNR)). Nevertheless, to compensate for this, at the start of each experimental block the gain of each photodetector was maximised without saturating the signal at 830 nm. Participant inclusion criteria in this analysis was limited to those where all 15, 25 and 35 mm channels fell below the standard deviation threshold.

Differential measurements for each participant were then detrended to remove linear trends, high- (0.01 Hz) and low- (first at 1 Hz and then again at 0.15 Hz) pass filtered using a fifth-order Butterworth filter, concatenated across blocks and averaged across each trial type, resampled to 1 Hz, baseline corrected, and *z*-transformed to eliminate variability across participants. Of each 30-second rest period in a single trial (rest-action pair), the first 10 s were used to restore a previous trial's motor-

evoked activity to baseline, whereas the latter 20 s were used as the baseline period for normalizing the following action cue's response. Between the two low-pass filters, intensity-based short channel regression was performed using the method outlined by Zeff and colleagues (Zeff et al., 2007). Extraction of first neighbourhood characteristics was performed to eliminate superficial effects present in the data of deeper sampled tissue. The resulting data from the three long-distant channels on each hemisphere were used for classification and statistical analysis.

3.2.3. Reconstruction of haemodynamic changes

To observe underlying changes in the concentration of oxy- (Δ[HbO]) and deoxy- (Δ[HbR]) haemoglobin from measured amplitude-modulated intensity and phase data required modelling and reconstruction of tissue optical properties, specifically changes in the absorption coefficient ($\Delta\mu_a$) at two source wavelengths (690 and 830 nm). This was achieved through forward and inverse models which is described next.

3.2.3.1. Forward model

Light propagation in tissue was modelled using analytical solutions of the FD diffusion equation:

$$-\nabla \cdot D(r)\nabla\Phi(r,\omega) + \left(\mu_a(r) + \frac{i\omega}{v_n(r)}\right)\Phi(r,\omega) = S(r,\omega) \qquad \textbf{[eq. 3.2]}$$

where $D(r)$ is the diffusion coefficient given by $D(r) = v_n/3\mu'_s$, μ_a and μ'_s are the absorption and reduced scattering coefficients respectively, and $v_n = v/n_1$ which describes the velocity of light in tissue (v) for a refractive index value of n_1. Here $n_1$was set to the refractive index of water (1.33) due to the abundance of this molecule within the brain. Analytical solutions of this equation exist for a

number of simple geometries (Arridge et al., 1992; Contini et al., 1997; Li et al., 1996) which describe the photon fluence $\Phi(r,\omega)$ at any arbitrary location r within a tissue for a source $S(r,\omega)$, which is sinusoidally modulated at frequency $\omega = 2\pi f$, where f is in the megahertz range. Assuming an infinite homogeneous medium where the diffusion coefficient is uniform throughout the volume, the first term in equation 3.2 reduces to the Helmholtz equation (Boas et al., 1995) with complex wavenumber, k, given by:

$$k = \sqrt{\frac{-v\mu_a + i\omega}{D}} \qquad \textbf{[eq. 3.3]}$$

The reduced diffusion equation requires boundary conditions to be solved. At the interface between two different media, specifically the air-tissue boundary, flux leaves the external boundary with some internal reflection of light back into the tissue. This mismatched refractive index between media can be derived from Fresnel's law as:

$$A = \frac{2/(1 - R_0) - 1 + |cos\theta_c|^3}{1 - |cos\theta_c|^2} \qquad \textbf{[eq. 3.4]}$$

where $\theta_c = arcsin(1/n_1)$ is the angle at which total internal reflection occurs, and $R_0 = (n_1 - 1)^2/(n_1 + 1)^2$. Extrapolated boundary conditions were employed whereby an isotropic source of photons was located at a depth of $z_0 = -1/\mu'_s$, and the fluence rate was zero at an extrapolated surface with a distance of $z_e = -2AD/v$ from the physical boundary. This extrapolated boundary condition has been previously discussed in the mirror image method (Aronson, 1995). In a semi-infinite homogeneous medium, the complex fluence can then be defined as:

$$\Phi(r,\omega) = \frac{c}{4\pi D}\left[\frac{exp(ikr_1)}{r_1} - \frac{exp(ikr_2)}{r_2}\right] \quad \textbf{[eq. 3.5]}$$

where c is a constant equal to $1/\sqrt{2\pi}$, and $r_1 = [(y - z_0)^2 + x^2)]^{1/2}$ and $r_2 = [(y + z_0 + 2z_e)^2 + x^2)]^{1/2}$ are the euclidean distances from the position of interest in the tissue, at depth $P = (\rho, z)$, where $\rho = (x, y)$ (distance between source and photodetectors on the scalp surface), to the positive ($z = -z_0$) and negative (mirror image, $z = -z_0 - 2z_e$) point impulse sources, respectively. The resulting complex fluence can then be mapped to intensity and phase signals by computing the absolute and arctan functions, respectively.

3.2.3.2. Inverse model

The inverse solution can be solved iteratively yielding values of $\Delta\mu_a$ that in turn can be used to compute $\Delta\Theta$ (changes in phase) and ΔI_{AC} (changes in intensity) equal to that of experimental measurements. Using a permutation approach (Arridge, 1999; Carraresi et al., 2001), the forward model was explicitly computed twice, once without and once with a 1% perturbation of the whole medium, thereby simulating a change in the optical properties (μ_a and μ'_s) of the brain tissue underlying the region spanned by the optodes. The finite difference of the derived phase and log-intensity values (as given by Rytov's approximation in equation 3.1) for all long detector channels gave rise to the Jacobian matrix, $\boldsymbol{J}$ (Pogue et al., 1995). This matrix is also referred to as the sensitivity or weight matrix as it represents changes in boundary fluence measurements with respect to small changes in underlying tissue optical parameters, $\Delta\mu_a$ (Doulgerakis et al., 2019a). Using this normalised matrix and a first-order Taylor expansion, a Newton-Raphson iterative algorithm (Yorkey et al., 1987) was used to calculate $\Delta\mu_a$ as follows:

$$\boldsymbol{J}^i(I_{AC}, \mu_a)(\Delta\mu_a^i) = \Delta I_{AC}^i \quad \textbf{[eq. 3.6]}$$

where i is the iteration number and $\Delta\mu_a^i$ is the updated change in μ_a, with respect to a change in intensity, ΔI_{AC}^i.

Tabulated values for μ_a and μ'_s are present in the literature for different head tissues (Barker et al., 2014). Using approximated initial conditions of $\mu_{a_{830\,nm}} = 0.0256$, $\mu_{a_{690\,nm}} = 0.0285$, $\mu'_{s_{830\,nm}} = 1.070$ and $\mu'_{s_{830\,nm}} = 1.440$ for brain tissue from the publication by Barker and colleagues, a single update was computed for the Jacobian. To calculate $\Delta\mu_a$ (equation 3.7), the inverse of the Jacobian matrix was multiplied to the observed changes in amplitude-modulated intensity at each detector. As the sensitivity matrix is non-square, the inversion of $\boldsymbol{J}$ required multiplication by its transpose, $\boldsymbol{J}'$, where $\boldsymbol{J}' \cdot \boldsymbol{J}$ is known as the Hessian ($Hess$), and the addition of a regularisation parameter $\lambda\boldsymbol{I}$, where $\boldsymbol{I}$ corresponds to the identity matrix.

$$\Delta\mu_a = [\boldsymbol{J}'(I_{AC}, \mu_a)\boldsymbol{J}(I_{AC}, \mu_a) + \lambda\boldsymbol{I}]^{-1}\boldsymbol{J}'(I_{AC}, \mu_a)\Delta I_{AC} \qquad \textbf{[eq. 3.7]}$$

Tikhonov regularisation was applied because as the distance between the source and detector increases, the Jacobian matrix results from low sensitivity changes in the absorption coefficient. This smoothing of the high spatial frequency noise is a minor loss in resolution whilst improving the accuracy of the inversion process. In this instance, the regularisation parameter λ was set at 0.01 following previously reported methods (Doulgerakis et al., 2019a; Eggebrecht et al., 2014). Using equation 3.7, changes in μ_a were computed for both amplitude-modulated intensity and phase measurements (using ΔI_{AC} and $\Delta\Theta$ respectively) at each wavelength. Furthermore, by extension of the Jacobian matrix, a single $\Delta\mu_a$ value for each wavelength was computed by combining the intensity- and phase-change measurements as follows:

$$\Delta\mu_a = [Hess(I_{AC}, \Theta, \mu_a) + \lambda\boldsymbol{I}]^{-1}\begin{bmatrix}\boldsymbol{J}(I_{AC}, \mu_a)\\ \boldsymbol{J}(\Theta, \mu_a)\end{bmatrix}'\begin{bmatrix}\Delta I_{AC}\\ \Delta\Theta\end{bmatrix} \qquad \textbf{[eq. 3.8]}$$

Assuming that vascular haemodynamic concentration changes are due only to changes in absorption (and therefore scattering effects are constant) (Villringer and Chance, 1997), the computed $\Delta\mu_a$ for both source wavelengths were used to derive changes in the concentration of oxy- (Δ[HbO]) and deoxy- (Δ[HbR]) haemoglobin as follows:

$$\begin{bmatrix}\Delta HbO \\ \Delta HbR\end{bmatrix} = \begin{bmatrix}\varepsilon_{HbO_{690\,nm}} & \varepsilon_{HbO_{830\,nm}} \\ \varepsilon_{HbR_{690\,nm}} & \varepsilon_{HbR_{830\,nm}}\end{bmatrix} \begin{bmatrix}\Delta\mu_{a_{690\,nm}} \\ \Delta\mu_{a_{830\,nm}}\end{bmatrix} \quad \textbf{[eq. 3.9]}$$

where ε is the extinction coefficient that provides a measure of how strongly each of the chromophores attenuate light at a given wavelength. These extinction coefficients were obtained from pre-tabulated results (Matcher et al., 1995).

3.2.4. Classification

Group- and subject-level classification was performed between left- and right-hand trials independently for both physical and imagined hand movements. For each trial, the 1 Hz time series was divided into 8-second sliding segments with an 87.5% overlap (Holper and Wolf, 2011). Having applied a six-fold cross-validation procedure, of the 36 *z*-normalised trials present for each participant across the three experimental blocks (i.e. 18 right-hand and 18 left-hand imagery trials), 30 were used for training and 6 for testing within each fold.

Feature extraction, selection and classification were independently performed on both derived haemodynamic and measured FD signals. Furthermore, results acquired from continuous-wave-like (CWL) measurements (log-intensity) were compared with those obtained from FD measurements (log-intensity and phase-shift). Classification of all raw channel measurements would have been suboptimal due to the dimensionality of the feature matrix being much larger than the number of testing trials (Bellman, 1957). As this problem was similar to high-density EEG data classification, the common spatial patterns (CSP) algorithm (see Chapter 2.2.3) was employed to reduce multi-channel

measurements to two most-important uncorrelated spatial filters that maximised the variance between two classes. The benefits of the CSP algorithm on multi-channel NIRS data classification has been previously evaluated by Zhang and colleagues (Zhang et al., 2017a). The authors reported significantly higher accuracy scores when classifying left- and right-hand trials in both a motor execution and imagery task (average accuracy with 180 features – 54%, average accuracy with 18 features derived following CSP – 74%).

Conversion of multi-channel FD measurements to haemodynamic parameters represents Δ[HbO] and Δ[HbR] within the region spanned by the optodes. Independently classifying each chromophore simply limits the feature space to two dimensions (a response within each hemisphere), however may not additionally separate the data into a form that can aid the classification of two classes. As such, classification performance excluding and including CSP-pre-processing was subsequently investigated for Δ[HbO] signals as this chromophore generally yields higher accuracy scores than Δ[HbR] for motor imagery (Fazli et al., 2012).

Statistical features were subsequently extracted from the CSP-transformed windowed time series. Several statistical features have previously been used in the NIRS literature including signal mean (Holper and Wolf, 2011; Hong et al., 2015; Naseer and Hong, 2013), signal peak (Holper and Wolf, 2011), signal slope (Naseer and Hong, 2013), signal variance (Holper and Wolf, 2011), signal kurtosis (Holper and Wolf, 2011), and signal skewness (Holper and Wolf, 2011). Of these measures, signal means have been reported most and therefore this statistical feature was employed for the classification of the current dataset.

Like the previous EEG study (Chapter 2.2.3), a support vector machine (SVM) classifier was used to classify the corresponding left- and right-hand features from each task. The calculated area-under-the-curve (AUC) values for all time windows were used to draw temporal accuracy curves for each participant (subject-level analyses) and the group (when averaging across participants - group-level analyses).

3.2.5. Statistical analysis

Group- and subject-level statistical analyses were performed using the cluster-based permutation test method described in Chapter 2.2.4. These tests were performed on the recorded (FD measured signals) and recovered (derived haemodynamic parameters) signals, and classification (AUC) results. Statistical analysis for the recorded and recovered signals included the identification of time windows within the action period where there were significant differences between left- and right-hand responses. FD signals at each of the three long range detectors are spatially connected due to the sampling of photons from a single light source that has penetrated a small region of brain tissue (Strangman et al., 2013). To account for this spatial connectivity in the test statistic and to gather spatio-temporal clusters, the Matlab function '*bwlabel.m*' was used with a pixel connectivity value of 4 to re-assign edge connected pixels the same test result of 1. Temporal clusters identified following a two-tailed Student's t-test were then tested against a distribution derived from 1000 individual permutation runs for significance at an alpha value of 0.0125 (Bonferroni corrected due to the individual tests performed for each hemisphere). In contrast, when statistically testing haemodynamic responses (single channel information over the left- and right-hemispheres), temporal clusters were identified following a one-tailed Student's t-test with the latter alpha value set to 0.025. This change in tail was performed due to previous findings in the literature demonstrating notable increases in Δ[HbO] and decreases in Δ[HbR] during both physical and imagined movements of the hand (Batula et al., 2017; Blokland et al., 2014; Fazli et al., 2012).

Statistical analyses were additionally performed on the AUC scores obtained following left- and right-hand classification. At the group-level, group average AUC scores were shuffled with a chance AUC score of 0.5, whereas at the subject-level individual class labels were shuffled and a distribution of classification scores were drawn. These statistical tests were applied on the AUC scores obtained following SVM classification of FD-derived and chromophore-derived statistical features. For both group- and subject-level significance tests the alpha value was set to 0.05. Furthermore, correlation analyses were performed between the AUC scores from movement and imagery cues in order to identify an approach (e.g. measured or recovered signals, including CSP or excluding CSP) most consistent for

the physical movement and imagery tasks. A one-tailed (alpha value of 0.05) Spearman's rank correlation analysis was conducted using the Matlab function '*corr.m*'.

3.3. Results

3.3.1. Data quality analysis

Three methods were employed to determine the quality of the data (section 3.2.2). The first method identified the two outputs of an FD-NIRS system (amplitude-modulated intensity and phase) to behave orthogonally at increasing source-detector separations (figure F3.2a). While the average decay in log-intensity was present for separations up to 45 mm, the average increase in phase shift was limited to only a distance of 35 mm. This lack of continuity for the fourth neighbourhood was perhaps likely due to poor phase SNR; detector sensitivity likely approached the noise floor for several participants thereby driving the greater deviation in phase shift from the mean. For the second method the metric previously demonstrated by Eggebrecht and colleagues was employed (Eggebrecht et al., 2014). It was found that, even though the maximum standard deviation change from baseline was 80% across all the measurements (figure F3.2b), a total of 7 participants fulfilled the criteria of having three (shortest channel) measurements on each hemisphere below the 7.5% standard deviation threshold (figure F3.2c).

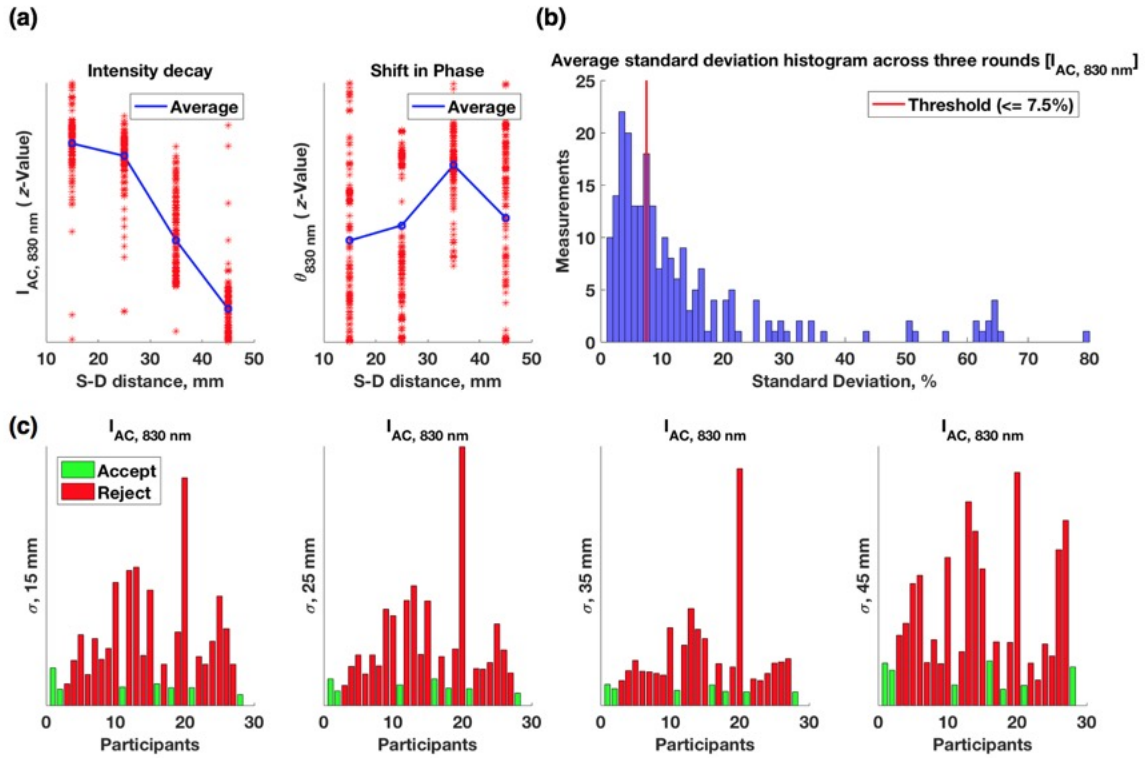

Figure F3.2: Data quality screening based on the methods described in (Eggebrecht et al., 2014). (a) Light level fall-offs and shifts in phase for increasing source-detector separations. For each FD component, participant data from each experimental block were averaged across time and *z*-scored across the four distance measures. (b) Percentage standard deviation change from the 'true' baseline. The average $I_{AC, 830\ nm}$ response across the three blocks was computed for each participant. The histogram was then drawn using the standard deviation percentages for all 8 channels (four channels across two hemispheres) and all 28 participants. Additionally, highlighted is the threshold used to determine measurements with relatively good SNR. (c) Standard deviation changes in the signals of each participant. Seven participants were identified with standard deviation percentages that were below the threshold for the first three source-detector distances.

The third method involved obtaining the Fourier transform of the time series in order to detect the presence or absence of characteristic physiological peaks (figure F3.3). The intensity derived power spectrum for an individual (figure F3.3 left) highlights superficial peaks at ~1.25 Hz, corresponding to a heart rate of 75 beats per minute, and ~0.11 Hz for respiratory effects and slow blood pressure oscillations (Mayer waves). This is present across all four source-detector distances. In addition to these physiological peaks is another peak of high power at 0.02 Hz representing the frequency of the stimulus every 50 seconds. In contrast to the intensity data, phase measurements (figure F3.3 right) appear to be

less sensitive to the aforementioned superficial noises and uniquely sample the stimulus of interest. Like the intensity data however, the frequency response of the stimulus peak is of a much lower energy in the shortest channel, however increases in power and rises above the noise at more distant source-detector separations.

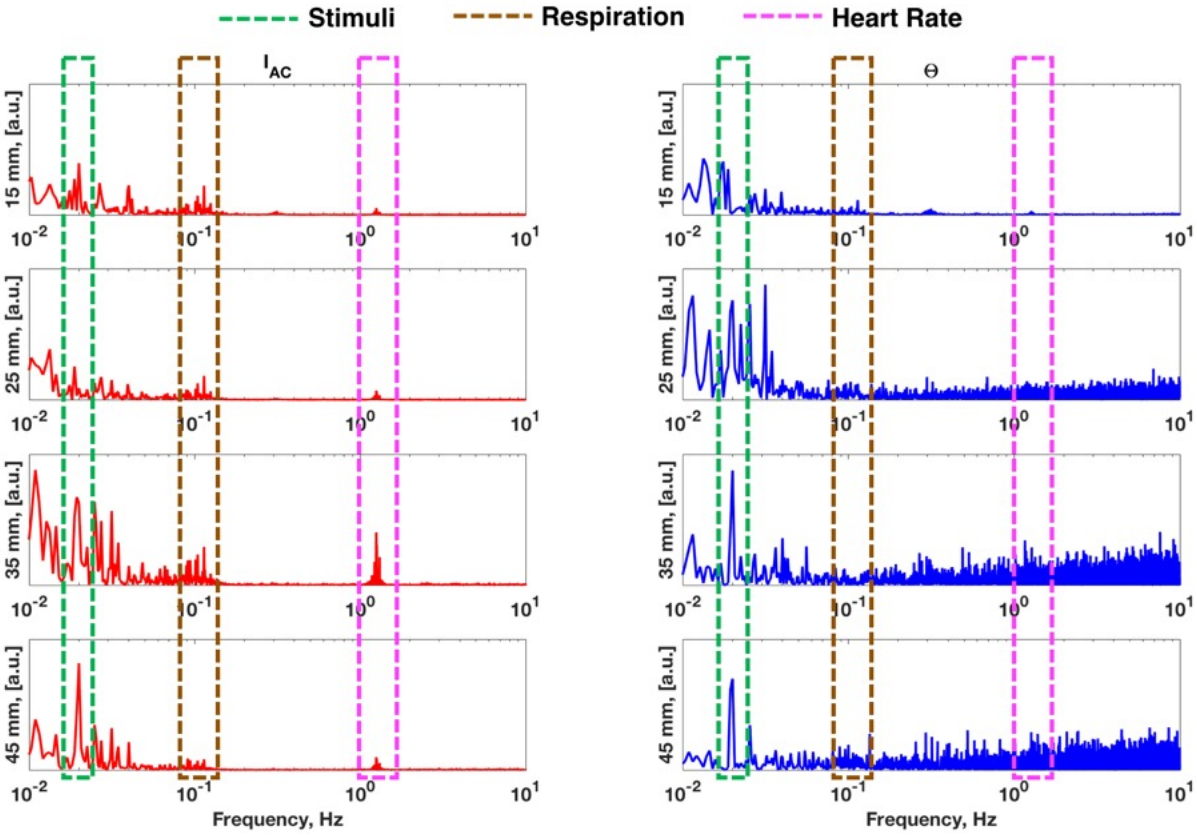

Figure F3.3: Intensity (left)- and phase (right)-derived Fourier spectrums for a single participant using the data from a single experimental block at all source-detector channels over the left hemisphere. For each parameter, the data were normalised across all four source-detector channels followed by the y-axis of each plot being scaled to the maximum power value of all channels. Highlighted are the frequency regions at which the stimulus peak and characteristic physiological peaks should be present.

3.3.2. Analysis of frequency-domain time series

Pre-processed time series for each of the four tasks are displayed in figure F3.4. For the majority of source-detector separations, the plots on the left (figure F3.4a) and right (figure F3.4b) hemispheres

highlight contralateral responses to be greater than ipsilateral responses during both physical and imagined tasks. In comparison to physical hand movement actions, responses to imagined hand movements were of a lower magnitude which was expected given the increased complexity of the task in the absence of any prior training or feedback. Interestingly, contralateral imagery responses for certain channels, for example the $\Delta I_{AC,\,830\,nm}$ 45 mm channel and the $\Delta\Theta_{830\,nm}$ 35 mm channel, peaked above the response created by the opposite hand when performing a physical movement. This demonstrates that on average imagery was performed well enough to generate localised contralateral activity patterns above that of any cross-talk. Generally, phase-shift measurements were weaker than log-intensity measurements, for example when comparing $\Delta I_{AC,\,830\,nm}$ and $\Delta\Theta_{830\,nm}$ 45 mm channel time series, thus reflecting the sensitivity of the parameter to noise at long range source-detector separations.

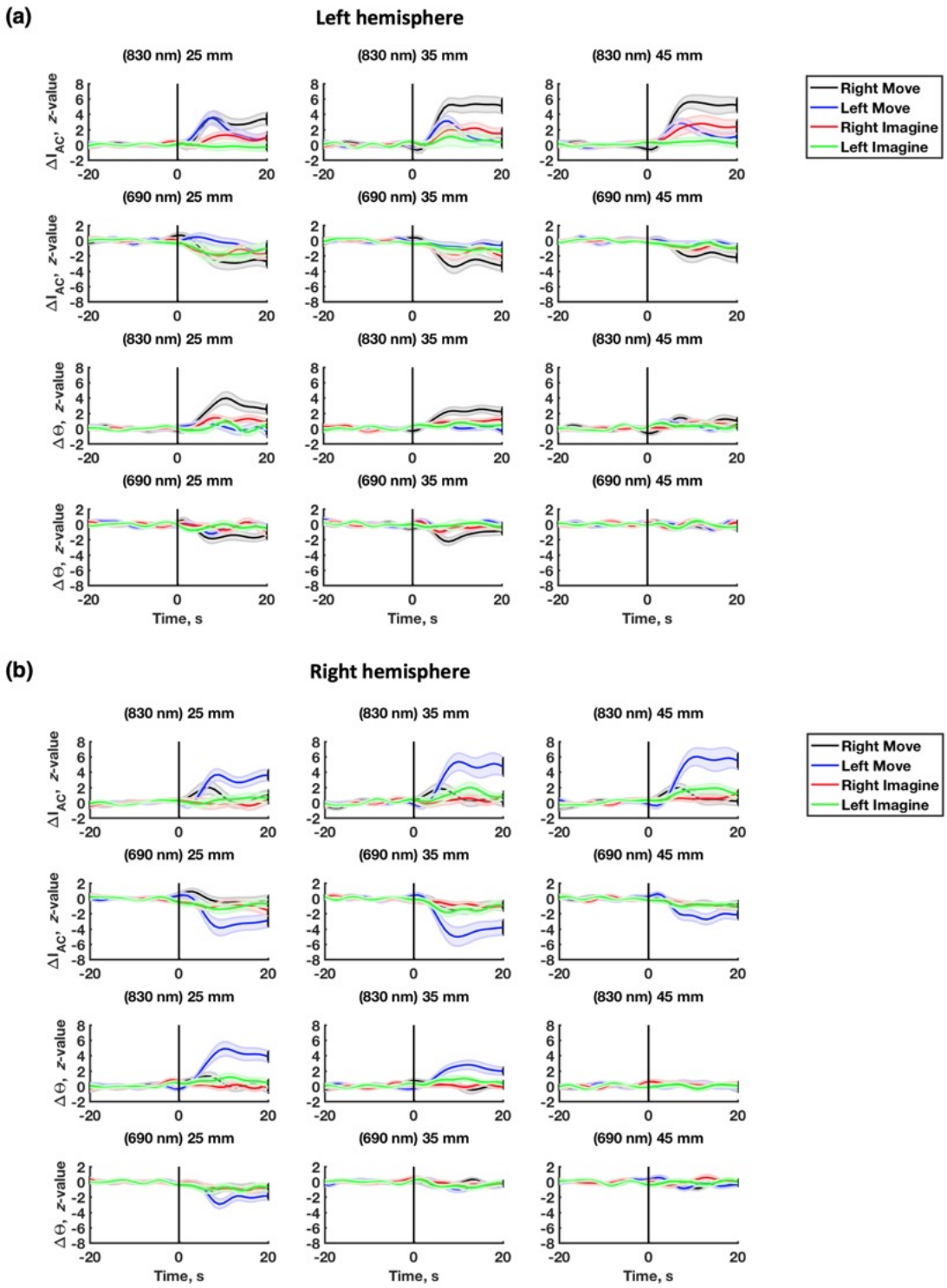

Figure F3.4: Blocked averaged and baseline corrected FD measured responses for each of the four task conditions. Log-intensity and phase shift profiles are shown for both left- (a) and right- (b) hemisphere channels. The data from the 15 mm channel was used to regress superficial noise from the three long-range channels and hence is not depicted.

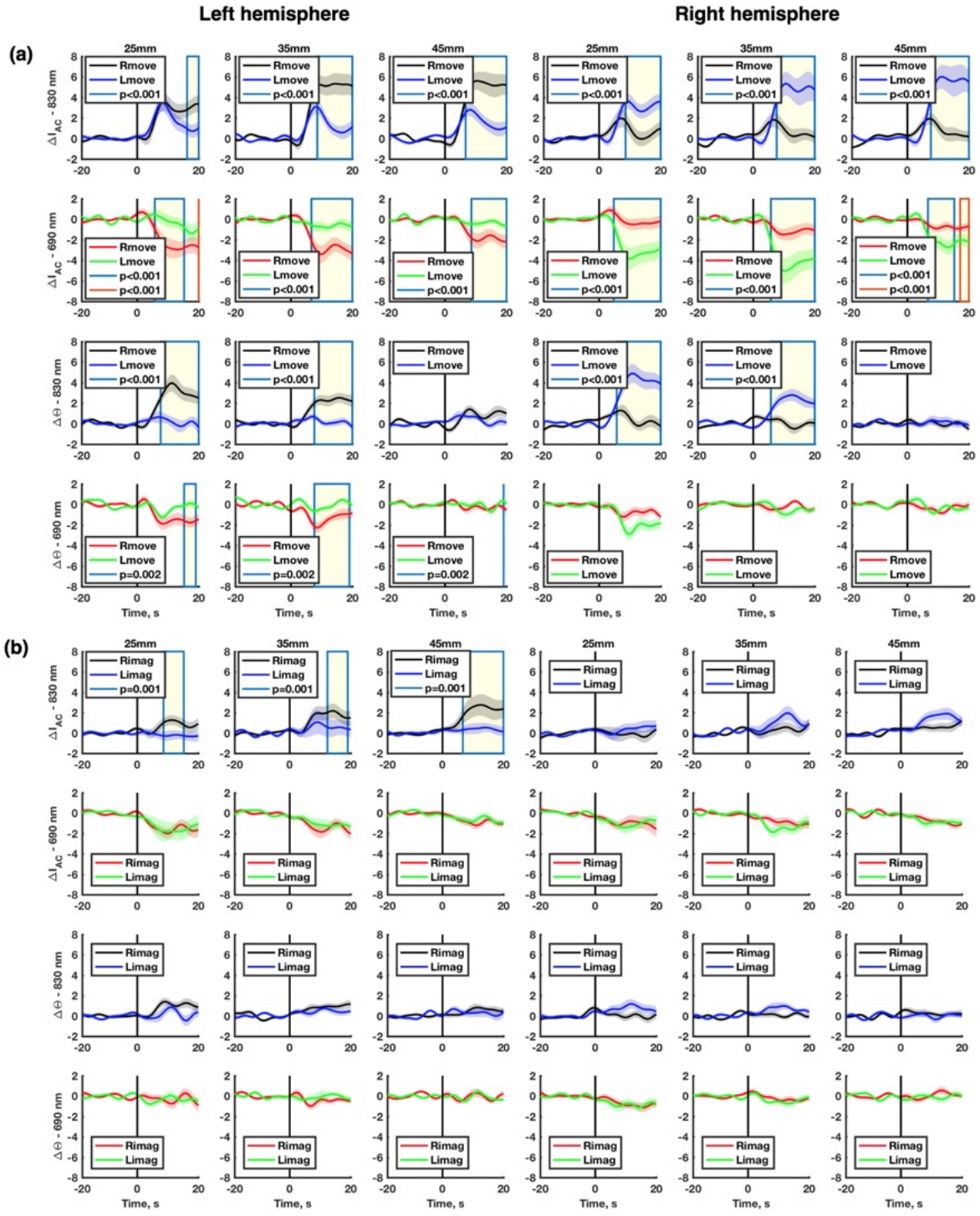

Figure F3.5: Statistical comparisons between the left- and right-hand responses shown in figure F3.4. Using an alpha value of 0.0125, significance was determined between left (L)- and right (R)-hand physical (move) (a) and imagined (imag) (b) movements independently.

Considering both left- and right-hemisphere activity and excluding the 45 mm channel data, statistical group comparisons between the two physical hand movement signals (figure F3.5a) highlight

right-hand responses as being significantly different ($p<0.001$) from left-hand responses after presentation of the instruction. Interestingly, significant differences were found ~5 seconds after the action cue was presented demonstrating the potential delay in contralateral haemodynamic activity. For the physical movement task, significant clusters were identified for all log-intensity measurements however for phase-shift measurements this was primarily found on the left-hemisphere. These greater effects observed on the left-hemisphere are consistent with the cohort being predominantly right handed. In contrast, significantly different ($p<0.001$) imagined hand responses (figure F3.5b) were found on the left-hemisphere for all $\Delta I_{AC,\ 830\ nm}$ channel measurements only. Interestingly, although a large overlap was present between the 35 mm channel responses, a significant cluster was identified due to its spatially connected neighbours having significantly different left- and right-hand activity.

FD-derived haemodynamic concentration changes are presented in figure F3.6. For both CWL (figure F3.6a) and FD (figure F3.6b) converted data, contralateral effects in Δ[HbO] and Δ[HbR] are present for both physical and imagined hand movements. The current tasks yielded an increase in Δ[HbO] and a decrease in Δ[HbR], with the latter being of a slightly lower magnitude. Interestingly, in the first 3 seconds post-stimulus, a characteristic undershoot (overshoot) is present for Δ[HbO] (Δ[HbR]), which increases in contrast for FD converted measurements. This profile is most prominent for left movement Δ[HbR] responses on the right hemisphere. The addition of the phase component also appears to reduce, to a small extent, the magnitude of the response otherwise generated by CWL measurements yet minimises the standard error about the mean (c.f. CWL (figure F3.6a) and FD (figure F3.6b) converted responses for the physical movement task) thereby further improving contrast between the recorded left- and right-hand signals. Statistical analysis of these signals identified all contralateral haemodynamic activity as significantly different ($p\leq0.01$) from ipsilateral activity during physical movement tasks (figures F3.7a and 3.7b). For the imagery task however, contralateral Δ[HbO] responses on the left hemisphere were only found to be significantly different ($p\leq0.01$) between the left- and right-hand responses (figures F3.7c and F3.7d).

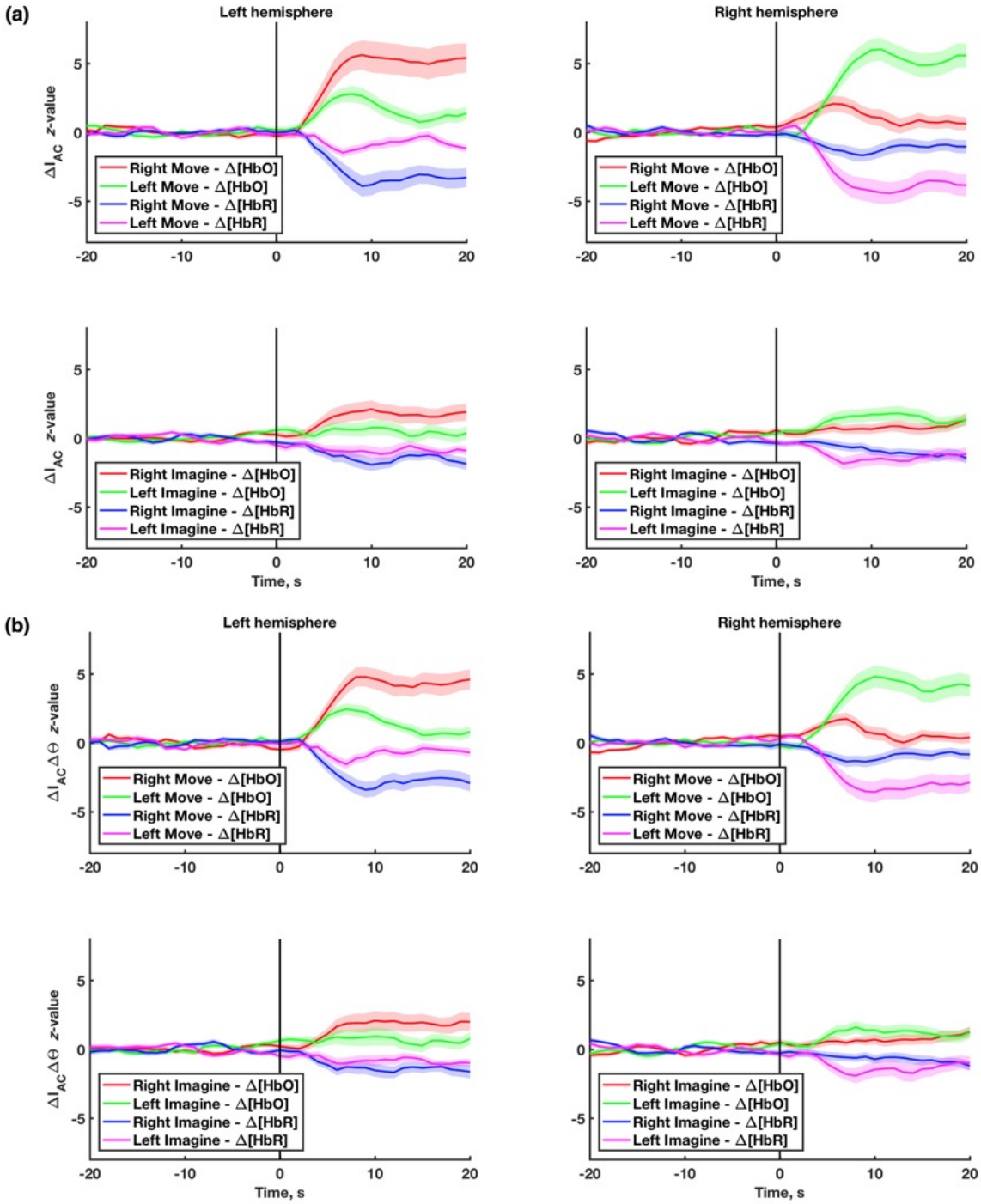

Figure F3.6: Block averaged and baseline corrected Δ[HbO] and Δ[HbR] derived responses for each of the four task conditions. Δ[HbO] and Δ[HbR] profiles explain brain haemodynamics in the region directly under the three long-distant channels. The transformation from CWL/FD measurements to haemodynamic parameters was achieved by using a Jacobian matrix composed of CWL (a) or FD (b) computed signals.

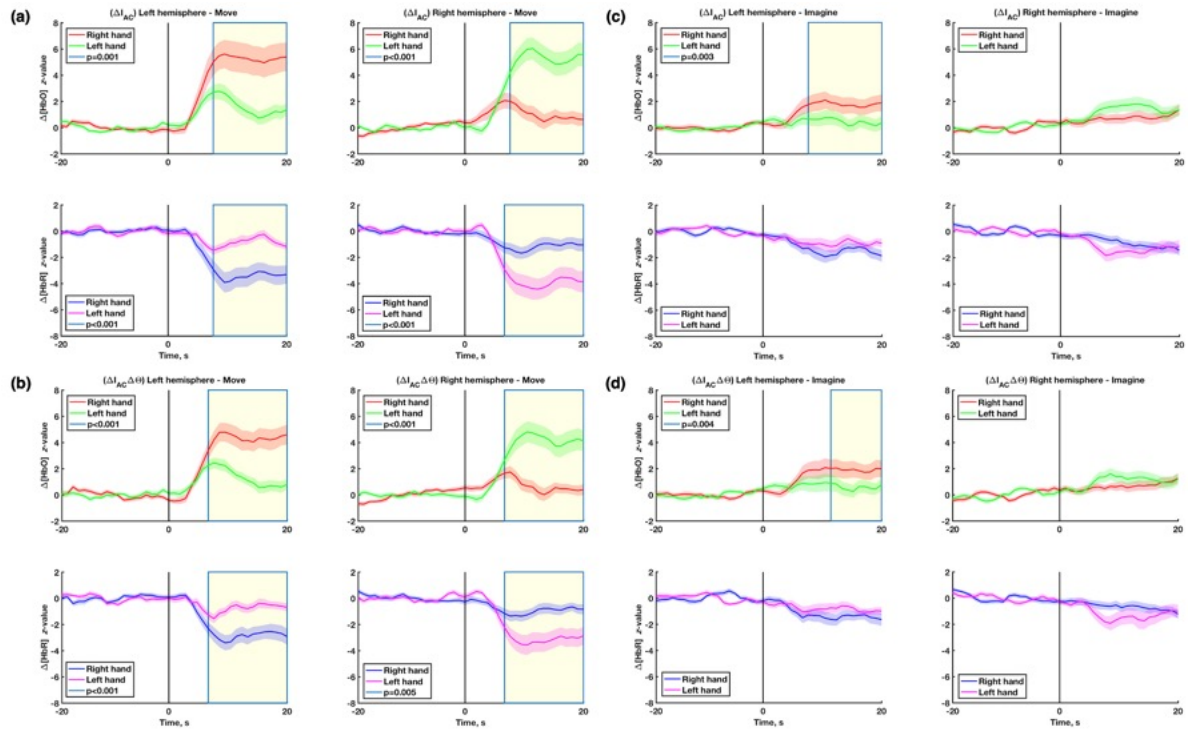

Figure F3.7: Statistical comparisons between the left- and right-hand responses shown in figure F3.6. Using an alpha value of 0.025, significance was determined between left- and right-hand physical (a, b) and imagined (c, d) movements independently.

Results from the subject-level statistical analysis are presented in table T3.1. Approximately seven times as many participants displayed at least one significant contralateral spatio-temporal cluster for physical movement responses than imagined responses at 830 nm. In contrast, approximately four times as many participants displayed at least one significant contralateral temporal cluster for CWL-derived Δ[HbO] physical movement signals. This ratio was however halved when considering phase shift- and FD-derived Δ[HbO]. Interestingly, for the imagery condition no participants were identified with a significant cluster for both 690 nm and Δ[HbR] signals. Although conversion to haemodynamic activity reduced the percentage of participants displaying a significant cluster for physical hand responses, the addition of the phase component enabled identification of more participants with a significant cluster for Δ[HbO] imagery signals.

Table T3.1: Percentage of participants displaying at least one statistically significant temporal ($p<0.025$ for chromophore signals) or spatio-temporal ($p<0.0125$ for FD signals) cluster of points for each of the two command types. Significant differences were determined between the left- and right-hand responses for both physical and imagined movements independently.

Percentage of participants with a significant cluster						
FD Output	**Move (%)**	**Imagine (%)**		**Chromophore**	**Move (%)**	**Imagine (%)**
830 nm (ΔI_{AC})	50.00	7.14		Δ[HbO] (ΔI_{AC})	39.29	10.71
830 nm ($\Delta\Theta$)	50.00	7.14		Δ[HbO] ($\Delta\Theta$)	14.29	7.14
-	-	-		Δ[HbO] ($\Delta I_{AC}\Delta\Theta$)	32.14	14.29
690 nm (ΔI_{AC})	17.86	0		Δ[HbR] (ΔI_{AC})	17.86	0.00
690 nm ($\Delta\Theta$)	17.86	0		Δ[HbR] ($\Delta\Theta$)	3.57	0.00
-	-	-		Δ[HbR] ($\Delta I_{AC}\Delta\Theta$)	17.86	0.00

3.3.3. Total group classification

In order to extend this two-class problem as a BCI application, statistical features were classified using an SVM to yield accuracy scores summarised by the AUC. Group-level classification results following CSP-pre-processing of FD and derived-haemodynamic measurements are presented in figure F3.8. The results from the physical movement tasks (figures F3.8a and F3.8b upper left and right) highlight that ~4 seconds after the action cue, classification scores begin to rise above chance to a maximum, plateauing ~10-12 seconds after the action is begun. The peak classification scores achieved were 0.70 for $FD_{830\ nm}$, 0.62 for $FD_{690\ nm}$, 0.68 for $FD_{\Delta[HbO]}$, and 0.64 for $FD_{\Delta[HbR]}$, ($p<0.05$). These FD-derived scores were greater than (0.66 for $CWL_{830\ nm}$, 0.61 for $CWL_{690\ nm}$ and 0.66 for $CWL_{\Delta[HbO]}$) or equal to (0.64 for $CWL_{\Delta[HbR]}$) the scores obtained from CWL measurements. This improvement in the positive prediction rate for FD measurements highlights the potential of additional phase signals in computing more separable classification features. In contrast however, classification results of the imagined hand responses (figures F3.8a and F3.8b lower left and right) remained close to chance reflecting an increased similarity between the left- and right-hand statistical features derived from these signals.

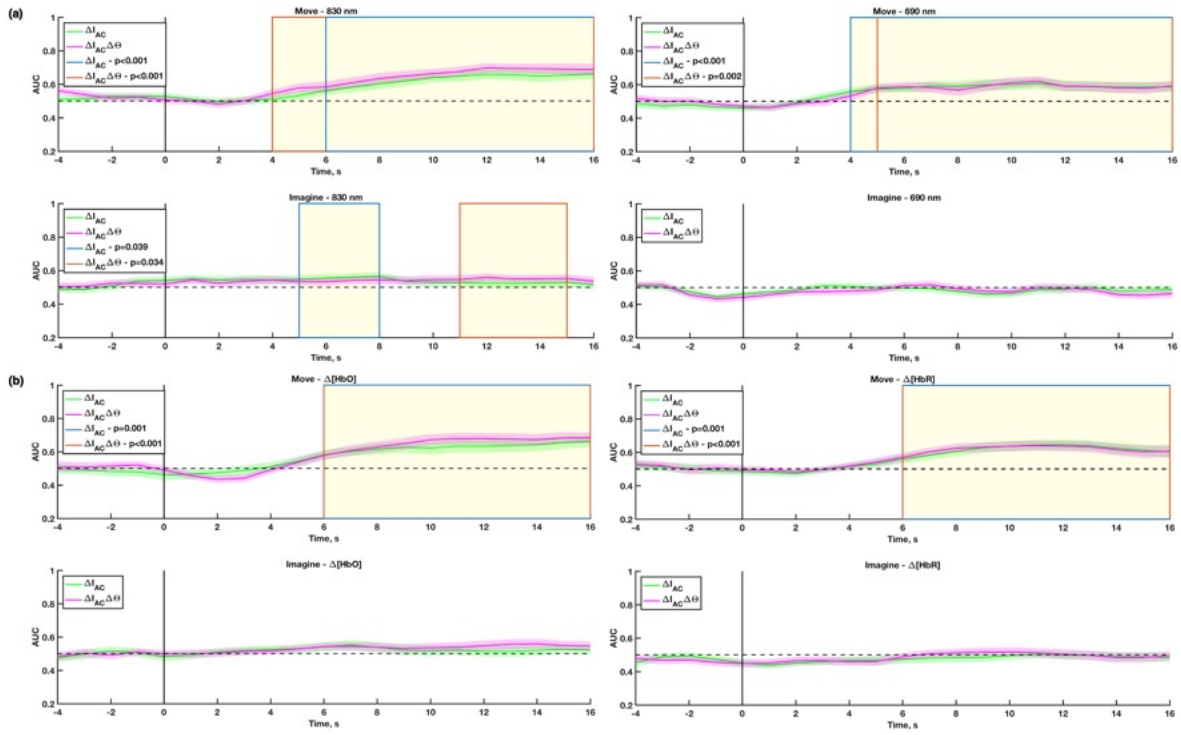

Figure F3.8: Group average classification scores for each sliding time window. SVM classification was performed between left- and right-hand responses for both physical movement and imagery tasks independently. Specifically, differences were studied in the classification results of CSP-pre-processed FD signals (830 nm and 690 nm) (a) and CSP-pre-processed haemodynamic signals (Δ[HbO] and Δ[HbR]) (b). For the former, either a two (features from CWL data) or four (features from FD data) column feature matrix was used for classification, whereas for the latter only a two-column feature matrix was classified which incorporated information from either CWL or FD signals. The first score at time -4 s represents the average of a time window spanning -8-0 seconds. The light shaded time course represents the standard error in the AUC scores. Clusters of statistically significant time (window) points ($p<0.05$) are highlighted as blocked yellow regions. AUC scores in the action period of the task (i.e. from a mean time of 4 seconds in the above plots) were only compared to those of chance (an AUC score of 0.5) in the statistical test.

Subject-level statistical analysis of calculated AUC scores were additionally performed in order to determine the suitability of this study's methodology for future extension within the clinic. Table 3.2 indicates that classification of 830 nm signals yielded the highest percentage of individuals with at least one significant AUC score. In comparison to the percentage of individuals obtained from Δ[HbO] signal classification, 830 nm results were greater for both physical movement and imagery tasks. The contrary

was however true for Δ[HbR] and 690 nm signal classification (except for physical movement scores obtained from FD-derived Δ[HbR] responses which found one participant fewer with a significant cluster). As both 830 nm and Δ[HbO] signals were better for subject-level classification and statistical analysis, subsequently compared were the peak AUC scores obtained by each participant for both tasks (table T3.3). The average peak AUC scores highlight that Δ[HbO] and 830 nm signals from FD measurements were marginally better classified than Δ[HbO] and 830 nm signals from CWL data. Furthermore, they reiterate that optical signals in comparison to haemodynamic measurements were in general better for classification of the current dataset. This is likely due to the classifier having access to both log-intensity and phase-shift measurements as independent features, whereas when classifying chromophore responses, the classifier is limited to a single feature only. However, from the correlation analyses in table T3.3 it appears that moderate (i.e. 0.5 – 0.7 (Mukaka, 2012)) monotonic positive correlations were only present for 830 nm signals from CWL data, whereas the remaining approaches gave rise to low (i.e. 0.3 – 0.5 (Mukaka, 2012)) monotonic positive correlations between move and imagine tasks. Furthermore, improved positive monotonic correlation effects are present between AUC scores from both Δ[HbO] and 830 nm signals from CWL data in comparison to Δ[HbO] and 830 nm signals from FD data, suggesting a negative impact on classification performance when introducing potential noisy phase measurements (whether that be as an additional feature or when reconstructing haemodynamic responses).

Table T3.2: Percentage of participants displaying at least one statistically significant ($p<0.05$) AUC score (or a cluster of scores at multiple time points) for each task and measured (FD)/derived (chromophore) signal. Unlike the group analysis in figure F3.8, statistical analysis was performed using the subject-level approach described in section 3.2.5.

Percentage of participants with a significant AUC score					
FD Output	**Move (%)**	**Imagine (%)**	**Chromophore**	**Move (%)**	**Imagine (%)**
830 nm (ΔI_{AC})	53.57	21.43	Δ[HbO] (ΔI_{AC})	42.86	17.86
830 nm ($\Delta I_{AC}\Delta\Theta$)	60.71	25.00	Δ[HbO] ($\Delta I_{AC}\Delta\Theta$)	46.43	17.86
690 nm (ΔI_{AC})	42.86	7.14	Δ[HbR] (ΔI_{AC})	46.43	10.71
690 nm ($\Delta I_{AC}\Delta\Theta$)	39.29	7.14	Δ[HbR] ($\Delta I_{AC}\Delta\Theta$)	35.71	14.29

Table T3.3: Peak classification AUC scores for each participant. Individual and average results are presented for physical movement and imagery tasks having classified left- and right-hand features derived from either 830 nm or Δ[HbO] signals. Additionally, presented are pairwise correlation coefficients (r_s) obtained between movement and imagery tasks for each classification approach and the corresponding p-values (p).

Peak AUC scores								
Participant	**830 nm (ΔI_{AC})**		**830 nm ($\Delta I_{AC}\Delta\Theta$)**		**Δ[HbO] (ΔI_{AC})**		**Δ[HbO] ($\Delta I_{AC}\Delta\Theta$)**	
	Move	**Imagine**	**Move**	**Imagine**	**Move**	**Imagine**	**Move**	**Imagine**
1	0.74*	0.65	0.71*	0.74	0.78*	0.40	0.75*	0.63
2	0.67	0.63	0.61	0.59	0.67	0.73	0.81*	0.74*
3	0.94*	0.80*	0.95*	0.77*	0.88*	0.77*	0.93	0.73*
4	0.67	0.58	0.69	0.62	0.76*	0.74*	0.55	0.73
5	0.66	0.62	0.70*	0.47	0.67	0.51	0.73	0.49
6	0.79*	0.65	0.74	0.55	0.62	0.41	0.51	0.45
7	0.61	0.48	0.59	0.40	0.72*	0.61	0.75*	0.52
8	0.76*	0.49	0.73*	0.61	0.59	0.59	0.53	0.53
9	0.81*	0.77*	0.84*	0.79*	0.70*	0.71	0.72	0.63
10	0.87*	0.65	0.85*	0.58	0.93*	0.63	0.81*	0.65
11	0.52	0.59	0.53	0.68	0.58	0.63	0.58	0.63
12	0.73	0.61	0.71	0.61	0.74	0.70	0.56	0.69
13	0.65	0.58	0.67	0.64	0.74	0.57	0.71	0.60
14	0.68	0.69	0.73	0.62	0.52	0.61	0.58	0.58
15	0.58	0.54	0.65	0.70	0.45	0.61	0.60	0.69
16	0.81*	0.70	0.87*	0.65	0.89	0.76*	0.83*	0.79*
17	0.80*	0.52	0.83*	0.44	0.95*	0.53	0.94*	0.57
18	0.75*	0.79*	0.86*	0.83*	0.75	0.60	0.89*	0.72
19	0.65	0.72	0.77*	0.79*	0.51	0.59	0.71*	0.63
20	0.45	0.55	0.59	0.63	0.48	0.46	0.65	0.62
21	1.00*	0.77*	1.00*	0.77*	1.00*	0.64	1.00*	0.73
22	0.81*	0.74	0.87*	0.78	0.75*	0.65	0.83*	0.61
23	0.84*	0.66	0.84*	0.72	0.61	0.30	0.77*	0.35
24	0.87*	0.67	0.94*	0.67	0.90*	0.73	0.92*	0.68
25	0.62	0.61	0.65	0.64	0.67	0.55	0.69	0.62
26	0.66	0.59	0.77*	0.67	0.65	0.71	0.69	0.65
27	0.81*	0.80*	0.80*	0.81*	0.79*	0.82*	0.78*	0.84*
28	0.95*	0.79*	0.93*	0.77*	0.89*	0.88*	0.87	0.81*
Average	**0.74**	**0.65**	**0.77**	**0.66**	**0.72**	**0.62**	**0.74**	**0.64**
r_s	0.67		0.49		0.45		0.37	
p	**<0.001**		**0.004**		**0.008**		**0.025**	

* indicates a significant AUC score ($p<0.05$) established from an empirical null distribution of classification accuracies (AUC scores) derived from random observations (i.e. shuffled class labels).

So far, it has been assumed that the use of CSP has aided classification of haemodynamic parameters, whereby like EEG, multivariate data are separated into spatial subcomponents that have maximum differences in their variances. In order to determine whether CSP-pre-processing was beneficial or detrimental to the classification of Δ[HbO] signals, classification of Δ[HbO] data was repeated in the absence of any CSP-pre-processing. The results in table T3.4 present there to be no significant differences ($p>0.05$) between the percentage of participants displaying a significant score having excluded or included CSP-pre-processing. Furthermore, the average peak AUC scores in table T3.5 are identical for both CSP excluded and included classification. The exactness of these values additionally mirrored the group level classification curves (see appendix figure AF3.1). Nevertheless, in table T3.4 there appears to be a minor loss in motor imagery classification performance when applying the additional filtering. Specifically, when excluding CSP, six participants were found to have at least one significant AUC score, however this decreased to five participants when including CSP. Examining the peak AUC scores for this individual (participant 18 in table T3.5) revealed them to be identical (both excluding and including CSP scores are 0.72). It is possible that additional randomisations during the statistical test may either find this value significant or the value generated by excluding CSP non-significant. This pattern is also present for peak scores obtained following classification of physical hand movements (participants 1 and 28), highlighting limitations of the statistical method to arbitrary thresholds. This similarity between CSP-present and -absent approaches for both physical movement and imagery AUC scores is likewise reflected by the closeness of the correlation coefficients in table T3.4 which both represent low (i.e. 0.3 – 0.5 (Mukaka, 2012)) monotonic positive trends. Nevertheless, it is clear from this correlation analysis and peak AUC scores that the addition of CSP-pre-processing to such a dataset does not negatively impact its classification performance for both movement and imagery tasks.

Table T3.4: Percentage of participants displaying at least one statistically significant ($p<0.05$) AUC score (or a cluster of scores at multiple time points) for each task having excluded or included CSP-pre-processing as part of the feature extraction process. Results are obtained from Δ[HbO] classification features derived using FD measurements. In order to determine whether a significant difference was present between the excluding/including CSP percentages for each task, a McNemar statistical test (Cardillo, 2007) was performed using an alpha value of 0.05. Additionally, presented are pairwise correlation coefficients (r_s) obtained between the AUC scores from movement and imagery tasks for each classification approach and the corresponding p-values (p).

Percentage of participants with a significant AUC score				**Correlation of AUC scores**	
Method	**Move (%)**	**Imagine (%)**		r_s	p
Excluding CSP	46.43	21.43		0.35	**0.035**
Including CSP	46.43	17.86		0.37	**0.025**
p	**>0.050**	**>0.050**			

Table T3.5: Peak classification AUC scores for each participant having excluded or included CSP-pre-processing as part of the feature extraction process. Individual and average results are presented for physical movement and imagery tasks having classified left- and right-hand statistical features from Δ[HbO] signals derived using FD measurements.

Peak AUC scores				
Participant	**Move**		**Imagine**	
	Excluding CSP	**Including CSP**	**Excluding CSP**	**Including CSP**
1	0.75	0.75*	0.64	0.63
2	0.81*	0.81*	0.74*	0.74*
3	0.93	0.93	0.73*	0.73*
4	0.56	0.55	0.73	0.73
5	0.73	0.73	0.49	0.49
6	0.49	0.51	0.45	0.45
7	0.75*	0.75*	0.52	0.52
8	0.53	0.53	0.54	0.53
9	0.72	0.72	0.62	0.63
10	0.80*	0.81*	0.65	0.65
11	0.59	0.58	0.63	0.63
12	0.55	0.56	0.69	0.69
13	0.71	0.71	0.60	0.60
14	0.58	0.58	0.57	0.58
15	0.59	0.60	0.69	0.69
16	0.83*	0.83*	0.78*	0.79*
17	0.94*	0.94*	0.57	0.57
18	0.89*	0.89*	0.72*	0.72
19	0.72*	0.71*	0.63	0.63
20	0.65	0.65	0.62	0.62
21	1.00*	1.00*	0.73	0.73
22	0.83*	0.83*	0.57	0.61
23	0.77*	0.77*	0.36	0.35
24	0.92*	0.92*	0.68	0.68
25	0.69	0.69	0.62	0.62
26	0.69	0.69	0.65	0.65
27	0.78*	0.78*	0.84*	0.84*
28	0.86*	0.87	0.81*	0.81*
Average	**0.74**	**0.74**	**0.64**	**0.64**

* indicates a significant AUC score ($p<0.05$) established from an empirical null distribution of classification accuracies (AUC scores) derived from random observations (i.e. shuffled class labels).

3.3.4. Reduced group classification

The large participant number in this study tightened the standard error about the mean AUC in the group classification plots (figure F3.8), yet the maximum scores achieved were only 70% ($FD_{830\,nm}$, $p<0.05$) for physical movement and 56% for imagery ($FD_{830\,nm}$ and $FD_{\Delta[HbO]}$). From the peak AUC scores for each individual however (table T3.3), it is evident that a select few participants with good data separation (i.e. highly distinct left- and right-hand features) positively drove the average classification score for the entire group. The data quality screening results in section 3.3.1 (figure F3.2) identified seven participants as having relatively noise free intensity measurements at source-detector separations of 25 and 35 mm. Group classification scores for these seven individuals with respect to the AUC curves generated by the remaining 21 participants are displayed in figure F3.9. These highlight the smaller cohort as generating better group classification scores than the larger cohort for both FD-optical and FD-haemodynamic data. Maximum group classification scores for the larger cohort were 69% ($FD_{830\,nm}$, $p<0.05$) for physical movement and 55% for imagery ($FD_{830\,nm}$), whereas for the smaller cohort, maximum results were 79% ($FD_{\Delta[HbO]}$, $p<0.05$) for physical movement and 64% ($FD_{\Delta[HbO]}$, $p<0.05$) for imagery with the peak AUC scores of $FD_{\Delta[HbO]/\Delta[HbR]}$ being greater than those of $FD_{830/690\,nm}$. Overall these plots highlight that this small cohort with relatively good SNR were able to yield responses during left- and right-hand imagery commands that could be separated by a classifier to a significantly good degree of accuracy.

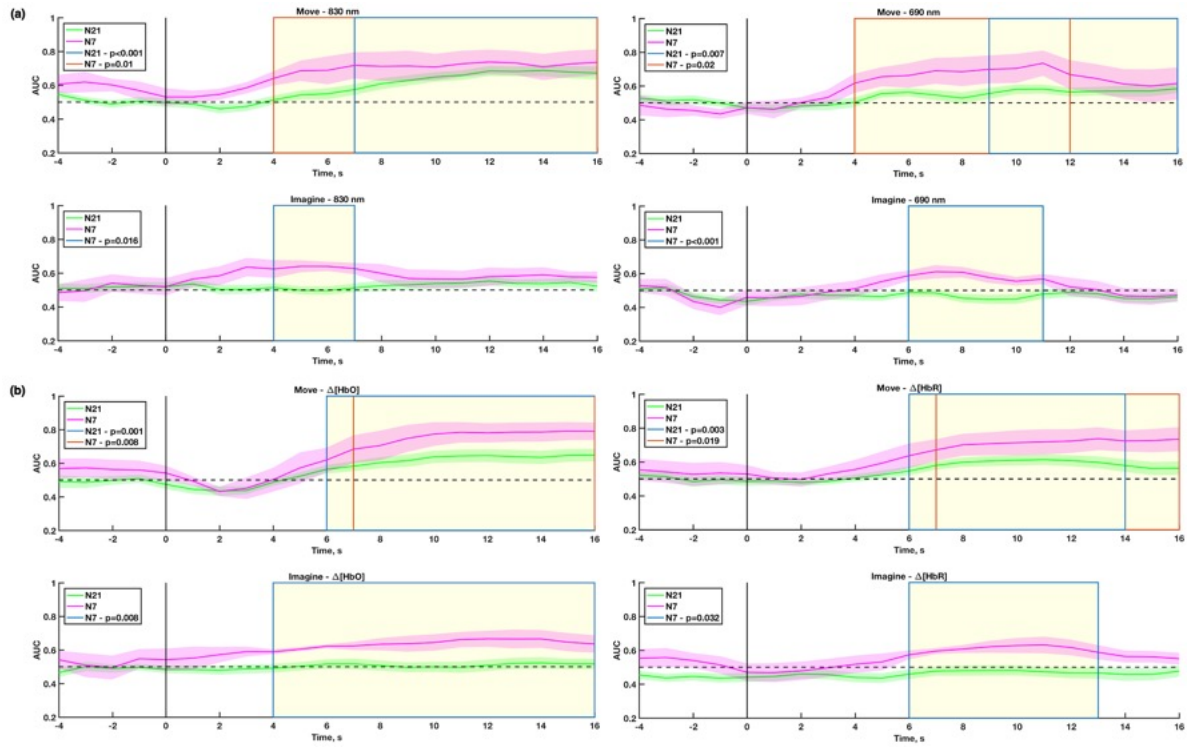

Figure F3.9: Average classification scores for a group of 21 participants with relatively low SNR and a group of 7 participants with a relatively high SNR. Classification was performed between left- and right-hand responses for both physical movement and imagery tasks independently. Specifically, differences were studied in the classification results of CSP-pre-processed 830 nm signals (a) and CSP-pre-processed Δ[HbO] signals (b) using FD measurements. Further details of these plots have previously been described in figure F3.8.

When considering the peak AUC scores achieved by each of these seven participants (table T3.6), the highest average score of 82% was obtained for classification of physical movement Δ[HbO] signals, whereas that of 72% was achieved for the classification of imagery Δ[HbO] and $FD_{830\ nm}$ signals. Interestingly, a difference between Δ[HbO] and $FD_{830\ nm}$ average peak scores was only identified for the physical movement condition. The average score of Δ[HbO] was 4% greater than that of $FD_{830\ nm}$, whereas no differences were observed between the average scores of Δ[HbR] and $FD_{690\ nm}$ for both types of command following. In comparison to the average peak scores obtained by the N=21 group (consisting of participants with a relatively low SNR), average scores were greater for the smaller cohort for both physical movement and imagery conditions. Statistical comparisons of these averages highlighted all but the $FD_{830\ nm}$ signals to be significantly different ($p<0.05$). This is reflective within

figure F3.9 whereby overlaps are present between the N=7 and N=21 groups when classifying $FD_{830\ nm}$ signals. For the physical movement condition, the overlap is quite extensive resulting in a large non-significant difference ($p>0.20$) between the average peak scores for the two cohorts. In contrast, the mild overlap for the imagery condition results in a non-significant p-value between the two average peak scores that is close to the 0.05 threshold.

Table T3.6: Peak classification AUC scores for each of the 7 participants with relatively high SNR. Individual and average results are presented for physical movement and imagery tasks having classified left- and right-hand statistical features from 830 nm and Δ[HbO] signals using FD measurements. Also presented are the average peak scores for the 21 participants with relatively low SNR. In order to statistically compare these averages, a subset of 7 participants were randomly selected from the N=21 group (with replacement) and their average peak AUC scores were calculated for each task and 830 nm/Δ[HbO] signal. This was repeated 1000 times to generate a distribution that could be used to test whether the average peak AUC scores from the 7 best participants were significantly different indeed ($p<0.05$).

Peak AUC scores								
Participant	**Move**				**Imagine**			
	830 nm	**Δ[HbO]**	**690 nm**	**Δ[HbR]**	**830 nm**	**Δ[HbO]**	**690 nm**	**Δ[HbR]**
1	0.71*	0.75*	0.51	0.64	0.74	0.63	0.60	0.54
2	0.61	0.81*	0.55	0.66	0.59	0.74*	0.64	0.68
11	0.53	0.58	0.63	0.61	0.68	0.63	0.66	0.63
16	0.87*	0.83*	0.94*	0.93*	0.65	0.79*	0.59	0.69
18	0.86*	0.89*	0.89*	0.89*	0.83*	0.72	0.81*	0.65
21	1.00*	1.00*	1.00*	1.00*	0.77*	0.73	0.66	0.70*
28	0.93*	0.87	0.85*	0.69	0.77*	0.81*	0.68	0.75*
Average (N=7)	**0.79**	**0.82**	**0.77**	**0.77**	**0.72**	**0.72**	**0.66**	**0.66**
Average (N=21)	**0.76**	**0.71**	**0.68**	**0.68**	**0.64**	**0.61**	**0.59**	**0.60**
p	**0.241**	**0.012**	**0.001**	**0.007**	**0.076**	**0.007**	**0.007**	**0.006**

* indicates a significant AUC score ($p<0.05$) established from an empirical null distribution of classification accuracies (AUC scores) derived from random observations (i.e. shuffled class labels).

3.4. Discussion

Using a FD-NIRS imaging system, physiologically expected contralateral effects were observed during physical gripping of the left- and right-hands. Furthermore, similar contralateral effects were identified during imagined hand movements, however these were of a lower magnitude. These patterns were identified in both measured FD (log-intensity and phase shift) and derived haemodynamic (Δ[HbO] and Δ[HbR]) signals. Haemodynamic responses across each hemisphere were derived from multi-channel FD scalp measurements using methods of functional diffuse optical topography. With respect to the classification of left- and right-hand signals, this study reported improved scores for feature matrices incorporating FD (over CWL) information. This was further enhanced in participants where these measurements had a relatively high SNR. The improved classification results obtained from different imagery responses indicate the potential of this technology for BCI application within the clinic in patients that show minimal or inconsistent physical behaviours.

3.4.1. Frequency-domain signal analysis

The benefits of FD data over continuous-wave signals have been recently evaluated by Doulgerakis and colleagues (Doulgerakis et al., 2019b, 2019a). In their first publication, the authors studied Fourier spectrums derived from log-intensity and phase-shift measurements at source-detector distances ranging between 13-48 mm (Doulgerakis et al., 2019b). They observed a peak corresponding to the frequency of the stimulus at all channels for phase but only for distances of 30 mm and above for intensity. Peaks for breathing and cardiac pulses were evident at all separations for intensity measurements, however these were much smaller and diminished at the second and third neighbourhoods for phase. This demonstrated a lack of sensitivity to signal contamination from the superficial tissues by the latter component. These results were likewise observed in the current study, whereby the Fourier spectrum of intensity data depicted peaks corresponding to cardiac, breathing and blood pressure that were present at all separations demonstrating the “hypersensitivity” of intensity measurements to superficial noise. However, unlike the intensity results presented by Doulgerakis and

colleagues, the current study observed a stimulus peak at all channels for a few participants. For the phase data, the present study similarly found this parameter to be less sensitive to physiological noises at all source-detector separations, however these measurements were generally noisier at longer channels due to strong signal attenuations. Furthermore, as the sampling distance increased the peak corresponding to the task frequency rapidly increased in power reaching a maximum at the third neighbourhood. The lack of a further increase in power at the fourth neighbourhood (which was also observed by Doulgerakis and colleagues for neighbourhoods greater than 48 mm (Doulgerakis et al., 2019b)) is expected given the poor SNR identified from the shifts in phase in figure F3.2a and could perhaps be improved by increasing the systems modulation frequency beyond the 140 MHz used in the current study.

In a second publication by Doulgerakis and colleagues, the authors identified the effective image resolution to improve by 21% with FD measurements as opposed to with CWL measurements (Doulgerakis et al., 2019a). This was a result of the phase-derived Jacobian having increased homogeneous sensitivity for deeper tissue regions and reduced sensitivity to physiological noises in the superficial layers. These authors' *in-vivo* studies on healthy participants performing a visual stimulus task gave rise to FD reconstructions showing activations overlapping the cortex of the brain and CWL reconstructions highlighting activations primarily in the superficial tissues. With respect to these findings, in the current study haemodynamic reconstructions from FD data (in comparison to reconstructions from CWL data) improved contrast between the two opposing hand responses for both physical and imagined movements. For the contralateral hand, increased contrast was present at the initial dip following presentation of the action cue whereas for the ipsilateral hand there was a more rapid recovery to baseline following an initial brief change in the haemodynamic response. This initial response for the ipsilateral hand was most likely due to the bilateral electrical response of hand movements (Yi et al., 2013). These left- and right-hand profiles at each hemisphere were found to be significantly different for a larger percentage of individuals for the 830 nm source. This percentage however decreased following Δ[HbO] signal reconstruction and is likely due to the incorporation of noisy channel (fourth neighbourhood) measurements into the model.

The observed group haemodynamic changes seen in the current study correspond well with the observations made by Batula and colleagues during motor execution and imagery of left- and right-hand taps (Batula et al., 2017). Using a continuous wave fNIRS device, they demonstrated stronger contralateral responses in Δ[HbO] to right-hand movements by thirteen right-handed participants. The increased ratio of right-handed participants in the current study may have driven a similar pattern to be observed. Specifically, contralateral responses to right-hand physical movements plateaued when reaching a maximum 8 seconds after action cue presentation, whereas contralateral responses to left-hand physical movements diminished after the first 15 seconds. Such early decreases in contralateral activity were however accompanied by an increase in the ipsilateral response. The present study's haemodynamic profiles therefore portray that constant physical activity with the dominant hand sustained increases in oxygenation to contralateral brain regions, whereas for the non-dominant hand activity was more bilateral therefore limiting the extent to which increased oxygenation was sustained in one region. Lateralisation differences such as these have also been observed during complex motor tasks (Lee et al., 2019a) and this is likely associated with the contralateral hemisphere for the dominant hand playing an important role in muscle contraction and relaxation (Yokoyama et al., 2019). During motor imagery, Batula and colleagues demonstrated a delayed and weakened contralateral response to hand taps. Whilst such a weakened haemodynamic response profile was likewise observed for the current imagery task, these responses however reached their maximums in the same interval as the responses for the physical movement task. This emphasises previous discussions in that FD systems enable better noise-free sampling of cortical tissues thereby allowing more accurate detection of imagined responses.

3.4.2. Classification

Due to the small number of trials performed for each task, a single statistical feature was derived from the data to prevent classifier overfitting. Calculating the mean over short (8 second) Δ[HbO] data segments gave rise to average peak accuracies of 74 and 64% for physical movement and imagery tasks respectively. However, a post-hoc analysis of the results revealed both the mean and peak statistical

features to yield equal peak accuracies for time window spanning 5-9 seconds (see appendix AT3.1). Several research groups have however demonstrated that using a combination of statistical features can further improve classification performance. Naseer and colleagues classified mental imagery stimuli using paired combinations of six statistical features (mean, variance, peak, slope, skewness and kurtosis) and found the mean and peak of the Δ[HbO] signal to yield an average SVM accuracy of 98% across a group of 7 participants (Naseer et al., 2016b). Qureshi and colleagues alternatively demonstrated classification performance using feature combinations extracted from estimated coefficients (beta values) of the general linear model (Qureshi et al., 2017). Classification of rest versus right-hand imagery Δ[HbO] signals from a group of 10 healthy participants resulted in accuracies above 80% for combinations that included the mean and skewness (82%), peak and skewness (81%), and mean and peak (81%). In comparison to two-dimensional combinations of features, Naseer and colleagues highlighted three-dimensional features to further improve accuracies for a number of different classifiers (Naseer et al., 2016b). Naseer and colleagues however in a second publication attributed this increase to the signal mean and peak, which as a pair yielded accuracies of 93 and 90% for Δ[HbO] and Δ[HbR] respectively, improving to 94 and 92% when combined with signal skewness (Naseer et al., 2016a).

The time segments that yielded each individual's peak response were primarily five seconds after the action cue was presented on the screen. This delay in classification performance corresponds well with the few second delay in the haemodynamic response (Liao et al., 2002; Logothetis et al., 2001). Optimal classification window lengths have been previously investigated for motor imagery tasks involving simple and complex finger taps (Holper and Wolf, 2011). For a single participant, Holper and Wolf recorded an accuracy of 75% for Δ[HbO] signal mean with a window length spanning 6 seconds (9-15 seconds post-stimulus). Maximum scores of 92% were however achieved for two participants with window lengths spanning 6 and 9 seconds and features of 3 and 4 dimensions respectively. The score of 75% achieved by these authors was lower than the peak score obtained for Δ[HbO] in the current study (88%- participant 28, table T3.3). Furthermore, the author's maximum score recorded is likely a result of overfitting having only performed 12 trials for each type of motor imagery stimulus.

Prior to statistical feature calculation, the data were pre-processed using the CSP algorithm in order to maximise the variance between left- and right-hand class labels. This algorithm is frequently applied in EEG-based motor imagery BCI applications (see chapter 2 for further details) (Blankertz et al., 2008; Ramoser et al., 2000; Wang et al., 2005). The CSP algorithm effectively projects multi-channel data into a lower dimensional spatial subspace (if possible) and dissociates signals into spatially separable task-common and task-specific components (Blankertz et al., 2008). Previously, classification of CSP-pre-processed fNIRS signals following a physical finger/thumb movement task yielded a 5% average increase in accuracy for a group of three participants (Jin et al., 2015). Zhang and colleagues however compared the impact of excluding and including CSP-pre-processing for classification of left- and right-finger physical and imagined taps (Zhang et al., 2017a). Having recorded haemodynamic signals over the C3 and C4 brain regions, for the motor imagery task the authors recorded a 15% (14%) increase in classification accuracy for a three-dimensional feature set (mean, slope, and variance) derived from Δ[HbO] (Δ[HbR]) CSP filtered signals.

When comparing the CSP-included Δ[HbO] classification scores for the current study with those obtained by Zhang and colleagues (Zhang et al., 2017a), differences were only found for the imagery condition (current study - 64%, Zhang and colleagues - 75%). Interestingly, even with two additional statistical features, Zhang and colleagues achieved a classification score for the physical movement task that closely matched the results of the current study (current study - 74%, Zhang and colleagues - 75%). This could perhaps reflect the improved cortical sampling of brain tissue and higher SNR provided by FD-NIRS imaging systems. Whilst Zhang and colleagues demonstrated positive differences between CSP-excluded and CSP-included classification methods, no such evidence consistent with this was found from the average peak AUC scores obtained in the present study for Δ[HbO] signal classification (however a marginally greater monotonic positive correlation was present for the CSP-including over the CSP-excluding classification method), and this is possibly due to the lack of multi-channel haemodynamic data available. Unlike multi-channel 830 nm signals (which yielded a CSP-included accuracy of 77%), spatial information was well accounted for within the two Δ[HbO] channels through the reconstruction of haemodynamic parameters, thereby limiting the

potential of the CSP algorithm to further maximise the variance between the left- and right-hand responses.

In comparison to the current study, the vast amount of NIRS motor imagery research for BCI applications have been performed on fewer healthy individuals (Chiarelli et al., 2018; Holper and Wolf, 2011; Khan et al., 2018; Shin et al., 2018; Zhang et al., 2017a) with equally low patient numbers examined (Rupawala et al., 2018). Classification performances were therefore additionally studied from a subset of seven participants with relatively high SNR. These individuals yielded an average peak Δ[HbO] accuracy markedly greater than the result obtained by Zhang and colleagues during physical movement (current study - 82%, Zhang and colleagues - 74%) (Zhang et al., 2017a). Additionally, AUC scores obtained for the imagery task were much improved yet marginally lower than the accuracy achieved by Zhang and colleagues (current study - 72%, Zhang and colleagues - 75%). Generally, average optical and haemodynamic peak scores for this reduced cohort were markedly greater than the average peak scores obtained by the remaining group. Interestingly however, despite these select participants displaying relatively noise-free data, not all these individuals were able to generate left- and right-hand responses that could be highly classified (c.f. participant 11 in table T3.6). This perhaps correlates with a lack of a strong contralateral response or a prominent bilateral response by these individuals or a suboptimal time segment for feature extraction.

From the results and discussions thus far, it can be summarised that classification of left- and right-hand physical/imagined movements is optimally performed (i.e. the SVM classifier can maximally separate classes in a manner that allows test data to be classified to a high accuracy) when using statistical feature means (derived from an 8 s time window length, 8 s after the action cue) obtained from FD-derived Δ[HbO] data that has undergone CSP-pre-processing. In order to achieve this finding, several classification assessments were performed on the entire dataset using a *k*-fold cross-validation approach. Cross validation is a technique that can be used to evaluate the performance of a classification model where there is limited data (Lemm et al., 2011). Through subsampling of the data (as in the *k*-fold scheme) the average error of a classifier can be computed when each *k* model is evaluated separately on its corresponding validation dataset (Lemm et al., 2011). When the processing is performed on training data within the cross-validation loop using methods from prior knowledge (e.g.

optimal data pre-processing steps, feature extraction and selection methods, and classifier hyperparameters) then the results can to some extent generalise well. However, in the case of the current study, multiple classification assessments were performed outside this cross-validation loop (e.g. effects of CSP-pre-processing, effects of different statistical features) using the data from all participants thereby limiting the significance of the final accuracies (AUC scores) obtained for the most optimal classification approach. Whilst others have taken a similar approach as this study and demonstrated best classification results for different analysis methods (Holper and Wolf, 2011; Zhang et al., 2017a), a better methodology would be to divide participant data into a training and validation cohort (which can be used to perform several cross-validation classifications) and a testing cohort whereby the unseen data are used to gather a true generalisation of the final classification approach (Coyle et al., 2008; Fazli et al., 2012; Koo et al., 2015; Lemm et al., 2011). Such well generalised accuracies could have been calculated by leaving out the participants with relatively good SNR for testing of the final optimal classification approach.

3.4.3. Summary

This study has extensively investigated both the amplitude-modulated intensity and phase parameters of a FD-NIRS system for brain imaging. Specifically, system capabilities were tested to measure motor activity in response to physical and imagined movements of the hand. In comparison to continuous-wave systems that output intensity measurements only, the additional phase component of FD systems was found to increase contrast between right- and left-hand movement profiles in the reconstructed haemodynamic response (i.e. a small 1% perturbation in attenuation caused large changes in the haemodynamic signals). Although this parameter is more sensitive to noise at longer range channels, it is however less sensitive to signal contamination from the superficial tissues (physiological noise) and can provide good depth selective information by primarily sampling cortical activity. Classification of CSP spatially filtered FD and haemodynamic motor imagery signals yielded average peak scores of 66% (830 nm) and 64% (Δ[HbO]) for the entire group and 72% (830 nm and Δ[HbO]) for a subset of participants with relativity high SNR. CSP spatial filtering was most effective on multi-

channel measurements (in this case multi-channel FD signals) and as such did not improve the classification scores of two-channel hemodynamic signals.

Overall, the findings from this chapter have presented good evidence for a FD-NIRS imaging system to be tested within the clinic, specifically for brain imaging in response to covert commands. However, it is recommended that data quality should be frequently checked each time either the source/detector positions or light levels are altered, or participants move their head, in order to maximise the spatial sensitivity of the instrument. Furthermore, when classifying multi-channel responses, the CSP algorithm should be used to reduce the dimensionality of the data and maximise class differences. Nevertheless, in order to further improve the classification success rate, the use of multiple statistical features and additional temporal sensitivity may be of benefit. One such inexpensive way both spatial and temporal sensitivity could be maximised is through recording simultaneous EEG-fNIRS measurements.

Chapter 4

Motor imagery detection using simultaneous EEG-fNIRS

4.1. Introduction

The brain dynamics captured by EEG and NIRS systems in response to covert command-following have been previously explored in chapters 2 and 3 respectively. As relatively inexpensive portable devices they offer a potential means to continually assess patient's brain function at the bedside for whom imaging methods such as fMRI are either inaccessible or inapplicable. Nevertheless, each technology is limited in their image resolution capacity: EEG can sample electrical neural activity at a millisecond time frame however offers poor spatial resolution due to volume conduction effects, whereas NIRS indirectly measures the slow haemodynamic changes in the brain to a relatively good spatial resolution only. Naturally, neural activity increases oxygen demands which in turn increases cerebral blood flow due to neurovascular coupling. The interrogation of this interconnected biology using simultaneous EEG-fNIRS measurements therefore has the capacity to yield a continuous time course into the changes in brain function and health in response to tasks (Blokland et al., 2014) or treatments (Jindal et al., 2015). Furthermore, as a hybrid technique, the overall increase in information content has the means of advancing the development of brain computer interface (BCI) applications utilising such covert command-following paradigms (Khan et al., 2014, 2018).

Previous literature has demonstrated an EEG-fNIRS bimodal system to better classify two classes of motor imagery than either system alone (Blokland et al., 2014; Ge et al., 2017; Khan et al., 2015; Shin et al., 2017). Whilst some bimodal BCI studies are based on multi-channel data (Fazli et al., 2012; Khan et al., 2014, 2015; Koo et al., 2015), there is a growing interest for the use of fewer channels to improve the portability and comfort of the BCI, and to reduce cost and preparation time. Ge at al. presented average hybrid classification accuracies of 81% (EEG alone: 75% and fNIRS alone: 57%) following a left- and right-hand motor imagery paradigm when analysing the data from three electrodes

and six optodes around the C3 and C4 regions (Ge et al., 2017). Whilst these accuracies were significantly greater than chance and have been obtained by others (Tam et al., 2011), the need for the authors to perform a preliminary multi-channel analysis to identify optimum BCI channels limits the scope of such methods as a fully few-channel hybrid system.

Khan and colleagues on the other hand demonstrated classification results between left-arm imagery and rest having used a six-channel hybrid EEG-fNIRS setup, primarily across the right hemisphere of the brain for the entire study (Khan et al., 2015). The authors observed that prior to training, the average motor imagery performance across five healthy participants was 66%. Once the right-handed participants were trained to physically perform the "adaptive reach" protocol with the assistance of a rehabilitation robot, average motor imagery classification scores increased to 94%. A key aim of this publication was to investigate the effects of both training and EEG-fNIRS in the classification of motor imagery signals. Similar to training, the addition of feedback can encourage, motivate and improve an individual's BCI skill development (and thus classification accuracy) by maintaining their interest (Guger et al., 2003; Neuper et al., 1999), however it can also impair performance due to diminished attention to the task or frustration caused by incorrect feedback. Studies that have presented individuals (naïve to motor imagery) positive and negative feedbacks have shown negative feedback to accelerate learning effects (González-Franco et al., 2011; Holper and Wolf, 2010). It is therefore suggested that the frustration primarily develops following multiple BCI sessions where either no such learning has taken place by the participant or when the paradigm, setup or classification models are not optimal to accurately measure the learnt effects. Training may not however be feasible in all patients depending on the severity of their brain injury, treatment course, and the need for long durations of engagement with the task. In contrast, Coyle and colleagues successfully demonstrated that after an initial BCI assessment, patients in a minimally conscious state could modulate their sensorimotor rhythms when provided with visual or auditory feedback (Coyle et al., 2012, 2015). This was because patients became aware that the motor imagery task could alone (i.e. without the need for any physical movement) affect the position of a sound or visual object on the screen thereby allowing them to learn to control their mental activity in order to achieve the best possible control of the interface (Coyle et al., 2012). From a clinical standpoint, an initial successful motor imagery BCI session can

therefore complement current awareness detection protocols as they can demonstrate the capacity for a patient to remain attentive, their working memory function, language comprehension skills and visual or auditory acuity. Furthermore, subsequent feedback BCI sessions can allow clinicians to monitor consciousness recovery due to the associated brain plasticity that occurs with increased mental practice of an overt movement.

Nevertheless, Blokland and colleagues demonstrated BCI performance of a few-channel EEG-fNIRS setup in the absence of any feedback or training in both healthy individuals and patients using a finger tapping motor execution and imagery paradigm (Blokland et al., 2014). Eight electrodes and two optodes were positioned around C3 and C4 scalp electrode locations on eight healthy participants and seven patients diagnosed with tetraplegia. Time-frequency analysis of EEG spectral features revealed that immediately following the executed finger tapping cue, healthy participants displayed a strong contralateral event-related desynchronisation (ERD) within the alpha (8-13 Hz) and beta (13-22 Hz) frequency bands demonstrating sensorimotor activation which lasted for the full 15 second task period. This was subsequently followed by a rest cue which resulted in a strong contralateral event-related synchronisation (ERS) within the 8-20 Hz frequency window highlighting sensorimotor inhibition. In contrast, healthy individuals displayed a strong contralateral ERD that lasted for only three seconds following the imagine finger tapping cue, and a weak contralateral ERS following the rest cue. Patients however only displayed weak contralateral ERDs following both executed and imagined finger tapping cues and no ERS following the rest cues. With respect to haemodynamic responses, both healthy controls and patients displayed increases in oxygenated haemoglobin from baseline on the contralateral hemisphere during both physical and imagined finger tapping cues which subsequently decreased towards baseline following the rest cue. The deoxygenated haemoglobin response, which was absent in patients during the executed finger tapping cue only, was characterised by a decrease from baseline during the action cue that recovered to baseline following the rest cue. The lack of significant electrical and haemodynamic responses to physical movement in patients is in agreement with their diagnosis, which prevents them from truly executing any such muscle activity. Classification of movement- verses rest-derived features resulted in improved average accuracy scores when simultaneously using both EEG and NIRS data. Furthermore, the average results were higher for actual (control: 87%, patients:

79%) compared to imagined (control: 79%, patients: 70%) movement with better scores overall achieved by healthy participants than patients.

Such progress in research highlights that both improved technology and advanced analysis methods can positively assess covert paradigm performance in the clinic without the need for extensive brain coverage and a large number of trials. Nevertheless, such research efforts are reliant on prior literature to guide scalp positions of electrodes and optodes to correctly sample underlying brain tissue activated in response to the task. With this knowledge, the study presented in this chapter similarly investigated simultaneous EEG-fNIRS BCI performance using a few EEG electrodes and frequency-domain (FD) derived hemodynamic responses from the NIRS montage presented in chapter 3. Findings of chapter 3 specifically demonstrated improved classification scores provided by haemodynamic parameters derived using both log-intensity and phase-shift components of an FD system. As this has not yet been explored in the literature (similar studies have used either a continuous-wave NIRS system (Blokland et al., 2014; Shin et al., 2017) or have limited their analysis to intensity measurements alone when using a FD NIRS device (Khan et al., 2018)), the aim of this chapter is to highlight that the addition of EEG measurements can benefit overt and covert command-following classification beyond that achieved using NIRS data alone. To align comparisons with previous studies, a similar left- and right-hand experimental paradigm to that presented in chapter 3 was used, as was an analysis pipeline featuring common spatial pattern (CSP)-pre-processing. Furthermore, having in-depth discussed the NIRS output to this paradigm in chapter 3, here the focus is on unimodal EEG and bimodal EEG-fNIRS classification performances.

4.2. Methods

4.2.1. Experimental setup and paradigm

Five healthy participants (four male and one female, aged between 20-30 years) volunteered to take part in this pilot study by providing their written and informed consent. This simultaneous EEG and FD-NIRS study had ethical permission obtained from the University of Birmingham STEM ethics

board. A limited number of participants were selected for this study (in comparison to the number of participants recruited for studies in chapters 2 and 3) in order to determine the effectiveness of a highly reduced EEG setup (with respect to the number of electrodes used and their scalp positions) alongside the NIRS setup used in chapter 3, and to identify an optimal processing/classification approach that could be directly tested on a larger cohort (as discussed within chapter 3, i.e. the need for training, validation and testing datasets). NIRS measurements were obtained using an FD-NIRS device (IMAGENT^{TM}, ISS Inc., Illinois) previously described in chapter 3.2.1, whereas EEG measurements were gathered using an ANT Neuro acquisition system (eego^{TM} mylab, Hengelo, Netherlands). Eight NIRS channels consisting of eight detectors and two sources were positioned over the central hemisphere spanning the C3 and C4 regions as previously detailed in chapter 3.2.1. Due to the success of previous studies utilising a sparse electrode montage scheme and the expected laterality of EEG responses (Cruse et al., 2012; Guger et al., 2003), four passive electrodes were positioned approximately 2.5 cm anterior (at locations of FC3 and FC4) and 2.5 cm posterior (at locations of CP3 and CP4) to electrode positions C3 and C4 of the international 10/20 electrode system (see schematic in figure F4.1a). Additionally, reference and ground electrodes were placed on the right- and left-mastoids respectively. The scalp was prepared for EEG recording using Nuprep® skin preparation gel and Ten20® conductive paste to improve the transmittance of electrical signals to the electrode. Data were sampled at 512 Hz and impedances were kept below 10 kohms.

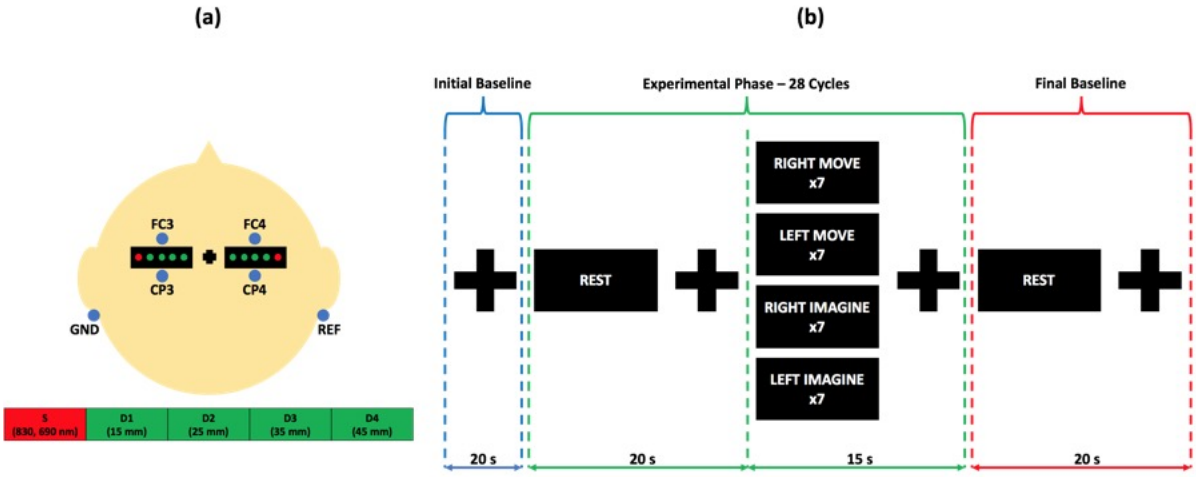

Figure F4.1: (a) Layout of NIRS optodes and EEG electrodes on the scalp. For each participant the intersection between the nasion-inion and left-right preauricular points was marked to reference the Cz location. The NIRS imaging pad was positioned on the scalp using the methodology described in chapter 3.2.1. In addition, EEG recording electrodes were positioned at locations FC3, FC4, CP3 and CP4. These were referenced online to the reference electrode positioned on the right-mastoid. The circuit was completed using a ground electrode positioned on the left-mastoid. (b) Experimental paradigm. The task performed was similar to that described in chapter 3.2.1. Differences between the current experimental paradigm and that used in chapter 3.2.1 were that (1) an initial fixation cross of ~20 s was presented at the start of the experiment to record baseline activity, (2) twenty-eight cycles of paired rest (~20 s) and action (~15 s) commands followed, and (3) a final rest command and fixation cross of ~20 s duration was presented to once again record baseline activity.

The instruction protocol provided to each participant was identical to that described in chapter 3.2.1. Participants performed four actions corresponding to right-hand gripping ("Right Move"), left hand gripping ("Left Move"), right hand imagined gripping ("Right Imagine") and left hand imagined gripping ("Left Imagine") that were randomised to ensure that no more than two of the same action were presented in a row. In comparison to the experimental protocol described in chapter 3.2.1., the duration of each rest and action cue was reduced (figure F4.1b, for a comparison please refer to figure F3.1b in chapter 3). Taking into account the high temporal resolution of EEG recordings and the large number of trials usually performed as a result, the left- and right-hand execution/imagery paradigm in chapter 3.2.1 was adjusted so that each rest period lasted 20 s whilst each action period was limited to 15 s. Based on the findings in chapter 3, a 15 s action period was sufficient to capture each

haemodynamic response's change to its maximum. With this reduced trial length, a total of 84 trials were conducted across the three rounds (21 of each of the four different action commands) with a total round duration of 20 minutes.

4.2.2. Data pre-processing

Using both log-intensity and phase-shift parameters of the FD-fNIRS system, changes in oxy- (Δ[HbO]) and deoxy- (Δ[HbR]) haemoglobin were recovered using the pre-processing methodology described previously in chapter 3.2.2. Due to a change in the duration of the rest period of the task, a 10 s period immediately prior to the action cue was used as the baseline for both pre-processing and analysis of the haemodynamic responses. However, for the action period of the task, the entire 15 s recording window was examined due to the slow development of the haemodynamic response (Batula et al., 2017).

EEG data were firstly re-referenced offline to form two bipolar channels (FC3-CP3, FC4-CP4) that shall be referred to as C3' and C4', respectively. In comparison to unipolar and common average referencing methods, a bipolar approach was chosen as it is known to detect sensorimotor mu and beta modulations with a high level of accuracy across a large proportion of healthy individuals, due to the larger contribution of localised EEG sources (within the premotor cortex, supplementary motor area, primary motor cortex and somatosensory cortex) to the bipolar signal (Cruse et al., 2012; Guger et al., 2003; Ramoser et al., 2000). The data at C3' and C4' were subsequently filtered between 0.5-40 Hz, segmented into 8 s epochs time-locked to the onset of each instruction (3 s prior to and 5 s following the cue), and baseline corrected using functions from the EEGLAB (version 14.1.1b, Swartz Center for Computational Neuroscience, UC San Diego) toolbox. Following data pre-processing, time-frequency analysis was performed on the epochs from each of the four independent conditions using a fifth-order Butterworth filter and the Hilbert transformation to yield the envelopes corresponding to the activities within the alpha (8-13 Hz) and beta (13-30 Hz) frequency bands (refer to chapter 2.2.2 on details of how this was achieved). The resulting averaged power series for each task was decibel baseline normalised to allow effective comparisons.

4.2.3. Classification

In this subsection a description is provided of the methodologies used for the classification of opposing executed/imagined hand commands from each of the three recorded measurements: EEG, fNIRS and EEG-fNIRS.

- *EEG*

Two methods were investigated for classifying the raw EEG signals from right- and left-hand physical/imagined movements. Based on the methodology described by Cruse and colleagues (Cruse et al., 2012), the first feature extraction technique estimated spectral power of each of the two frequency bands using a short-time Fourier transform (STFT) (Matlab function '*spectrogram.m*') with a sliding window of 1000 ms moving in 125 ms steps (representing an 80% overlap). Having set the number of discrete Fourier transform points to four times the sampling rate, the output of the '*spectrogram.m*' function for each time window yielded 89 equally spaced spectral values between 8 and 30 Hz. These spectral values at C3' and C4' were averaged within the alpha and beta windows and together used as individual features for classification.

The second feature extraction method employed was the CSP algorithm as a means of spatial filtering the time series of each opposing hand condition such that their variances were optimal (in the least squares sense) for discrimination (refer to chapter 2.2.3 for a detailed methodology). Each of the four time series (right move, left move, right imagine, left imagine) were filtered using a fifth-order Butterworth filter into the respective alpha and beta frequency bands, centred and scaled prior to being subjected to CSP-based spatial filtering. The algorithm was only applied on the training dataset yielding two filter components that were used to transform the training and testing time series for discrimination. Obtaining the log variance provided the four individual features (two filter components x two frequency bands) for classification.

Using a seven-fold cross validation scheme, the data within each condition were divided into even blocks such that each fold contained 18 trials for training and 3 trials for testing. Classification

was performed using a support vector machine (SVM) with four features (two frequency band x two channels/filter components). As previously demonstrated in chapter 2 and 3, classification scores were estimated with an empirical receiver-operating curve (ROC) analysis applied on trials' predicted probabilities and the results of this analysis were summarised by the area under the curve (AUC).

- *fNIRS*

Classification of haemodynamic parameters were independently performed using a methodology similar to that described in chapter 3.2.4. To corroborate with the two EEG feature selection methods previously described, a non-CSP and CSP-based methodology were likewise constructed for Δ[HbO] and Δ[HbR] classification. Haemodynamic responses over the right (C3) and left (C4) motor regions were divided into short 6 s segments (as recommended by (Holper and Wolf, 2011)) with a 5 s overlap. Previously discussed in chapter 3.4.2 were the results from several publications reporting improved classification performances with a combination of statistical features. Specifically, for these studies, the mean and peak were found to be most effective (Naseer et al., 2016b, 2016a; Qureshi et al., 2017). These two statistics were therefore computed for each sliding time window and used as individual features (two data statistics x two channels/filter components) for SVM classification of Δ[HbO] and Δ[HbR] signals.

- *EEG-fNIRS*

In chapter 3, it was demonstrated how well Δ[HbO] and Δ[HbR] signals corresponding to right- and left-hand execution/imagery could be discriminated using an SVM classifier. In this study, having simultaneously measured these same motor responses using EEG and FD-fNIRS, the aim was to determine whether the addition of high temporally resolved EEG measurements further improved classification performance beyond that achieved by fNIRS alone. In order to resolve this for both (previously discussed) CSP present and absent classification schemes, the four features obtained from each EEG time window (two frequency band x two channels/filter components) were in turn classified

alongside the four features derived from each NIRS time window (two data statistics x two channels/filter components) using SVM. Percentage AUC changes were then determined between the resulting EEG+Δ[HbO]/EEG+Δ[HbR] matrix of AUC scores and those derived solely from NIRS (Δ[HbO]/Δ[HbR]) classification.

Joint classification was additionally performed between a single AUC scoring EEG time window and every 6 s sliding NIRS period. To determine this EEG time window for each participant, the following four steps were applied:

1. Select a single participant, for example participant 1.
2. Obtain the AUC scores calculated for the other four participants (in this example participants 2-5) for each EEG time window.
3. Average these scores across the group.
4. The window containing the maximum average score is assigned as the optimal window for the selected participant in step 1.

The selected EEG window for each participant was subsequently used to derive EEG-related features that were classified alongside NIRS statistical features. This process yielded an unbiased group EEG-fNIRS AUC score that would emphasise either the benefits or drawbacks of including EEG measurements on Δ[HbO] and Δ[HbR] classification of right- and left-hand executed/imagined movements.

4.2.4. Statistical analysis

Statistical analysis was performed on both pre-processed EEG and NIRS data sets and classification results using the cluster-based permutation test described in chapters 2.2.4 and 3.2.5. For both haemodynamic responses and EEG frequency band measurements, a one-tailed Student's t-test was performed between the left- and right-hand responses and the resulting temporal clusters were tested for significance ($p<0.025$, Bonferroni corrected) against a set of 1000 largest clusters obtained through randomisation runs. At the group level this randomised shuffling involved all trials from

individual participants, whereas at the subject-level this randomised shuffling took place between individuals trials pertaining to left- and right-hand commands for execution/imagery.

Similarly, statistical analysis of subject-level classification scores was performed by testing time-window clusters derived using the Mann-Whitney *U*-test statistic against the biggest clusters obtained following 200 randomisation tests ($p<0.05$). This reduced number of randomisations runs was once again due to extensive computational demands. Cohort level AUC scores however were compared against a 50% chance level of accuracy by using a one-tailed Student's t-test. The resulting temporal clusters were tested for significance ($p<0.05$) against 1000 largest clusters obtained by randomly shuffling a participants' AUC score with a score of 0.5.

In addition to this, statistical testing was also performed between the AUC scores obtained from joint EEG-fNIRS classification and that of Δ[HbO] and Δ[HbR] classification alone. Each row of the EEG-fNIRS AUC matrix (where each row pertains to a single EEG time window) was randomly shuffled with the vector of AUC scores obtained from sole NIRS classification, following which percentage changes were computed. The true percentage AUC changes for joint EEG-fNIRS classification were subsequently tested for significance against this randomised set at the alpha value of 0.05 for each condition type (physical movement/imagery). As such, the impact of this test was to statistically demonstrate the effect of additional EEG features on NIRS classification performance.

4.3. Results

4.3.1. Time-frequency analysis

Average group haemodynamic responses and EEG frequency band profiles are presented in figures F4.2 and F4.3 respectively. Similar to the Δ[HbO] and Δ[HbR] figures shown in chapter 3.3.2, the concentration curves in this study for both left- and right-hand execution/imagery, as derived using FD measurements (amplitude-modulated intensity and phase), demonstrate a large increase (decrease) in contralateral oxygenation (deoxygenation) changes that plateaus to a maximum (minimum) ~8 seconds after the action cue is presented. This is additionally accompanied by a relatively small increase

(decrease) in ipsilateral oxygenation (deoxygenation) change that much rapidly returns to baseline. Figure F4.2 qualitatively highlights both physical and imagined responses to be similar, however with the latter being much noisier across the group. Executed movement of the instructed hand generates a response approximately two (at C3) to three (at C4) times greater in strength to that of imagined movements. Furthermore, there is much greater separation of the contralateral and ipsilateral profiles for physical than imagined movement. Statistical analysis of these left- and right-hand average responses using the cluster-based permutation test method identified significant differences ($p<0.025$, Bonferroni corrected) at C4 and C3 positions for Δ[HbO] and Δ[HbR] respectively during physical movement only. These statistically significant differences are due to the large separation between left- and right-hand standard deviation curves, which are otherwise lacking in some movement (C3-Δ[HbO] and C4-Δ[HbR]) and all imagery responses. In addition to group level statistical testing, significance analysis was also performed at the subject level by randomizing individual left- and right-hand trials during the cluster-based permutation test. Across the five participants, 80% displayed a significant cluster at either C3 or C4 positions for the Δ[HbO] response to physical movement ($p<0.025$) whereas 20% generated a significant cluster for the Δ[HbR] response to physical movement and both Δ[HbO] and Δ[HbR] responses for imagery ($p<0.025$).

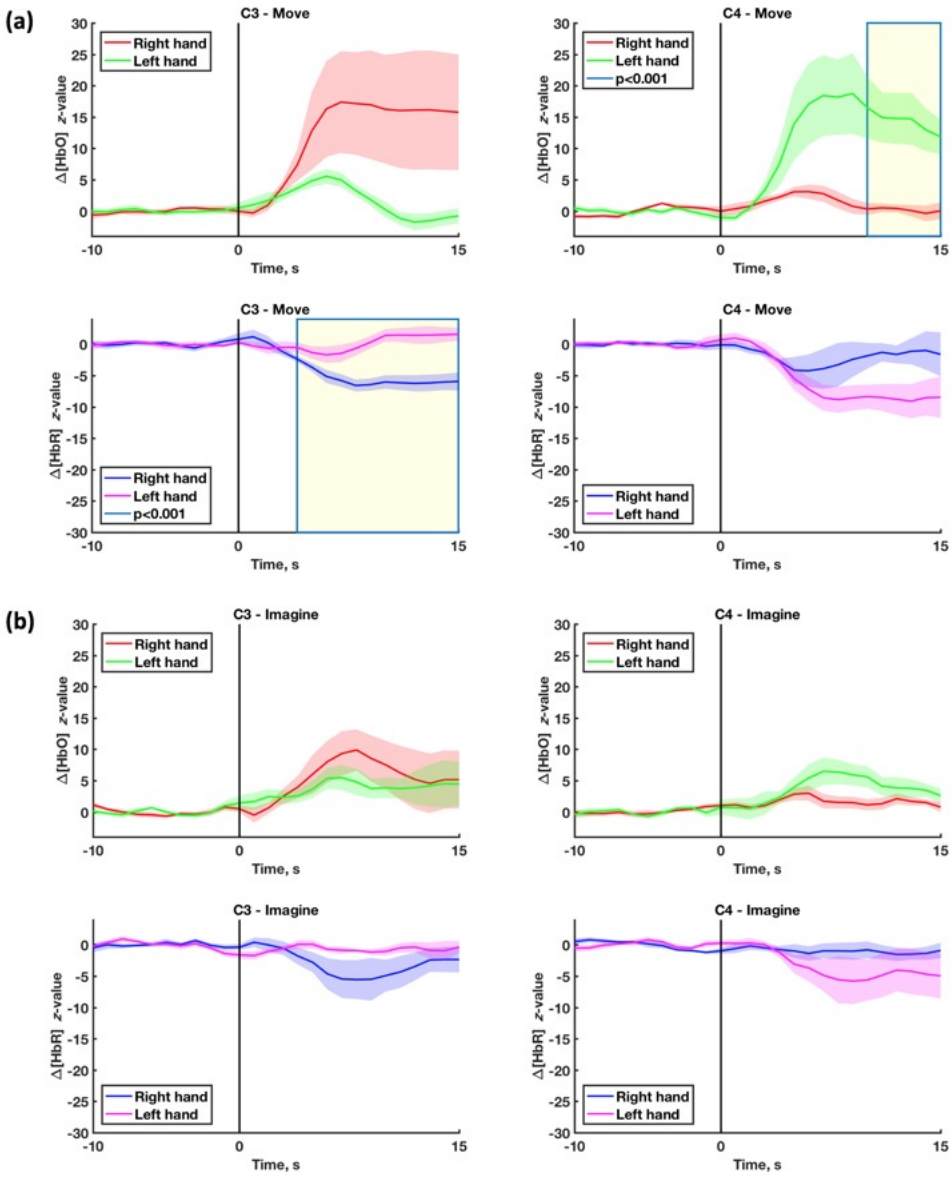

Figure F4.2: Block averaged and baseline corrected Δ[HbO] and Δ[HbR] responses for each of the four task conditions. Δ[HbO] and Δ[HbR] signals were derived using both log-intensity and phase-shift components and as such explain brain haemodynamics in the region directly under the three long-distant channels. Using an alpha value of 0.025, statistical significance was tested between left- and right-hand physical movement (a) and imagined (b) responses independently at both C3 and C4 regions.

In comparison to the haemodynamic responses to left- and right-hand physical movement/imagery, the group average alpha and beta band EEG profiles (figure F4.3) appear much more closely overlapped. Generally, immediately following the action cue a bilateral desynchronisation appears to occur for each type of hand command with somewhat greater contralateral signatures present

for imagery. These desynchronisations tend to last ~2 seconds before recovering towards baseline. Such profiles are in agreement with the right-hand alpha responses presented in chapter 2.3.1, which displayed a much stronger bilateral event related desynchronisation at both C3 and C4 electrodes during physical movement than imagery. The increasing similarity of the left- and right-hand responses at C3' and C4' electrode locations resulted in no significant clusters (at the $p<0.025$ confidence level) being identified for both group and single subject statistical analyses during both motor execution and imagery.

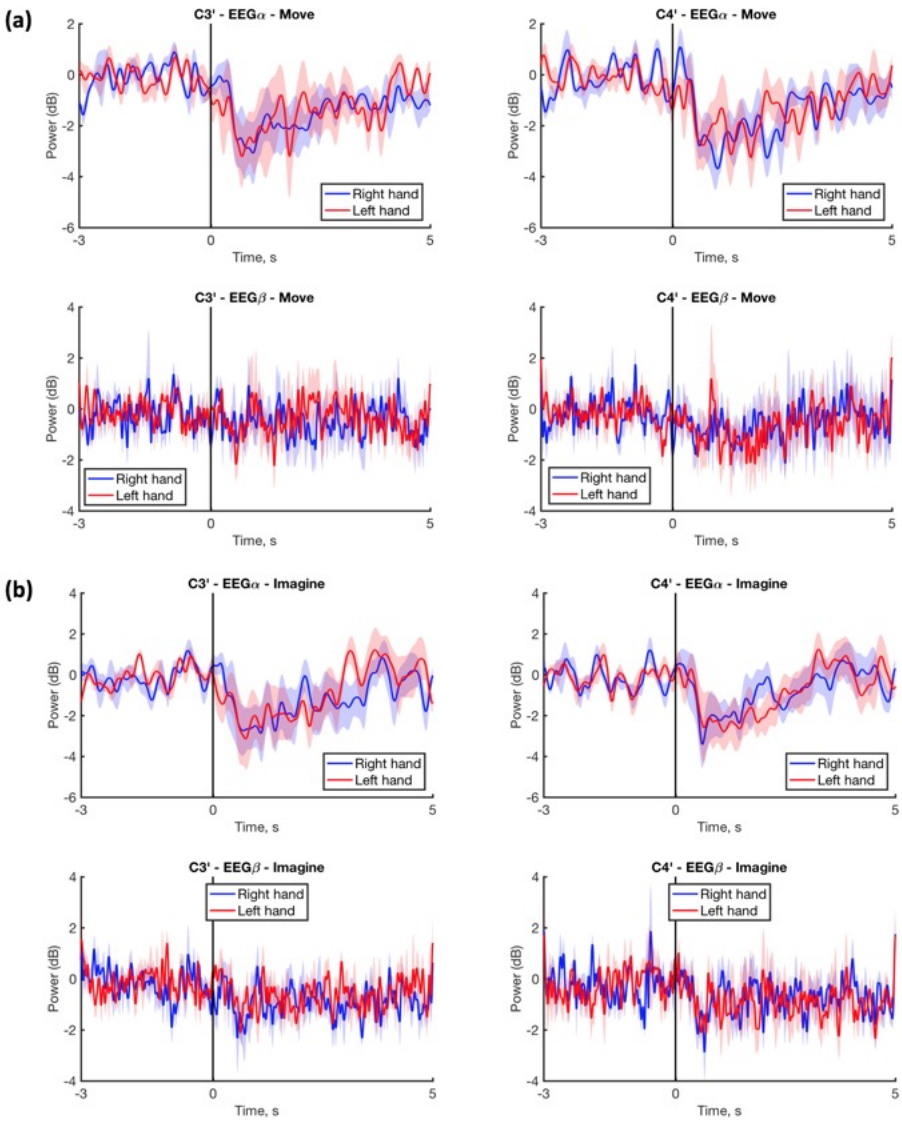

Figure F4.3: Block averaged and decibel baseline corrected EEG power signals for each of the four task conditions. EEG signals were filtered into alpha (8-13 Hz) and beta (13-30 Hz) band frequencies using a fifth-order Butterworth filter. These were then Hilbert transformed to extract the envelope of the signal. Using a statistical alpha value of 0.025, significance was determined between left- and right-hand physical movement (a) and imagined (b) responses independently at both C3' and C4' regions.

4.3.2. Classification

Classification of simultaneous EEG-fNIRS measurements was achieved by the joint use of frequency band EEG and statistical fNIRS features for each sliding time window. Two methods of feature extraction were investigated that either utilised the CSP algorithm as a prior to filter the data

into spatial subcomponents or directly selected features from pre-processed measurements. The resulting AUC scores were compared to those obtained by sole NIRS data classification yielding the percentage AUC change matrix presented in figure F4.4. In the absence of CSP-pre-processing, the addition of EEG features appears to improve NIRS classification performance for time windows spanning 0-6 and 1-7 seconds (mean of 3 and 4 seconds respectively). These percentage changes in AUC are much greater for imagery (EEG+Δ[HbO]: 17.37%, EEG+Δ[HbR]: 27.29%) than physical movement (EEG+Δ[HbO]: 10.46%, EEG+Δ[HbR]: 9.35%) and generally appear for mean EEG time windows 3 seconds after the action cue (except EEG+Δ[HbR], where the maximum changes were recorded for mean EEG windows at 1.5 and 2 seconds after the action cue). Interestingly, the addition of EEG features between time windows 1.5 and 2.5 seconds appear to also substantially decrease haemodynamic response classification performance. For physical movement this appears predominantly when the Δ[HbO] curve climbs and plateaus at its maximum response (EEG+Δ[HbO]: -12.81%), whereas for imagery the decrease is across the entire NIRS profile (EEG+Δ[HbO]: -22.71%, EEG+Δ[HbR]: -17.3%). Statistical analysis of these percentage AUC changes highlighted that whilst no significant time windows were found for physical movement, for imagery however, EEG features significantly ($p<0.05$) improved Δ[HbO] and Δ[HbR] classification performance between 0-9 seconds. For Δ[HbO], these EEG features corresponded to mean time windows of 3.75 and 3.875 seconds whereas for Δ[HbR] these were in the first 1.5 seconds or after 3.5 seconds. In the presence of CSP similar AUC change matrices are found with percentage increases predominantly occurring within the first two NIRS windows. In contrast however, the actual maximum value of the change appears to be greater for both physical movement (EEG+Δ[HbO]: 13.14%, EEG+Δ[HbR]: 14.31%) and imagery (EEG+Δ[HbO]: 22.84%, EEG+Δ[HbR]: 37.91%). In the case of the imagery paradigm, unlike a widespread increase in classification performance along the NIRS and EEG axes for non-CSP EEG+Δ[HbO] and EEG+Δ[HbR] respectively, the CSP algorithm transforms the data in a manner that results in classification improvements principally localised across EEG windows 3 seconds after the action cue. Similarly, this is accompanied by a greater number of statistically significant ($p<0.05$) clusters within the region in comparison to the non-CSP case.

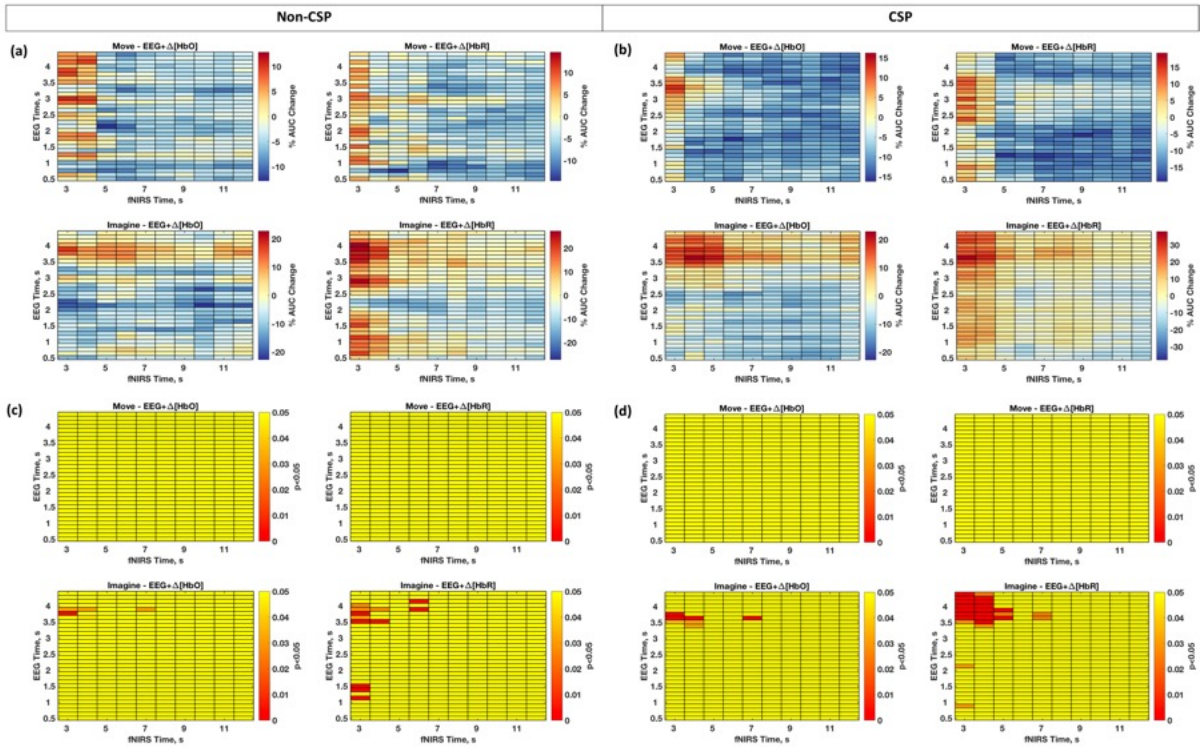

Figure F4.4: Group average percentage change in the AUC scores for each EEG and NIRS sliding time windows. SVM classification was performed between left- and right-hand responses for both physical movement and imagery tasks independently. Specifically, differences were studied in the classification results of (a) non-CSP and (b) CSP-pre-processed Δ[HbO], Δ[HbR] and EEG signals. AUC scores were computed from the classification of Δ[HbO] and Δ[HbR] statistical features with the addition of EEG frequency-band-derived features for all combinations of time windows. Presented in (a) and (b) are percentage AUC score changes between the classification of EEG+NIRS features and that of NIRS features alone. These were then statistically compared to determine whether EEG+NIRS classification was significantly different ($p<0.05$) from that of NIRS alone classification in (c) and (d). This was performed by computing a distribution from 1000 permutation runs where the AUC data from the simultaneous group was randomised with that of the NIRS. The simultaneous data were then tested against this distribution for significance (see section 4.2.4 for further details). The first EEG score at time 0.5 seconds represents the average of a time window spanning 0-1 seconds, whereas the first NIRS score at time 3 seconds represents the average of a time window spanning 0-6 seconds. The colour bar and scale presented in (a) and (b) represent percentage change in the AUC score whereas the colour bar and scale presented in (c) and (d) represent p-values less than the alpha value of 0.05.

Such added benefits of EEG features on NIRS classification performance can be better understood when studying the EEG classification time course alone. Figure F4.5 highlights that across the group, statistically significant clusters above chance ($p<0.05$) can be found at mean time windows of 3.375-4.375 seconds after stimulus onset for the imagery paradigm and 3.375-3.625 seconds for the physical movement data transformed using CSP. In these statistically significant regions, the standard deviation across the group is tightened and peak AUC scores are 0.58 for execution+CSP, 0.66 for imagery+STFT and 0.68 for imagery+CSP. For imagined movements in the latter EEG time windows, the good separation of left- and right-hand conditions by the SVM classifier therefore drives an improvement in the AUC scores that is statistically significant when the EEG data is jointly classified with features derived from Δ[HbO] and Δ[HbR] (figures F4.4c and F4.4d).

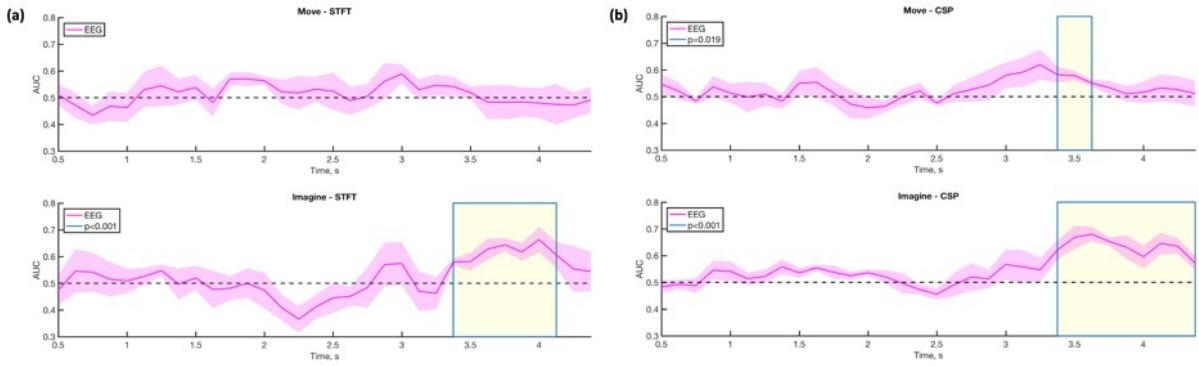

Figure F4.5: Group average classification scores for each EEG sliding time window. SVM classification was performed between left- and right-hand responses for both physical movement and imagery tasks independently. Specifically, differences were studied in the classification results of (a) short-time Fourier transformed (STFT) and (b) CSP-pre-processed EEG signals. AUC scores were computed from the classification of EEG features derived from alpha and beta frequency band filtered signals. The first score at time 0.5 seconds represents the average of a time window spanning 0-1 seconds. The light shaded time course represents the standard error in the AUC scores. Clusters of statistically significant time (window) points ($p<0.05$) are highlighted as blocked yellow regions. AUC scores in this command-following period were compared to those of chance (an AUC score of 0.5) in the statistical test.

Another important characteristic identified from the simultaneous EEG-fNIRS classification matrix (figure F4.4) was that the EEG feature vectors primarily improved Δ[HbO] and Δ[HbR] classification performance in the first two time windows spanning 0-6 and 1-7 seconds. By solely studying group Δ[HbO] and Δ[HbR] AUC scores (figure F4.6), this effect becomes clear as these portray that in the first two time windows classification scores ranged between 0.46 (non-CSP, imagery, Δ[HbR], mean time of 3 s) and 0.64 (CSP, execution, Δ[HbO], mean time of 4 s) whilst peak AUC scores ranged between 0.62 (imagery, Δ[HbO]) and 0.86 (execution, Δ[HbO]) as the haemodynamic response increased over time. Furthermore, for most haemodynamic group analyses in figure F4.6, the low scores of the early time windows were found to be statistically insignificant ($p>0.05$) from chance, except the CSP classified Δ[HbO] response to physical movement that yielded an AUC result of 0.64 at the 4 s mean time point.

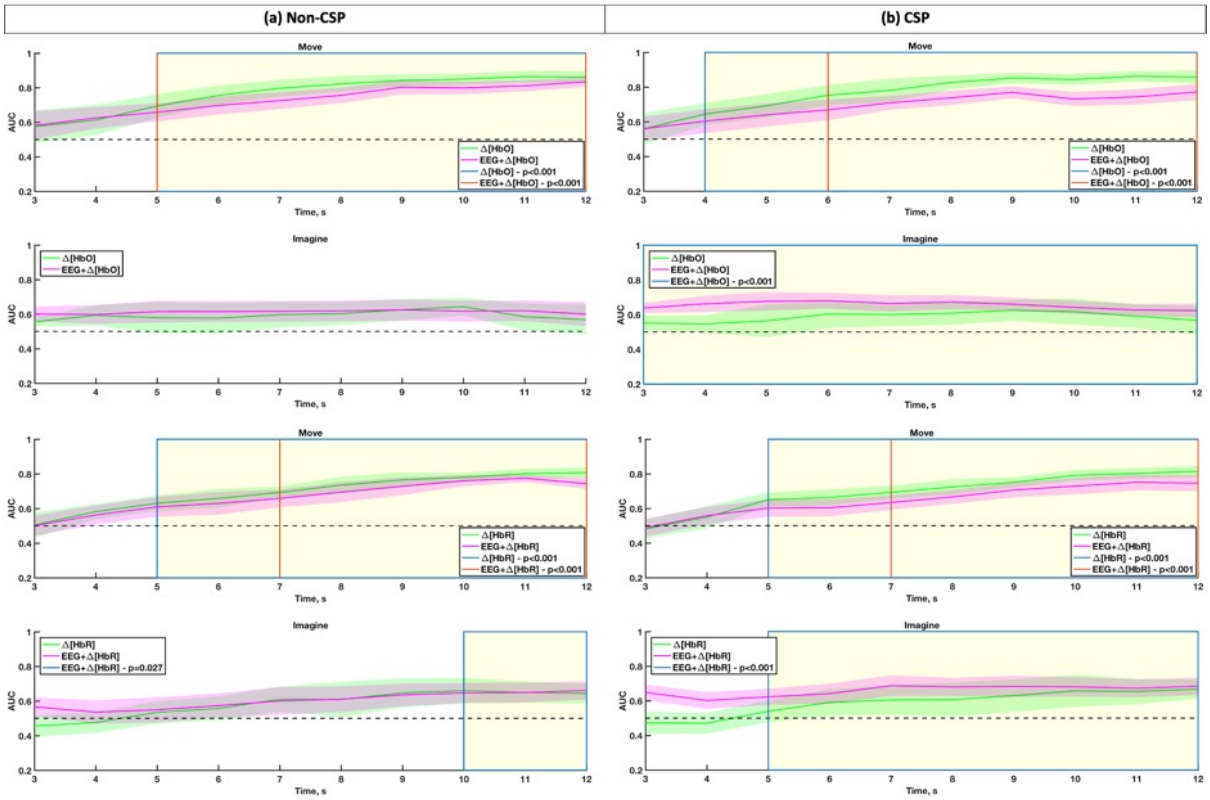

Figure F4.6: Group average classification scores for each NIRS sliding time window. SVM classification was performed between left- and right-hand responses for both physical movement and imagery tasks independently. Specifically, differences were studied in the classification results of (a) non-CSP and (b) CSP-pre-processed Δ[HbO], Δ[HbR] and EEG signals. AUC scores were computed from the classification of Δ[HbO] and Δ[HbR] statistical features. Additionally, presented above are the scores from the joint classification of Δ[HbO]/Δ[HbR] statistical features alongside EEG frequency-band-derived features. Here the EEG features for each participant were derived from an optimal sliding window that was computed using the method described in section 4.2.3. The first score at time 3 seconds represents the average of a time window spanning 0-6 seconds. The light shaded time course represents the standard error in the AUC scores. Clusters of statistically significant time (window) points ($p<0.05$) are highlighted as blocked yellow regions. AUC scores in this command-following period were compared to those of chance (an AUC score of 0.5) in the statistical test.

Figure F4.6 additionally highlights group AUC performance having used both EEG and fNIRS features for classification. Unlike the matrix in figure F4.4, here EEG features for each participant were obtained from the most optimal EEG time window (see section 4.2.3. for further details). Interestingly, the plots highlight that CSP filtering, in comparison to no CSP transformation, marginally improves

classification performance, evident by the fact that, for EEG+Δ[HbO] motor imagery classification, statistical significance ($p<0.05$) was found for the entire mean time series. Furthermore, for CSP filtered data, simultaneous EEG-fNIRS, in contrast to NIRS alone classification, improves AUC scores for the imagery data by approximately 15% (EEG+Δ[HbR]) however decreases accuracy by approximately 13% (EEG+Δ[HbO]) for physical movement data. This decrease is likely due to the low classification performance of EEG execution data thus negatively impacting the feature plane that would otherwise be derived using only NIRS-based statistical features.

Table T4.1: Peak classification AUC scores for each participant for the physical movement task. Individual and average results are presented following classification of features derived from EEG and haemodynamic signals independently and simultaneously. These features were extracted using a methodology that either excluded or included CSP-pre-processing. The p-values on the bottom row of the table represent the results of a one-tailed Student's t-test ($p<0.05$) between the peak scores of the two feature selection methods.

Peak AUC score during physical movement					
Non-CSP					
Participant	**EEG**	**Δ[HbO]**	**Δ[HbR]**	**EEG+Δ[HbO]**	**EEG+Δ[HbR]**
1	0.76*	0.84*	0.82*	0.81*	0.87*
2	0.71	0.90*	0.72*	0.90*	0.75*
3	0.76*	0.82*	0.78*	0.79*	0.74*
4	0.62	0.96*	0.90*	0.92*	0.88*
5	0.81*	0.90*	0.86*	0.85*	0.77*
Average	**0.73**	**0.88**	**0.82**	**0.85**	**0.80**
CSP					
Participant	**EEG**	**Δ[HbO]**	**Δ[HbR]**	**EEG+Δ[HbO]**	**EEG+Δ[HbR]**
1	0.66	0.85*	0.81*	0.75*	0.76*
2	0.63	0.90*	0.74	0.88*	0.70*
3	0.63	0.84*	0.80*	0.77*	0.78*
4	0.65	0.96*	0.92*	0.87*	0.92*
5	0.83*	0.89*	0.85*	0.81*	0.78*
Average	**0.68**	**0.89**	**0.82**	**0.82**	**0.79**
p	**>0.05**	**>0.05**	**>0.05**	**0.008**	**>0.05**

* indicates a significant AUC score ($p<0.05$) established from an empirical null distribution of classification accuracies (AUC scores) derived from random observations (i.e. shuffled class labels).

In addition to group analyses, statistical analyses were also performed at the subject-level by randomising individual trials corresponding to the two opposing hand conditions. Peak AUC score for each participant along with those participants that displayed significant clusters are reflected in Table T4.1 for physical movement and Table T4.2 for imagery. For executed movements, nearly all participants (except CSP-filtered, Δ[HbR], participant 2) were found to have at least one statistically significant cluster when classification was performed using only haemodynamic responses or simultaneous EEG-fNIRS features. In contrast, whilst 60% of participants were found to have a significant EEG cluster using a non-CSP method, this reduced to a single participant when CSP was used. Furthermore, EEG classification yielded an average peak AUC score below 75%, whereas NIRS alone and joint EEG+NIRS yielded an average peak AUC score above this value. It is likely that the high peak AUC scores for simultaneous EEG+NIRS classification is primarily driven by the separation of Δ[HbO] and Δ[HbR] statistical features. For most measures, both CSP and non-CSP methods yielded peak AUC scores that were similar or equal. However, for EEG and EEG+Δ[HbO] classification, non-CSP methods performed better with that of joint classification being found to be significant ($p<0.05$).

Table T4.2: Peak classification AUC scores for each participant for the imagery task. See table T4.1 for further details.

Peak AUC score during imagery					
Non-CSP					
Participant	**EEG**	**Δ[HbO]**	**Δ[HbR]**	**EEG+Δ[HbO]**	**EEG+Δ[HbR]**
1	0.65	0.64	0.51	0.64	0.58
2	0.80*	0.76*	0.87*	0.74*	0.83*
3	0.68	0.71*	0.70*	0.65	0.62
4	0.78*	0.75*	0.78*	0.79*	0.81*
5	0.71	0.56	0.57	0.51	0.56
Average	**0.72**	**0.68**	**0.69**	**0.67**	**0.68**
CSP					
Participant	**EEG**	**Δ[HbO]**	**Δ[HbR]**	**EEG+Δ[HbO]**	**EEG+Δ[HbR]**
1	0.70*	0.59	0.49	0.73*	0.59
2	0.83*	0.74*	0.87*	0.82*	0.82*
3	0.68	0.71*	0.75*	0.63	0.69*
4	0.72*	0.75*	0.80*	0.78*	0.86*
5	0.70*	0.58	0.58	0.60	0.63
Average	**0.73**	**0.67**	**0.70**	**0.71**	**0.72**
p	**>0.05**	**>0.05**	**>0.05**	**>0.05**	**0.037**

* indicates a significant AUC score ($p<0.05$) established from an empirical null distribution of classification accuracies (AUC scores) derived from random observations (i.e. shuffled class labels).

In contrast to physical movement, classification of left- and right-hand imagined responses yielded similar average peak accuracies for all three classification methods, with those of EEG alone performing best. Furthermore, whilst CSP and non-CSP techniques generated similar average peak scores for EEG alone and NIRS alone classification, CSP filtering however better aided EEG+Δ[HbO] and EEG+Δ[HbR] classification resulting in the latter to be statistically significant ($p<0.05$). Unlike executed movements, classification of imagined haemodynamic responses in the presence and absence of EEG yielded fewer peak AUC scores that were significant ($p<0.05$). However, when comparing CSP filtered EEG accuracies between physical movement and imagery tasks, there was a large improvement in the peak AUC scores of 80% of participants. Overall, the group classification results highlighted that, (1) hybrid physical and imagined movement scores were worse off than those of NIRS and EEG alone

scores respectively, and (2) hybrid feature classification of imagined responses yielded better average scores than those of NIRS feature classification when applying a CSP transformation.

4.4. Discussion

Having previously demonstrated the effectiveness of unimodal EEG (chapter 2) and NIRS (chapter 3) for motor imagery detection and classification, this study aimed to demonstrate the added benefits of a hybrid approach (simultaneous EEG-fNIRS) on the classification of right- and left-hand executed and imagined movements. The results identified that the combination of EEG and NIRS features compensated the low performing time windows of each device. Specifically, bilateral EEG responses at C3' and C4' improved NIRS data classification in the early time windows where a limited separable NIRS response was observed between the two hand actions. The addition of CSP pre-processing primarily aided the classification of imagined responses, whereas a non-CSP method was better for physically executed actions. For the former, this only resulted in average peak accuracies for the hybrid approach (EEG+Δ[HbO] and EEG+Δ[HbR]) being greater than the unimodal NIRS approach (Δ[HbO] and Δ[HbR]), whereas for the latter, hybrid peak classification results were only better than EEG peak classification scores.

In this study a bipolar re-referencing scheme was applied to the EEG measurements in the data pre-processing stage. For portable BCI applications, bipolar recording a few electrodes positioned around the task-relevant sensorimotor areas are recommended as they reduce the need for a multi-channel electrode setup (Leeb et al., 2007; Lou et al., 2008). Furthermore, as bipolar recordings derive potential differences between two monopolar electrodes, this can improve the signal-to-noise ratio (SNR) by eliminating shared artifacts of both electrodes (Leeb et al., 2007; Lou et al., 2008). As such, bipolar recording can be considered as the simplest form of a spatial filter. The first use of a bipolar montage setup for hand motor imagery classification was presented by Pfurtscheller and colleagues (Pfurtscheller et al., 1997). Six electrodes attached at a distance of 2.5 cm anterior to and posterior to C3, C4 and Cz were used to form the three bipolar channels. Three participants that were asked to imagine moving their left- or right-hand presented different ERD/ERS time courses. Whilst one

displayed a contralateral transient desynchronisation for both mu and beta rhythms, another showed a bilateral desynchronisation in the alpha band but an ERD followed by ERS in the beta band. Having provided feedback to these three participants, classification accuracy scores ranged between 68-92%.

A later study by Ramoser and colleagues compared CSP-transformed spatial patterns and classification scores of differently referenced EEG data following left and right imagined hand movements (Ramoser et al., 2000). Across three participants the authors compared referential, bipolar, Laplacian and common average referencing methods. They observed that the spatial patterns for all referencing schemes were very similar with that of the Laplacian showing more distinct spatial differences. However, in terms of classification accuracy, the highest scoring reference methods for each of the three participants were a 56-channel referential (100%), 34-channel bipolar (93%) and 18-channel common average reference (91%) scheme. Interestingly, the authors noted that the patterns for left- and right-hand imagery were not centered exactly at C3 and C4 electrode positions. Instead as the electrode with the maximum discriminatory power was either anterior or posterior to these fundamental electrodes, this justified the need for multiple channels (over a two-channel montage) to improve classification accuracy. Similar findings and discussions to these arguments have also been presented in several other publications (Cruse et al., 2012; Guger et al., 2003; Kalcher et al., 1996; Lou et al., 2008; Pfurtscheller et al., 2006a; Yang et al., 2014; Yi et al., 2013).

Putting these arguments together explains the EEG time frequency course observed in this study. The group average neural response to both right- and left-hand physical/imagined movement was predominantly bilateral. Following presentation of the action instruction, the average immediate response in the alpha frequency band was a desynchronisation in energy that lasted approximately 1.5 seconds before recovering to baseline. Akin to an individual's profile shown by Pfurtscheller and colleagues (Pfurtscheller et al., 1997), in the current study separable energy distributions were likewise observed following these initial desynchronisations for right- and left-hand imagery. At C3' right-hand electrical responses were of lower energy to left-hand responses 3 seconds after the action cue whereas at C4' this profile was evident at the start of baseline recovery. In the beta frequency band similar profiles were also seen at specific time points after participants began performing the action. However, the lack of a prominent group beta ERD after the action cue in this study (which is commonly observed

during right- and left-hand movements (McFarland et al., 2000; Pfurtscheller et al., 1997)) can be largely attributed to the broad beta frequency window averaged for each individual. As shown by Pfurtscheller and colleagues, each of the three participants in their study displayed a strong contralateral ERD in a narrow beta window following the left-/right-hand motor imagery cue (e.g. 18-26 and 20-23 Hz) (Pfurtscheller et al., 1997). As such, harnessing these narrow windows within the current study for each participant would have perhaps revealed contralateral statistically significant differences between right- and left-hand movements (at the alpha value of 0.05). Another reason for the lack of a prominent group beta ERD is possibly due to differences in the shape and position of M1 for each individual with respect to their skull (Morash et al., 2008). Such differences would inherently change the relationship between scalp channel locations and M1 thereby limiting such a simple setup from effectively sampling motor activity. Given the broad activation field of the task (Dechent et al., 2004; Kim et al., 2018; Morash et al., 2008; Pfurtscheller and Neuper, 1997), it is possible that with a larger EEG array more separable hand responses could be detected around C3 and C4 electrode positions through greater sampling of the motor cortex (which includes the primary somatosensory cortex, primary motor cortex, supplementary motor area, premotor cortex and posterior parietal cortex).

Despite the suggestion for an increased number of electrodes to improve neural signal localisation and to better BCI development, this may not always be applicable in the instance of patient, infant and multi-modality brain recording. In this study, the size of the NIRS imaging pad eliminated the possibility of attaching electrodes directly over the left- (C3) and right- (C4) hand brain activation regions. Cruse and colleagues used a similar bipolar electrode montage to measure left- and right-hand movements in six healthy individuals and a single patient diagnosed with a Prolonged Disorder of Consciousness (PDOC) (Cruse et al., 2012). Of the six healthy participants, three displayed a bilateral time-frequency response to each hand movement, however, unlike these individuals, the patient presented only a significant ipsilateral response in the late beta frequency window. Using a short time Fourier transformation and sliding window approach, 7-30 Hz spectral responses were divided into four small frequency band features that could be used together to classify single action and rest activity trials. Using a naïve Bayes classifier, the authors presented accuracy scores between 61-80% across the healthy group, whereas for the patient, a maximum score of approximately 68% was achieved 1-1.5

seconds after the instruction when classifying left-hand to rest response trials. Using a similar methodology but classifying the features of two motor responses (rather than the features of one motor response to rest), the current study yielded peak EEG accuracy scores between 62-81% for execution and 65-80% for imagery. The closeness of these scores to those achieved by Cruse and colleagues (Cruse et al., 2012) extends their work by highlighting the potential of a two-class motor imagery paradigm as a means of BCI communication.

Having simultaneously recorded both electrical and haemodynamic brain responses, the joint classification of EEG and NIRS features resulted in group average classification scores upwards of 75% for physical movement and 60% for imagery. Interestingly however, when compared to the AUC scores obtained from NIRS data classification, the addition of EEG features generally gave rise to an AUC time course that was lower for physical movement but greater for imagery. This increase in imagery data classification performance was primarily driven by significant EEG accuracy scores three seconds after the action cue. In both the alpha and beta band filtered EEG response, this period was predominantly characterised by a slower contralateral recovery to baseline from the initial ERD following the stimulus. Furthermore, this improvement to NIRS data classification was observed in early time windows where changes in haemodynamic responses between tasks were relatively small and reflected characteristic under/over-shoots of the haemodynamic response function. A recent EEG+NIRS motor imagery study by Shin and colleagues similarly reflected hybrid classification scores in comparison to those achieved by each modality individually (Shin et al., 2017). In their study, a sparse EEG electrode and NIRS optode setup was used to record 29 participants performing left- and right-hand motor imagery by imagining opening and closing the corresponding hand as they grabbed a ball. EEG data were pre-processed into mu and beta frequency band content and these were spatially filtered using CSP. Using the first and last three CSP components yielded a maximum group average classification score of 66%. In contrast, Δ[HbO] and Δ[HbR] classification using mean and slope features resulted in maximum accuracy scores of 59% and 61% respectively. These scores are in line with the maximum group average scores obtained in this study, with a similar EEG maximum being obtained 3 seconds after presentation of the instruction. Interestingly, Shin and colleagues observed that joint classification using both EEG and NIRS features resulted in average maximum accuracy scores

increasing to 64% and 67% for EEG+Δ[HbO] and EEG+Δ[HbR] respectively. The improved classification scores obtained by the researchers using a hybrid feature set primarily mirrored the EEG accuracy time course. NIRS features whilst mildly augmenting EEG scores in the first 5 seconds after the action cue, prominently improved the accuracy of the latter time windows at which the delayed NIRS signal was fully developed. As a similar but opposing profile was likewise reflected in the current study, it is clear that a hybrid BCI has an overall benefit of improving classification of covert actions by compensating the inferior temporal/spatial responsiveness of NIRS/EEG.

Another aspect compared in this study was the classification results of a CSP inclusive and exclusive methodology. In the hybrid BCI model, overall it was observed that CSP transformation aided classification of left- and right-hand imagined actions, whereas diminished the subject maximum accuracy scores of physical movements. The effects of the CSP method on EEG and NIRS classification have previously been detailed in chapters 2 and 3 respectively. However, in contrast to the study in chapter 2 where the EEG electrode montage covered the entire head, here the bipolar layout eliminated a key function of the algorithm to reduce channel dimensionality and it simply purposed as a spatial filter. The effects of CSP in a few-channel BCI have been previously explored by Tam and colleagues and Górski (Górski, 2014; Tam et al., 2011). In the former study, a CSP-rank method was used to order 64 electrodes based on CSP filter coefficients following a motor imagery paradigm performed by five patients with a chronic stroke condition. Across subsequent recording sessions, the data from the first *N* channels (where *N* ranged between 2 to 50 electrodes as previously ranked) were CSP filtered and classified using SVM yielding an accuracy curve that began at 75% (for a two-electrode analysis) and plateaued slightly above 90% for an analysis that utilised between 8-38 electrodes. From their results it is clear that CSP does not require a large electrode setup to be effective (refer to the publication by Ge and colleagues however for a contradictory argument (Ge et al., 2014)), and can deliver accuracy scores significantly above chance for simple montages limiting the time spent in channel preparation or the cost of a BCI system (where more amplifiers are required). Nevertheless, such a publication is somewhat biased to its findings having obtained its accuracy scores for each set of electrodes using prior CSP-rank analysed whole head data on the same cohort.

However, a later study by Górski compared classification performances of left- and right-hand imagined actions in the presence and absence of CSP pre-processing (Górski, 2014). In a single participant, three bipolar EEG channels (C3, Cz and C4) were used to record the electrical activity during the task and classification accuracies were obtained using the data from one, two and three sets of electrodes. Using both C3 and C4 data for classification, a mean accuracy of 91% was achieved on the raw signal, which decreased to 87% when an additional CSP-transformation was applied. Having observed better classification results on raw signals, the author concluded by emphasizing the use of a multi-channel system when applying the CSP algorithm. However, the strength of this argument is limited given that the study was only performed on a single participant. With respect to the current study, whether application of CSP pre-processing can benefit classification performance requires a more large-scale experiment to be performed given that it only elevated the results of the imagery dataset. Nevertheless, like the results of Górski (Górski, 2014), the general closeness of the average maximum scores for CSP and non-CSP methods (despite there being significant differences for EEG+Δ[HbO] during physical movement and EEG+Δ[HbR] during imagery) suggests that a simple hybrid approach has significant information content to drive classification scores of either haemodynamic or electrical responses without the added processing provided by CSP. It can however be hypothesised that, where 4-8 bipolar EEG electrodes are used in combination with NIRS optodes for BCI development of a similar paradigm, the addition of CSP pre-processing may prove to better enhance hybrid classification performances as suggested by Ramoser and colleagues and Tam and colleagues (Ramoser et al., 2000; Tam et al., 2011).

Alternatively, a more computational approach for improving CSP-based classification of two-channel montages following left and right-hand imagery trials was presented by Coyle and colleagues (Coyle, 2009; Coyle et al., 2008). In their study the authors highlighted that a joint neural-time-series-prediction-preprocessing and CSP (2-components) classification approach using an SVM classifier yielded significantly higher accuracies in comparison to a classification approach that only included CSP (2-components) (Coyle et al., 2008). Their results from a two-channel montage (one channel adjacent to C3 and another adjacent to C4) were comparable to the accuracies obtained following classification of three CSP components from a sixty-channel montage in the absence of neural-time-

series-prediction-preprocessing. The neural-time-series-prediction-preprocessing method maps and filters the original time series into a higher dimensional space using prediction/regression models (Coyle, 2009; Coyle et al., 2005b, 2006, 2008). In the two-channel montage case, this mapping results in a higher number of signals from which extracted features are more separable with respect to intra-class variance. As such, the additional CSP filtering is more effective at maximising differences in variance between classes as a lower data dimensionality can be reached. Such an approach may therefore facilitate motor imagery BCI in patients where extensive brain damage hinders the possibility of greater electrode scalp coverage (i.e. greater than eight electrodes) or where the signal-to-noise ratio of several recording channels is extremely low thereby limiting the analysis to be performed on as few as two recording channels.

The present discussion has so far largely been biased towards hybrid features facilitating the classification of unimodal EEG/NIRS features in the regions where the temporal/spatial responsiveness was low. By this notion however, it is acknowledged that average peak hybrid scores were worse off than those of NIRS and EEG alone for physical movement and imagery respectively in the CSP inclusive case. Although this may indicate that hybrid (in comparison to unimodal) feature classification is less successful than first thought, this effect is likely due to the low number of participants that took part in this study, the compactness of the current montage used, and the simplicity of the hybrid classification approach utilised for this study. Several publications have previously addressed hybrid EEG-NIRS classification of motor imagery tasks using either shrinkage classifiers (Blokland et al., 2014), meta-classifiers (Fazli et al., 2012), or both (Kwon et al., 2020; Shin et al., 2017, 2018). Shrinkage regularised classifiers effectively mitigate the negative effects (reduced predictive power of a model) of using high-dimensional feature vectors (i.e. they improve the estimation of covariance matrices when the trials-to-features ratio is low) and can be used in addition to CSP pre-processing. The shrinkage regularised linear discriminant analysis (LDA) classifier has been compared with other LDA variants and SVM classification by Bauernfeind and colleagues (Bauernfeind et al., 2014). Eight participants performed 18-24 trials of mental arithmetic during which haemodynamic responses (Δ[HbO] and Δ[HbR]) were measured using fNIRS. The authors identified that classification between mental arithmetic and rest Δ[HbO] responses using shrinkage regularised LDA yielded accuracies

significantly different from LDA with no regularisation (shrinkage regularised LDA: 86.3%, LDA with no regularisation: 69.2%), yet not statistically different from linear SVM (86.6%). The lack of a significant difference between shrinkage regularised LDA and linear SVM accuracies has likewise been found by another publication where the paradigm involved mental arithmetic (Shin et al., 2016). Whilst this may suggest that linear SVM (as used in the current study), like shrinkage regularised LDA, is able to deal with a low trial-to-feature ratio, these classifiers need to be compared on motor task data in order for a general statement on classifier suitability to be made. In comparison to shrinkage classifiers, meta-classifiers classify a stack of trained weak learner models, i.e. predictions of multiple classifiers are used as new features to train a meta-classifier. Using a meta-classifier to classify EEG, Δ[HbO] and Δ[HbR] trained models, Fazli and colleagues demonstrated that hybrid classification of left- and right-hand imagined actions yielded better average accuracy scores than either unimodal analysis (Fazli et al., 2012). Based on the successes of these publications it is clear that the future of covert command-following BCI will benefit from hybrid measurements.

The lack of a clear positive improvement of hybrid classification is one limitation of the current study. Other limitations include the low chance level used to determine statistically significant AUC scores and the absence of any electromyography (EMG) measurements. Like in previous studies (chapters 2 and 3), the chance level used in the current study for group-level statistical analysis of classification scores was 50% (i.e. an AUC score of 0.5). However, the theoretical chance level (as calculated using the Matlab function '*binoinv.m*', see Chapter 2.4) for the number of trials used for physical movement/imagery tasks and an alpha value of 0.05 was 62%. It would therefore appear that for the motor imagery task, time windows which gave rise to significant group AUC scores for hybrid classification at the 0.50 chance level would no longer be significant at the 0.62 theoretical chance level due to group average accuracies ranging close to this value between 0.62-0.69 (figure F4.6). Such low group average performances were predominantly driven by a subset of participants (1, 3 and 5 in table T4.2) that generally had peak classification scores below 70% for the motor imagery task. The use of the theoretical chance level is therefore recommended in order to confirm many of these assumptions and to accurately determine a classifier's performance.

Surface EMG like EEG is a non-invasive technique that can measure electrical currents generated by muscle fibres prior to the production of a muscle force using electrodes that are placed on the surface of the skin (Drost et al., 2006). Guillot and colleagues have shown motor imagery to initiate small muscular contractions that can be detected by surface EMG (Guillot et al., 2007). Thirty healthy participants performed motor imagery and actual movements of lifting a dumbbell with surface EMG electrodes placed on the right biceps and triceps. The authors identified that the changes in the EMG pattern recorded during motor imagery mirrored the pattern recorded during physical movement. However, the magnitude of the muscular activity observed during motor imagery was a fraction of that observed during physical movement. Nevertheless, the EMG activity pattern recorded during motor imagery was significantly greater than that during rest with goniometric data revealing no such physical movements. Such muscle activity during motor imagery is thought to be a result of an incomplete inhibition of motor output which involves the cerebellum (Bonnet et al., 1997; Lotze et al., 1999). The addition of surface EMG would therefore benefit a simultaneous EEG-fNIRS setup as it would allow confirmation that the regions of the body involved in the task were not moved during a motor imagery cue and that a kinaesthetic motor imagery was indeed performed.

4.4.1. Summary

This study has partially proved simultaneous EEG-fNIRS to enhance motor execution and imagery detection in healthy individuals. fNIRS measurements highlighted clear contralateral changes in the haemodynamic response from baseline following right- and left-hand physical and imagined movement cues. This signified potential command following even though clear contralateral ERDs were not present in the EEG signal. Nevertheless, joint classification of these signals identified NIRS-derived features to aid EEG signal classification only, resulting in accuracy scores that were greater than the scores obtained following NIRS signal classification alone. In addition, the few EEG bipolar channel approach combined with CSP pre-processing only aided classification of motor imagery left- and right-hand responses and not physical movement responses of the hand. This is likely due to limitations of the current setup which prevented the CSP algorithm from filtering the data into lower

channel dimensions that contained condition specific variances. It is therefore possible that with advanced data processing (e.g. joint neural-time-series-prediction-preprocessing and CSP pre-processing) and classification (e.g. meta-classifiers) methods, simultaneous EEG and FD-fNIRS could better classify motor imagery responses beyond that achieved using EEG and continuous-wave fNIRS hybrid systems.

Chapter 5

Conclusions

5.1. Contributions of chapters

Improving diagnostic accuracy and establishing a means of communication between clinicians and patients has been a significant goal of the field of Prolonged Disorders of Consciousness (PDOC) over the last two decades. A fundamental aim of this thesis was therefore to contribute to this research effort by demonstrating the potential of simultaneous EEG-fNIRS and its scope for clinical utility in patients diagnosed with unresponsive wakefulness syndrome (UWS). Using this method, the chapters within this thesis specifically aimed to improve the accuracy of detecting covert command-following as a means of overcoming the need to observe physical behaviours, which in such patients can be both minimal and inconsistent. Relatively inexpensive and portable EEG and NIRS devices are widely used biomedical research tools aided additionally by the reduced costs in computation and the availability of free and user-friendly analysis software. However, the technology's underlying limitations (EEG: spatial resolution, fNIRS: temporal resolution) have resulted in the increased exploration of hybrid techniques in recent years. The breadth of this avenue and the drive to achieve clinical success has revealed several gaps within the literature requiring further examination.

Taking a bottom-up approach, both EEG and NIRS systems were re-evaluated using novel experimental paradigms and state-of-the-art technology prior to demonstrating the potential of a simultaneous EEG-fNIRS protocol in healthy participants. Across the three experimental studies different analysis techniques were implemented to showcase the varying results brought about by each method and thus its ultimate impact on brain computer interface (BCI) performance. Specifically examined were different EEG re-referencing methods (mean mastoids: chapter 2, current source density: chapter 2 and bipolar: chapter 4), spatial filtering approaches (current source density: chapter 2, and common spatial patterns: chapters 2 to 4); time-frequency signal analysis tools (wavelet

transform: chapter 2, Hilbert transform: chapters 2 and 4, and short time Fourier transform: chapter 4) and a widely used BCI channel reduction technique, common spatial patterns (CSP) (chapters 2 and 3).

5.1.1. Experiment 1 - Chapter 2

This first study explored the potential of goal-oriented tasks to guide covert command-following. Specifically, it was hypothesised that EEG sampled object-oriented motor imagery responses could yield better classification results than simple limb (non-object-based) motor imagery actions. Recent functional magnetic resonance imaging (fMRI) evidence indicates a higher level of brain activation when individuals are asked to perform a complex motor imagery task in the presence of a task-related object (Mizuguchi et al., 2013). This variant of motor imagery is known to produce long-lasting cortical reorganisation (Hubbard et al., 2009; Krebs et al., 2009) and is better for achieving higher EEG control accuracy when classifying non-goal- and goal-oriented imagery movements (Yong and Menon, 2015). Furthermore, as the performance of covert command-following varies across participants and is dependent on their mental imagery ability, such object-oriented motor imagery paradigms have shown to capture the attention of the participant better (Li et al., 2015; Perry et al., 2011).

EEG measured responses to ‘cup’ and ‘comb’ imagined movements generated a beta frequency-band topography representing predominant event-related desynchronisation (ERDs) over the contralateral centro-parietal brain regions. Furthermore, these profiles were in line with those generated following non-object-oriented hand imagery and physical hand movements. Unlike physical movement responses however, imagined movement topographies were of a lower power and more wide spread across the supplementary motor and premotor areas. Having experimented with different filters and frequency envelope extraction tools, it was generally observed that both the Morlet-wavelet and Hilbert methods yielded similar topographic results owing to their mathematical equivalence (Bruns, 2004). An addition to the EEG data pre-processing pipeline was to spatially filter the signals. The choice of spatial filter is highly dependent on the electrode montage and if applied correctly can improve the signal-to-noise ratio (SNR) at each electrode. EEGs are measured by calculating the difference in

electrical potentials between a reference electrode and recording electrodes. As these reference sites can have varying electrical potentials (Junghöfer et al., 1999), spatial filters can correct any skewed characteristics. The Laplacian spatial filter has been shown in the literature to outperform other spatial filtering techniques such as common average referencing (Syam et al., 2017). Application of this filter on the 64 EEG channel dataset improved the localisation of right-hand and toe activation around the C3 and Cz/CPz electrode locations respectively. As a reference free method that estimates current flow through the scalp surface, it effectively filtered shallow broadband volume conduction noises to localise electrode specific brain activity (Yao et al., 2019).

Classification of right-hand versus toes and cup versus comb responses were performed on CSP filtered data. The CSP algorithm is a spatial filtering and channel reduction technique commonly applied in EEG BCI research (Alotaiby et al., 2015; Padfield et al., 2019). The basis of this algorithm is to linearly project multi-channel data into a lower-dimensional spatial subspace that maximises the variances of two-class conditions (Wang et al., 2005). To focus the algorithm to maximise spatial variances within task-related brain regions, the computation was applied on a subset of scalp electrodes as frequently conducted in the literature (Wang et al., 2004). It was found that a subset of 35 pre-processed EEG channels centered around the centro-frontal and centro-parietal regions could be reduced to just two components that maximally separated the variances of the two conditions in each of the three tasks (physically executed, non-object-oriented imagined and object-oriented imagined movements). Classification of traditional (hand vs. toes) and object-oriented (cup vs. comb) imagery tasks using data from these two filter components revealed improved accuracy scores for the former. With respect to this chapter's hypothesis, no further motor imagery classification improvements were found with the addition of an object. Previous research has equally reported low success rates when classifying multiple object-oriented imagery responses, highlighting the difficulty in discriminating motor imagery of different movements within the same limb (Zhang et al., 2017b). Nevertheless, Zhang and colleagues concluded that sufficient EEG control accuracy could be achieved by training a classifier on simple one-joint imagined movements (e.g. "imagine opening and closing a drawer with the dominant hand") and then testing multiple goal-oriented motor imagery tasks which require multi-joint synergy and trajectory planning (e.g. "imagine cutting a pizza with a pizza cutter with the dominant

hand") (Zhang et al., 2017b). A fundamental limitation of this chapters objected-oriented task was the lack of detail provided within the instructions for comb imagery. Whereas Zhang and colleagues instructed their participants to "imagine combing hair with the dominant hand", the current instructions to participants were to simply to imagine "combing" when presented with the comb cue. The ambiguity associated with this instruction would have increased the complexity of the task in a population that was provided with no feedback or lacked prior mental imagery training. This was evident in the alpha frequency-band topographies that were far different from those of simple hand imagery and cup imagery and those presented by Zhang and colleagues. Despite this, a goal-based motor imagery paradigm utilising objects activating different limbs or joints (such as a cup for "drinking" and a ball for "kicking into a goal") has the potential to improve a patient's mental imagery ability and attentional focus, and the clinician's ability to conclude the true presence or absence of command following or initialise a means of 'yes' and 'no' based communication.

5.1.2. Experiment 2 - Chapter 3

A novelty of the NIRS research within this thesis was the use of a frequency-domain (FD) imaging system. Currently, very few researchers performing NIRS motor imagery studies make use of such a device (Chiarelli et al., 2018; Khan et al., 2018; Koo et al., 2015). The majority present findings from relatively simpler continuous-wave technology (Rupawala et al., 2018) that lacks the spatial resolution and penetration depth that can otherwise be achieved with advanced frequency- and time-domain fNIRS systems. Unfortunately, those studies utilising a FD-fNIRS system in the field fail to evaluate the phase component (known to sample deeper tissues and to be less sensitive to superficial contamination (Doulgerakis et al., 2019b, 2019a)), either due to a reduced understanding of the parameter, or a lack of standardisation in the NIRS research community for reconstructing haemodynamic concentration changes from raw measurements. Nevertheless, chapter 3 was specifically designed to interrogate each component of the system and evaluate the device's overall utility for motor imagery detection. It was hypothesised that the additional phase component would more sensitively sample the underlying brain tissue, thereby enhancing the classification of multiple

motor imagery actions in comparison to intensity measurements alone. During the data quality analysis, the Fourier spectrum of phase-shift measurements from individual participants highlighted this component to have increasing sensitivity for the frequency of the stimulus and less to superficial physiological noises. This was highlighted by an increasing power to the stimulus frequency at longer separation channels (between 25-45 mm), and significantly diminished power responses to physiological signals at all separation channels. These results were in-line with previously published results (Doulgerakis et al., 2019b, 2019a). At these longer separation channels, both log-intensity and phase-shift components demonstrated contralateral activity on average for physical/imagined left- and right-hand movements. Such contralateral responses were however much greater and statistically significant with the 830 nm source. Similar strong contralateral effects were observed when comparing left- and right-hand changes in the concentration of oxy- (Δ[HbO]) and deoxy- (Δ[HbR]) haemoglobin signals. Reconstruction of these biological chromophores using FD (log-intensity and phase-shift) measurements improved signal contrast over reconstructions using continuous-wave-like (CWL) (log-intensity) data. It is therefore clear that phase measurements should be studied where available and where the data is of sufficient good quality. This is because the parameter's high sensitivity to cortical tissue sampling (increased depth penetration) can enable differences between motor imagery responses to be better observed in the absence of superficial noise contamination. However, at longer source-detector separations (up to approximately 50 mm (Doulgerakis et al., 2019a)), a reduction in the phase shift profile may suggest the need for increasing the systems modulation frequency in order to improve the SNR.

Classification of FD data overall yielded greater accuracies than classification of CWL data. In chapter 3.3.3 it was demonstrated that higher group area-under-the-curve (AUC) scores were achieved when classifying both raw (830 nm) and haemodynamic (Δ[HbO]) signals in the presence of phase information. Physically executed and imagined hand stimuli classification scores using raw measurements were however only slightly better than haemodynamic responses due to the addition of a second feature vector. The added impact of reconstructing and classifying FD-derived haemodynamic components (in comparison to raw signal classification) was later shown in chapter 3.3.4 in a subset of participants with relatively good SNR. For these participants, the improved Δ[HbO]/Δ[HbR] contrast

between the two hand cues outweighed the loss of a second feature vector and as such resulted in higher group AUC scores over a longer duration for both physical movement and imagery tasks.

Like the EEG study (chapter 2), the impact of the CSP algorithm on NIRS data classification performance was also investigated. Only one publication to date has applied this signal spatial filtering and channel dimensionality reduction technique to fNIRS measurements (Zhang et al., 2017a). Application of this algorithm on multi-channel 830 nm FD measurements and two-channel Δ[HbO] profiles (chapter 3.3) resulted in average classification accuracies of 79% (82%) and 72% (72%) respectively for the physical movement (imagined movement) task. Although in this chapter the haemodynamic classification scores for the motor imagery task were slightly lower than the accuracies achieved by Zhang and colleagues, the results obtained following physical left- and right-hand movement classification were found to be significantly greater (Zhang et al., 2017a). The CSP algorithm was an effective tool for pre-processing multi-channel FD signals because a dimensionality lower than the measured six-channel data space could be achieved that better explained task-specific effects and additionally prevented classifier overfitting (Zhang et al., 2017a). By additionally investigating the effects of the CSP algorithm on two-channel Δ[HbO] signals, it was identified that this spatial filtering tool did not yield any significant improvement in classification performance. Potential reasons for this include not being able to extract a lower dimensional filter space that can maximise task differences, or not computing the variance statistical feature from CSP filter results as suggested by Zhang and colleagues (Zhang et al., 2017a). Alternatively, during the construction of two-channel Δ[HbO] profiles, the inverse model itself maximises multi-channel spatial effects each time the system is perturbed and an update for the change in the absorption coefficient is computed, resulting in little or no added effect of the CSP algorithm. Nevertheless, as the algorithm did not negatively impact the classification results of this few-channel dataset, it can be suggested that even where a lower dimensional space cannot be found, the CSP calculation can potentially be a good NIRS pre-processing step for BCI development with a minimal computation cost. With respect to the hypothesis for this chapter, the results presented have demonstrated that the phase parameter is a fundamental component for aiding classification of motor imagery signals. Whether classifying raw or haemodynamic signals, phase data transforms either

the feature space or the reconstruction of the haemodynamic response in a manner that can benefit a classifier in separating two-class features.

5.1.3. Experiment 3 - Chapter 4

In the final study of this thesis, the methods of EEG (chapter 2) and NIRS (chapter 3) were extended to observe and classify motor imagery responses obtained using simultaneous EEG-fNIRS measurements. It was specifically hypothesised that the simultaneous recording of EEG and FD fNIRS signals could improve the classification of imagined actions beyond that achieved by a FD fNIRS system alone. In fitting with the overall thesis aim to develop a multi-modal imaging system for applicability within the clinic, electrical activity was measured using only a four-channel EEG setup (previously used in (Cruse et al., 2012)) that sampled the C3' and C4' regions. These few electrodes positioned around the task-relevant sensorimotor areas were bipolar re-referenced in order to improve the SNR by eliminating shared artifacts of two monopolar electrodes (Leeb et al., 2007; Lou et al., 2008; Yao et al., 2019). Immediately after the action cue, both left- and right-hand imagined movements generated a predominant EEG bilateral response in the alpha and beta frequency band envelopes. Nevertheless, contralateral effects were present on average across the group approximately 1500 ms onwards. These results were in-line with previous research (Cruse et al., 2012; Yang et al., 2014).

Joint classification of EEG and NIRS features compensated the low performing time windows of each device, thus improving single trial classification accuracies across the group. These findings were in agreement with previous research conducted by Shin and colleagues (Shin et al., 2017). Based on the concept of neurovascular coupling, the delayed haemodynamic response is secondary to the immediate electrical burst of activity that can be measured in the first few seconds following a stimulus using EEG (Huneau et al., 2015). As such, contralateral EEG responses between 1500-4000 ms primarily improved NIRS data classification in the early time windows (0-5000 ms), where a limited separable NIRS response was observed between the two tasks. With respect to this chapter's hypothesis, simultaneous EEG and FD-fNIRS measurements did further enhance NIRS motor imagery scores. Nevertheless, hybrid classification was neither better than EEG motor imagery scores nor NIRS

physical movement scores. One explanation for this can be related to the small study cohort of five participants on which these results were obtained. Given that others have reported increased classification success with this hybrid imaging method (Fazli et al., 2012), a larger scale study would confirm whether these additional findings were chance related or true effects of the current methodology. Another reason for this is possibly related to the sparseness of the EEG montage used and the effectiveness of CSP spatial filtering. In this bipolar channel setup, the CSP algorithm could not generate more than two spatial filter components and therefore could not project the data to a lower dimensional space that maximised class variances. Where a higher electrode montage is used, such as that in chapter 2, such dimensionality reduction and maximisation of class variances eliminates strong bilateral features inherently captured by poor spatial resolution EEG measurements. In the absence of this additional pre-processing, short-time Fourier transform filtered EEG signals were classified better for the physical movement task, however the CSP transformation provided minor improvements in the average peak AUC scores for the imagery task. To optimise hybrid classification, one could perhaps use more than two bipolar channels in order to better localise contralateral responses following CSP pre-processing. A final explanation for the findings of this study can be related to the high dimensionality of the classification feature space, given that the impact of multiple NIRS statistical features on classification performance was explored here in comparison to methodology used in chapter 3. Despite having increased the number of trials within the study, it is possible that classification of hybrid features (eight-dimensional feature space) would have yielded greater results with the inclusion of a shrinkage- (Shin et al., 2018) or meta-classifier (Fazli et al., 2012).

Overall these experimental chapters have formed the fundamental building blocks to guide future simultaneous EEG and FD-fNIRS research. As represented in chapter 4 and several referenced publications, hybrid technologies such as these can be a relatively inexpensive and portable means of examining the complete underlying pattern of brain activation in response to a task. With respect to covert command-following, the work presented within this thesis demonstrated that both electrical and haemodynamic signals complement each other to further improve the localisation and strength of a response due to the reduced sampling of noise (as provided by phase measurements). This inherently improved the BCI classification of imagined actions in the absence of any training or feedback.

Provided that a sufficient area of the scalp is sampled and an attention demanding paradigm is selected, simultaneous EEG and FD-fNIRS has much potential in the research community to be eventually extended into the clinic for either patient communication or bedside examination of awareness.

5.1.4. Limitations of experiments

Discussions across each of the three experimental chapters have nevertheless highlighted three fundamental limitations of the work presented within this thesis. These include, the chance level used for significance testing of classification accuracies, the lack of a testing set used to validate classification performance for an optimal data processing, feature extraction and classifier approach, and the absence of any electromyography (EMG) measurements.

Group-level significance testing of AUC scores was performed using a permutation approach where subject accuracies were randomly shuffled with a chance score of 0.5 (i.e. 50%). At this level, classification accuracies significantly different (in the statistical sense) from a theoretical chance level (based on the number of classes) were determined. Subject-level significance testing of AUC scores was likewise performed using a permutation approach however class labels were shuffled, and the classifier performance was re-estimated for each permutation. Statistical significance at this level was therefore established from an empirical null distribution of classification accuracies using an alpha value of 0.05. Permutation tests as used for subject-level statistical analyses provide a reliable and data-driven approach to estimating the significance boundary for classifier performance whilst not making any assumptions about the distribution of the data (Combrisson and Jerbi, 2015). However, the low number of permutations computed for the subject-level statistical analyses (200 permutations) highlight the computational burden of such a method. This cost increases further when there is a greater sample size and when a lower statistical significance level is required (Combrisson and Jerbi, 2015). In comparison to the permutation approach, the theoretical chance level used for the group-level analyses was suboptimal given that the 50% accuracy assumption (which is based on 2-class decoding) holds true only for infinite sample sizes. As discussed in chapter 2, for a 2-class paradigm, the chance level is 50% with a confidence interval that is dependent of the critical alpha value and the sample size

(Müller-Putz et al., 2008). By assuming that classifier prediction error is binomially distributed (Kohavi, 1995), the upper confidence interval can be derived from the binomial cumulative distribution function. For smaller sample sizes the derived chance level therefore dramatically increases in order to reflect how little such a limited number of trials reflect true randomness. Furthermore, it has been shown that the small sample size problem cannot be circumvented by changing classifiers or the number of cross-validation folds (Combrisson and Jerbi, 2015). In order to prevent erroneous interpretation of classification results, future statistical group analyses should therefore make use of the binomial formula to estimate chance level accuracies, as on reflection of the group-level accuracies presented in the three experimental chapters it would appear that many of the scores are non-significant at the derived chance level.

With respect to the second limitation, data within each of the studies was divided into a training and validation set on which *k*-fold cross-validation classification was performed. Such a division was used for all classification approaches examined with the accuracy scores reported reflecting the best possible outcome for the group. In the absence of an unseen (testing) dataset, the true generalisability of the optimally suggested classification approach could not be determined. This argument was presented in chapter 3 where an optimal fNIRS classification approach to left- and right-hand physical/imagined movements was suggested to include CSP-pre-processing of oxygenated haemoglobin responses (derived using amplitude-modulated intensity and phase measurements), extraction of the signal mean within an 8 second time window and linear SVM classification. Nevertheless, having identified an optimal method, a future large scale simultaneous EEG-fNIRS study could adopt these processes and parameters in order to gather the classification performances that would determine the effectiveness of such an approach for awareness detection and/or communication.

Despite having reported the best accuracies for simultaneous EEG-fNIRS classification of motor imagery signals (i.e. using a tuning dataset that underwent cross-validation classification), the group average accuracies remained below 75% suggesting that alternative data processing and classification approaches need to be investigated before the method can be claimed to be clinically viable. Indeed, whilst several motor imagery studies concluding clinical potential of their methods have reported classification accuracies upwards of 80% in healthy participants (Abdalmalak et al., 2020;

Fazli et al., 2012; Guger et al., 2017), others have reported average accuracies below this threshold (Blokland et al., 2014; Cruse et al., 2012). In particular Cruse and colleagues presented average accuracies following classification of right-/left-hand motor imagery and rest signals for a single patient in a vegetative state and six healthy controls to be below 70% (Cruse et al., 2012). The threshold for effective BCI communication and control is highly variable and dependent upon factors including the application. Furthermore, a direct comparison of final accuracies achieved across different studies is limited due to variability in the number of participants, number of trials, number of sessions, presence or absence of feedback/training, complexity of paradigm and differences in analysis and classification methods. Nevertheless, it has been evaluated that the majority of healthy participants (92 out of 99 participants in (Guger et al., 2003) and 19 out of 20 participants in (Ortner et al., 2015)) are able to control a two-class motor imagery BCI, achieving classification accuracies above 60% which has likewise been shown in our case. Interestingly, the majority of these BCI studies report final classification accuracies following multiple motor imagery sessions. Despite a multisession paradigm not being explored in this thesis, it is likely that data from the same experimental paradigm recorded on different days or at different times on the same day would exhibit some variation due to shifts in EEG/NIRS channel positions and changes in electrical impedances/detector signal gains which will alter how accurately (i.e. whether task specific brain regions are probed) and how sensitively (i.e. signal-to-noise ratio) cortical activity is sampled at the level of the scalp. In addition, the participants mental state, for example if they are stressed, may impact their ability to remain focussed on the task and generate specific mental events. Whilst commonly performed simple and complex (i.e. goal-oriented) motor imageries (e.g. hand/feet movements, tennis playing, spatial navigation) are known to map onto the same homuncular organisation in the sensorimotor network as the physical movement (Ehrsson et al., 2003; Stippich et al., 2002), the added workload of using motor imagery to communicate or to control an on-screen game can overwhelm naïve BCI study participants resulting in low classification performances (Guger et al., 2003). Nevertheless, it is more often the case that multiple sessions combined with feedback can improve motor imagery BCI performance as participants become more attentive to the task, show further interest and become skilled at adapting their mental performance (Bigirimana et al., 2020; Coyle et al., 2015; Guger et al., 2017). This together with EMG measurements

can indicate how reliable the final classification accuracy scores are because correctly performed motor imagery is known to initiate weak muscular activity patterns at the targeted limb that can be detected by surface EMG electrodes (Guillot et al., 2007).

Another reason for the need for multiple simultaneous EEG-fNIRS motor imagery sessions relates to the non-stationarity of EEG signals. The signals have task related information encoded in both the time and frequency domains. Planning and execution of kinaesthetic motor imagery results in changes in brain frequency rhythms over the motor cortex; specifically, in the mu and beta frequency bands the typical initial response is an event-related desynchronisation where there is a suppression in synchronisation of frequency rhythms (decrease in frequency band power) followed by an event-related synchronisation (increase in frequency band power) corresponding to the termination of the imagined movement (Pfurtscheller and Lopes da Silva, 1999; Rao and Scherer, 2010). Time-frequency domain analysis can capture sudden temporal variations with respect to each frequency component however these signals are known to fluctuate with mental states, such as when an individual is stressed, anxious or attentive (Shen and Lin, 2019), and with age (Matoušek et al., 1967). A paradigm that is repeatedly performed over multiple sessions would therefore allow for such oscillatory changes to be tracked and the BCI to be regularly updated thereby yielding a model that can more accurately detect (i.e. with a lower false positive rate) covert commanding-following which in turn can be used as a proxy for communication.

Taking into consideration each of these limitations would allow future work to better realise the true potential of the experiment and its effectiveness within the clinic. Indeed, the results and discussions presented within this thesis demonstrate that simultaneous EEG-fNIRS can be used to detect covert command-following using motor imagery in healthy individuals. With further research the improved technology and methodology shall ultimately prove to be sufficiently reliable for use in the bedside examination of awareness in patients with PDOC.

5.2. Clinical potential and future perspective

When considering the field of PDOC, EEG has a large and ever-growing community of researchers dedicated to studying and developing the technology for bedside applications in the clinic, whereas fNIRS can be considered to be in its infancy with only a few publications to date demonstrating the instrument's applicability in such patients (table T5.1). Nevertheless, the coupled advantages of the two devices and their complementing information content has sparked a new research avenue, specifically simultaneous or hybrid EEG-fNIRS, as a potential means to better assist clinicians in diagnosing and communicating with patients beyond the level of accuracy achieved using fMRI, MEG, EEG or fNIRS alone. The ongoing clinical challenge in the PDOC field is to quantitatively estimate a patient's brain state in order to more accurately detect awareness, if present, in those diagnosed with UWS. The hope from such dual imaging systems is therefore better diagnostic utility in probing brain activity to differentiate between unresponsive wakefulness and minimally conscious states. The major aim of this thesis was therefore to develop the simultaneous EEG-fNIRS technology in a manner that would assist future investigators to translate this research into the clinic and address these fundamental questions.

Table T5.1: Summary of the current literature using fNIRS in patients with PDOC or LiS.

Diagnosis	Number of patients	Overview of main results	References
PDOC	2 – MCS	● Functional activation (i.e. Δ[HbO] and Δ[HbR]) during passive and somatosensory stimulation. ● Weak brain activations during active hand opening and closing.	(Molteni et al., 2013)
PDOC	5 – UWS 11 – MCS	● Hemispheric differences during motor imagery of squeezing a ball with the right-hand. ● Patients in a minimally conscious state shared fNIRS profiles similar to healthy participants.	(Kempny et al., 2016)
PDOC	7 – UWS 2 – MCS	● In eight of the nine patients, spinal cord stimulation for 30 seconds induced sustained cerebral blood volume changes in the prefrontal cortex (an area important in the consciousness system; measured through an increase in total haemoglobin concentration). ● An inter-stimulus interval of two minutes significantly improved amplitudes of the total haemoglobin concentration across blocks.	(Zhang et al., 2018b)
LiS	40	● The intentions of 23 patients were successfully detected (80% correctly identified) by assigning different mental tasks to 'yes' and 'no' responses.	(Naito et al., 2007)
LiS	1	● The responses to open sentences were detected by instructing the patient to think 'yes' and 'no' to several questions. ● 72% of responses were correctly identified at the bedside.	(Gallegos-Ayala et al., 2014)
LiS	1	● Without any prior training, tennis playing motor imagery was used successfully by a patient as a proxy to communicate responses to three questions. ● Results were confirmed by the patient's residual eye-movement communication channel.	(Abdalmalak et al., 2017b)

PDOC: prolonged disorders of consciousness; LiS: locked in syndrome; UWS: unresponsive wakefulness syndrome; MCS: minimally conscious state

The research within this thesis serves much prospect for future clinical investigation provided that fundamental studies are conducted on healthy participants, such as demonstrating object-oriented imagery performance using a simultaneous EEG and FD-fNIRS setup. Whilst the EEG research presented in chapter 2 extended basic covert command-following studies to explore motor imagery

performance with the aid of an object, a substantial portion of this thesis was dedicated to probing a highly complex FD-fNIRS system for motor imagery detection alone and in combination with EEG. The novelty of this system was primarily the output of a phase component that has the potential to assist clinicians in detecting sufficiently sensitive task-relevant cortical activations in a single-subject by measuring physiological noise-free brain responses. Furthermore, in the face of BCI development, such dual instrumentation can also enable neural features of multiple tasks to be classified to a higher accuracy. When comparing the classification accuracies presented in this thesis by healthy participants following motor imagery movements with those yielded by patients with a PDOC (Coyle et al., 2015; Cruse et al., 2011), from a BCI standpoint it would be considered that several of these participants were unaware. On the contrary, these healthy participants were in fact aware, yet the current BCI model failed to dissociate their task responses to a significant degree above chance (where chance is 50% with an upper confidence limit) that would reflect their mental state. This was primarily due to a single session of motor imagery being performed in the absence of any feedback. As discussed in section 5.1.4, a single BCI session has limited scope in capturing variability within EEG rhythms particularly because the first motor imagery session is influenced by brain states corresponding to fatigue (depending on the time of day the study is performed), anxiety (having to perform a novel complex paradigm) and stress levels (external factors that may initiate mind wandering), which will inevitably vary on a day to day basis. It is therefore unlikely that a single session of covert command-following would be effective for confirming the brain state of a patient in a PDOC. However, the data from a single session of a few motor imagery trials was investigated here to demonstrate performances of an array of analysis and classification methods with discussions surrounding how these could translate to a patient population where each recording session could be of variable durations and spread across several months depending on the severity of the patient's injury. Whilst fundamental methods and results have been presented here, it is acknowledged that there remains significant work in terms of signal processing and analyses especially for those researchers and clinicians who are not experts in electrical and optical imaging.

According to a recent investigation by Pfeifer and colleagues, the lack of standardised signal processing methods or guidelines for fNIRS data is likely to cause novice users to employ data analysis

tools provided by commercial companies (i.e. a “black box”), which are unlikely to take into account the parameters of the study (Pfeifer et al., 2018) and may increase false positives or false negatives in the final published results (Tachtsidis and Scholkmann, 2016). Indeed, Pfeifer and colleagues demonstrated statistical discrepancies between a “black box” signal processing stream, and that of a relatively simple self-implemented signal processing stream that involved motion artifact removal and band-pass filtering of haemodynamic data (Pfeifer et al., 2018). With the increasingly widespread use of NIRS devices across biomedical research, the field will clearly benefit from standardisation, as adopted in much of fMRI (e.g. FMRIB Software Library; FSL and Statistical Parametric Mapping; SPM) (Caballero-Gaudes and Reynolds, 2017; Frackowiak et al., 2004; Fristen, 1997; Jenkinson et al., 2012; Smith et al., 2004; Strother, 2006) and EEG research (e.g. EEGLAB and FieldTrip) (Delorme and Makeig, 2004; Oostenveld et al., 2011). Nevertheless, there are increasing signs towards this given that, for example, the modified Beer Lambert's law is a widely accepted means for recovering haemodynamic parameters from continuous-wave data. This however results in research groups less frequently progressing to advanced systems (i.e. FD and time-domain NIRS) or opting to only investigate intensity outputs when imaging from FD devices. When using signal processing methods as provided by manufactures, it is however paramount that the research team have an advanced understanding of every step to ensure that the data and conclusions are valid, reliable and interpretable.

Another future consideration is the optimal number of EEG and NIRS channels during simultaneous EEG-fNIRS acquisition. A large number can in some cases be suboptimal due to an elevation in patient discomfort, increase in preparation time, added expenses of purchasing more amplifiers, reduced portability, high dimensionality of the data, and associated computational costs during classification. A high feature dimension space requires more trials and a longer time to train the classifier – first introduced by Bellman as the “curse of dimensionality” (Bellman, 1957). Furthermore, a large number of predictor variables may increase the complexity and instability of the classifier resulting in the overall degradation of classification accuracy scores. A benefit of high density EEG however is that whole head coverage allows the researcher to confirm the physiological plausibility of the spatial pattern maps associated with each task - i.e. is the activity restricted to electrodes over contralateral sensorimotor cortices for hand imagery? While focusing on a small area of the scalp is

beneficial from the perspectives of statistical multiple-comparisons, data dimensionality, and where a patient has sustained extensive brain damage, it is not possible to however ensure that the recorded electrical and haemodynamic changes are physiologically plausible, or whether they reflect a global amplification in neural activity and blood flow across the entire brain. Therefore, in order to balance these fundamental issues, future research could extend towards moderately increasing scalp coverage (beyond that presented in chapter 4) to better sample the underlying brain activity and in turn utilise spatial filters, such as the Laplacian, data pre-processing methods such as neural-time-series-prediction-preprocessing (Coyle et al., 2008) and dimensionality reduction techniques, such as common spatial patterns, to aid in the classification of the signals. Furthermore, with respect to hybrid data classification, promising methods for limiting the dimensionality of the feature space, in addition to the method depicted in chapter 4, include the use of shrinkage- (Shin et al., 2018) and meta-classifiers (Fazli et al., 2012).

One final future directive considers the applicability of patient training or feedback as part of the experimental protocol. Whilst motor or mental imagery is an effective noise-limiting tool for assessing command following, the absence of these fundamental elements can cause difficulties in ensuring that the individual remains engaged with the task and that novice imagers refrain from performing a third person covert response. Furthermore, given the need to perform tens of trials in order to accurately classify the responses, this can be an exhaustive repetitive task. The benefits of training and feedback on BCI performance have been widely explored in healthy individuals (Guger et al., 2003), with recent evidence of its effectiveness in patients diagnosed with MCS (Coyle et al., 2012, 2013, 2015; Dayan et al., 2019) and UWS (see chapter 1.2. for further details) (Dayan et al., 2019). Coyle and colleagues for example performed an EEG-based assessment of awareness in four patients with MSC and determined whether control of an EEG-based BCI could be improved with the addition of visual and/or auditory feedback during a motor imagery task (Coyle et al., 2015). The authors reported peak classification accuracies to be greater during feedback assessments (>70%) as patients realised they could modulate their brain activity and also appeared to be more attentive with the task. The authors also found patients to be more alert during audio than visual feedback assessments with the former increasing sensorimotor rhythm BCI control. Although this can be attributed to the large palette

of musical genres presented to the patients, auditory feedback is feasible for patients with UWS or MCS that have limited gaze control or visual acuity (Coyle et al., 2015; Giacino et al., 2004). Nevertheless, as such training and feedback can have limited scope in many of these patients, as an alternative this thesis took the approach of concretely improving both the analysis pipeline and technology to ensure that single subject responses are reliable from as few trials as possible. However, it is necessary to emphasise that where possible, for example if the patient is showing signs of compliance, training and feedback should be used to maximise the accuracy of the BCI system.

It is clear that for simultaneous EEG-fNIRS to realise its potential in PDOC assessment, research teams must incorporate multidisciplinary expertise in cognition, clinical practice, physical sciences, and computational sciences. With principled paradigms for diagnosing covert awareness in combination with state-of-the-art devices and algorithms for data processing, modelling, and feature extraction/classification, EEG-fNIRS has great potential to improve diagnostic accuracy in PDOC and enable patients to communicate their true mental state to the outside world.

References

Abdalmalak, A., Milej, D., Diop, M., Naci, L., Owen, A. M., and Lawrence, K. St. (2016). Assessing the feasibility of time-resolved fNIRS to detect brain activity during motor imagery. in *Proc. SPIE 9690, Clinical and Translational Neurophotonics; Neural Imaging and Sensing; and Optogenetics and Optical Manipulation*, 969002. doi:10.1117/12.2209587.

Abdalmalak, A., Milej, D., Diop, M., Shokouhi, M., Naci, L., Owen, A. M., et al. (2017a). Can time-resolved NIRS provide the sensitivity to detect brain activity during motor imagery consistently? *Biomed. Opt. Express* 8, 2162–2172. doi:10.1364/BOE.8.002162.

Abdalmalak, A., Milej, D., Norton, L., Debicki, D. B., Gofton, T., Diop, M., et al. (2017b). Single-session communication with a locked-in patient by functional near-infrared spectroscopy. *Neurophotonics* 4, 40501. doi:10.1117/1.NPh.4.4.040501.

Abdalmalak, A., Milej, D., Yip, L. C. M., Khan, A. R., Diop, M., Owen, A. M., et al. (2020). Assessing Time-Resolved fNIRS for Brain-Computer Interface Applications of Mental Communication. *Front. Neurosci.* 14, 105. doi:10.3389/fnins.2020.00105.

Acqualagna, L., Botrel, L., Vidaurre, C., Kübler, A., and Blankertz, B. (2016). Large-Scale Assessment of a Fully Automatic Co-Adaptive Motor Imagery-Based Brain Computer Interface. *PLoS One* 11, e0148886. doi:10.1371/journal.pone.0148886.

Addis, D. R., Wong, A. T., and Schacter, D. L. (2007). Remembering the past and imagining the future: Common and distinct neural substrates during event construction and elaboration. *Neuropsychologia* 45, 1363–1377. doi:10.1016/j.neuropsychologia.2006.10.016.

Akselrod, M., Martuzzi, R., Serino, A., van der Zwaag, W., Gassert, R., and Blanke, O. (2017). Anatomical and functional properties of the foot and leg representation in areas 3b, 1 and 2 of primary somatosensory cortex in humans: A 7T fMRI study. *Neuroimage* 159, 473–487. doi:10.1016/j.neuroimage.2017.06.021.

Allami, N., Paulignan, Y., Brovelli, A., and Boussaoud, D. (2008). Visuo-motor learning with combination of different rates of motor imagery and physical practice. *Exp. Brain Res.* 184,

105–113. doi:10.1007/s00221-007-1086-x.

Allen, D. P., and MacKinnon, C. D. (2010). Time-frequency analysis of movement-related spectral power in EEG during repetitive movements: A comparison of methods. *J. Neurosci. Methods* 186, 107–115. doi:10.1016/j.jneumeth.2009.10.022.

Alotaiby, T., El-Samie, F. E. A., Alshebeili, S. A., and Ahmad, I. (2015). A review of channel selection algorithms for EEG signal processing. *EURASIP J. Adv. Signal Process.* 2015, 66. doi:10.1186/s13634-015-0251-9.

Ang, K. K., Chin, Z. Y., Zhang, H., and Guan, C. (2008). Filter Bank Common Spatial Pattern (FBCSP) in brain-computer interface. in *2008 IEEE International Joint Conference on Neural Networks (IEEE World Congress on Computational Intelligence)*, 2390–2397. doi:10.1109/IJCNN.2008.4634130.

Aronson, R. (1995). Boundary conditions for diffusion of light. *J. Opt. Soc. Am. A* 12, 2532. doi:10.1364/josaa.12.002532.

Arridge, S. R. (1999). Optical tomography in medical imaging. *Inverse Probl.* 15, R41–R93. doi:10.1088/0266-5611/15/2/022.

Arridge, S. R., Cope, M., and Delpy, D. T. (1992). The theoretical basis for the determination of optical pathlengths in tissue: temporal and frequency analysis. *Phys. Med. Biol.* 37, 1531–1560.

Arridge, S., and Schotland, J. (2009). Optical tomography: forward and inverse problems. *Inverse Probl.* 25, 123010.

Asensio-Cubero, J., Palaniappan, R., and Gan, J. (2011). A study on temporal segmentation strategies for extracting common spatial patterns for brain computer interfacing. in *Proceedings of the 11th UK Workshop on Computational Intelligence*, 98–102.

Babiloni, C., Sarà, M., Vecchio, F., Pistoia, F., Sebastiano, F., Onorati, P., et al. (2009). Cortical sources of resting-state alpha rhythms are abnormal in persistent vegetative state patients. *Clin. Neurophysiol.* 120, 719–729. doi:10.1016/j.clinph.2009.02.157.

Bai, O., Mari, Z., Vorbach, S., and Hallett, M. (2005). Asymmetric spatiotemporal patterns of event-related desynchronization preceding voluntary sequential finger movements: A high-resolution EEG study. *Clin. Neurophysiol.* 116, 1213–1221. doi:10.1016/j.clinph.2005.01.006.

Baillet, S., Mosher, J. C., and Leahy, R. M. (2001). Electromagnetic brain mapping. *IEEE Signal Process. Mag.* 18, 14–30. doi:10.1109/79.962275.

Banville, H., Rishabh Gupta, and Falk, T. H. (2017). Mental Task Evaluation for Hybrid NIRS-EEG Brain-Computer Interfaces. *Comput. Intell. Neurosci.* 2017, 3524208. doi:10.1155/2017/3524208.

Bardin, J. C., Fins, J. J., Katz, D. I., Hersh, J., Heier, L. A., Tabelow, K., et al. (2011). Dissociations between behavioural and functional magnetic resonance imaging-based evaluations of cognitive function after brain injury. *Brain* 134, 769–782. doi:10.1093/brain/awr005.

Barker, J. W., Panigrahy, A., and Huppert, T. J. (2014). Accuracy of oxygen saturation and total hemoglobin estimates in the neonatal brain using the semi-infinite slab model for FD-NIRS data analysis. *Biomed. Opt. Express* 5, 4300. doi:10.1364/boe.5.004300.

Batula, A. M., Ayaz, H., and Kim, Y. E. (2014). Evaluating a four-class motor-imagery-based optical brain-computer interface. in *2014 36th Annual International Conference of the IEEE Engineering in Medicine and Biology Society*, 2000–2003. doi:10.1109/EMBC.2014.6944007.

Batula, A. M., Mark, J. A., Kim, Y. E., and Ayaz, H. (2017). Comparison of Brain Activation during Motor Imagery and Motor Movement Using fNIRS. *Comput. Intell. Neurosci.* 2017, 5491296. doi:10.1155/2017/5491296.

Bauer, G., Gerstenbrand, F., and Rumpl, E. (1979). Varieties of the locked-in syndrome. *J. Neurol.* 221, 77–91. doi:10.1007/bf00313105.

Bauernfeind, G., Steyrl, D., Brunner, C., and Muller-Putz, G. R. (2014). Single trial classification of fNIRS-based brain-computer interface mental arithmetic data: A comparison between different classifiers. in *2014 36th Annual International Conference of the IEEE Engineering in Medicine and Biology Society, EMBC 2014*, 2004–2007. doi:10.1109/EMBC.2014.6944008.

Bayne, T., Hohwy, J., and Owen, A. M. (2016). Are There Levels of Consciousness? *Trends Cogn. Sci.* 20, 405–413. doi:10.1016/j.tics.2016.03.009.

Bellman, R. (1957). *Dynamic programming*. Princeton: Princeton University Press.

Biggins, C. A., Fein, G., Raz, J., and Amir, A. (1991). Artifactually high coherences result from using spherical spline computation of scalp current density. *Electroencephalogr. Clin. Neurophysiol.*

79, 413–419. doi:10.1016/0013-4694(91)90206-J.

Bigirimana, A. D., Siddique, N., and Coyle, D. (2017). Brain-Computer Interfacing with Emotion-Inducing Imagery: A Pilot Study. in *The 7th Graz Brain-Computer Interface Conference*, 26–31. doi:10.3217/978-3-85125-533-1-06.

Bigirimana, A. D., Siddique, N., and Coyle, D. (2020). Emotion-Inducing Imagery Versus Motor Imagery for a Brain-Computer Interface. *IEEE Trans. Neural Syst. Rehabil. Eng.* 28, 850–859. doi:10.1109/TNSRE.2020.2978951.

Bishop, C. (2006). *Pattern Recognition and Machine Learning*. New York, NY, United States: Springer-Verlag.

Blankertz, B., Dornhege, G., Krauledat, M., Muller, K.-R., and Curio, G. (2007). The non-invasive Berlin Brain-Computer Interface: fast acquisition of effective performance in untrained subjects. *Neuroimage* 37, 539–550. doi:10.1016/j.neuroimage.2007.01.051.

Blankertz, B., Tomioka, R., Lemm, S., Kawanabe, M., and Müller, K.-R. (2008). Optimizing Spatial filters for Robust EEG Single-Trial Analysis. *IEEE Signal Process. Mag.* 25, 41–56. doi:10.1109/MSP.2008.4408441.

Blokland, Y., Spyrou, L., Thijssen, D., Eijsvogels, T., Colier, W., Floor-Westerdijk, M., et al. (2014). Combined EEG-fNIRS decoding of motor attempt and imagery for brain switch control: An offline study in patients with tetraplegia. *IEEE Trans. Neural Syst. Rehabil. Eng.* 22, 222–229. doi:10.1109/TNSRE.2013.2292995.

Boas, D. A., Campbell, L. E., and Yodh, A. G. (1995). Scattering and imaging with diffusing temporal field correlations. *Phys. Rev. Lett.* 75, 1855–1858. doi:10.1103/PhysRevLett.75.1855.

Boas, D. A., Culver, J. P., Stott, J. J., and Dunn, A. K. (2002). Three dimensional Monte Carlo code for photon migration through complex heterogeneous media including the adult human head. *Opt. Express* 10, 159–170. doi:10.1364/oe.10.000159.

Boas, D. A., Dale, A. M., and Franceschini, M. A. (2004). Diffuse optical imaging of brain activation: approaches to optimizing image sensitivity, resolution, and accuracy. *Neuroimage* 23, S275–S288. doi:10.1016/j.neuroimage.2004.07.011.

Boly, M., Coleman, M. R., Davis, M. H., Hampshire, A., Bor, D., Moonen, G., et al. (2007). When

thoughts become action: An fMRI paradigm to study volitional brain activity in non-communicative brain injured patients. *Neuroimage* 36, 979–992. doi:10.1016/j.neuroimage.2007.02.047.

Bonnet, M., Decety, J., Jeannerod, M., and Requin, J. (1997). Mental simulation of an action modulates the excitability of spinal reflex pathways in man. *Cogn. Brain Res.* 5, 221–228. doi:10.1016/S0926-6410(96)00072-9.

Bouguer, P. (1729). *Essai d'optique, sur la gradation de la lumiere*.

Brainard, D. H. (1997). The Psychophysics Toolbox. *Spat. Vis.* 10, 433-436.

Britton, J. W., Frey, L. C., Hopp, J. L., Korb, P., Koubeissi, M. Z., Lievens, W. E., et al. (2016). *Electroencephalography (EEG): An Introductory Text and Atlas of Normal and Abnormal Findings in Adults, Children, and Infants*. Chicago: American Epilepsy Society.

Brunner, C., Billinger, M., Seeber, M., Mullen, T. R., and Makeig, S. (2016). Volume Conduction Influences Scalp-Based Connectivity Estimates. *Front. Comput. Neurosci.* 10, 121. doi:10.3389/fncom.2016.00121.

Bruns, A. (2004). Fourier-, Hilbert- and wavelet-based signal analysis: Are they really different approaches? *J. Neurosci. Methods* 137, 321–332. doi:10.1016/j.jneumeth.2004.03.002.

Buccino, A. P., Keles, H. O., and Omurtag, A. (2016). Hybrid EEG-fNIRS Asynchronous Brain-Computer Interface for Multiple Motor Tasks. *PLoS One* 11, e0146610. doi:10.1371/journal.pone.0146610.

Burle, B., Spieser, L., Roger, C., Casini, L., Hasbroucq, T., and Vidal, F. (2015). Spatial and temporal resolutions of EEG: Is it really black and white? A scalp current density view. *Int. J. Psychophysiol.* 97, 210–220. doi:10.1016/j.ijpsycho.2015.05.004.

Buxton, R. B., and Frank, L. R. (1997). A model for the coupling between cerebral blood flow and oxygen metabolism during neural stimulation. *J. Cereb. Blood Flow Metab.* 17, 64–72. doi:10.1097/00004647-199701000-00009.

Buxton, R. B., Uludağ, K., Dubowitz, D. J., and Liu, T. T. (2004). Modeling the hemodynamic response to brain activation. *Neuroimage* 23, S220–S233. doi:10.1016/j.neuroimage.2004.07.013.

Caballero-Gaudes, C., and Reynolds, R. C. (2017). Methods for cleaning the BOLD fMRI signal. *Neuroimage* 154, 128–149. doi:10.1016/j.neuroimage.2016.12.018.

Cannestra, A. F., Wartenburger, I., Obrig, H., Villringer, A., and Toga, A. W. (2003). Functional assessment of Broca's area using near infrared spectroscopy in humans. *Neuroreport* 14, 1961–1965. doi:10.1097/00001756-200310270-00016.

Cardillo, G. (2007). McNemar test. Available at: https://www.github.com/dnafinder/mcnemar [Accessed February 1, 2020].

Carraresi, S., Shatir, T. S. M., Martelli, F., and Zaccanti, G. (2001). Accuracy of a Perturbation Model to Predict the Effect of Scattering and Absorbing Inhomogeneities on Photon Migration. *Appl. Opt.* 40, 4622–4632. doi:10.1364/AO.40.004622.

Carvalhaes, C., and de Barros, J. A. (2015). The surface Laplacian technique in EEG: Theory and methods. *Int. J. Psychophysiol.* 97, 174–188. doi:10.1016/j.ijpsycho.2015.04.023.

Cavaliere, C., Aiello, M., Di Perri, C., Fernandez-Espejo, D., Owen, A. M., and Soddu, A. (2015). Diffusion tensor imaging and white matter abnormalities in patients with disorders of consciousness. *Front. Hum. Neurosci.* 8, 1028. doi:10.3389/fnhum.2014.01028.

Charland-Verville, V., Lesenfants, D., Sela, L., Noirhomme, Q., Ziegler, E., Chatelle, C., et al. (2014). Detection of response to command using voluntary control of breathing in disorders of consciousness. *Front. Hum. Neurosci.* 8, 1020. doi:10.3389/fnhum.2014.01020.

Chennu, S., Annen, J., Wannez, S., Thibaut, A., Chatelle, C., Cassol, H., et al. (2017). Brain networks predict metabolism, diagnosis and prognosis at the bedside in disorders of consciousness. *Brain A J. Neurol.* 140, 2120–2132. doi:10.1093/brain/awx163.

Cheyne, D., Kristeva, R., and Deecke, L. (1991). Homuncular organization of human motor cortex as indicated by neuromagnetic recordings. *Neurosci. Lett.* 122, 17–20.

Chiarelli, A. M., Croce, P., Merla, A., and Zappasodi, F. (2018). Deep learning for hybrid EEG-fNIRS brain–computer interface: application to motor imagery classification. *J. Neural Eng.* 15, 036028. doi:10.1088/1741-2552/aaaf82.

Cohen, M. X. (2014a). "Bandpass Filtering and the Hilbert Transform," in *Analyzing neural time series data: Theory and practice* (MIT Press), 175–193.

Cohen, M. X. (2014b). “Surface Laplacian,” in *Analyzing neural time series data: Theory and practice* (MIT Press), 275–290.

Cohen, M. X. (2019). A better way to define and describe Morlet wavelets for time-frequency analysis. *Neuroimage* 199, 81–86. doi:10.1016/j.neuroimage.2019.05.048.

Combrisson, E., and Jerbi, K. (2015). Exceeding chance level by chance: The caveat of theoretical chance levels in brain signal classification and statistical assessment of decoding accuracy. *J. Neurosci. Methods* 250, 126–136. doi:10.1016/j.jneumeth.2015.01.010.

Comon, P. (1994). Independent component analysis, A new concept? *Signal Processing* 36, 287–314. doi:10.1016/0165-1684(94)90029-9.

Contini, D., Martelli, F., and Zaccanti, G. (1997). Photon migration through a turbid slab described by a model based on diffusion approximation I Theory. *Appl. Opt.* 36, 4587. doi:10.1364/ao.36.004587.

Cortes, C., and Vapnik, V. (1995). Support-vector networks. *Mach. Learn.* 20, 273–297. doi:10.1007/bf00994018.

Coyle, D. (2009). Neural network based auto association and time-series prediction for biosignal processing in brain-computer interfaces. *IEEE Comput. Intell. Mag.* 4, 47–59. doi:10.1109/MCI.2009.934560.

Coyle, D., Carroll, Á., Stow, J., Mccreadie, K., and Mcelligott, J. (2013). Visual and Stereo Audio Sensorimotor Rhythm Feedback in the Minimally Conscious State. in *Proceedings of the Fifth International Brain-Computer Interface Meeting* (TU Graz), 2–3. doi:10.3217/978-3-85125-260-6-18.

Coyle, D. H., Carroll, A., Stow, J., McCann, A., Ally, A., and McElligott, J. (2012). Enabling Control in the Minimally Conscious State in a Single Session with a Three Channel BCI. in *The 1st international DECODER Workshop* (Paris).

Coyle, D., McGinnity, T. M., and Prasad, G. (2006). Creating a nonparametric brain-computer interface with neural time-series prediction preprocessing. in *Annual International Conference of the IEEE Engineering in Medicine and Biology* (New York, NY, United States), 2183–2186. doi:10.1109/IEMBS.2006.260626.

Coyle, D., Prasad, G., and McGinnity, T. M. (2005a). A time-frequency approach to feature extraction for a brain-computer interface with a comparative analysis of performance measures. *EURASIP J. Appl. Signal Processing* 2005, 3141–3151. doi:10.1155/ASP.2005.3141.

Coyle, D., Prasad, G., and McGinnity, T. M. (2005b). A time-series prediction approach for feature extraction in a brain-computer interface. *IEEE Trans. Neural Syst. Rehabil. Eng.* 13, 461–467. doi:10.1109/TNSRE.2005.857690.

Coyle, D., Satti, A., Prasad, G., and McGinnity, T. M. (2008). Neural time-series prediction preprocessing meets common spatial patterns in a brain-computer interface. in *Proceedings of the 30th Annual International Conference of the IEEE Engineering in Medicine and Biology Society, EMBS'08* (Vancouver, BC), 2626–2629. doi:10.1109/iembs.2008.4649739.

Coyle, D., Stow, J., McCreadie, K., McElligott, J., and Carroll, Á. (2015). Sensorimotor modulation assessment and brain-computer interface training in disorders of consciousness. *Arch. Phys. Med. Rehabil.* 96, S62–S70. doi:10.1016/j.apmr.2014.08.024.

Coyle, S. M., Ward, T. E., and Markham, C. M. (2007). Brain-computer interface using a simplified functional near-infrared spectroscopy system. *J. Neural Eng.* 4, 219–226.

Cramer, S. C., Finklestein, S. P., Schaechter, J. D., Bush, G., and Rosen, B. R. (1999). Activation of Distinct Motor Cortex Regions During Ipsilateral and Contralateral Finger Movements. *J. Neurophysiol.* 81, 383–387.

Cruse, D., Chennu, S., Chatelle, C., Bekinschtein, T. A., Fernández-Espejo, D., Pickard, J. D., et al. (2011). Bedside detection of awareness in the vegetative state: A cohort study. *Lancet* 378, 2088–2094. doi:10.1016/S0140-6736(11)61224-5.

Cruse, D., Chennu, S., Fernández-Espejo, D., Payne, W. L., Young, G. B., and Owen, A. M. (2012). Detecting Awareness in the Vegetative State: Electroencephalographic Evidence for Attempted Movements to Command. *PLoS One* 7, e49933. doi:10.1371/journal.pone.0049933.

Cui, W., Kumar, C., and Chance, B. (1991). Experimental study of migration depth for the photons measured at sample surface. in *Proc. SPIE 1431, Time-Resolved Spectroscopy and Imaging of Tissues*, 1412–1431. doi:doi.org/10.1117/12.44189.

Cui, X., Bray, S., Bryant, D. M., Glover, G. H., and Reiss, A. L. (2011). A quantitative comparison of

NIRS and fMRI across multiple cognitive tasks. *Neuroimage* 54, 2808–2821. doi:10.1016/j.neuroimage.2010.10.069.

Curran, E., Sykacek, P., Stokes, M., Roberts, S. J., Penny, W., Johnsrude, I., et al. (2004). Cognitive Tasks for Driving a Brain-Computer Interfacing System: A Pilot Study. *IEEE Trans. Neural Syst. Rehabil. Eng.* 12, 48–54. doi:10.1109/TNSRE.2003.821372.

Davies, D. J., Su, Z., Clancy, M. T., Lucas, S. J. E., Dehghani, H., Logan, A., et al. (2015). Near-Infrared Spectroscopy in the Monitoring of Adult Traumatic Brain Injury: A Review. *J. Neurotrauma* 32, 933–941. doi:10.1089/neu.2014.3748.

Dayan, N., Bigirimana, A., Mccann, A., Stow, J., Mcelligott, J., Carroll, A., et al. (2019). Towards Answering Questions In Disorders Of Consciousness And Locked-In Sydrome With A SMR-BCI. in *Proceedings of the 8th Graz Brain-Computer Interface Conference 2019* doi:10.3217/978-3-85125-682-6-65.

Dechent, P., Merboldt, K. D., and Frahm, J. (2004). Is the human primary motor cortex involved in motor imagery? *Cogn. Brain Res.* 19, 138–144. doi:10.1016/j.cogbrainres.2003.11.012.

Dehghani, H., Eames, M. E., Yalavarthy, P. K., Davis, S. C., Srinivasan, S., Carpenter, C. M., et al. (2008). Near infrared optical tomography using NIRFAST: Algorithm for numerical model and image reconstruction. *Commun. Numer. Methods Eng.* 25, 711–732. doi:10.1002/cnm.1162.

Dehghani, H., White, B. R., Zeff, B. W., Tizzard, A., and Culver, J. P. (2009). Depth sensitivity and image reconstruction analysis of dense imaging arrays for mapping brain function with diffuse optical tomography. *Appl. Opt.* 48, D137–D143. doi:10.1364/AO.48.00D137.

Delorme, A., and Makeig, S. (2004). EEGLAB: An open source toolbox for analysis of single-trial EEG dynamics including independent component analysis. *J. Neurosci. Methods* 134, 9–21. doi:10.1016/j.jneumeth.2003.10.009.

Delpy, D. T., Cope, M., van der Zee, P., Arridge, S., Wray, S., and Wyatt, J. (1988). Estimation of optical pathlength through tissue from direct time of flight measurement. *Phys. Med. Biol.* 33, 1433–1442. doi:10.1088/0031-9155/33/12/008.

Demertzi, A., Racine, E., Bruno, M.-A., Ledoux, D., Gosseries, O., Vanhaudenhuyse, A., et al. (2013). Pain Perception in Disorders of Consciousness: Neuroscience, Clinical Care, and Ethics

in Dialogue. *Neuroethics* 6, 37–50. doi:10.1007/s12152-011-9149-x.

Demertzi, A., Schnakers, C., Ledoux, D., Chatelle, C., Bruno, M.-A., Vanhaudenhuyse, A., et al. (2009). Different beliefs about pain perception in the vegetative and minimally conscious states: a European survey of medical and paramedical professionals. *Prog. Brain Res.* 177, 329–338. doi:10.1016/S0079-6123(09)17722-1.

Diop, M., and Lawrence, K. St. (2012). Deconvolution method for recovering the photon time-of-flight distribution from time-resolved measurements. *Opt. Lett.* 37, 2358–2360. doi:10.1364/OL.37.002358.

Diop, M., and St. Lawrence, K. (2013). Improving the depth sensitivity of time-resolved measurements by extracting the distribution of times-of-flight. *Biomed. Opt. Express* 4, 447–459. doi:10.1364/BOE.4.000447.

Dornhege, G., Blankertz, B., Krauledat, M., Losch, F., Curio, G., and Müller, K. R. (2006). Combined optimization of spatial and temporal filters for improving brain-computer interfacing. *IEEE Trans. Biomed. Eng.* 53, 2274–2281. doi:10.1109/TBME.2006.883649.

Doulgerakis, M. K., Eggebrecht, A. T., and Dehghani, H. (2019a). High-density functional diffuse optical tomography based on frequency-domain measurements improves image quality and spatial resolution. *Neurophotonics* 6, 1. doi:10.1117/1.nph.6.3.035007.

Doulgerakis, M. K., Eggebrecht, A. T., and Dehghani, H. (2019b). Information rich phase content of frequency domain functional Near Infrared Spectroscopy. in *Proc. SPIE 10865, Neural Imaging and Sensing 2019*, 10865C. doi:10.1117/12.2505874.

Drost, G., Stegeman, D. F., van Engelen, B. G. M., and Zwarts, M. J. (2006). Clinical applications of high-density surface EMG: A systematic review. *J. Electromyogr. Kinesiol.* 16, 586–602. doi:10.1016/j.jelekin.2006.09.005.

Durduran, T., Choe, R., Baker, W. B., and Yodh, A. G. (2010). Diffuse Optics for Tissue Monitoring and Tomography. *Rep. Prog. Phys.* 73. doi:10.1088/0034-4885/73/7/076701.

Edlow, B. L., Chatelle, C., Spencer, C. A., Chu, C. J., Bodien, Y. G., O'Connor, K. L., et al. (2017). Early detection of consciousness in patients with acute severe traumatic brain injury. *Brain A J. Neurol.* 140, 2399–2414. doi:10.1093/brain/awx176.

Eggebrecht, A. (2017). NeuroDOT_Beta. Available at: https://github.com/WUSTL-ORL/NeuroDOT_Beta.

Eggebrecht, A. T., Ferradal, S. L., Robichaux-Viehoever, A., Hassanpour, M. S., Dehghani, H., Snyder, A. Z., et al. (2014). Mapping distributed brain function and networks with diffuse optical tomography. *Nat. Photonics* 8, 448–454. doi:10.1038/nphoton.2014.107.

Ehrsson, H. H., Geyer, S., and Naito, E. (2003). Imagery of Voluntary Movement of Fingers, Toes, and Tongue Activates Corresponding Body-Part-Specific Motor Representations. *J. Neurophysiol.* 90, 3304–3316. doi:10.1152/jn.01113.2002.

Erbil, N., and Ungan, P. (2007). Changes in the alpha and beta amplitudes of the central EEG during the onset, continuation, and offset of long-duration repetitive hand movements. *Brain Res.* 1169, 44–56. doi:10.1016/j.brainres.2007.07.014.

Fantini, S. (1995). Frequency-domain multichannel optical detector for noninvasive tissue spectroscopy and oximetry. *Opt. Eng.* 34, 32. doi:10.1117/12.183988.

Fantini, S., and Sassaroli, A. (2020). Frequency-Domain Techniques for Cerebral and Functional Near-Infrared Spectroscopy. *Front. Neurosci.* 14, 300. doi:10.3389/fnins.2020.00300.

Fazli, S., Mehnert, J., Steinbrink, J., Curio, G., Villringer, A., Müller, K.-R., et al. (2012). Enhanced performance by a hybrid NIRS–EEG brain computer interface. *Neuroimage* 59, 519–529. doi:10.1016/j.neuroimage.2011.07.084.

Fernández-Espejo, D., Bekinschtein, T., Monti, M. M., Pickard, J. D., Junque, C., Coleman, M. R., et al. (2011). Diffusion weighted imaging distinguishes the vegetative state from the minimally conscious state. *Neuroimage* 54, 103–112. doi:10.1016/j.neuroimage.2010.08.035.

Fernández-Espejo, D., Junque, C., Bernabeu, M., Roig-Rovira, T., Vendrell, P., and Mercader, J. M. (2010a). Reductions of thalamic volume and regional shape changes in the vegetative and the minimally conscious states. *J. Neurotrauma* 27, 1187–1193. doi:10.1089/neu.2010.1297.

Fernández-Espejo, D., Junque, C., Cruse, D., Bernabeu, M., Roig-Rovira, T., Fábregas, N., et al. (2010b). Combination of diffusion tensor and functional magnetic resonance imaging during recovery from the vegetative state. *BMC Neurol.* 10, 77. doi:10.1186/1471-2377-10-77.

Fernández-Espejo, D., Norton, L., and Owen, A. M. (2014). The Clinical Utility of fMRI for

Identifying Covert Awareness in the Vegetative State: A Comparison of Sensitivity between 3T and 1.5T. *PLoS One* 9, e95082. doi:10.1371/journal.pone.0095082.

Fernández-Espejo, D., and Owen, A. M. (2013). Detecting awareness after severe brain injury. *Nat. Rev. Neurosci.* 14, 801–809. doi:10.1038/nrn3608.

Fernández-Espejo, D., Rossit, S., and Owen, A. M. (2015). A thalamocortical mechanism for the absence of overt motor behavior in covertly aware patients. *JAMA Neurol.* 72, 1442–1450. doi:10.1001/jamaneurol.2015.2614.

Ferrante, A., Gavriel, C., and Faisal, A. (2015). Data-efficient hand motor imagery decoding in EEG-BCI by using Morlet wavelets & Common Spatial Pattern algorithms. in *International IEEE/EMBS Conference on Neural Engineering (NER)* (Montpellier), 948–951. doi:10.1109/NER.2015.7146782.

Ferrari, M., Giannini, I., Sideri, G., and Zanette, E. (1985). Continuous non invasive monitoring of human brain by near infrared spectroscopy. *Adv. Exp. Med. Biol.* 191, 873–882. doi:10.1007/978-1-4684-3291-6_88.

Ferrari, M., and Quaresima, V. (2012). A brief review on the history of human functional near-infrared spectroscopy (fNIRS) development and fields of application. *Neuroimage* 63, 921–935. doi:10.1016/j.neuroimage.2012.03.049.

Ferree, T. C., Clay, M. T., and Tucker, D. M. (2001). The spatial resolution of scalp EEG. *Neurocomputing* 38–40, 1209–1216. doi:10.1016/S0925-2312(01)00568-9.

Frackowiak, R. S. J., Friston, K. J., Frith, C. D., Dolan, R. J., Price, C. J., Zeki, S., et al. (2004). *Human Brain Function*. 2nd ed. USA: Academic Press.

Franceschini, M. A., Boas, D. A., Zourabian, A., Diamond, S. G., Nadgir, S., Lin, D. W., et al. (2002). Near-infrared spiroximetry: noninvasive measurements of venous saturation in piglets and human subjects. *J. Appl. Physiol.* 92, 372–384. doi:10.1152/jappl.2002.92.1.372.

Franceschini, M. A., Fantini, S., Thompson, J. H., Culver, J. P., and Boas, D. A. (2003). Hemodynamic evoked response of the sensorimotor cortex measured noninvasively with near-infrared optical imaging. *Psychophysiology* 40, 548–560. doi:10.1111/1469-8986.00057.

Friedrich, E. V. C. C., Scherer, R., and Neuper, C. (2012). The effect of distinct mental strategies on

classification performance for brain-computer interfaces. *Int. J. Psychophysiol.* 84, 86–94. doi:10.1016/j.ijpsycho.2012.01.014.

Fristen, K. J. (1997). Imaging cognitive anatomy. *Trends Cogn. Sci.* 1, 21–27. doi:10.1016/S1364-6613(97)01001-2.

Funane, T., Atsumori, H., Katura, T., Obata, A. N., Sato, H., Tanikawa, Y., et al. (2014). Quantitative evaluation of deep and shallow tissue layers' contribution to fNIRS signal using multi-distance optodes and independent component analysis. *Neuroimage* 85, 150–165. doi:10.1016/j.neuroimage.2013.02.026.

Gagnon, L., Cooper, R. J., Yücel, M. A., Perdue, K. L., Greve, D. N., and Boas, D. A. (2012). Short separation channel location impacts the performance of short channel regression in NIRS. *Neuroimage* 59, 2518–2528. doi:10.1016/j.neuroimage.2011.08.095.

Gagnon, L., Perdue, K., Greve, D. N., Goldenholz, D., Kaskhedikar, G., and Boas, D. A. (2011). Improved recovery of the hemodynamic response in Diffuse Optical Imaging using short optode separations and state-space modeling. *Neuroimage* 56, 1362–1371. doi:10.1016/j.neuroimage.2011.03.001.

Gallegos-Ayala, G., Furdea, A., Takano, K., Ruf, C. A., Flor, H., and Birbaumer, N. (2014). Brain communication in a completely locked-in patient using bedside near-infrared spectroscopy. *Neurology* 82, 1930–1932. doi:10.1212/WNL.0000000000000449.

Ge, S., Wang, R., and Yu, D. (2014). Classification of four-class motor imagery employing single-channel electroencephalography. *PLoS One* 9, e98019. doi:10.1371/journal.pone.0098019.

Ge, S., Yang, Q., Wang, R., Lin, P., Gao, J., Leng, Y., et al. (2017). A Brain-Computer Interface Based on a Few-Channel EEG-fNIRS Bimodal System. *IEEE Access* 5, 208–218. doi:10.1109/ACCESS.2016.2637409.

Gerardin, E., Sirigu, A., Lehéricy, S., Poline, J.-B., Gaymard, B., Marsault, C., et al. (2000). Partially Overlapping Neural Networks for Real and Imagined Hand Movements. *Cereb. Cortex* 10, 1093–1104. doi:10.1093/cercor/10.11.1093.

Gervain, J., Mehler, J., Werker, J. F., Nelson, C. A., Csibra, G., Lloyd-Fox, S., et al. (2011). Near-infrared spectroscopy: A report from the McDonnell infant methodology consortium. *Dev.*

Cogn. Neurosci. 1, 22–46. doi:10.1016/j.dcn.2010.07.004.

Giacino, J. T., Ashwal, S., Childs, N., Cranford, R., Jennett, B., Katz, D. I., et al. (2002). The minimally conscious state: definition and diagnostic criteria. *Neurology* 58, 349–353. doi:10.1212/wnl.58.3.349.

Giacino, J. T., Kalmar, K., and Whyte, J. (2004). The JFK Coma Recovery Scale-Revised: Measurement characteristics and diagnostic utility. *Arch. Phys. Med. Rehabil.* 85, 2020–2029. doi:10.1016/j.apmr.2004.02.033.

Gibson, R. M., Chennu, S., Owen, A. M., and Cruse, D. (2014a). Complexity and familiarity enhance single-trial detectability of imagined movements with electroencephalography. *Clin. Neurophysiol.* 125, 1556–1567. doi:10.1016/j.clinph.2013.11.034.

Gibson, R. M., Fernández-Espejo, D., Gonzalez-Lara, L. E., Kwan, B. Y., Lee, D. H., Owen, A. M., et al. (2014b). Multiple tasks and neuroimaging modalities increase the likelihood of detecting covert awareness in patients with disorders of consciousness. *Front. Hum. Neurosci.* 8, 950. doi:10.3389/fnhum.2014.00950.

Glover, G. H. (2011). Overview of functional magnetic resonance imaging. *Neurosurg. Clin. N. Am.* 22, 133–139. doi:10.1016/j.nec.2010.11.001.

Goldfine, A. M., Victor, J. D., Conte, M. M., Bardin, J. C., and Schiff, N. D. (2011). Determination of awareness in patients with severe brain injury using EEG power spectral analysis. *Clin. Neurophysiol. Off. J. Int. Fed. Clin. Neurophysiol.* 122, 2157–2168. doi:10.1016/j.clinph.2011.03.022.

González-Franco, M., Yuan, P., Zhang, D., Hong, B., and Gao, S. (2011). Motor imagery based brain-computer interface: A study of the effect of positive and negative feedback. in *Proceedings of the Annual International Conference of the IEEE Engineering in Medicine and Biology Society* (Boston, MA), 6323–6326. doi:10.1109/IEMBS.2011.6091560.

Górski, P. (2014). Common Spatial Patterns in a few channel BCI interface. *J. Theor. Appl. Comput. Sci.* 8, 56–63.

Gosseries, O., Vanhaudenhuyse, A., Bruno, M.-A., Demertzi, A., Schnakers, C., Boly, M., et al. (2011). "Disorders of Consciousness: Coma, Vegetative and Minimally Conscious States," in

States of Consciousness, eds. D. Cvetkovic and I. Cosic (The Frontiers Collection. Springer, Berlin, Heidelberg), 29–55.

Graimann, B., Allison, B., and Pfurtscheller, G. (2010). "Brain–Computer Interfaces: A Gentle Introduction," in *Brain-Computer Interfaces. The Frontiers Collection.*, eds. B. Graimann, G. Pfurtscheller, and B. Allison (Berlin, Heidelberg: Springer Berlin Heidelberg), 1–27. doi:10.1007/978-3-642-02091-9_1.

Gratton, G., and Corballis, P. M. (1995). Removing the heart from the brain: compensation for the pulse artifact in the photon migration signal. *Psychophysiology* 32, 292–299.

Gratton, G., Corballis, P. M., Cho, E., Fabiani, M., and Hood, D. C. (1995a). Shades of gray matter: noninvasive optical images of human brain responses during visual stimulation. *Psychophysiology* 32, 505–509.

Gratton, G., and Fabiani, M. (2009). "Fast Optical Signals: Principles, Methods, and Experimental Results," in *In Vivo Optical Imaging of Brain Function*, ed. R. D. Frostig (Boca Raton (FL): CRC Press/Taylor & Francis).

Gratton, G., and Fabiani, M. (2010). Fast Optical Imaging of Human Brain Function. *Front. Hum. Neurosci.* 4, 52. doi:10.3389/fnhum.2010.00052.

Gratton, G., Fabiani, M., Friedman, D., Franceschini, M. A., Fantini, S., Corballis, P., et al. (1995b). Rapid Changes of Optical Parameters in the Human Brain During a Tapping Task. *J. Cogn. Neurosci.* 7, 446–456.

Gratton, G., Maier, J. S., Fabiani, M., Mantulin, W. W., and Gratton, E. (1994). Feasibility of intracranial near-infrared optical scanning. *Psychophysiology* 31, 211–215.

Grech, R., Cassar, T., Muscat, J., Camilleri, K. P., Fabri, S. G., Zervakis, M., et al. (2008). Review on solving the inverse problem in EEG source analysis. *J. Neuroeng. Rehabil.* 5, 25. doi:10.1186/1743-0003-5-25.

Guger, C., Edlinger, G., Harkam, W., Niedermayer, I., and Pfurtscheller, G. (2003). How many people are able to operate an EEG-based brain-computer interface (BCI)? *IEEE Trans. neural Syst. Rehabil. Eng. a Publ. IEEE Eng. Med. Biol. Soc.* 11, 145–147. doi:10.1109/TNSRE.2003.814481.

Guger, C., Spataro, R., Allison, B. Z., Heilinger, A., Ortner, R., Cho, W., et al. (2017). Complete Locked-in and Locked-in Patients: Command Following Assessment and Communication with Vibro-Tactile P300 and Motor Imagery Brain-Computer Interface Tools. *Front. Neurosci.* 11, 251. doi:10.3389/fnins.2017.00251.

Guger, C., Spataro, R., Pellas, F., Allison, B. Z., Heilinger, A., Ortner, R., et al. (2018). Assessing Command-Following and Communication With Vibro-Tactile P300 Brain-Computer Interface Tools in Patients With Unresponsive Wakefulness Syndrome. *Front. Neurosci.* 12, 423. doi:10.3389/fnins.2018.00423.

Guillot, A., Collet, C., Nguyen, V. A., Malouin, F., Richards, C., and Doyon, J. (2009). Brain activity during visual versus kinesthetic imagery: an fMRI study. *Hum. Brain Mapp.* 30, 2157–2172.

Guillot, A., Lebon, F., Rouffet, D., Champely, S., Doyon, J., and Collet, C. (2007). Muscular responses during motor imagery as a function of muscle contraction types. *Int. J. Psychophysiol.* 66, 18–27. doi:10.1016/j.ijpsycho.2007.05.009.

Gunadi, S., Leung, T. S., Elwell, C. E., and Tachtsidis, I. (2014). Spatial sensitivity and penetration depth of three cerebral oxygenation monitors. *Biomed. Opt. Express* 5, 2896–2912. doi:10.1364/BOE.5.002896.

Hallez, H., Vanrumste, B., Grech, R., Muscat, J., De Clercq, W., Vergult, A., et al. (2007). Review on solving the forward problem in EEG source analysis. *J. Neuroeng. Rehabil.* 4, 46. doi:10.1186/1743-0003-4-46.

Han, C.-H., Kim, Y.-W., Kim, D. Y., Kim, S. H., Nenadic, Z., and Im, C.-H. (2019). Electroencephalography-based endogenous brain-computer interface for online communication with a completely locked-in patient. *J. Neuroeng. Rehabil.* 16, 18. doi:10.1186/s12984-019-0493-0.

Hanakawa, T., Dimyan, M. A., and Hallett, M. (2008). Motor Planning, Imagery, and Execution in the Distributed Motor Network: A Time-Course Study with Functional MRI. *Cereb. Cortex* 18, 2775–2788. doi:10.1093/cercor/bhn036.

Hanakawa, T., Immisch, I., Toma, K., Dimyan, M. A., Van Gelderen, P., and Hallett, M. (2003). Functional properties of brain areas associated with motor execution and imagery. *J.*

Neurophysiol. 89, 989–1002. doi:10.1152/jn.00132.2002.

Headway (2017). Brain Injury Statistics. Available at: https://www.headway.org.uk/about-brain-injury/further-information/statistics/ [Accessed February 1, 2017].

Hiraoka, M., Firbank, M., Essenpreis, M., Cope, M., Arridge, S. R., Van Der Zee, P., et al. (1993). A Monte Carlo investigation of optical pathlength in inhomogeneous tissue and its application to near-infrared spectroscopy. *Phys. Med. Biol* 38, 1859–1876.

Hoffmann, S., and Falkenstein, M. (2008). The Correction of Eye Blink Artefacts in the EEG: A Comparison of Two Prominent Methods. *PLoS One* 3, e3004. doi:10.1371/journal.pone.0003004.

Holper, L., and Wolf, M. (2010). Motor imagery in response to fake feedback measured by functional near-infrared spectroscopy. *Neuroimage* 50, 190–197. doi:10.1016/j.neuroimage.2009.12.055.

Holper, L., and Wolf, M. (2011). Single-trial classification of motor imagery differing in task complexity: a functional near-infrared spectroscopy study. *J. Neuroeng. Rehabil.* 8, 34. doi:10.1186/1743-0003-8-34.

Hong, K.-S., Naseer, N., and Kim, Y.-H. (2015). Classification of prefrontal and motor cortex signals for three-class fNIRS–BCI. *Neurosci. Lett.* 587, 87–92.

Horki, P., Bauernfeind, G., Klobassa, D. S., Pokorny, C., Pichler, G., Schippinger, W., et al. (2014). Detection of mental imagery and attempted movements in patients with disorders of consciousness using EEG. *Front. Hum. Neurosci.* 8, 1009. doi:10.3389/fnhum.2014.01009.

Hsu, W.-C., Lin, L.-F., Chou, C.-W., Hsiao, Y.-T., and Liu, Y.-H. (2017). EEG Classification of Imaginary Lower Limb Stepping Movements Based on Fuzzy Support Vector Machine with Kernel-Induced Membership Function. *Int. J. Fuzzy Syst.* 19, 566–579.

Hubbard, I. J., Parsons, M. W., Neilson, C., and Carey, L. M. (2009). Task-specific training: Evidence for and translation to clinical practice. *Occup. Ther. Int.* 16, 175–189. doi:10.1002/oti.275.

Hughes, J. R. (1978). Limitations of the EEG in coma and brain death. *Ann. N. Y. Acad. Sci.* 315, 121–136. doi:10.1111/j.1749-6632.1978.tb50335.x.

Huneau, C., Benali, H., and Chabriat, H. (2015). Investigating Human Neurovascular Coupling Using Functional Neuroimaging: A Critical Review of Dynamic Models. *Front. Neurosci.* 9, 467.

doi:10.3389/fnins.2015.00467.

Huppert, T. J., Diamond, S. G., Franceschini, M. A., and Boas, D. A. (2009). HomER: A review of time-series analysis methods for near-infrared spectroscopy of the brain. *Appl. Opt.* 48, D280–D298. doi:10.1364/AO.48.00D280.

Huppert, T. J., Hoge, R. D., Diamond, S. G., Franceschini, M. A., and Boas, D. A. (2006). A temporal comparison of BOLD, ASL, and NIRS hemodynamic responses to motor stimuli in adult humans. *Neuroimage* 29, 368–382.

Iacoviello, D., Petracca, A., Spezialetti, M., and Placidi, G. (2015). A real-time classification algorithm for EEG-based BCI driven by self-induced emotions. *Comput. Methods Programs Biomed.* 122, 293–303. doi:10.1016/j.cmpb.2015.08.011.

Iso, N., Moriuchi, T., Sagari, A., Kitajima, E., Iso, F., Tanaka, K., et al. (2015). Monitoring Local Regional Hemodynamic Signal Changes during Motor Execution and Motor Imagery Using Near-Infrared Spectroscopy. *Front. Physiol.* 6, 416. doi:10.3389/fphys.2015.00416.

Jackson, A. F., and Bolger, D. J. (2014). The neurophysiological bases of EEG and EEG measurement: A review for the rest of us. *Psychophysiology* 51, 1061–1071.

Jackson, P. L., Lafleur, M. F., Malouin, F., Richards, C., and Doyon, J. (2001). Potential role of mental practice using motor imagery in neurologic rehabilitation. *Arch. Phys. Med. Rehabil.* 82, 1133–1141. doi:10.1053/apmr.2001.24286.

Jacques, S. L., and Pogue, B. W. (2008). Tutorial on diffuse light transport. *J. Biomed. Opt.* 13, 041302. doi:10.1117/1.2967535.

Jahn, K., Deutschländer, A., Stephan, T., Strupp, M., Wiesmann, M., and Brandt, T. (2004). Brain activation patterns during imagined stance and locomotion in functional magnetic resonance imaging. *Neuroimage* 22, 1722–1731. doi:10.1016/j.neuroimage.2004.05.017.

Jain, A. K., Duin, R. P. W., and Mao, J. (2000). Statistical pattern recognition: A review. *IEEE Trans. Pattern Anal. Mach. Intell.* 22, 4–37. doi:10.1109/34.824819.

Jeannerod, M. (1994). The representing brain: Neural correlates of motor intention and imagery. *Behav. Brain Sci.* 17, 187–202. doi:10.1017/S0140525X00034026.

Jeannerod, M. (1995). Mental imagery in the motor context. *Neuropsychologia* 33, 1419–1432.

doi:10.1016/0028-3932(95)00073-C.

Jenkinson, M., Beckmann, C. F., Behrens, T. E. J., Woolrich, M. W., and Smith, S. M. (2012). FSL. *Neuroimage* 62, 782–790.

Jerbic, A. B., Horki, P., Sovilj, S., Isgum, V., and Cifrek, M. (2015). Hilbert-Huang time-frequency analysis of motor imagery EEG data for brain-computer interfaces. in *6th European Conference of the International Federation for Medical and Biological Engineering*, eds. I. Lacković and D. Vasic (Springer Verlag), 62–65. doi:10.1007/978-3-319-11128-5_16.

Jin, S. H., Lee, S. H., Jang, G., Lee, Y. J., Shik, H. K., and An, J. (2015). An application of common spatial pattern algorithm for accuracy improvement in classification of cortical activation pattern according to finger movement. in *2015 54th Annual Conference of the Society of Instrument and Control Engineers of Japan (SICE)* (Hangzhou), 1260–1264. doi:10.1109/SICE.2015.7285539.

Jindal, U., Sood, M., Dutta, A., and Chowdhury, S. R. (2015). Development of point of care testing device for neurovascular coupling from simultaneous recording of EEG and NIRS during anodal transcranial direct current stimulation. *IEEE J. Transl. Eng. Heal. Med.* 3, 2000112. doi:10.1109/JTEHM.2015.2389230.

Jobsis, F. F. (1977). Noninvasive, infrared monitoring of cerebral and myocardial oxygen sufficiency and circulatory parameters. *Science.* 198, 1264–1267.

Jung, T.-P., Makeig, S., Bell, A. J., and Sejnowski, T. J. (1998). "Independent Component Analysis of Electroencephalographic and Event-Related Potential Data," in *Central Auditory Processing and Neural Modeling* (Springer US), 189–197. doi:10.1007/978-1-4615-5351-9_17.

Junghöfer, M., Elbert, T., Tucker, D. M., and Braun, C. (1999). The polar average reference effect: A bias in estimating the head surface integral in EEG recording. *Clin. Neurophysiol.* 110, 1149–1155. doi:10.1016/S1388-2457(99)00044-9.

Kak, A. C., Slaney, M., and Wang, G. (2002). Principles of Computerized Tomographic Imaging. *Med. Phys.* 29, 107–107. doi:10.1118/1.1455742.

Kalcher, J., Flotzinger, D., Neuper, C., Gölly, S., and Pfurtscheller, G. (1996). Graz brain-computer interface II: Towards communication between humans and computers based on online classification of three different EEG patterns. *Med. Biol. Eng. Comput.* 34, 382–388.

doi:10.1007/BF02520010.

Katura, T., Sato, H., Fuchino, Y., Yoshida, T., Atsumori, H., Kiguchi, M., et al. (2008). Extracting task-related activation components from optical topography measurement using independent components analysis. *J. Biomed. Opt.* 13, 54008. doi:10.1117/1.2981829.

Kayser, J. (2009). Current source density (CSD) interpolation using spherical splines - CSD Toolbox (Version 1.1). Available at: http://psychophysiology.cpmc.columbia.edu/Software/CSDtoolbox.

Kayser, J., and Tenke, C. E. (2006). Principal components analysis of Laplacian waveforms as a generic method for identifying ERP generator patterns: I. Evaluation with auditory oddball tasks. *Clin. Neurophysiol.* 117, 348–368. doi:10.1016/j.clinph.2005.08.034.

Kayser, J., and Tenke, C. E. (2015). On the benefits of using surface Laplacian (current source density) methodology in electrophysiology. *Int. J. Psychophysiol.* 97, 171–173. doi:10.1016/j.ijpsycho.2015.06.001.

Kempny, A. M., James, L., Yelden, K., Duport, S., Farmer, S., Playford, E. D., et al. (2016). Functional near infrared spectroscopy as a probe of brain function in people with prolonged disorders of consciousness. *NeuroImage Clin.* 12, 312–319.

Khan, M. J., Ghafoor, U., and Hong, K.-S. (2018). Early Detection of Hemodynamic Responses Using EEG: A Hybrid EEG-fNIRS Study. *Front. Hum. Neurosci.* 12, 479. doi:10.3389/fnhum.2018.00479.

Khan, M. J., Hong, K. S., Naseer, N., and Bhutta, M. R. (2015). Motor imagery performance evaluation using hybrid EEG-NIRS for BCI. in *2015 54th Annual Conference of the Society of Instrument and Control Engineers of Japan (SICE)* (Hangzhou), 1150–1155. doi:10.1109/SICE.2015.7285318.

Khan, M. J., Hong, M. J., and Hong, K.-S. (2014). Decoding of four movement directions using hybrid NIRS-EEG brain-computer interface. *Front. Hum. Neurosci.* 8, 244. doi:10.3389/fnhum.2014.00244.

Khan, M. J., Zafar, A., and Hong, K. S. (2017). Comparison of brain areas for executed and imagined movements after motor training: An fNIRS study. in *2017 10th International Conference on Human System Interactions (HSI)* (Ulsan), 125–130. doi:10.1109/HSI.2017.8005013.

Kim, Y. K., Park, E., Lee, A., Im, C.-H., and Kim, Y.-H. (2018). Changes in network connectivity during motor imagery and execution. *PLoS One* 13, e0190715. doi:10.1371/journal.pone.0190715.

King, J. R., Faugeras, F., Gramfort, A., Schurger, A., El Karoui, I., Sitt, J. D., et al. (2013). Single-trial decoding of auditory novelty responses facilitates the detection of residual consciousness. *Neuroimage* 83, 726–738. doi:10.1016/j.neuroimage.2013.07.013.

Kirilina, E., Jelzow, A., Heine, A., Niessing, M., Wabnitz, H., Bruhl, R., et al. (2012). The physiological origin of task-evoked systemic artefacts in functional near infrared spectroscopy. *Neuroimage* 61, 70–81.

Klem, G. H., Luders, H. O., Jasper, H. H., and Elger, C. (1999). The ten-twenty electrode system of the International Federation. The International Federation of Clinical Neurophysiology. *Electroencephalogr. Clin. Neurophysiol. Suppl.* 52, 3–6.

Kohavi, R. (1995). A Study of Cross-Validation and Bootstrap for Accuracy Estimation and Model Selection. in *Proceedings of the 14th International Joint Conference on Artificial Intelligence* (Montreal), 1137–1143.

Kohl-Bareis, M., Obrig, H., Steinbrink, J., Malak, J., Uludag, K., and Villringer, A. (2002). Noninvasive monitoring of cerebral blood flow by a dye bolus method: separation of brain from skin and skull signals. *J. Biomed. Opt.* 7, 464–470.

Koles, Z. J., Lazar, M. S., and Zhou, S. Z. (1990). Spatial patterns underlying population differences in the background EEG. *Brain Topogr.* 2, 275–284. doi:10.1007/BF01129656.

Kondziella, D., Friberg, C. K., Frokjaer, V. G., Fabricius, M., and Møller, K. (2016). Preserved consciousness in vegetative and minimal conscious states: systematic review and meta-analysis. *J. Neurol. Neurosurg. Psychiatry* 87, 485–492.

Koo, B., Lee, H.-G., Nam, Y., Kang, H., Koh, C. S., Shin, H.-C., et al. (2015). A hybrid NIRS-EEG system for self-paced brain computer interface with online motor imagery. *J. Neurosci. Methods* 244, 26–32.

Krebs, H. I., Volpe, B., and Hogan, N. (2009). A working model of stroke recovery from rehabilitation robotics practitioners. *J. Neuroeng. Rehabil.* 6, 6. doi:10.1186/1743-0003-6-6.

Kuhlman, W. N. (1978). Functional topography of the human mu rhythm. *Electroencephalogr. Clin. Neurophysiol.* 44, 83–93. doi:10.1016/0013-4694(78)90107-4.

Kuhtz-Buschbeck, J. P., Mahnkopf, C., Holzknecht, C., Siebner, H., Ulmer, S., and Jansen, O. (2003). Effector-independent representations of simple and complex imagined finger movements: A combined fMRI and TMS study. *Eur. J. Neurosci.* 18, 3375–3387. doi:10.1111/j.1460-9568.2003.03066.x.

Kumar, J. S., and Bhuvaneswari, P. (2012). Analysis of Electroencephalography (EEG) Signals and Its Categorization–A Study. *Procedia Eng.* 38, 2525–2536. doi:10.1016/j.proeng.2012.06.298.

Kwon, J., Shin, J., and Im, C.-H. (2020). Toward a compact hybrid brain-computer interface (BCI): Performance evaluation of multi-class hybrid EEG-fNIRS BCIs with limited number of channels. *PLoS One* 15, e0230491. doi:10.1371/journal.pone.0230491.

Lancioni, G. E., Singh, N. N., O'Reilly, M. F., Sigafoos, J., Amenduni, M. T., Navarro, J., et al. (2012). Microswitch technology and contingent stimulation to promote adaptive engagement in persons with minimally conscious state: a case evaluation. *Cogn. Process.* 13, 133–137. doi:10.1007/s10339-011-0428-6.

Lange, F., and Tachtsidis, I. (2019). Clinical Brain Monitoring with Time Domain NIRS: A Review and Future Perspectives. *Appl. Sci.* 9, 1612. doi:10.3390/app9081612.

Laureys, S., Celesia, G. G., Cohadon, F., Lavrijsen, J., León-Carrión, J., Sannita, W. G., et al. (2010). Unresponsive wakefulness syndrome: A new name for the vegetative state or apallic syndrome. *BMC Med.* 8, 68. doi:10.1186/1741-7015-8-68.

Laureys, S., Lemaire, C., Maquet, P., Phillips, C., and Franck, G. (1999). Cerebral metabolism during vegetative state and after recovery to consciousness. *J. Neurol. Neurosurg. Psychiatry* 67, 121. doi:10.1136/jnnp.67.1.121.

Laureys, S., Owen, A. M., and Schiff, N. D. (2004). Brain function in coma, vegetative state, and related disorders. *Lancet Neurol.* 3, 537–546. doi:10.1016/S1474-4422(04)00852-X.

Laureys, S., Pellas, F., Van Eeckhout, P., Ghorbel, S., Schnakers, C., Perrin, F., et al. (2005). The locked-in syndrome: What is it like to be conscious but paralyzed and voiceless? *Prog. Brain Res.* 150, 495–511. doi:10.1016/S0079-6123(05)50034-7.

Lee, G., Song, C., Lee, Y., Cho, H., and Lee, S. (2011). Effects of Motor Imagery Training on Gait Ability of Patients with Chronic Stroke. *J. Phys. Ther. Sci.* 23, 197–200. doi:10.1589/jpts.23.197.

Lee, S. H., Jin, S. H., and An, J. (2019a). The difference in cortical activation pattern for complex motor skills: A functional near- infrared spectroscopy study. *Sci. Rep.* 9, 14066. doi:10.1038/s41598-019-50644-9.

Lee, W. H., Kim, E., Seo, H. G., Oh, B. M., Nam, H. S., Kim, Y. J., et al. (2019b). Target-oriented motor imagery for grasping action: different characteristics of brain activation between kinesthetic and visual imagery. *Sci. Rep.* 9, 1–14. doi:10.1038/s41598-019-49254-2.

Leeb, R., Lee, F., Keinrath, C., Scherer, R., Bischof, H., and Pfurtscheller, G. (2007). Brain-computer communication: Motivation, aim, and impact of exploring a virtual apartment. *IEEE Trans. Neural Syst. Rehabil. Eng.* 15, 473–482. doi:10.1109/TNSRE.2007.906956.

Leff, D. R., Orihuela-Espina, F., Elwell, C. E., Athanasiou, T., Delpy, D. T., Darzi, A. W., et al. (2011). Assessment of the cerebral cortex during motor task behaviours in adults: a systematic review of functional near infrared spectroscopy (fNIRS) studies. *Neuroimage* 54, 2922–2936.

Lehembre, R., Gosseries, O., Lugo, Z., Jedidi, Z., Chatelle, C., Sadzot, B., et al. (2012). Electrophysiological investigations of brain function in coma, vegetative and minimally conscious patients. *Arch. Ital. Biol.* 150, 122–139. doi:10.4449/aib.v150i2.1374.

Lei, X., and Liao, K. (2017). Understanding the Influences of EEG Reference: A Large-Scale Brain Network Perspective. *Front. Neurosci.* 11, 205. doi:10.3389/fnins.2017.00205.

Lemm, S., Blankertz, B., Curio, G., and Müller, K. R. (2005). Spatio-spectral filters for improving the classification of single trial EEG. *IEEE Trans. Biomed. Eng.* 52, 1541–1548. doi:10.1109/TBME.2005.851521.

Lemm, S., Blankertz, B., Dickhaus, T., and Müller, K. R. (2011). Introduction to machine learning for brain imaging. *Neuroimage* 56, 387–399. doi:10.1016/j.neuroimage.2010.11.004.

Leon-Carrion, J., Damas, J., Izzetoglu, K., Pourrezai, K., Martin-Rodriguez, J. F., Barroso y Martin, J. M., et al. (2006). Differential time course and intensity of PFC activation for men and women in response to emotional stimuli: a functional near-infrared spectroscopy (fNIRS) study. *Neurosci.*

Lett. 403, 90–95.

Leon-Carrion, J., Izzetoglu, M., Izzetoglu, K., Martin-Rodriguez, J. F., Damas-Lopez, J., Barroso y Martin, J. M., et al. (2010). Efficient learning produces spontaneous neural repetition suppression in prefrontal cortex. *Behav. Brain Res.* 208, 502–508.

León-Carrión, J., and León-Domínguez, U. (2012). "Functional Near-Infrared Spectroscopy (fNIRS): Principles and Neuroscientific Applications," in *Neuroimaging - Methods*, ed. P. Bright (InTech), 47–74.

Li, L., Wang, J., Xu, G., Li, M., and Xie, J. (2015). The Study of Object-Oriented Motor Imagery Based on EEG Suppression. *PLoS One* 10, e0144256. doi:10.1371/journal.pone.0144256.

Li, R., Potter, T., Huang, W., and Zhang, Y. (2017). Enhancing performance of a hybrid EEG-fNIRS system using channel selection and early temporal features. *Front. Hum. Neurosci.* 11. doi:10.3389/fnhum.2017.00462.

Li, X. D., O'Leary, M. A., Boas, D. A., Chance, B., and Yodh, A. G. (1996). Fluorescent diffuse photon density waves in homogeneous and heterogeneous turbid media: analytic solutions and applications. *Appl. Opt.* 35, 3746. doi:10.1364/ao.35.003746.

Liao, C. H., Worsley, K. J., Poline, J. B., Aston, J. A. D., Duncan, G. H., and Evans, A. C. (2002). Estimating the delay of the fMRI response. *Neuroimage* 16, 593–606. doi:10.1006/nimg.2002.1096.

Lina, J.-M., Dehaes, M., Matteau-Pelletier, C., and Lesage, F. (2008). Complex wavelets applied to diffuse optical spectroscopy for brain activity detection. *Opt. Express* 16, 1029–1050.

Lisman, J., and Buzsáki, G. (2008). A neural coding scheme formed by the combined function of gamma and theta oscillations. *Schizophr. Bull.* 34, 974–980. doi:10.1093/schbul/sbn060.

Logothetis, N. K., Pauls, J., Augath, M., Trinath, T., and Oeltermann, A. (2001). Neurophysiological investigation of the basis of the fMRI signal. *Nature* 412, 150–157. doi:10.1038/35084005.

Lotte, F., Bougrain, L., Cichocki, A., Clerc, M., Congedo, M., Rakotomamonjy, A., et al. (2018). A review of classification algorithms for EEG-based brain-computer interfaces: A 10 year update. *J. Neural Eng.* 15, 031005. doi:10.1088/1741-2552/aab2f2.

Lotte, F., Congedo, M., Lécuyer, A., Lamarche, F., and Arnaldi, B. (2007). A review of classification

algorithms for EEG-based brain-computer interfaces. *J. Neural Eng.* 4, R1–R13. doi:10.1088/1741-2560/4/2/R01.

Lotte, F., and Guan, C. (2011). Regularizing common spatial patterns to improve BCI designs: Unified theory and new algorithms. *IEEE Trans. Biomed. Eng.* 58, 355–362. doi:10.1109/TBME.2010.2082539.

Lotze, M., Montoya, P., Erb, M., Hülsmann, E., Flor, H., Klose, U., et al. (1999). Activation of cortical and cerebellar motor areas during executed and imagined hand movements: An fMRI study. *J. Cogn. Neurosci.* 11, 491–501. doi:10.1162/089892999563553.

Lou, B., Hong, B., Gao, X., and Gao, S. (2008). Bipolar electrode selection for a motor imagery based brain–computer interface. *J. Neural Eng.* 5, 342–349. doi:10.1088/1741-2560/5/3/007.

Lourenço, C. F., Santos, R. M., Barbosa, R. M., Cadenas, E., Radi, R., and Laranjinha, J. (2014). Neurovascular coupling in hippocampus is mediated via diffusion by neuronal-derived nitric oxide. *Free Radic. Biol. Med.* 73, 421–429. doi:10.1016/j.freeradbiomed.2014.05.021.

Luu, S., and Chau, T. (2009). Decoding Subjective Preference From Single-Trial Near-Infrared Spectroscopy Signals. *J. Neural Eng.* 6, 016003. doi:10.1088/1741-2560/6/1/016003.

Mangia, A. L., Pirini, M., Simoncini, L., and Cappello, A. (2014). A feasibility study of an improved procedure for using EEG to detect brain responses to imagery instruction in patients with disorders of consciousness. *PLoS One* 9, e99289. doi:10.1371/journal.pone.0099289.

Maris, E., and Oostenveld, R. (2007). Nonparametric statistical testing of EEG- and MEG-data. *J. Neurosci. Methods* 164, 177–190. doi:10.1016/j.jneumeth.2007.03.024.

Matcher, S. J., Elwell, C. E., Cooper, C. E., Cope, M., and Delpy, D. T. (1995). Performance comparison of several published tissue near-infrared spectroscopy algorithms. *Anal. Biochem.* 227, 54–68. doi:10.1006/abio.1995.1252.

Mathewson, K. E., Harrison, T. J. L., and Kizuk, S. A. D. (2017). High and dry? Comparing active dry EEG electrodes to active and passive wet electrodes. *Psychophysiology* 54, 74–82. doi:10.1111/psyp.12536.

Matoušek, M., Volavka, J., Roubíček, J., and Roth, Z. (1967). EEG frequency analysis related to age in normal adults. *Electroencephalogr. Clin. Neurophysiol.* 23, 162–167. doi:10.1016/0013-

4694(67)90106-X.

McFarland, D. J., Miner, L. A., Vaughan, T. M., and Wolpaw, J. R. (2000). Mu and beta rhythm topographies during motor imagery and actual movements. *Brain Topogr.* 12, 177–186. doi:10.1023/A:1023437823106.

Michel, C. M., and He, B. (2019). EEG source localization. *Handb. Clin. Neurol.* 160, 85–101. doi:10.1016/B978-0-444-64032-1.00006-0.

Mihara, M., Miyai, I., Hattori, N., Hatakenaka, M., Yagura, H., Kawano, T., et al. (2012). Neurofeedback Using Real-Time Near-Infrared Spectroscopy Enhances Motor Imagery Related Cortical Activation. *PLoS One* 7, e32234. doi:10.1371/journal.pone.0032234.

Mikołajewska, E., and Mikołajewski, D. (2014). Non-invasive EEG-based brain-computer interfaces in patients with disorders of consciousness. *Mil. Med. Res.* 1, 14. doi:10.1186/2054-9369-1-14.

Millan, J. del R., Renkens, F., Mourino, J., and Gerstner, W. (2004). Noninvasive brain-actuated control of a mobile robot by human EEG. *IEEE Trans. Biomed. Eng.* 51, 1026–1033.

Miller, K. J., Schalk, G., Fetz, E. E., den Nijs, M., Ojemann, J. G., and Rao, R. P. N. (2010). Cortical activity during motor execution, motor imagery, and imagery-based online feedback. *Proc. Natl. Acad. Sci. U. S. A.* 107, 4430–4435.

Mizuguchi, N., Nakata, H., Hayashi, T., Sakamoto, M., Muraoka, T., Uchida, Y., et al. (2013). Brain activity during motor imagery of an action with an object: a functional magnetic resonance imaging study. *Neurosci. Res.* 76, 150–155. doi:10.1016/j.neures.2013.03.012.

Molteni, E., Arrigoni, F., Bardoni, A., Galbiati, S., Villa, F., Colombo, K., et al. (2013). Bedside assessment of residual functional activation in minimally conscious state using NIRS and general linear models. in *2013 35th Annual International Conference of the IEEE Engineering in Medicine and Biology Society*, 3551–3554. doi:10.1109/EMBC.2013.6610309.

Monti, M. M., Vanhaudenhuyse, A., Coleman, M. R., Boly, M., Pickard, J. D., Tshibanda, L., et al. (2010). Willful Modulation of Brain Activity in Disorders of Consciousness. *N. Engl. J. Med.* 362, 579–589.

Morash, V., Bai, O., Furlani, S., Lin, P., and Hallett, M. (2008). Classifying EEG signals preceding right hand, left hand, tongue, and right foot movements and motor imageries. *Clin.*

Neurophysiol. 119, 2570–2578. doi:10.1016/j.clinph.2008.08.013.

Morren, G., Wolf, M., Lemmerling, P., Wolf, U., Choi, J. H., Gratton, E., et al. (2004). Detection of fast neuronal signals in the motor cortex from functional near infrared spectroscopy measurements using independent component analysis. *Med. Biol. Eng. Comput.* 42, 92–99.

Morrissey, A.-M., Gill-Thwaites, H., Wilson, B., Leonard, R., McLellan, L., Pundole, A., et al. (2018). The role of the SMART and WHIM in behavioural assessment of disorders of consciousness: clinical utility and scope for a symbiotic relationship. *Neuropsychol. Rehabil.* 28, 1254–1265. doi:10.1080/09602011.2017.1354769.

Mukaka, M. M. (2012). A guide to appropriate use of correlation coefficient in medical research. *Malawi Med. J.* 24, 69–71.

Müller-Gerking, J., Pfurtscheller, G., and Flyvbjerg, H. (1999). Designing optimal spatial filters for single-trial EEG classification in a movement task. *Clin. Neurophysiol.* 110, 787–798. doi:10.1016/S1388-2457(98)00038-8.

Müller-Putz, G. R., Kaiser, V., Solis-Escalante, T., and Pfurtscheller, G. (2010). Fast set-up asynchronous brain-switch based on detection of foot motor imagery in 1-channel EEG. *Med. Biol. Eng. Comput.* 48, 229–233. doi:10.1007/s11517-009-0572-7.

Müller-Putz, G., Scherer, R., Brunner, C., Leeb, R., and Pfurtscheller, G. (2008). Better than random? A closer look on BCI results. *Int. J. Bioelectromagn.* 10, 52–55.

Murphy, S. M. (1994). Imagery interventions in sport. *Med. Sci. Sports Exerc.* 26, 486–494. doi:10.1249/00005768-199404000-00014.

Naci, L., and Owen, A. (2013). Making Every Word Count for Nonresponsive Patients. *JAMA Neurol.* 70, 1235–1241.

Naito, M., Michioka, Y., Ozawa, K., Ito, Y., Kiguchi, M., and Kanazawa, T. (2007). A Communication Means for Totally Locked-in ALS Patients Based on Changes in Cerebral Blood Volume Measured with Near-Infrared Light. *IEICE Trans. Inf. Syst.* E90-D, 1028–1037. doi:10.1093/ietisy/e90-d.7.1028.

Nakata, H., Domoto, R., Mizuguchi, N., Sakamoto, K., and Kanosue, K. (2019). Negative BOLD responses during hand and foot movements: An fMRI study. *PLoS One* 14, e0215736.

doi:10.1371/journal.pone.0215736.

Naro, A., Chillura, A., Portaro, S., Bramanti, A., De Luca, R., Bramanti, P., et al. (2018). Novel Approaches to the Diagnosis of Chronic Disorders of Consciousness: Detecting Peripersonal Space by Using Ultrasonics. *Front. Neurol.* 9, 47. doi:10.3389/fneur.2018.00047.

Naseer, N., and Hong, K.-S. (2013). Classification of functional near-infrared spectroscopy signals corresponding to the right- and left-wrist motor imagery for development of a brain-computer interface. *Neurosci. Lett.* 553, 84–89. doi:10.1016/j.neulet.2013.08.021.

Naseer, N., and Hong, K.-S. (2015). fNIRS-based brain-computer interfaces: a review. *Front. Hum. Neurosci.* 9, 3. doi:10.3389/fnhum.2015.00003.

Naseer, N., Noori, F. M., Qureshi, N. K., and Hong, K.-S. (2016a). Determining Optimal Feature-Combination for LDA Classification of Functional Near-Infrared Spectroscopy Signals in Brain-Computer Interface Application. *Front. Hum. Neurosci.* 10, 237. doi:10.3389/fnhum.2016.00237.

Naseer, N., Qureshi, N. K., Noori, F. M., and Hong, K.-S. (2016b). Analysis of Different Classification Techniques for Two-Class Functional Near-Infrared Spectroscopy-Based Brain-Computer Interface. *Intell. Neurosci.* 2016, 5480760. doi:10.1155/2016/5480760.

Neuper, C., and Pfurtscheller, G. (2001). Evidence for distinct beta resonance frequencies in human EEG related to specific sensorimotor cortical areas. *Clin. Neurophysiol.* 112, 2084–2097. doi:10.1016/S1388-2457(01)00661-7.

Neuper, C., Schlögl, A., and Pfurtscheller, G. (1999). Enhancement of left-right sensorimotor EEG differences during feedback-regulated motor imagery. *J. Clin. Neurophysiol.* 16, 373–382. doi:10.1097/00004691-199907000-00010.

Nicholson, V. P., Keogh, J. W. L., and Choy, N. L. L. (2018). Can a single session of motor imagery promote motor learning of locomotion in older adults? A randomized controlled trial. *Clin. Interv. Aging* 13, 713–722. doi:10.2147/CIA.S164401.

Novi, Q., Guan, C., Dat, T. H., and Xue, P. (2007). Sub-band common spatial pattern (SBCSP) for brain-computer interface. in *2007 3rd International IEEE/EMBS Conference on Neural Engineering*, 204–207. doi:10.1109/CNE.2007.369647.

Nunez, P. L., Silberstein, R. B., Cadusch, P. J., Wijesinghe, R. S., Westdorp, A. F., and Srinivasan, R. (1994). A theoretical and experimental study of high resolution EEG based on surface Laplacians and cortical imaging. *Electroencephalogr. Clin. Neurophysiol.* 90, 40–57. doi:10.1016/0013-4694(94)90112-0.

Obrig, H., Neufang, M., Wenzel, R., Kohl, M., Steinbrink, J., Einhaupl, K., et al. (2000). Spontaneous low frequency oscillations of cerebral hemodynamics and metabolism in human adults. *Neuroimage* 12, 623–639.

Okada, E., and Delpy, D. T. (2003). Near-Infrared Light Propagation in an Adult Head Model. II. Effect of Superficial Tissue Thickness on the Sensitivity of the Near-Infrared Spectroscopy Signal. *Appl. Opt.* 42, 2915–2922.

Oostenveld, R., Fries, P., Maris, E., and Schoffelen, J.-M. (2011). FieldTrip: Open Source Software for Advanced Analysis of MEG, EEG, and Invasive Electrophysiological Data. *Comput. Intell. Neurosci.* 2011, 156869. doi:10.1155/2011/156869.

Ortner, R., Scharinger, J., Lechner, A., and Guger, C. (2015). How many people can control a motor imagery based BCI using common spatial patterns? in *7th International IEEE/EMBS Conference on Neural Engineering (NER)* (Montpellier), 202–205. doi:10.1109/NER.2015.7146595.

Owen, A. M., Coleman, M. R., Boly, M., Davis, M. H., Laureys, S., and Pickard, J. D. (2006). Detecting Awareness in the Vegetative State. *Science.* 313, 1402. doi:10.1126/science.1130197.

Padfield, N., Zabalza, J., Zhao, H., Masero, V., and Ren, J. (2019). EEG-based brain-computer interfaces using motor-imagery: Techniques and challenges. *Sensors (Switzerland)* 19, 1423. doi:10.3390/s19061423.

Papoulis, A. (1977). *Signal analysis*. New York, NY, United States: McGraw-Hill.

Parra, L., and Sajda, P. (2003). Blind Source Separation via Generalized Eigenvalue Decomposition. *J. Mach. Learn. Res.* 4, 1261–1269. doi:10.1162/jmlr.2003.4.7-8.1261.

Patterson, M. S., Chance, B., and Wilson, B. C. (1989). Time resolved reflectance and transmittance for the noninvasive measurement of tissue optical properties. *Appl. Opt.* 28, 2331–2336.

Pelli, D. G. (1997). The VideoToolbox software for visual psychophysics: Transforming numbers into movies. *Spat. Vis.* 10, 437–442. doi:10.1163/156856897X00366.

Perry, A., Stein, L., and Bentin, S. (2011). Motor and attentional mechanisms involved in social interaction-Evidence from mu and alpha EEG suppression. *Neuroimage* 58, 895–904. doi:10.1016/j.neuroimage.2011.06.060.

Pfeifer, M. D., Scholkmann, F., and Labruyère, R. (2018). Signal Processing in Functional Near-Infrared Spectroscopy (fNIRS): Methodological Differences Lead to Different Statistical Results. *Front. Hum. Neurosci.* 11, 641. doi:10.3389/fnhum.2017.00641.

Pfurtscheller, G. (2001). Functional brain imaging based on ERD/ERS. *Vision Res.* 41, 1257–1260. doi:10.1016/S0042-6989(00)00235-2.

Pfurtscheller, G., and Aranibar, A. (1977). Event-related cortical desynchronization detected by power measurements of scalp EEG. *Electroencephalogr. Clin. Neurophysiol.* 42, 817–826. doi:10.1016/0013-4694(77)90235-8.

Pfurtscheller, G., Brunner, C., Schlögl, A., and Lopes da Silva, F. H. (2006a). Mu rhythm (de)synchronization and EEG single-trial classification of different motor imagery tasks. *Neuroimage* 31, 153–159. doi:10.1016/j.neuroimage.2005.12.003.

Pfurtscheller, G., Leeb, R., and Slater, M. (2006b). Cardiac responses induced during thought-based control of a virtual environment. *Int. J. Psychophysiol. Off. J. Int. Organ. Psychophysiol.* 62, 134–140. doi:10.1016/j.ijpsycho.2006.03.001.

Pfurtscheller, G., and Lopes da Silva, F. H. (1999). Event-related EEG/MEG synchronization and desynchronization: basic principles. *Clin. Neurophysiol.* 110, 1842–1857. doi:10.1016/s1388-2457(99)00141-8.

Pfurtscheller, G., and Neuper, C. (1997). Motor imagery activates primary sensorimotor area in humans. *Neurosci. Lett.* 239, 65–68. doi:10.1016/S0304-3940(97)00889-6.

Pfurtscheller, G., Neuper, C., Brunner, C., and Lopes Da Silva, F. (2005). Beta rebound after different types of motor imagery in man. *Neurosci. Lett.* 378, 156–159. doi:10.1016/j.neulet.2004.12.034.

Pfurtscheller, G., Neuper, C., Flotzinger, D., and Pregenzer, M. (1997). EEG-based discrimination between imagination of right and left hand movement. *Electroencephalogr. Clin. Neurophysiol.* 103, 642–651. doi:10.1016/S0013-4694(97)00080-1.

Pfurtscheller, G., Neuper, C., and Mohl, W. (1994). Event-related desynchronization (ERD) during

visual processing. *Int. J. Psychophysiol.* 16, 147–153. doi:10.1016/0167-8760(89)90041-X.

Pfurtscheller, G., Neuper, C., Schlogl, A., and Lugger, K. (1998). Separability of EEG signals recorded during right and left motor imagery using adaptive autoregressive parameters. *IEEE Trans. Rehabil. Eng.* 6, 316–325. doi:10.1109/86.712230.

Pfurtscheller, G., Scherer, R., Müller-Putz, G. R., and Lopes da Silva, F. H. (2008). Short-lived brain state after cued motor imagery in naive subjects. *Eur. J. Neurosci.* 28, 1419–1426. doi:10.1111/j.1460-9568.2008.06441.x.

Pfurtscheller, G., and Solis-Escalante, T. (2009). Could the beta rebound in the EEG be suitable to realize a "brain switch"? *Clin. Neurophysiol.* 120, 24–29. doi:10.1016/j.clinph.2008.09.027.

Plichta, M. M., Heinzel, S., Ehlis, A.-C., Pauli, P., and Fallgatter, A. J. (2007). Model-based analysis of rapid event-related functional near-infrared spectroscopy (NIRS) data: A parametric validation study. *Neuroimage* 35, 625–634.

Pogue, B. W., and Patterson, M. S. (1994). Frequency-domain optical absorption spectroscopy of finite tissue volumes using diffusion theory. *Phys. Med. Biol.* 39, 1157–1180.

Pogue, B. W., Patterson, M. S., Jiang, H., and Paulsen, K. D. (1995). Initial assessment of a simple system for frequency domain diffuse optical tomography. *Phys. Med. Biol.* 40, 1709–1729. doi:10.1088/0031-9155/40/10/011.

Porro, C. A., Francescato, M. P., Cettolo, V., Diamond, M. E., Baraldi, P., Zuiani, C., et al. (1996). Primary motor and sensory cortex activation during motor performance and motor imagery: A functional magnetic resonance imaging study. *J. Neurosci.* 16, 7688–7698. doi:10.1523/jneurosci.16-23-07688.1996.

Power, S. D., Falk, T. H., and Chau, T. (2010). Classification of Prefrontal Activity Due to Mental Arithmetic and Music Imagery Using Hidden Markov Models and Frequency Domain Near-Infrared Spectroscopy. *J. Neural Eng.* 7, 26002. doi:10.1088/1741-2560/7/2/026002.

Qin, L., and He, B. (2005). A wavelet-based time–frequency analysis approach for classification of motor imagery for brain–computer interface applications. *J. Neural Eng.* 2, 65. doi:10.1088/1741-2560/2/4/001.

Qureshi, N. K., Naseer, N., Noori, F. M., Nazeer, H., Khan, R. A., and Saleem, S. (2017). Enhancing

Classification Performance of Functional Near-Infrared Spectroscopy- Brain–Computer Interface Using Adaptive Estimation of General Linear Model Coefficients. *Front. Neurorobot.* 11, 33. doi:10.3389/fnbot.2017.00033.

Ramoser, H., Müller-Gerking, J., and Pfurtscheller, G. (2000). Optimal spatial filtering of single trial EEG during imagined hand movement. *IEEE Trans. Rehabil. Eng.* 8, 441–446. doi:10.1109/86.895946.

Rao, R., and Scherer, R. (2010). Brain-Computer Interfacing [In the Spotlight]. *IEEE Signal Process. Mag.* 27, 152–150. doi:10.1109/MSP.2010.936774.

Rathee, D., Raza, H., Prasad, G., and Cecotti, H. (2017). Current source density estimation enhances the performance of motor-imagery-related brain–computer interface. *IEEE Trans. Neural Syst. Rehabil. Eng.* 25, 2461–2471. doi:10.1109/TNSRE.2017.2726779.

Roach, B. J., and Mathalon, D. H. (2008). Event-related EEG time-frequency analysis: An overview of measures and an analysis of early gamma band phase locking in schizophrenia. *Schizophr. Bull.* 34, 907–926. doi:10.1093/schbul/sbn093.

Royal College of Physicians (2020). *Prolonged disorders of consciousness following sudden onset brain injury: National clinical guidelines.* London: RCP.

Rupawala, M., Dehghani, H., Lucas, S. J. E., Tino, P., and Cruse, D. (2018). Shining a Light on Awareness: A Review of Functional Near-Infrared Spectroscopy for Prolonged Disorders of Consciousness. *Front. Neurol.* 9, 350. doi:10.3389/fneur.2018.00350.

Sato, T., Ito, M., Suto, T., Kameyama, M., Suda, M., Yamagishi, Y., et al. (2007). Time courses of brain activation and their implications for function: a multichannel near-infrared spectroscopy study during finger tapping. *Neurosci. Res.* 58, 297–304.

Schieber, M. H., and Hibbard, L. S. (1993). How somatotopic is the motor cortex hand area? *Science.* 261, 489–492. doi:10.1126/science.8332915.

Schiff, N. D. (2015). Cognitive motor dissociation following severe brain injuries. *JAMA Neurol.* 72, 1413–1415. doi:10.1001/jamaneurol.2015.2899.

Schiff, N. D., Nauvel, T., and Victor, J. D. (2014). Large-scale brain dynamics in disorders of consciousness. *Curr. Opin. Neurobiol.* 25, 7–14. doi:10.1016/j.conb.2013.10.007.

Schiff, N. D., Ribary, U., Moreno, D. R., Beattie, B., Kronberg, E., Blasberg, R., et al. (2002). Residual cerebral activity and behavioural fragments can remain in the persistently vegetative brain. *Brain* 125, 1210–1234. doi:10.1093/brain/awf131.

Schnakers, C., Vanhaudenhuyse, A., Giacino, J., Ventura, M., Boly, M., Majerus, S., et al. (2009). Diagnostic accuracy of the vegetative and minimally conscious state: Clinical consensus versus standardized neurobehavioral assessment. *BMC Neurol.* 9, 35. doi:10.1186/1471-2377-9-35.

Scholkmann, F., Kleiser, S., Metz, A. J., Zimmermann, R., Mata Pavia, J., Wolf, U., et al. (2014). A review on continuous wave functional near-infrared spectroscopy and imaging instrumentation and methodology. *Neuroimage* 85, 6–27.

Schomer, D., and Silva, F. Da eds. (2012). "Recording Principles: Analog and Digital Principles; Polarity and Field Determinations; Multimodal Monitoring; Polygraphy (EOG, EMG, ECG, SAO2)," in *Niedermeyer's electroencephalography: basic principles, clinical applications, and related fields* (Oxford University Press).

Schweiger, M., and Arridge, S. (2014). The Toast++ software suite for forward and inverse modeling in optical tomography. *J. Biomed. Opt.* 19, 040801. doi:10.1117/1.jbo.19.4.040801.

Schweiger, M., Arridge, S. R., and Delpy, D. T. (1993). Application of the finite-element method for the forward and inverse models in optical tomography. *J. Math. Imaging Vis.* 3, 263–283.

Scott, R. B., Minati, L., Dienes, Z., Critchley, H. D., and Seth, A. K. (2011). Detecting conscious awareness from involuntary autonomic responses. *Conscious. Cogn.* 20, 936–942. doi:10.1016/j.concog.2010.11.009.

Sellers, E. W., and Donchin, E. (2006). A P300-based brain-computer interface: initial tests by ALS patients. *Clin. Neurophysiol.* 117, 538–548.

Sharma, N., Baron, J. C., and Rowe, J. B. (2009). Motor imagery after stroke: Relating outcome to motor network connectivity. *Ann. Neurol.* 66, 604–616. doi:10.1002/ana.21810.

Shen, Y.-W., and Lin, Y.-P. (2019). Challenge for Affective Brain-Computer Interfaces: Non-stationary Spatio-spectral EEG Oscillations of Emotional Responses. *Front. Hum. Neurosci.* 13, 366. doi:10.3389/fnhum.2019.00366.

Shiel, A., Horn, S. A., Wilson, B. A., Watson, M. J., Campbell, M. J., and McLellan, D. L. (2000).

The wessex head injury matrix (WHIM) main scale: A preliminary report on a scale to assess and monitor patient recovery after severe head injury. *Clin. Rehabil.* 14, 408–416. doi:10.1191/0269215500cr326oa.

Shin, J., Kwon, J., and Im, C.-H. (2018). A Ternary Hybrid EEG-NIRS Brain-Computer Interface for the Classification of Brain Activation Patterns during Mental Arithmetic, Motor Imagery, and Idle State. *Front. Neuroinform.* 12, 5. doi:10.3389/fninf.2018.00005.

Shin, J., Müller, K. R., and Hwang, H. J. (2016). Near-infrared spectroscopy (NIRS)-based eyes-closed brain-computer interface (BCI) using prefrontal cortex activation due to mental arithmetic. *Sci. Rep.* 6, 36203. doi:10.1038/srep36203.

Shin, J., Von Luhmann, A., Blankertz, B., Kim, D. W., Jeong, J., Hwang, H. J., et al. (2017). Open Access Dataset for EEG+NIRS Single-Trial Classification. *IEEE Trans. Neural Syst. Rehabil. Eng.* 25, 1735–1745. doi:10.1109/TNSRE.2016.2628057.

Shmuel, A., Yacoub, E., Chaimow, D., Logothetis, N. K., and Ugurbil, K. (2007). Spatio-temporal point-spread function of fMRI signal in human gray matter at 7 Tesla. *Neuroimage* 35, 539–552. doi:10.1016/j.neuroimage.2006.12.030.

Silvoni, S., Ramos-Murguialday, A., Cavinato, M., Volpato, C., Cisotto, G., Turolla, A., et al. (2011). Brain-computer interface in stroke: A review of progress. *Clin. EEG Neurosci.* 42, 245–252. doi:10.1177/155005941104200410.

Sitaram, R., Lee, S., Ruiz, S., Rana, M., Veit, R., and Birbaumer, N. (2011). Real-time support vector classification and feedback of multiple emotional brain states. *Neuroimage* 56, 753–765. doi:10.1016/j.neuroimage.2010.08.007.

Sitaram, R., Zhang, H., Guan, C., Thulasidas, M., Hoshi, Y., Ishikawa, A., et al. (2007). Temporal classification of multichannel near-infrared spectroscopy signals of motor imagery for developing a brain-computer interface. *Neuroimage* 34, 1416–1427.

Smith, S. M., Jenkinson, M., Woolrich, M. W., Beckmann, C. F., Behrens, T. E. J., Johansen-Berg, H., et al. (2004). Advances in functional and structural MR image analysis and implementation as FSL. *Neuroimage* 23, S208–S219.

Solis-Escalante, T., Müller-Putz, G. R., Pfurtscheller, G., and Neuper, C. (2012). Cue-induced beta

rebound during withholding of overt and covert foot movement. *Clin. Neurophysiol.* 123, 1182–1190. doi:10.1016/j.clinph.2012.01.013.

Solodkin, A., Hlustik, P., Chen, E. E., and Small, S. L. (2004). Fine Modulation in Network Activation during Motor Execution and Motor Imagery. *Cereb. Cortex* 14, 1246–1255. doi:10.1093/cercor/bhh086.

Stippich, C., Ochmann, H., and Sartor, K. (2002). Somatotopic mapping of the human primary sensorimotor cortex during motor imagery and motor execution by functional magnetic resonance imaging. *Neurosci. Lett.* 331, 50–54. doi:10.1016/S0304-3940(02)00826-1.

Stoll, J., Chatelle, C., Carter, O., Koch, C., Laureys, S., and Einhäuser, W. (2013). Pupil responses allow communication in locked-in syndrome patients. *Curr. Biol.* 23, R647–R648. doi:10.1016/j.cub.2013.06.011.

Strangman, G., Boas, D. A., and Sutton, J. P. (2002). Non-invasive neuroimaging using near-infrared light. *Biol. Psychiatry* 52, 679–693.

Strangman, G. E., Li, Z., and Zhang, Q. (2013). Depth Sensitivity and Source-Detector Separations for Near Infrared Spectroscopy Based on the Colin27 Brain Template. *PLoS One* 8, e66319. doi:10.1371/journal.pone.0066319.

Strangman, G. E., Zhang, Q., and Li, Z. (2014). Scalp and skull influence on near infrared photon propagation in the Colin27 brain template. *Neuroimage* 85, 136–149.

Strother, S. C. (2006). Evaluating fMRI preprocessing pipelines. *IEEE Eng. Med. Biol. Mag.* 25, 27–41.

Syam, S. H.-F., Lakany, H., Ahmad, R. B., and Conway, B. A. (2017). Comparing Common Average Referencing to Laplacian Referencing in Detecting Imagination and Intention of Movement for Brain Computer Interface. in *2017 International Conference on Emerging Electronic Solutions for IoT (ICEESI)*, 01028. doi:10.1051/MATECCONF/201714001028.

Szameitat, A. J., Shen, S., and Sterr, A. (2007). Motor imagery of complex everyday movements. An fMRI study. *Neuroimage* 34, 702–713. doi:10.1016/j.neuroimage.2006.09.033.

Tachtsidis, I., and Scholkmann, F. (2016). False positives and false negatives in functional near-infrared spectroscopy: issues, challenges, and the way forward. *Neurophotonics* 3, 31405.

doi:10.1117/1.NPh.3.3.031405.

Tam, W. K., Ke, Z., and Tong, K. Y. (2011). Performance of common spatial pattern under a smaller set of EEG electrodes in brain-computer interface on chronic stroke patients: A multi-session dataset study. in *2011 Annual International Conference of the IEEE Engineering in Medicine and Biology Society* (Boston, MA), 6344–6347. doi:10.1109/IEMBS.2011.6091566.

Tavakolan, M., Yong, X., Zhang, X., and Menon, C. (2016). Classification scheme for arm motor imagery. *J. Med. Biol. Eng.* 36, 12–21. doi:10.1007/s40846-016-0102-7.

The Multi-Society Task Force on PVS (1994). Medical aspects of the persistent vegetative state (1). *N. Engl. J. Med.* 330, 1499–508. doi:10.1056/NEJM199405263302107.

Van Oostende, S., Van Hecke, P., Sunaert, S., Nuttin, B., and Marchal, G. (1997). FMRI studies of the supplementary motor area and the premotor cortex. *Neuroimage* 6, 181–90. doi:10.1006/nimg.1997.0287.

Vanni, S., Revonsuo, A., and Hari, R. (1997). Modulation of the parieto-occipital alpha rhythm during object detection. *J. Neurosci.* 17, 7141–7147. doi:10.1523/jneurosci.17-18-07141.1997.

Velliste, M., Perel, S., Spalding, M. C., Whitford, A. S., and Schwartz, A. B. (2008). Cortical control of a prosthetic arm for self-feeding. *Nature* 453, 1098–1101.

Verstynen, T., Diedrichsen, J., Albert, N., Aparicio, P., and Ivry, R. B. (2005). Ipsilateral Motor Cortex Activity During Unimanual Hand Movements Relates to Task Complexity. *J. Neurophysiol.* 93, 1209–1222.

Villringer, A., and Chance, B. (1997). Non-invasive optical spectroscopy and imaging of human brain function. *Trends Neurosci.* 20, 435–442.

Virtanen, J., Noponen, T., and Merilainen, P. (2009). Comparison of principal and independent component analysis in removing extracerebral interference from near-infrared spectroscopy signals. *J. Biomed. Opt.* 14, 54032. doi:10.1117/1.3253323.

Vogel, D., Markl, A., Yu, T., Kotchoubey, B., Lang, S., and Müller, F. (2013). Can mental imagery functional magnetic resonance imaging predict recovery in patients with disorders of consciousness? *Arch. Phys. Med. Rehabil.* 94, 1891–1898. doi:10.1016/j.apmr.2012.11.053.

Wang, T., Deng, J., and He, B. (2004). Classifying EEG-based motor imagery tasks by means of

time-frequency synthesized spatial patterns. *Clin. Neurophysiol.* 115, 2744–2753. doi:10.1016/j.clinph.2004.06.022.

Wang, T., and He, B. (2004). An Efficient Rhythmic Component Expression and Weighting Synthesis Strategy for Classifying Motor Imagery EEG in a Brain-Computer Interface. *J. Neural Eng.* 1. doi:10.1088/1741-2560/1/1/001.

Wang, Y., Gao, S., and Gao, X. (2005). Common Spatial Pattern Method for Channel Selelction in Motor Imagery Based Brain-computer Interface. in *2005 IEEE Engineering in Medicine and Biology 27th Annual Conference*, 5392–5395. doi:10.1109/IEMBS.2005.1615701.

Wang, Z., Cao, L., Zhang, Z., Gong, X., Sun, Y., and Wang, H. (2018). Short time Fourier transformation and deep neural networks for motor imagery brain computer interface recognition. *Concurr. Comput. Pract. Exp.* 30, e4413. doi:10.1002/cpe.4413.

White, B. R., and Culver, J. P. (2010). Quantitative evaluation of high-density diffuse optical tomography: in vivo resolution and mapping performance. *J. Biomed. Opt.* 15, 026006. doi:10.1117/1.3368999.

Wilson, T. W., Kurz, M. J., and Arpin, D. J. (2014). Functional specialization within the supplementary motor area: a fNIRS study of bimanual coordination. *Neuroimage* 85, 445–450.

Wold, S., Esbensen, K., and Geladi, P. (1987). Principal component analysis. *Chemom. Intell. Lab. Syst.* 2, 37–52. doi:10.1016/0169-7439(87)80084-9.

Wolf, M., Wolf, U., Choi, J. H., Gupta, R., Safonova, L. P., Paunescu, L. A., et al. (2002). Functional frequency-domain near-infrared spectroscopy detects fast neuronal signal in the motor cortex. *Neuroimage* 17, 1868–1875.

Wolpaw, J. R., Birbaumer, N., McFarland, D. J., Pfurtscheller, G., and Vaughan, T. M. (2002). Brain–computer interfaces for communication and control. *Clin. Neurophysiol.* 113, 767–791.

Wriessnegger, S. C., Brunner, C., and Müller-Putz, G. R. (2018). Frequency specific cortical dynamics during motor imagery are influenced by prior physical activity. *Front. Psychol.* 9, 1976. doi:10.3389/fpsyg.2018.01976.

Wriessnegger, S. C., Kurzmann, J., and Neuper, C. (2008). Spatio-temporal differences in brain oxygenation between movement execution and imagery: A multichannel near-infrared

spectroscopy study. *Int. J. Psychophysiol.* 67, 54–63.

Wriessnegger, S. C., Steyrl, D., Koschutnig, K., and Müller-Putz, G. R. (2014). Short time sports exercise boosts motor imagery patterns: Implications of mental practice in rehabilitation programs. *Front. Hum. Neurosci.* 8, 469. doi:10.3389/fnhum.2014.00469.

Yang, Y., Chevallier, S., Wiart, J., and Bloch, I. (2014). Time-frequency optimization for discrimination between imagination of right and left hand movements based on two bipolar electroencephalography channels. *EURASIP J. Adv. Signal Process.* 2014, 38. doi:10.1186/1687-6180-2014-38.

Yao, D., Qin, Y., Hu, S., Dong, L., Bringas Vega, M. L., and Valdés Sosa, P. A. (2019). Which Reference Should We Use for EEG and ERP practice? *Brain Topogr.* 32, 530–549. doi:10.1007/s10548-019-00707-x.

Yeom, S.-K., Won, D.-O., Chi, S. I., Seo, K.-S., Kim, H. J., Müller, K.-R., et al. (2017). Spatio-temporal dynamics of multimodal EEG-fNIRS signals in the loss and recovery of consciousness under sedation using midazolam and propofol. *PLoS One* 12, e0187743. doi:10.1371/journal.pone.0187743.

Yi, W., Qiu, S., Qi, H., Zhang, L., Wan, B., and Ming, D. (2013). EEG feature comparison and classification of simple and compound limb motor imagery. *J. Neuroeng. Rehabil.* 10, 106. doi:10.1186/1743-0003-10-106.

Yokoyama, N., Ohtaka, C., Kato, K., Kubo, H., and Nakata, H. (2019). The difference in hemodynamic responses between dominant and non-dominant hands during muscle contraction and relaxation: An fNIRS study. *PLoS One* 14, e0220100. doi:10.1371/journal.pone.0220100.

Yong, X., and Menon, C. (2015). EEG classification of different imaginary movements within the same limb. *PLoS One* 10, e0121896. doi:10.1371/journal.pone.0121896.

Yong, X., Ward, R. K., and Birch, G. E. (2008). Robust common spatial patterns for EEG signal preprocessing. in *2008 30th Annual International Conference of the IEEE Engineering in Medicine and Biology Society*, 2087–2090. doi:10.1109/iembs.2008.4649604.

Yorkey, T. J., Webster, J. G., and Tompkins, W. J. (1987). Comparing Reconstruction Algorithms for Electrical Impedance Tomography. *IEEE Trans. Biomed. Eng.* BME-34, 843–852.

doi:10.1109/TBME.1987.326032.

Yucel, M. A., Aasted, C. M., Petkov, M. P., Borsook, D., Boas, D. A., and Becerra, L. (2015). Specificity of hemodynamic brain responses to painful stimuli: a functional near-infrared spectroscopy study. *Sci. Rep.* 5, 9469. doi:10.1038/srep09469.

Yücel, M. A., Selb, J., Aasted, C. M., Petkov, M. P., Becerra, L., Borsook, D., et al. (2015). Short separation regression improves statistical significance and better localizes the hemodynamic response obtained by near-infrared spectroscopy for tasks with differing autonomic responses. *Neurophotonics* 2, 35005. doi:10.1117/1.NPh.2.3.035005.

Zaramella, P., Freato, F., Amigoni, A., Salvadori, S., Marangoni, P., Suppjei, A., et al. (2001). Brain Auditory Activation Measured by Near-Infrared Spectroscopy (NIRS) in Neonates. *Pediatr Res* 49, 213–219.

Zeff, B. W., White, B. R., Dehghani, H., Schlaggar, B. L., and Culver, J. P. (2007). Retinotopic mapping of adult human visual cortex with high-density diffuse optical tomography. *Proc. Natl. Acad. Sci.* 104, 12169–12174. doi:10.1073/pnas.0611266104.

Zeman, A. (2001). Consciousness. *Brain* 124, 1263–1289. doi:10.1093/brain/124.7.1263.

Zhang, R., Xiao, X., Liu, Z., Jiang, W., Li, J., Cao, Y., et al. (2018a). A new motor imagery EEG classification method FB-TRCSP+RF based on CSP and random forest. *IEEE Access* 6, 44944–44950. doi:10.1109/ACCESS.2018.2860633.

Zhang, S., Zheng, Y., Wang, D., Wang, L., Ma, J., Zhang, J., et al. (2017a). Application of a common spatial pattern-based algorithm for an fNIRS-based motor imagery brain-computer interface. *Neurosci. Lett.* 655, 35–40.

Zhang, X., Yong, X., and Menon, C. (2017b). Evaluating the versatility of EEG models generated from motor imagery tasks: An exploratory investigation on upper-limb elbow-centered motor imagery tasks. *PLoS One* 12, e0188293. doi:10.1371/journal.pone.0188293.

Zhang, Y., Yang, Y., Si, J., Xia, X., He, J., and Jiang, T. (2018b). Influence of inter-stimulus interval of spinal cord stimulation in patients with disorders of consciousness: A preliminary functional near-infrared spectroscopy study. *NeuroImage Clin.* 17, 1–9.

Zich, C., Debener, S., Thoene, A.-K., Chen, L.-C., and Kranczioch, C. (2016). Simultaneous EEG-

fNIRS reveals how age and feedback affect motor imagery signatures. *Neurobiol. Aging* 49, 183–197.

Appendix

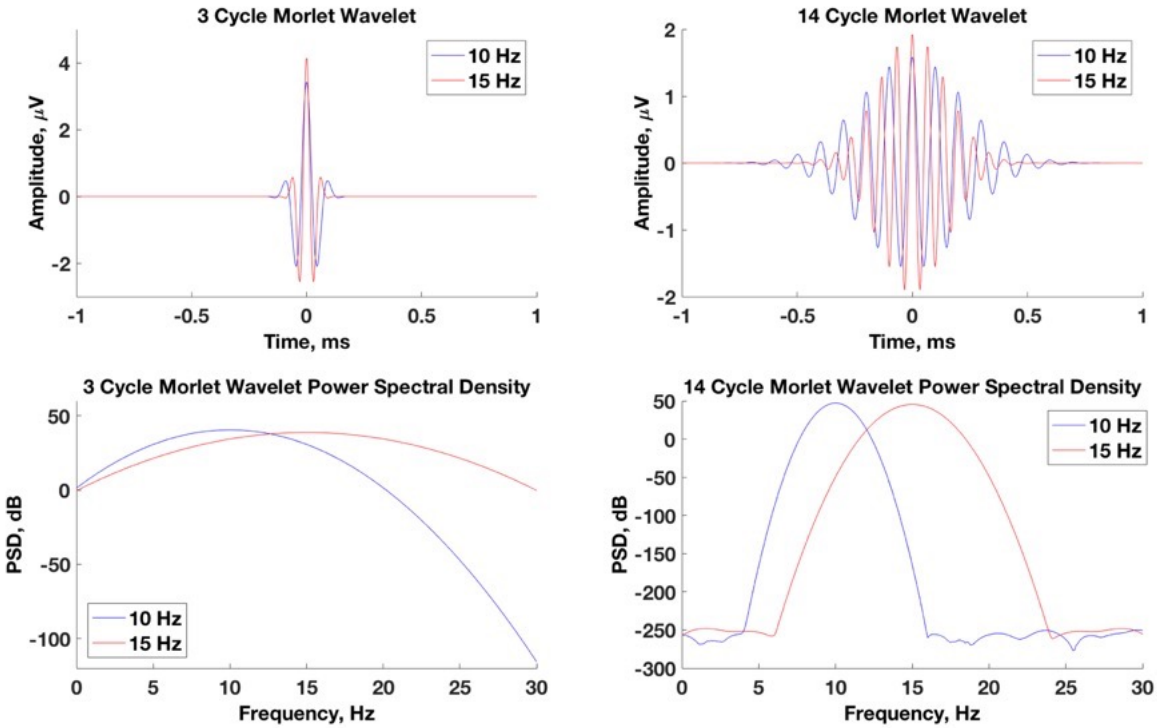

Figure AF2.1: Effect of complex Morlet wavelet cycle number on time series signal convolution. Convolution of the time series signal with the complex Morlet wavelet yields a complex-valued signal from which instantaneous power can be extracted at each time point. Presented here are examples of 10 and 15 Hz centered wavelets and their corresponding power spectral densities. The number of cycles, which defines the width of the Gaussian taper has significant importance for controlling the trade-off between temporal and frequency precision. A narrow Gaussian (small number of cycles) leads to an increased temporal precision at the cost of decreased spectral precision, and vice versa for a wider Gaussian. Here the three-cycle wavelet is more sensitive to transient activations whereas the fourteen-cycle wavelet is more sensitive to longer activations at specific frequencies.

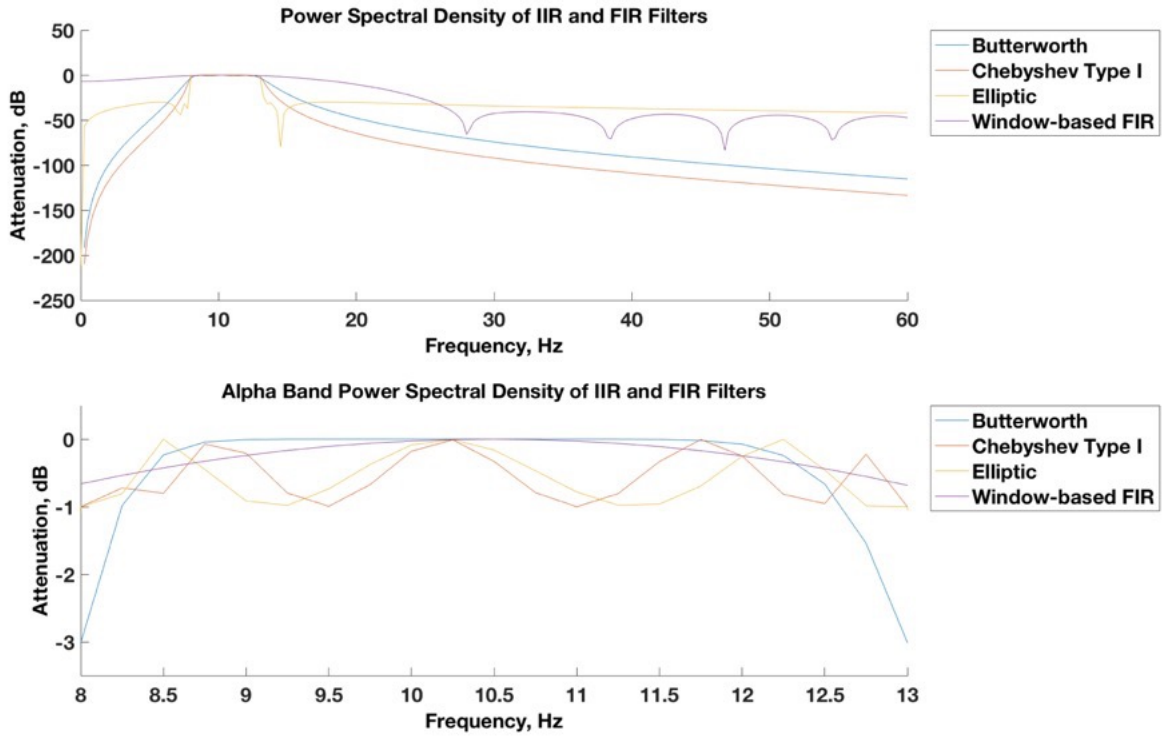

Figure AF2.2: Power spectral density of different finite impulse response (FIR) and infinite impulse response (IIR) filters. A systems impulse response is the output signal that results from input of an impulse, i.e. a short duration time domain signal. An IIR filters response is a slow and infinitely decays towards zero, whereas a FIR filters response is a settling to zero in finite time (top plot). The termination of the FIR filter kernels response (and a decay to zero amplitude in the time domain) is marked by an oscillatory component in the stop band. FIR (e.g. windowed linear phase) and IIR (e.g. Butterworth, Chebyshev and Elliptic) filters are suggested to provide extra frequency specificity by plateauing maximally in the desired pass band (top plot). However, a detailed inspection of these responses reveals (bottom plot) that only the window-based FIR and Butterworth IIR filters are maximally flat in the passband whereas the others generate ripple artifacts in the frequency response. Of both the window-based FIR and Butterworth IIR filters, the latter is preferred as it allows for a sharper transition zone in the frequency response without introducing ringing artifacts in the time domain.

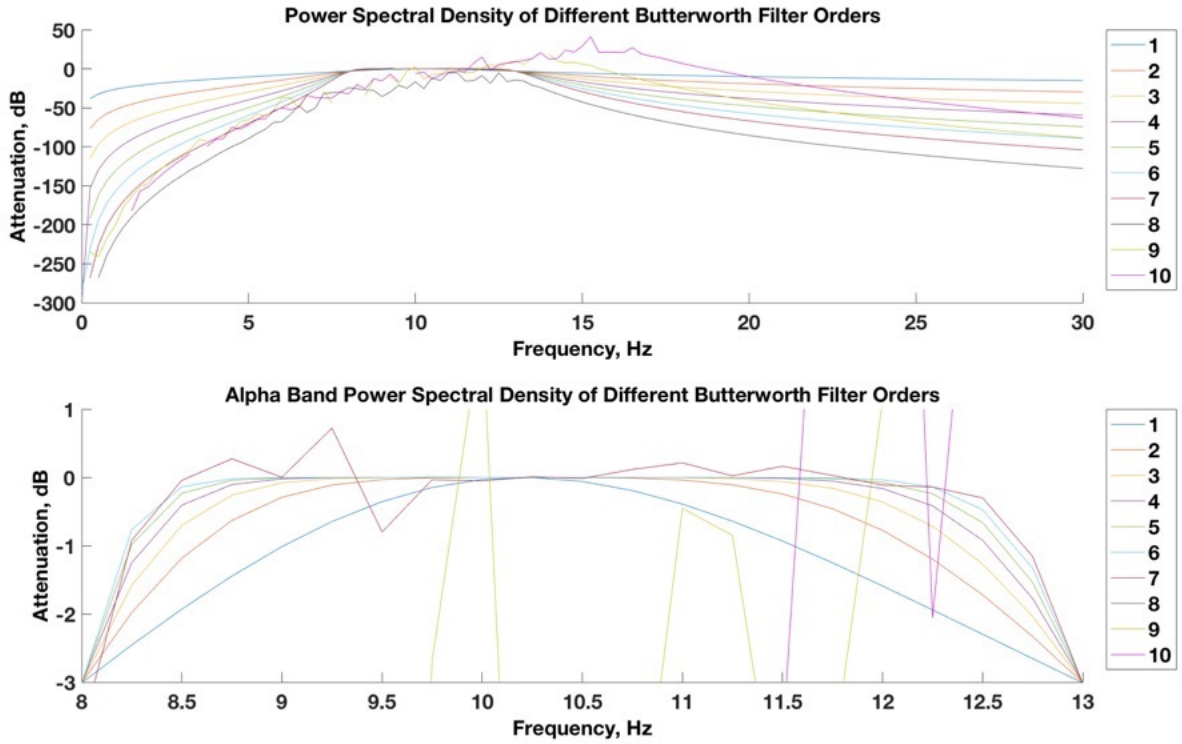

Figure AF2.3: Effect of order number on the Butterworth filters response. The quality of a Butterworth filters response is dependent on its order which governs its frequency precision. Very low filter orders (1-3) attenuate much more of the desired alpha band whereas at higher orders (7-10) breaks and ripples are more prominent in both the pass and stop bands.

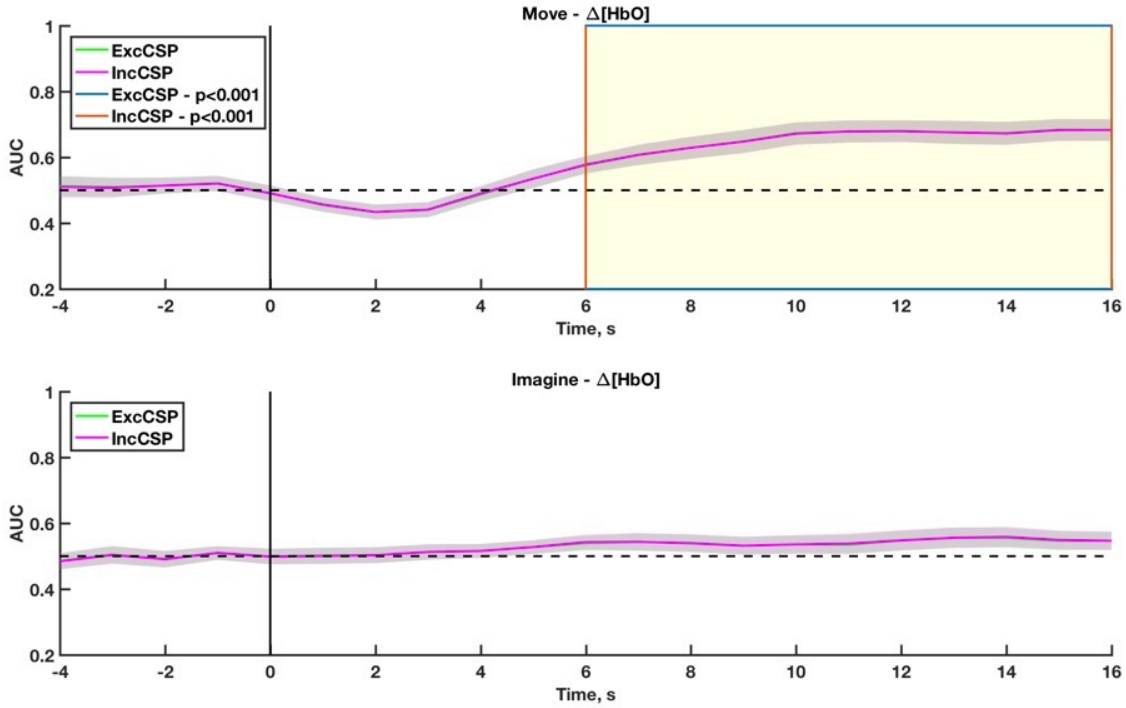

Figure AF3.1: Group average classification scores for each sliding time window having excluded or included CSP-pre-processing as part of the feature extraction process. Results are presented for physical movement and imagery tasks having classified left- and right-hand statistical features from Δ[HbO] signals derived using frequency domain measurements. These plots demonstrate identical maximum AUC values for CSP-excluding and -including classification during physical movement (peak AUC of 0.68, $p<0.05$) and imagery (peak AUC of 0.56) tasks.

Table AT3.1: Group average maximum classification scores for different statistical features and sliding window lengths. Presented here are group average maximum AUC scores that have additionally been averaged between the results obtained from both the physical movement and imagery tasks. A sliding window length between 5-9 s appears to be most effective. Furthermore, of the six statistical features tested, both the mean and the peak appear to generate the highest classification scores with AUC values greater than 60%.

Sliding window length (s)	**Average peak AUC**					
	Mean	**Variance**	**Slope**	**Peak**	**Skewness**	**Kurtosis**
1	0.61	0.53	0.60	0.60	0.54	0.54
2	0.62	0.53	0.54	0.61	0.54	0.54
3	0.62	0.53	0.59	0.61	0.52	0.52
4	0.62	0.53	0.55	0.62	0.53	0.53
5	0.63	0.53	0.59	0.62	0.52	0.53
6	0.63	0.55	0.54	0.62	0.54	0.54
7	0.63	0.54	0.60	0.63	0.54	0.52
8	**0.63**	**0.54**	**0.57**	**0.63**	**0.54**	**0.53**
9	0.63	0.55	0.60	0.62	0.53	0.52
10	0.63	0.55	0.59	0.63	0.53	0.52